Università degli Studi di Salerno
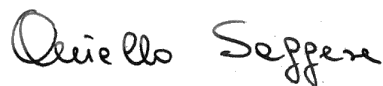
Dipartimento di Fisica *"E.R.Caianiello"*

_____

Dottorato di ricerca in Matematica, Fisica ed Applicazioni

Curriculum in Fisica – XXXII ciclo – Nuova Serie

Tesi di dottorato in
Applied Superconductivity to Accelerator Magnets

Dr. Aniello Saggese

Coordinatore: Prof. Carmine Attanasio   Tutor: Prof. Salvatore De Pasquale

Co-Tutor: Dr. Umberto Gambardella

Anno Accademico 2019/20

To my lovely father and mother.

They have grown a son free to do what he wishes to do

Acknowledgements

I wish to thank my thesis tutor and all the people that, with their help, contributed to the realization of this research. The first and most important is my guide through all this work. He was my inspiring light, with his unique ability to calm my stress crises, and at the same time, to give me so many useful advice, and suggestions. Thank you, Umberto, without you this work would have been different, and surely much less interesting. On my shoulders, I had two angels, Gerardo and Domenico. Their careful reading of the manuscript and their suggestions, allowed me to remember many things I have forgotten. Part of my experimental activity, consisting of the test on the dipoles and on the first quadrupole module, was carried out at the GSI in Darmstadt. I wish to thank all the engineers that spent their time explaining to me the many measures they routinely do on the modules and for letting me try, under their supervision, some measures by myself. They are too many and I really can't name everybody, but I remember all of them and I wish to thank all, for their patience in answering my, sometimes, silly questions. While staying in Darmstadt a person was really important for me. I wish to thank Anna for her warm friendship. Her guide through the GSI laboratories was precious for me, as well as the bike I borrowed from her. During the last three years, I have been very sick and hospitalized three times in three different hospitals with two surgeries. I wish to thank all doctors and nurses for my recovery and for letting me remain in good health. My last thanks go to my friend Amedeo and to my family. To manage a young student sometimes is difficult, but the management of a very old student is unbelievably difficult. But nevertheless, my family succeeded in doing it. Thanks a lot to all of you. This is now and will be forever, my lovely family.

Aniello Saggese

Table of Contents

4. Tests on SIS100 quadrupole modules

Introduction

The superconductivity, after more than a century from its discovery, has been applied in many fields with a wide range of devices based on this technology. More recently the research of the compounds with high critical temperature has been stimulated by the discovery of ceramic superconductors. The liquid nitrogen barrier seems more approaching, but presently the reliable applications are mostly confined to the liquid helium cryogenics.

From the point of view of the power applications of the superconductivity, the realization of superconducting cables, able to transport an almost lossless huge amount of electrical current and powerful magnets, able to reach magnetic fields impossible to obtain by using normal metals, has opened the way to applications unattainable in other ways. These power applications of superconductivity require the production of long superconducting wires with the highest possible current density. On the LTS, Low Temperature Superconductors, such as $Nb\,Ti$ or the Nb_3Sn, the development of the technology has achieved remarkable goals. The realization of cables, obtained by binding many wires with lengths of the order of kilometers, has made commercially available and nowadays they are mainly used to realize superconducting coils for magnets and other high current applications. The optimizations of the performances of the cables are not unique but have to be done considering the requests of each specific application. In the future, the new ceramic HTS, High Temperature Superconductors, such as the $ReBCO$, with their ability to carry huge currents in very high magnetic fields, will increase the possibilities of using superconductors.

This thesis may be considered made of four parts. In the first part, after a brief introduction, the cables made of both LTS and HTS superconducting wires and tapes are presented with their different fabrication processes. The properties of windings made using these cables and the problems related to their usage are described. The experimental technique for the characterization of these superconductors will close this section. In the second section, the problem of dissipation in a superconducting

5

wire is described, as it represents the main limitation when a device has to be designed. The phenomenon of the superconducting quench is discussed with the presentation of original analytical and numerical analysis and the experimental measurements on various samples and different techniques. The third and fourth parts introduce to the power application of superconductivity. In particular, the third part will deal with the problem of delivering high current to superconducting devices. After a short description of cryogenic high current leads our solution of superconducting high current leads for a specific application is presented. Finally, the fourth part is devoted to the electrical and cryogenic tests on the dipoles and quadrupoles. These magnets will be used in the new particle accelerator SIS100 for the FAIR project under construction at GSI laboratory in Darmstadt. The dipole and quadrupole modules testing activity at the GSI laboratory is briefly presented. This part of the research was carried out during my stay at the GSI laboratory in Darmstadt. Finally, the experimental apparatus build in our laboratory for the site acceptance test of the SIS100 quadrupole modules is described in detail. The electrical tests, as well as the other vacuum-tight and cryogenic tests, are described. A description of the final assembly of the modules and their management will end this work.

1

SUPERCONDUCTORS FOR HIGH CURRENT APPLICATIONS

1.1   Introduction

The age of superconductivity began in 1911. The ability to reach low temperatures, with what we now call cryogenic apparatus, and the discovery of the abrupt drop of the electrical resistance on mercury, and some other ordinary metals, opened this new research field. The temperature value, at which this sudden drop of the electrical resistance is observed, is the critical temperature T_C. Many metals and alloys become superconductors, each of them with its T_C value. Another feature is that the superconducting state is observed below T_C only up to a value of the transport electrical current, called critical current I_C. The critical current value is temperature-dependent: the more T approaches to T_C the lower is the I_C and becomes zero at $T = T_C$.

A more remarkable effect observed on the superconductors is the complete diamagnetisms. Meissner and Ochsenfeld first discovered this effect in 1934. [MS33] This effect consists of the complete expulsion of the magnetic field within the bulk of a superconductor. It is worth to remark that the perfect diamagnetism below T_C is a more specific finding because it automatically requires a complete loss of resistivity, but the reverse is not true.

The complete diamagnetism or Meissner effect below T_C may be canceled by the application of a magnetic field larger than the critical magnetic field H_C. The magnetic field H_C is temperature-dependent: the more T approaches to T_C the lower is H_C and, becomes zero at $T = T_C$.

After the exploitation of the superconductivity in metals, new kind of superconducting materials were discovered in metallic alloys. Nowadays superconducting materials may be separated into two categories. In the bulk superconductors of type I, the Meissner effect is present until a temperature-dependent critical magnetic field $H_C(T)$ is reached. On type II superconductors, there is a lower critical field $H_{C1}(T)$ above that the magnetic field starts to penetrate within the bulk superconductor in the form of flux quanta. The penetration will continue until the value of the magnetic field reaches the upper critical field $H_{C2}(T)$. Above $H_{C2}(T)$ the superconductor becomes completely normal. Besides the normal and the Meissner states, type II superconductors may also fall into a mixed state. In this state, the superconductivity is still present in the type II superconductors, but it coexists with the presence of tiny normal filaments where the magnetic field penetrates. Within the tiny normal zone, a magnetic flux quantum is present, so these filaments are called fluxons. These fluxons may move inside the bulk material and arrange themselves into an array-like structure known as Abrikosov lattice from the name of the scientist, which predicted it. [TN96]

In the following years, many other properties were discovered together with the advancement of the comprehension of the superconducting mechanisms. An early explanation of the superconducting phenomena began in 1935 with the phenomenological London model. In the electrodynamic London model, the external magnetic field in a bulk superconductor is completely shielded by mean of surface currents that flows only within a tiny shell having a thickness called London penetration depth λ_L. [TL90]

In the two fluids model of the Gorter and Casimir theory, the presence in the superconductor of two components of the electron fluids was considered.

The amount of these fluids was temperature-dependent on the superconducting component vanishing above the critical temperature. A model, based on the second-order thermodynamic phase transition is due to Ginzburg and Landau theory. Their theory introduces a complex order parameter ψ related to the density of the superconducting electrons. The Ginzburg-Landau equations can be obtained by minimizing the Free Energy respect to the variations in the order parameter ψ and the magnetic vector potential. Within this theory, the magnetic field penetration depth λ is recovered with the additional meaning of the magnetic penetration depth around the vortex lines, together with the addition of another characteristic length ξ known as coherence length. This length in the Ginzburg Landau model represents the density variation of the superconducting component and is a characteristic length for the variations of the order parameter ψ. The penetration depth $\lambda(T)$ and the coherence length $\xi(T)$ are both temperature-dependent and near T_C both diverge as $(T_C - T)^{-1/2}$ so that, their ratio $k = \lambda / \xi$ is nearly temperature independent. The ratio k is known as the Ginzburg Landau parameter and permits to distinguish between Type I and Type II superconductors. Abrikosov showed that the exact breakpoint between the two types was at $k = 1/\sqrt{2}$. For typical type I classic pure superconductors is $k < 1/\sqrt{2}$ while for the type II superconductors is $k > 1/\sqrt{2}$. [TN96]

The discovery of the isotope effect, found by measuring the critical temperature on separate mercury isotopes, proved that ion mass is important and lattice vibrations must be involved in the theory of superconductivity. Later on, after various attempts to build a microscopic theory able to explain this behavior, J.Bardeen, L.N.Cooper, and J.R.Schrieffer with their famous BCS theory, shed a light on this phenomenon. [SC99] The BCS theory was really successful in its explanation of the observed phenomena for 30 years, until the discovery of High-Temperature Superconductors or HTS. These, mainly ceramic compounds, were found with a critical temperature well above any value that

9

could be predicted by the BCS theory. Despite the development of materials and devices based on these new HTS composite superconducting materials, the comprehension of the mechanisms behind the behavior of this new class of HTS material is still not well understood. Many models have been developed but, a comprehensive theory, able to explain the behavior of all HTS, discovered so far and, perhaps, forecast new kind of compounds able to be used near room temperature, has not yet been found.

1.2 Technological applications

The first technological application of interest seen since the discovery of superconductivity was the construction of electromagnets. The comparison between normal conducting and superconducting technologies is with copper Cu wires. In air a Cu wire has a current density of the order of $4 \cdot 10^6 \, A/m^2$ and when water-cooled it can reach the values of $10^7 \, A/m^2$. Practically, with the exception of Bitter magnets [GA96], Cu magnets cooling, requirement, and the value of the current density, limits the maximum achievable field strength to $2 \, T$ in continuous mode. Two parameters are important in this comparison: the energy accumulated into the magnet and the power consumption to charge and keep it. The magnet energy is $(1/2) \, L \, I^2$, being L the inductance, and I the current bias to achieve the target field. The inductance L is a function of the geometry, while the field strength is related to the current bias. Being the current in a superconducting wire 100 times larger than the current in a copper wire of the same size, it turns out that for the same field the superconducting magnet is more compact with less wire, lower dimensions, and inductance. For a particular geometry, if a $100 \, m$ of superconducting wire is required, the corresponding Cu magnet will take $10000 \, m$. The resistance of $1 \, m$ of Cu wire with a diameter of $1.13 \, mm$ and resistivity $\rho = 1.72 \cdot 10^{-8} \, \Omega \, m$ is $17.2 \, m\Omega$ thus the whole magnet will be $172 \, \Omega$. If the bias current is $10 \, A$ it is evident that the normal Cu magnet will produce $17 \, kW$ of Joule heating, further the fact of requiring about $1700 \, V$ for the power supply. The corresponding superconducting magnet will dissipate nothing but the cryogenic cooler, which can be as low as few kW, depending on the quality of the thermal insulation. Incidentally, the power supply operates at negligible voltage, and also the energy for charging the magnets is reduced. In conclusion, the superconducting magnets would be able to generate a very strong magnetic field by using only the energy needed by cryogenic refrigerators. The generation of a constant high magnetic field with superconducting coils offers the additional possibility of the persistent mode.

In fact, a superconducting magnet once charged may be shorted on itself using a superconducting switch. In this way, it is possible to save part of the cryogenic losses by removing the resistive junction between the room temperature and the cold magnet terminals. [KY97]

This goal in 1911 and for the following four decades was just a dream. In fact, it was found that in pure metal and, in general, on the type I superconductors, the presence of superconductivity can be easily destroyed by increasing the flowing current above the threshold current density limit J_C known as critical current density. The superconducting state in these materials is also destroyed by the presence of a magnetic field above their small H_C value. On the other hand, for the construction of superconducting coils able to produce strong magnetic field high values for all these three parameters T_C, H_C and J_C are needed. In order to understand how these three parameters combine it is convenient to plot a three-dimensional graphic where they are represented as shown in Fig.1.01.

While the shape of the surface limiting the superconducting zone is similar for all superconductors, the values reported on the scales may change by orders of magnitude. Any material has a specific value of T_C , but its critical current and field, J_C and H_C, are properties that can be enhanced by adopting a suitable fabrication process. This becomes clear in 1961 when, using only metallurgical processes, it was possible to enhance dramatically the J_C value in the $NbTi$ superconducting wires. [BR61] [KN61]

All attempts to realize superconducting magnets, in the early days of the discovery of superconductivity, failed. These failures were due to the fact that, despite the known zero resistance state, the superconductors presented an intrinsic dissipation mechanism. Apart from pure metal type I superconductors, having values of the critical field H_C too weak to be usable in current transport applications, the type II superconductors have a much higher critical filed H_{C2}. In type II superconductors the fluxons feel the action of the Lorentz force under the current flow. The moving fluxons induce a magnetic flux variation,

which, according to Lenz's law, generates a voltage across the material. This voltage times the flowing current represents a heat dissipation, that, if not removed, heats-up the superconductor and at the end destroys the superconductivity. [WL02]
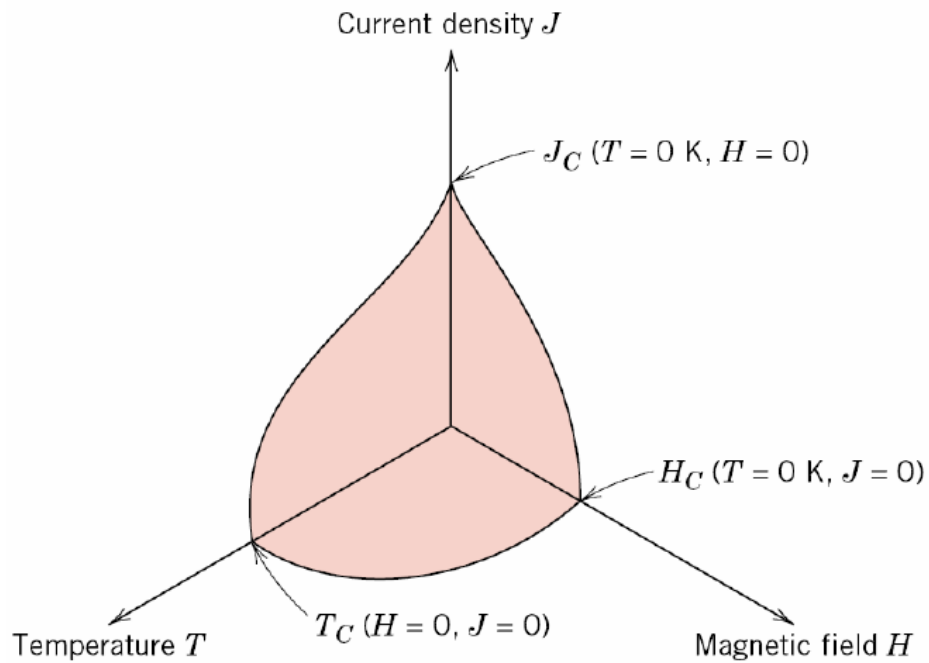
Fig.1.01 Graphic representation of the Temperature, Current Density, and Magnetic Field. Within the volume under the surface defined by these three parameters T_C, H_C, J_C the sample is in the superconducting state. Above this surface, the sample lays in the normal state.

In order to avoid these dissipations, several fabrication strategies have been applied. The most successful actions are based on freezing the fluxons movement by using the presence of structural defects or diluted impurities, called pinning centers. A pinning center is a localized point in the superconductor where the superconductivity is locally weakened. The fluxon into a pinning center needs less energy than in other parts of the superconductor, thus energetically speaking, they prefer to remain anchored to it. The presence of many pinning centers occupied by fluxons also called

frozen fluxons, make a magnetic barrier that contrasts the movements of the free fluxons. In conclusion, the pinning centers leads to higher critical currents. The artificial addition of diluted impurities may increase the pinning centers and also the value of the transport critical current. Unfortunately under certain conditions the Lorentz force, with the help of thermal excitation, may overcome the binding energy of some pinning centers and several fluxons may escape at the same time. Because of the thermal implication of fluxon movements, positive feedback is triggered until the complete destruction of the superconducting state. The flux jumping inconveniences may be reduced by reducing, both the flux motion and, the heat generated by the dissipations. Both targets may be reached by using a fine subdivision of the superconducting materials. The computation of the filament dimensions is presented in the section devoted to the thermal stability for a composite superconductor. [WL02] [CR01] [ST06] [ZH10]

On the following, the experimental measurement of the critical current J_C rely on the voltage detection, thus we define it not when the superconducting state is destroyed, but when a detectable dissipation occurs.

1.3   Technological devices

The large usage of the high current application of superconductivity is mainly based on the realization of superconducting magnets. Within this branch, there are small-scales applications and large-scale applications. After the pioneering research superconducting magnets were first considered as powerful tools on the research in physics and then applied in other areas of sciences. These areas are enlarging as well as the technological development can produce better magnets. In this paragraph, a small summary of the main application branch of the superconducting magnets is presented with a brief description of the peculiarities that characterize these magnets. [WL02]

Research Magnets: These magnets usually are small enough to be placed within a laboratory cryostat. The main applications of these magnets are in all the research experiments where high magnetic fields up to 15 T are needed in small volumes. These magnets are nowadays commercially available in the form of cylindrical solenoids of various dimensions and shapes. The applications are in solid-state physics and in particular in the superconductivity research as well and, in particular, when small material samples need to be magnetically characterized. Superconducting magnets are well suited for nuclear magnetic resonance measurements where a highly uniform magnetic field is needed. In particular, this application requires extremely stable magnetic field values, with a drift typically below $0.01\,ppm/h$, which can be obtained by coils placed in the persistent mode. Within this working modality, the magnet is first fed with a current up to the value needed to generate the required magnetic field, and then a superconducting "short circuit" is switched on. The ability to allow the lossless current circulation will avoid the currents decay and the magnetic field remains perfectly stable for a very long time like a permanent magnet. [KY97][YM88]

High Energy Particle Detectors: These magnets windings surrounding all the particle detectors apparatus placed into the collision specific areas of the particle beams. These magnets act only on the charged particles generated by the beam collision and bend their trajectories. From the measure of the curvature of their trajectories, it is possible to determine their momentum and identify their nature and the nuclear reaction from which they are generated. This particle identification method was successfully applied to bubble chambers using normal magnets. Nowadays, the higher energy of created particles by the beam collision and, the larger volumes of their detectors, require the construction of solenoids with inner volumes of hundred of cubic meters and magnetic fields with values impossible to achieve by using magnets made with copper windings. [NN16] [SC08]

High Energy particles Accelerators: The particle accelerators are usually made with a linear injector that creates a beam of particles that is feed into a high vacuum ring-shaped beam pipe where they are accelerated up to the required energy and directed to the collision areas. The trajectory of the charged particle beam in the accelerator ring is bent by the application of an ad hoc magnetic field. In order to bent particles, usually, high-energy protons with speeds close to the speed of light, very strong magnetic fields are needed. Moreover, since the beam particles accelerate, in order to keep the bending radius constant the bending magnetic field needs to increases accordingly. Superconducting dipole magnets, with a ramp shaped current feed, will provide the magnetic field high enough to apply the correct bending. [DV04] On the high energy accelerators there are also superconducting quadrupole and exapolar magnets that apply a magnetic field that can correct and focus the particle beam. For all these magnets, the simple solenoidal geometry is not adequate and special shapes of the winding configurations have been developed. [RS04] [KS09]

Controlled thermonuclear fusion: The controlled nuclear fusion requires the plasma confinement. The temperatures of million degrees, needed to ignite the reaction, in the tokamak reactors are such that only strong magnetic confinement can be used. In the past, confinement was done employing conventional magnets. Nowadays, the dimensions of the ITER reactor and the enormous dissipation that would be needed by copper windings require the use of superconducting magnets. Building these magnets it is not an easy task. The magnet cables have to be radiation resistant and the dimensions of this magnet are comparable with the size of a small building. [RZ13] [PN08]

Magnetic Resonance Imaging: Based on the Nuclear Magnetic Resonance principle this apparatus can generate a map of the object placed within it. The medical use of these instruments is the observation of the human body tissues and the detection of illnesses without surgery or the hazards related to the use of x-ray radiation. The required sensitivity needs a magnetic field of about 2 T on a space sufficient for a human body investigation. Only superconducting magnets can achieve the required temporal stability and space uniformity of the order of few parts per millions. The widespread of these instruments, is mainly limited by the cryogenic apparatus or the cost of liquid helium needed to keep the magnet at the liquid helium temperature. [BT82] Liquid nitrogen HTS magnets are under development. [SN17]

Superconducting Motors and Generators: The size of electrical motors and generators increases with the required or generated power. Motors and generators made with superconducting coils can be smaller and lighter than the corresponding conventional devices. Generators with higher power and less weight can be usefully mounted on the top of wind turbines. Smaller electrical motors can be successfully placed inside ships and be considered as a convenient replacement of the propulsion with internal combustion engines. [ST77] [KL06]

17

The Electrical Energy Storage: The Superconducting Magnetic Energy Storage or SMES systems consist of a superconducting coil that transforms the electrical energy into the magnetic energy. The lossless currents allow the storage of the energy for a long time and its quick extraction when it is required. Very large SMES can be used to smooth the daily load fluctuations of the electrical networks. Small or micro SMES can be used to guarantee the power quality to critical users who need high-quality electrical energy without flickering or small voltage shortages. The actual usage of large SMES is limited by the very high realization costs while small SMES prototypes show promising developments. [MN16]

There are many other applications based on the power superconductivity like the magnetic separation that may be successfully used in waste processing for the magnetic separation of ferrous waste. An interesting application of superconductivity is also the creation of magnetic levitation trains that can float on magnetic tracks propelled by magnetic field traveling waves. The availability of superconducting magnets with low energy consumption and lightweight my turn this dream into reality. With these trains, the travel would be smooth, with high speed and safety. A Japanese prototype train has been realized with a record speed of almost $600\,km/h$ without any moving part.

1.4 Tapes and wires

Superconducting wires cannot be realized by direct metallurgical processes on the nude superconducting material, for many reasons described in the next sec.1.6.2. They have to be considered as an ensemble of different metals, superconducting and non-superconducting, which have to be engineered for a peculiar usage. As an example, conductors to be used on ac applications, needs to be optimized, for the reduction of ac losses. This type of optimization is quite different than the optimization required if the same conductor has to be used for the construction of a magnet used in the dc regime applications.

The state of the art for the LTS based superconducting tapes and wires shows a well-established presence of different kinds of superconductors. A large mass of products is commercially available and more specific products are under production for fulfilling more particular needs. At the same time, the development of HTS based tapes is searching the way to replace the well-established niobium based LTS technological superconductors. The higher T_C of HTS materials opens the possibility to use cryocoolers instead of cryogenic liquids and opens the way to the realization of coils with magnetic fields unreachable by the LTS materials. In the following sections are presented a short overview of superconducting wires and tapes used in technological applications, as well as a summary of their features and property characterizations. [SN16]

1.4.1 LTS wires and cables

The most used and reliable LTS technical superconductors are the $NbTi$ alloy and the Nb_3Sn compounds. The fabrication process, for these two types of materials, has been subject to continuous developments with the improvement of the critical currents. The fabrication process of $NbTi$ multicore wires starts with the preparation of $NbTi$ alloy rods. The preparation of the $NbTi$ rods is obtained by the extrusion of a $NbTi$ billet placed inside a sealed copper tube. This process is repeated until a single rod is obtained. Because a final filament diameter of the tens of microns can carry less than one Ampere, it is necessary to put hundreds of filament in parallel. Stacking into another copper tube, hundred of rods do this. Hexagonal rods are preferred because the usual cylindrical rods when stacked inside a tube leave some empty space that should be avoided. Some copper strips are added on the boundaries to fill up completely this copper cylindrical billet. This billet is sealed, heated, and extruded again. The obtained multicore wire is twisted and then undergoes the final heat treatment in order to relax the tensile stress accumulated during the cold draw and then, at the end of the process, eventually tested. While thinner filaments are desirable, practical considerations during the stacking processes restrict the minimum diameter of the rods to about $1.5\ mm$. Thinner filaments may be obtained with a double stacking process where, in this case, the multicore wire is made with a hexagonal shape and then stacked again for another extrusion. The filament thicknesses cannot be as thin as possible, because, below a certain diameter, the elementary filaments become quite distorted with an increase of the *effective filament* diameter and therefore of the loss. At the beginning of the filaments process, before the first extrusion, the $NbTi$ billet must be protected by a niobium shield. This foil will protect the filaments by making a diffusion barrier. This barrier is needed because during the following heat treatments on the Cu - $NbTi$ interface of the cylindrical billet there could be the formation of $CuTi$ grains. These hard lumps do not deform during the extrusion and, at the

end of the wire fabrication process, the size of these grains becomes comparable with the filament diameter. The presence of these impurities causes filament distortion and, in extreme cases, filaments break. [WL08]

Beside the J_C optimization process, the continuous request of wires and cables having higher performances pushed the use of another technological superconducting material with higher T_C and H_{C2} values. These features are in Nb_3Sn material, that is already produced and commercially available. The Nb_3Sn unlike the $NbTi$ is a brittle intermetallic compound. Its crystal structure is of the $A15$ type like many other intermetallic compounds. Because of its brittle nature, the Nb_3Sn superconducting wires cannot be fabricated as the $NbTi$ wires. The most used fabrication technique consists of the bronze process [WL08]. In this process, niobium rods are placed into a $CuSn$ bronze matrix and then extruded. The magnets are then realized following the wind & react procedure: first, the magnet is wound and then final heat treatments at 575 °C provide the finest grain structure and then at 625 °C to accelerate the full Nb conversion to the Nb_3Sn. [PN08] The source of flux pinning is within the grain boundary, so a fine grain structure is required. Unfortunately, the optimization of T_C and H_C values can be achieved with long high-temperature treatments, but this also increases the grain size. The optimum heat treatment will be a compromise between the good stoichiometry and fine grain structure.

The internal-tin process is an alternative to the bronze process. In this process, the niobium rods are placed into a pure copper matrix and the tin is provided by a central core or by separate sources, distributed over the strand cross-section. The magnet heat treatment requires a low-temperature step at 200 °C with a slow temperature ramp. This long process allows better diffusion of tin into the copper matrix, with the creation of a tin rich bronze alloy, which promotes the reaction of tin with the niobium filaments. [RD00] In the Nb_3Sn cables recently developed for the ITER controlled nuclear fusion project, some $NbTi$ rods are added into the billet with a small addition of manganese in the copper matrix. The $NbTi$ rods are added because it has been found that the

usage of these composite filaments, enable them to effectively regulate the grains size of niobium on the copper-niobium sub-elements before the cold deformation by drawing. The manganese addition plays a positive influence on the kinetics of the Nb_3Sn formations and the reduction of the hysteresis loss. [SD10]

Large magnets with a fast ramping magnetic field require low inductance and large currents of the order of $10 \div 20\ kA$ or even more. To achieve these currents a cable with many wires have to be built. There is not a general-purpose cable that can fit all the needs, but the correct choice has to be made case-by-case and optimized by taking into account the particular application. Here some popular $NbTi$ and Nb_3Sn based cables with their characteristics are presented:

Rutherford cables: This type of cable has been developed for several particle accelerator magnets. The Fig.1.02 shows the typical section of a Rutherford cross-section of the LHC cable.
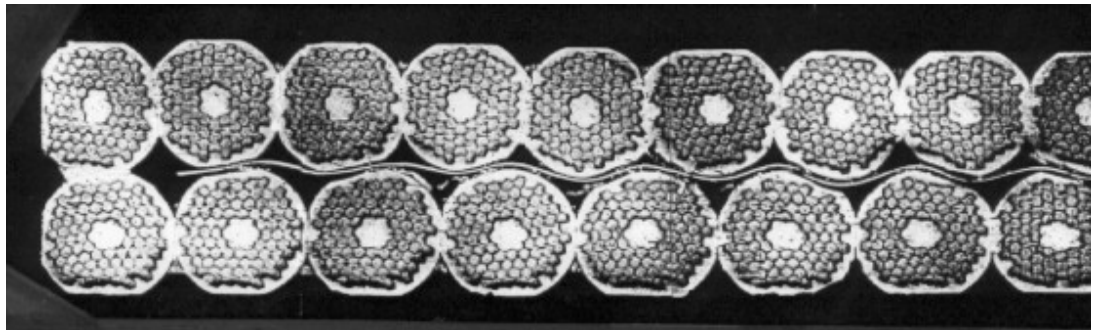

Fig.1.02 Cross-section of the left part of a Rutherford cable used at LHC accelerator.

The Rutherford cables are usually made with $20 \div 40\ NbTi$ strands assembled together and arranged into a rectangular shape. The cable is transposed because in this way it is possible to control the resistance and inductance homogeneity among the strands. The unbalance of the electrical impedances among strands leads to an unbalance of the current distribution and then a reduction of the comprehensive critical current of the cable and

improves the magnetic field homogeneity, which is an important factor in the accelerator magnets. The Rutherford cable is kept porous so that the helium may penetrate inside the windings and improve its thermal stability. One of the two kinds of Rutherford cable used on the LHC is made with 28 strands. Each strand, with a diameter of $1.065\,mm$, is made of 8800 filaments, with a diameter of $7\,\mu m$. The averaged critical current of a single strand, at the working temperature of $1.9\,K$ and in the presence of a magnetic field of 10 T is $515\,A$. The LHC dipole magnets cable has been designed to generate a magnetic field up $9\,T$ but it operates at $8.3\,T$ with a working temperature of $1.9\,K$ obtained with pressurized superfluid helium. The small value of the inductance chosen for these cables requires, for the main dipoles and quadrupoles, a transport current of about $12\,kA$. [RS04].

The ITER cables: The magnetic field strength for confining the plasma in the fusion reactor requires a rapid change of the magnetic field in case of plasma disruption. Because the magnets are also very large, the required currents may be up to $50\,kA$. The International Thermonuclear Experimental Reactor ITER adopted a Cable in Conduit Conductor containing a thousand wires with a diameter of less than a millimeter of fine Nb_3Sn filaments. The Nb_3Sn choice is due to the large operating field, up to $13\,T$, required. In order to support large electromagnetic forces, the cable is enclosed into a stainless steel jacket. The example of one of the cables of the ITER coil is shown in Fig.1.03.

Fig.1.03 Cross-section of the 1080 strands on a CICC cable of the ITER coil.

This cable made of 1080 strands is divided into six sub-cables twisted around a central stainless steel helicoidal tape. The cooling is obtained by using a forced flow of supercritical helium at the temperature $T_0 \approx 5K$ and a pressure $p \approx 0.6\ MPa$ [ZN06]. The cryogenic fluid freely flows in the central hole and also wets the strands improving the overall cable cooling. A stainless steel foil is wrapped around each sub-cable in order to improve the transverse resistance. Another stainless foil surrounds and holds all sub-cables together. Each sub-cable consists of standard Litz cables where, three strands are twisted together, in order to improve the uniformity of the current sharing. The twisted Litz cables are twisted again and again until all strands are grouped. The ITER sub-cables are made of 3 x 3 x 4 x 5 Litz cables.

The Nuclotron cables: This kind of cable, developed at the Joint Institute for Nuclear Research, JINR in Dubna, has been the choice for the fast ramped superconducting dipoles and quadrupoles of the new SIS100 accelerator at the GSI in Darmstadt. The Fig.1.04 shows a schematic design of this Nuclotron cable. [KH05]
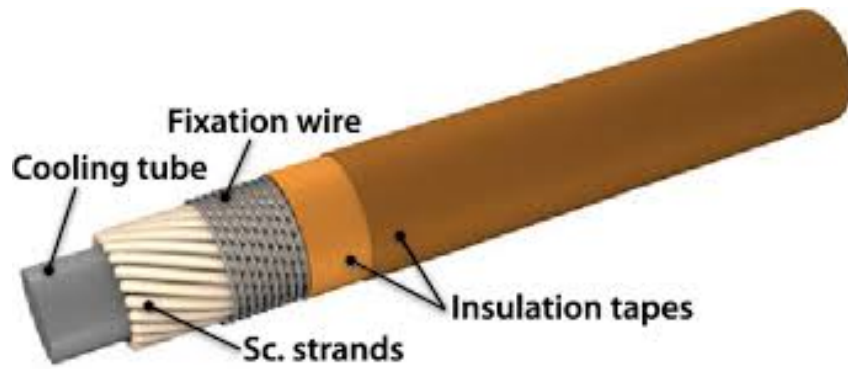
Fig.1.04 Schematic design of the Nucletron cable for the SIS100 coils.

On a $CuNi$ tube, there is only one layer of 23 $NbTi$ strands with a diameter of $0.8\ mm$. In the strands, each filament has a diameter of $2.9\ \mu m$. A $NiCr$ fixation wire surrounds the strands and the cable is protected with two layers of polyimide insulation tape. The superconducting strands are cooled with the liquid helium flowing into the $CuNi$ tube. With this cable at the GSI, a dipole with a single layer with an 8-turn coil has been realized. This coil can reach a peak magnetic field of $1.9\ T$ with a ramped cycled frequency of $1\ Hz$. [SC14]

1.4.2 HTS wires, tapes and cables

The recent discovery of High-Temperature Superconducting materials HTS with their T_C mostly above the Liquid Nitrogen LN boiling temperature and H_C higher than the LTS material have been seen as a valid improvement for superconducting magnets. Unfortunately, the brittle nature of this ceramic material needed the development of new fabrication technologies. Nowadays after more than thirty years of research HTS wires and tapes are now available in kilometer lengths, which supported the development of technological applications. [DM16] Two main production processes are available for the realization of tapes and cables with HTS materials: the Powder In Tube or PIT process and the Coating technology.

The PIT process is used for making cables and tapes of MgB_2 and the ceramic cuprate superconductors of the $BSCCO$ family. In this process, a pipe is filled with a fine superconducting powder and undergoes several press deformations to realize thin pipes. In $BSCCO$ due to the reaction with oxygen, a silver pipe must be used. If needed the pipes are heated in order to make a chemical reaction of the precursors' components. These pipes with the superconducting cores are bundled together into metallic sheaths and squeezed into composite tapes and wires that are not so flexible as LTS but still usable for several applications. [VN07]

The Rare-earth Barium Copper Oxides or $ReBCO$ based on Yttrium and Gadolinium Rare-earth, known as Second Generation 2G-HTS, cannot use the PIT process because of their grain boundaries properties: to overcome this a thin film coating technique has been developed. $ReBCO$ films require a substrate with an adequate crystal structure to generate bi-dimensional texture. This fabrication process is based on the deposition of the $ReBCO$ on a metallic substrate coated with a buffer stack that acts as a lattice match buffer layers for the c-axis oriented groth of the film. The rather complex structure of these $ReBCO$ tapes is shown in Fig.1.05 for a tape fabricated by the

26

Superpower©. This tape is obtained with the Metal Oxide Chemical Vapor Deposition or $MOCVD$ by growing $1.6\,\mu m$ of $ReBCO$ film on a buffer stack layer. This buffer-stack with a thickness of about $0.2\,\mu m$ is obtained by using the Ion Beam Assisted Deposition or $IBAD$ process. The deposition is done on a Hastelloy substrate needed for mechanical support.
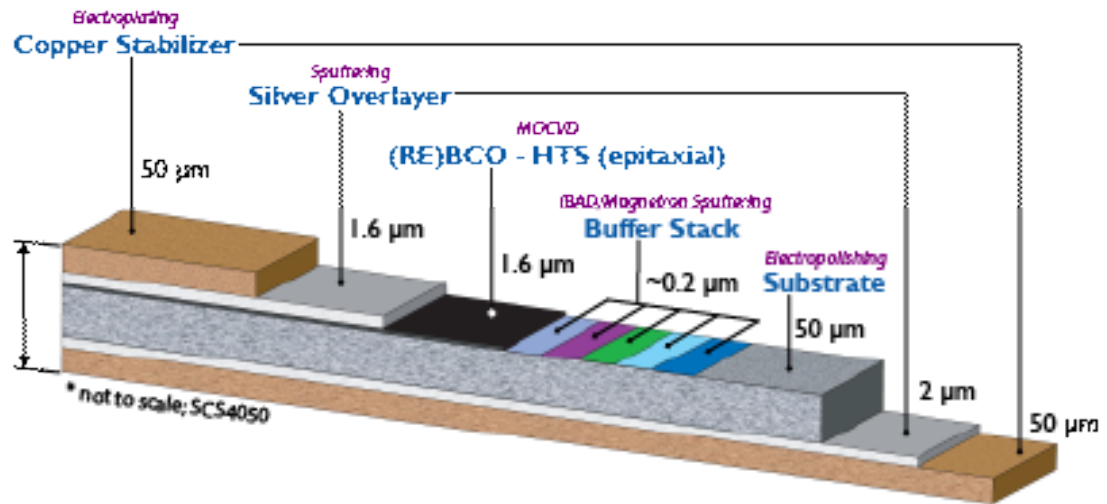

Fig.1.05 Structure of the Superpower© SCS4050 superconducting tape.

Around the tape, there is one protective silver overlayer. Finally, the tape is usually thermally stabilized by covering both sides with a $50\,\mu m$ copper layer for thermal stabilization and in the normal state as an electrical current bypass.

The request of $ReBCO$ tapes for future dc applications, with long length, and increasing current performances, were satisfied by the commercial availability of wider and thicker tapes. Unfortunately for such large tapes, the ac loss may become really high. For a tape with a $4\,mm$ width, the thickness of $1.5\,\mu m$, and $J_C = 10^{10}\,A/m^2$ in case of an applied field magnitude of one or more Tesla the loss per cycle has a value of $10^8\,J/m^3$. [CR01 p.182] Like in the LTS cables, the ac loss can be reduced, by separating the coating in many filaments and twisting them. On tapes, this can be done, by making striated conductors with many narrows filaments. Within this approach, the reduction of the hysteresis loss, have to overcome two problems. On tapes, twisted architecture is difficult to realize, but twisted tapes are necessary to preserve

the advantages of the striation. Moreover, a copper stabilizer has to be added without reconnecting the filaments with a short resistance path. A practical solution for the reduction of ac loss problems is the creation of a Roebel cable. The original Roebel conductor was developed by Siemens on a BSCCO and then also on $YBCO$. The idea, on the base of the Roebel shaped tapes, is the ability to cut from a superconducting tape several strips, in a way that is then possible to interlace them together. The drawing of a Roebel cable is shown in Fig.1.06 where a single transposition of two strips is shown. [LN08]
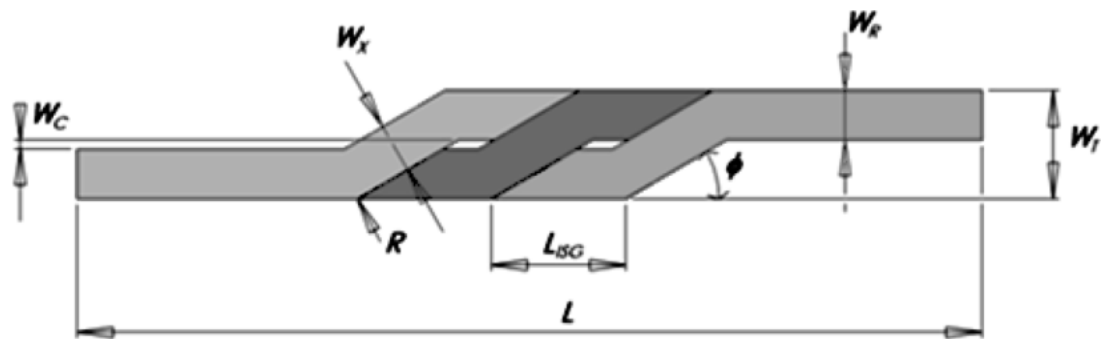

Fig.1.06 Diagram of a partially assembled Roebel cable taken from Ref. [BD09]

More complex structures are also possible by assembling more than two strips on a single cable. The strands cutting is obtained from the widest possible tape in order to reduce the loss of material arising from the cutting of these shapes. The cutting itself can be obtained with several different techniques. Due to the high cost of the tapes, the cutting method has to be reliable with reasonable speed and cause the least damage to the strands. The realization of automatized punching machines with a winding apparatus has been found able to realize Roebel cables with complex structures and length up to 35 meters without significant dc degradation. The measurements of ac loss on the Roebel cables confirm the nominal reduction of losses in comparison with the wide tape. The expected ac loss in the low field, due to the shielding of the external strands are less than the sum of the individual strands. [LN08]

1.5   Stresses and degradation

Any current-carrying conductor, in the presence of a magnetic field, is subject to the Lorentz force $\vec{F} = \vec{J} \times \vec{B}$. This force is relevant in superconducting magnets where, both the current densities and the magnetic field are relevant. If these forces are not adequately considered, during the design and construction of a superconducting magnet, they may lead to severe damages. The computation of forces and stresses needs the knowledge of the magnet field all over the coil winding. These forces can be computed numerically and, for simple geometries, by using approximate analytical expressions.

The mechanical forces on the superconducting winding and in general the mechanical stresses produce deformations and, above the elastic limit, induce deformations and fractures. Composite superconductors are made with several different materials where the fine filaments of superconductor are embedded into a metallic matrix. Under moderate stress, the $NbTi$ composite total stress, for a given strain, appears to be the volume-weighted mean of the stress of each component. Unfortunately, at high stresses, the fracture on the $NbTi$ composite appears at stresses lower than either component taken separately. This behavior is not observed at room temperature, where large deformations of the $NbTi$ composite are seen before the fracture.

The mechanical stress at cryogenic temperature can also modify the superconducting properties of the $NbTi$ composites. A measure of the critical current reduction, on a wire subject to mechanical stress, is shown in Fig.1.07. In this figure, the dotted line represents the measured value of $I_C(4K)$ under the preliminary stress load of about $10^8\ N/m^2$. Solid lines connect the critical current values measured while the wire is under stress. The crosses on the dashed lines are the values critical current measured after a reduction of the tensile load to the preliminary stress load values. These measures have been carried out for several values of the magnetic field and show a reduction of the value of the critical currents up to 20% respect to the original values. These reductions, as it can be seen, in Fig.1.07, that the observed critical currents

reductions are reversible because, when the stress has been partially removed, the measured critical currents return to almost their original values. For this particular $NbTi$ composite, a good choice for the allowed working maximum stress may be chosen around $5 \cdot 10^8 \, N/m^2$. [KN77]
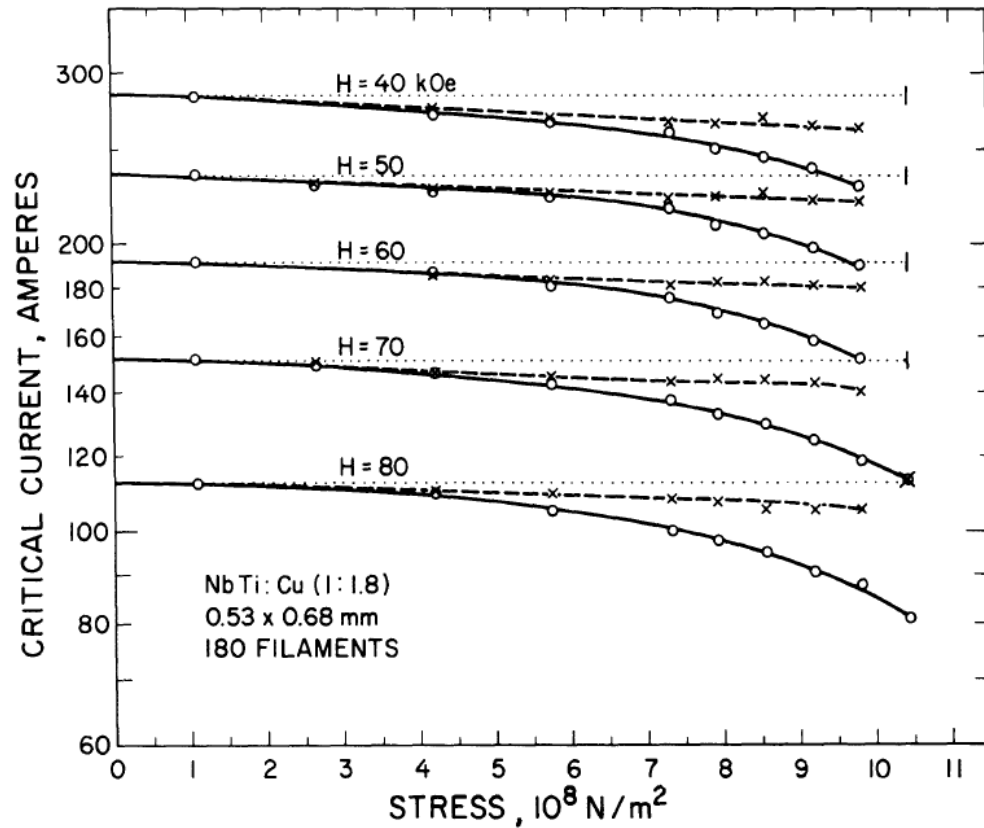

Fig.1.07 Critical current for a $NbTi$ composite for several values of the magnetic field. Solid lines show I_C reductions due to the applied stress. Dashed lines are the I_C measures with the stress almost removed. [KN77]

The bulk form of Nb_3Sn is a brittle material that will fracture under a strain of about 2%. It is possible to exceed this value by using Nb_3Sn in filamentary form. The effect of stress on the critical current in filamentary Nb_3Sn composites is more complicated and varies greatly between samples. This behavior may be explained by the different thermal conduction of the Nb_3Sn filaments respect to the metallic matrix. In fact from a temperature of about $970 \, K$ of the heat treatment, down to the temperature of liquid helium,

the bronze matrix contracts by 1.8% and they formed Nb_3Sn contracts only of 0.8%. This contraction of the metallic matrix applies the compression on the filaments with a consequent reduction of the critical temperature. If this compression is removed by acid etching the metallic matrix, the values of the measured critical temperature of the filaments return very close to the strain-free values. This fact proves that, on the Nb_3Sn, more than the applied stress, what is really important is the stress felt by the filaments. It has been found that the observed reduction of J_C on Nb_3Sn under intrinsic strains up to 0.5% is reversible. Above this value, the intrinsic strain will form filaments micro crack with permanent damages of the conductor. In general, it is rather simple to keep the electromagnetic stress around the safe value of about 0.3% but a greater problem is the bending where the value of the safe stress can be easily exceeded. A solution to this problem is the adoption of the react after winding technique. With this technique, the heat treatment is applied after the winding. In order to preserve the coil integrity lower temperatures are used, but with longer times to allow the formation of the Nb_3Sn compound.

The discovery of HTS and the remarkable processes made in the recent years and, in particular, the introduction of industrial processes that achieve length over a kilometer, have boosted their usage as high field magnetic conductors. In particular, at $4.2\,K$ above magnetic fields of $23\,T$, where the LTS conductors reach their performance limit, there are only three HTS conductors that can be used: $ReBCO$, $Bi-2212$, and $Bi-2223$. As in LTS materials, the stress is made of two components. The reversible stress, that can be recovered when the forces are removed, and the irreversible stress that, above a strain limit, degrade irreversibly the critical current. The long length performance homogeneity has been done on $Bi-2223$ tape, obtained with metallic lamination, either by using copper or stainless steel. Measures at $4.2\,K$ and with a magnetic field of $4\,T$ on samples with a length of $1.7\,m$ subject to the bending on a $108\,mm$ winding diameter, shows that the reversible stress does not induce sign of degradation for strains up to

31

$200\ MPa$. These conductors proved to have a high tolerance to the application of axial tensile strain with the additional bending stress from the coil winding. Degradations above these stresses, investigated by measuring the critical current in different points of the winding, show a uniform degradation through the whole length. [MY14]

On $ReBCO$, due to the intrinsic brittleness of the superconducting layer, the strain during operation may degrade irreversibly the critical current. The reversible stress follows an almost parabolic dependence as a function of strain, independent of angle, and magnetic field up to $H/Hc_2 = 0.4$. This behavior is dissimilar to that observed in Nb_3Sn wires, where the effects on the critical current of the applied strain, become more pronounced at a higher magnetic field. This difference is due to the stronger strain dependence of Hc_2 and T_C in Nb_3Sn compared with that in the bi-axially textured $ReBCO$ layer. [SN14] The irreversible stress limit under axial loads of $ReBCO$ is influenced by the conductor design. Due to the large metallic fractional section area, mechanical strength is a big asset for $ReBCO$ compared with $Bi - 2223$ tape and wire. With the usage of stainless steel or Hastelloy substrate, the tape can withstand critical axial stress with retention of 95% of I_C for tensile strain up to $700\ MPa$, depending on the copper fractional area. On the contrary, the maximum tensile stress of $Bi - 2223$ tapes can be improved only up to $430\ MPa$ by a new lamination technique. In conclusion, the mechanical strength, $ReBCO$, as well as its current-carrying capacity, makes the $ReBCO$ as the only HTS superconductor applicable to high-field magnets. It is unlikely that in the near future, even with continued progress in the development of better $Bi - 2212$ and $Bi - 2223$ conductors it will be possible to recover their inherent disadvantage in mechanical strength versus $ReBCO$. [SN14]

Compared to $Bi - 2223$ tapes, $ReBCO$ tape could be made thinner and tougher. However, in some cases, the application of mechanical strains produced by electromagnetic and thermal forces may repeat tens of thousands of times during their lifetime. It is important to investigate the I_C degradation

of YBCO tapes under strains. In order to prove the resilience against cyclic mechanical stress, two samples of HTS with $40\ \mu m$ and $100\ \mu m$ of copper stabilization layer and one HTS sample with stainless steel stabilization layer with a thickness of $175\ \mu m$ were subject to cyclical strain by using a four-point bending method. The tapes displacement under a strain of 0.2% and 0.4%, are respectively shown in Fig.1.08 (a) and Fig.1.08 (b). [XU20]
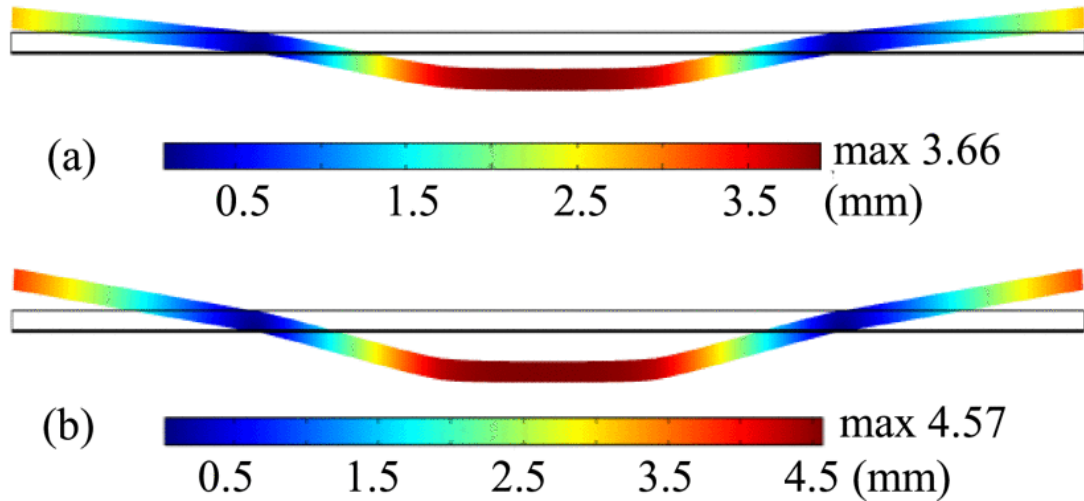

Fig.1.08 Displacement and deformation of a $ReBCO$ tape subject to a four-point bending with orthogonal strains of 0.2% (a) and 0.4% (b). Values computed with Comsol© by using a mechanical analysis model. [XU20]

The comparison, between the measures of I_C after the application of 60000 strain cycles at room temperature, with the preliminary measure of I_C, both at $77K$, showed negligible differences. Considering that, the I_C obtained by repeated measurements have slight differences even if to the sample, is not applied any strain, and that some samples have shown a small increase in I_C after undergoing multiple strains, it is possible to affirm that all measured samples showed no degradation or less than 1% degradation in I_C after 60,000 cycles with up to 0.4% strain. [XU20]

1.6   Dissipations and stability

The reliability of tapes and wires has been improved by a better knowledge of the aspects linked to the presence of instabilities. In the field of the superconducting magnets, one of the major instability sources is represented by the increase of the temperature. In fact, a temperature rise leads to a partial or complete transition in the normal state of a superconducting magnet. This phenomenon is called Superconducting Quench and a magnet, if not accurately designed, may be destroyed by the magnetic energy accumulated in it. [WL02] [WS99]

The starting point, for studying the general thermal properties of any Composite Superconductor, *cd*, is given by the power per unit length heat balance equation. [WS99]

$$C_{cd}(T)\frac{\partial T}{\partial t} = \nabla \cdot [k_{cd}(T)\,\nabla T] + \rho_{cd}(T)\,J_{cd}^2(t) + g_d(T) - \left(\frac{f_p\,P_D}{A_{cd}}\right) g_q(T) \qquad (1.01)$$

In its complete form, the Eq.1.01 considers all the terms that affect the temperature T for a unit volume of composite superconductor. The first term represents the rate of variation of the thermal energy density for a conductor with a unit volume heat capacity $C_{cd}(T)$ of both superconductor and a normal metal. The second term is the thermal conduction inside the composite superconductor with a thermal conductivity $k_{cd}(T)$. The third term represents the Joule heating with a composite electrical resistivity $\rho_{cd}(T)$ and the time-dependent current density $J_{cd}(t)$. The fourth term $g_d(T)$ takes into account all the heating processes not related to the Joule heating, usually due to magnetic or mechanical effect. Finally, the last term is the cryogenic fluid cooling energy. In this term, f_p is the fraction of the perimeter P_D in contact with the cryogenic fluid. The product $f_p\,P_D$ is also called the wet perimeter. Also in this term, A_{cd} is the composite cross-section and $g_q(T)$ a function that takes into account all the heat removal processes related to the convective heat transfer, from the cryogenic fluid to the composite superconductor. [WS99]

In stationary thermal stability conditions, the right member of Eq.1.01 must be always equal to zero. Other terms of Eq.1.01, that are zero or may be neglected, are the thermal gradient inside the composite superconductor $\nabla T = 0$ and the term $g_d(T)$ dealing with the heating processes not related to the Joule effect. The function $g_q(T)$ can be expressed in many ways. A simple choice is to consider $g_q(T)$ proportional to the temperature difference $T - T_0$ where T_0 is the temperature of the cryogenic cooling liquid, usually helium or nitrogen, and h_q the constant thermal exchange coefficient.

$$g_q(T) = h_q\ (T - T_0) \tag{1.02}$$

Considering these approximations and with the substitution of Eq.1.02, the Eq.1.01, dealing with the cryo-stability analysis, reduces to the expression.

$$C_{cd}(T)\frac{\partial T}{\partial t} = \rho_{cd}(T)\,J_{cd}^2(t) - \left(\frac{f_p\,P_D}{A_{cd}}\right)\,h_q\ (T - T_0) \tag{1.03}$$

In the following parts, the first term of Eq.1.03 will be analyzed by using the current sharing concept and, Eq.1.03 will be used to derive the Stekly criterion for the cryogenic stability in presence of the Joule effect dissipation.

1.6.1   Current sharing in composite superconductors

Composite superconductors take advantage of the presence of a good thermal and electrical metallic matrix. As seen, superconducting wires are a composite, made of superconducting filaments embedded into a normal metal matrix, usually copper. The electrical behavior of these wires can be schematized with electrical discrete components. [FR18] The chosen model may be more or less complex in order to describe its behavior in dc or ac regime. A superconductor in the dc regime may be well described by a simplified model with only resistors. [WS99 p.362]

The simplest model that may be used for dc powered composite superconductors feed with a current I_T, kept constant, is reported in Fig.1.09. In this model, there are only two components in parallel with each other. This model is useful only to explain the composite superconductor behavior in the dc regime with a constant feeding current.
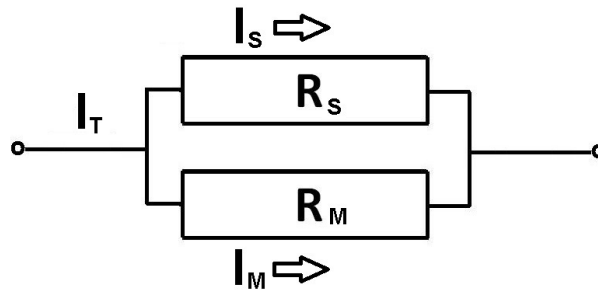

Fig.1.09 Simplified model, R_S describes the superconducting filaments and R_M the normal matrix. I_S and I_M are their respective currents ($I_T = I_S + I_M$).

The circuit shown in Fig.1.09 may be used as a model for the behavior of the composite superconductor and the computation of the value of the total Joule dissipation G_J. In the model of Fig.1.09, for an ideal superconductor, the value of the resistance R_S is zero for any temperature below T_C and R_N above T_C. The behavior of the current I_T and how it split is shown in Fig.1.10. In this figure, both the current I_T and the magnetic field B are considered constant and the critical current in the temperature range from T_0 to T_C is assumed to be linearly dependent on the temperature.
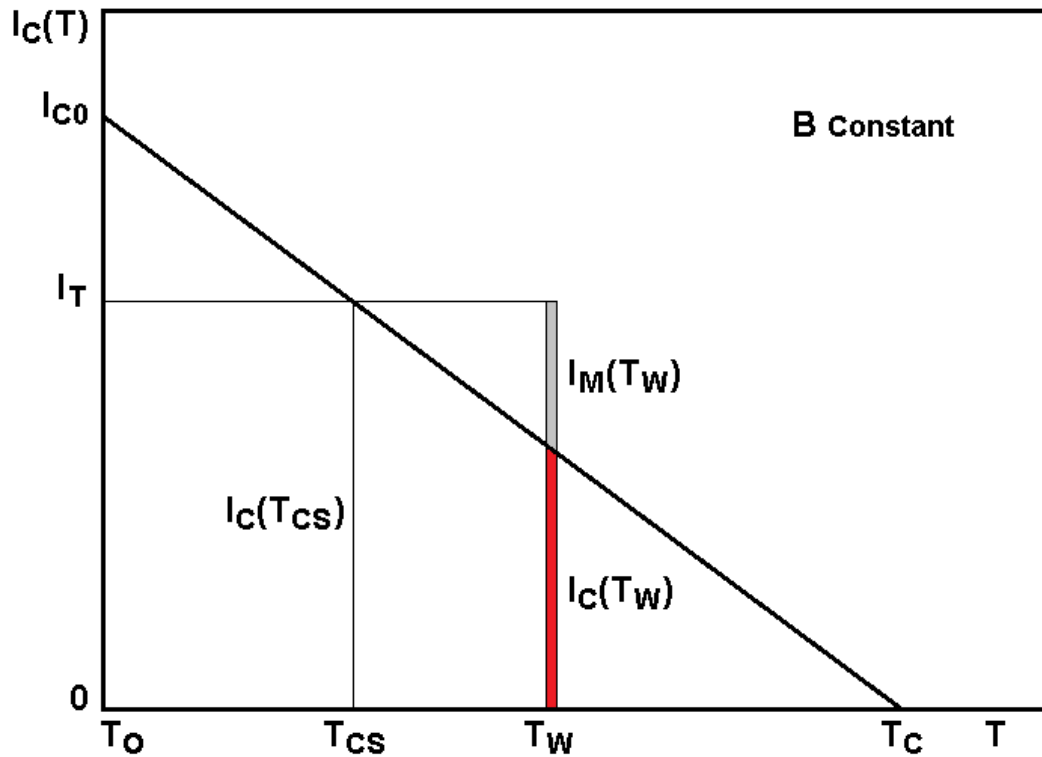
36

Fig.1.10 Picture of how, for a given working temperature T_W, the total current I_T splits between the superconducting component $I_S = I_C(T_W)$ (Red Bar) and the dissipative normal component $I_M(T_W) = I_T - I_C(T_W)$ (Grey Bar).

In the first part, on the left of Fig.1.10, in the region where $I_T \leq I_C(T)$, the whole current is transported by the superconducting element so that $I_T = I_S$ and $I_M = 0$. In this condition, the voltage drop $V = R_M I_M$ across the composite is zero, and the Joule dissipation $G_J(I_T) = V I_T$ is also zero.

In the second part, on the right of Fig.1.10, in the region where it is $I_T > I_C(T)$, there is a current $I_M > 0$, called sharing current. In fact, for a given working temperature $T_W < T_C$, when $I_T > I_C(T_W)$, the current flowing into the superconducting parts is only $I_S(T_W) = I_C(T_W)$, a fraction of the total current I_T transported by the composite. Only in this case the total current I_T is the sum of two components $I_T = I_S(T_W) + I_M(T_W)$ where $I_M(T_W) = I_T - I_C(T_W)$ is the current flowing through the metallic matrix, having normal resistance R_M. The computation of the $G_J(I_T)$ can be separated into two parts.

Under the current sharing, the I_T dependent total Joule dissipation $G_J(I_T)$ can be obtained as follows.

$$G_J(I_T) = V\,I_T = R_M I_M I_T = R_M I_T (I_T - I_C(T)) \tag{1.04}$$

According to Eq.1.04, the normal metal matrix R_M is temperature independent, but it is known that the resistivity of the metal matrix is temperature-dependent. The temperature dependence of $R_M(T)$ for the stability analysis of LTS cables may be omitted because for temperatures up to $30\,K$ its value can be safely assumed as constant. On the contrary, the temperature dependence of $I_C(T)$ needs to be considered. For a constant magnetic field, a linear dependence of $I_C(T)$, in the temperature interval between T_0, the operating temperature, and T_C, can be written as follows.

$$I_C(T) = I_{C0}\left(\frac{T_C - T}{T_C - T_0}\right) \qquad T \in [T_0, T_C] \tag{1.05}$$

In Eq.1.05 the current $I_C(T)$ is maximum at the temperature $T = T_0$ where $I_C(T_0) = I_{C0}$ and then, linearly decreases, reaching at T_C the value $I_C(T_C) = 0$. For any value of the constant total current $I_T < I_{C0}$ there is a temperature value, in the interval $[T_0, T_C]$, called Current Sharing Temperature T_{CS} where, the total current I_T, is equal to the critical current at this value of temperature $I_T = I_C(T_{CS})$. For all temperatures, $T \leq T_{CS}$ the current I_T will flow only in the superconductor. On the other hand, for $T > T_{CS}$ the current I_T will split into two parts. As said before, the critical current $I_C(T_{CS})$ will be transported by the superconductor and, the remaining part will be flowing in the metallic matrix $I_M = I_T - I_C(T_{CS})$. The computation of the temperature dependence of $G_J(T)$ for a given current I_T can be separated into three different temperature regions.

In the first region, with $T_0 \leq T \leq T_{CS}$ the current is $I_T \leq I_C(T)$ and $I_M = 0$. As said before, the voltage drop $V = R_M I_M = 0$ and $G_J(T) = V\,I_T$ is also zero.

In the second range where $T_{CS} \leq T \leq T_C$ the Eq.1.04 has to be modified by replacing the I_C with linearized temperature dependence $I_C(T)$ in Eq.1.05.

$$G_J(T) = R_M I_T \left[I_T - I_{C0} \left(\frac{T_C - T}{T_C - T_0} \right) \right] \tag{1.06}$$

The dependence of $G_J(T)$ from I_{C0} and T_0 can be removed by computing at the temperature T_{CS} the critical current for the value of $I_C(T_{CS})$ in Eq.1.05.

$$I_C(T_{CS}) = I_{C0} \left(\frac{T_C - T_{CS}}{T_C - T_0} \right) \tag{1.07}$$

Solving this Eq.1.07 respect to the current I_{C0} and remembering that, in this case, we have the current sharing $I_C(T_{CS}) = I_T$, it is possible to obtain.

$$I_{C0} = I_T \left(\frac{T_C - T_0}{T_C - T_{CS}} \right) \tag{1.08}$$

The substitution of I_{C0} obtained from Eq.1.08 into the Eq.1.06 cancel the value of the temperature difference $T_C - T_0$ and leads to the final result.

$$G_J(T) = R_M I_T^2 \left(\frac{T - T_{CS}}{T_C - T_{CS}} \right) \tag{1.09}$$

In the third range where $T > T_C$ the superconductor behave as a normal metal with its own normal resistance $R_S \to R_N$, and if the approximation $R_N \gg R_M$ is valid, I_T flows only in the metallic matrix and $G_J(T) = R_M I_T^2$

The constant value of R_M is not valid for HTS superconductors working at temperatures above $30\ K$. To remove this constraint it is sufficient to replace the constant value R_M with its temperature dependence $R_M(T)$.

$$G_J(T) = \begin{cases} 0 & T_0 \leq T \leq T_{CS} \\ R_M(T)\, I_T^2 \left(\dfrac{T - T_{CS}}{T_C - T_{CS}} \right) & T_{CS} \leq T \leq T_C \\ R_M(T)\, I_T^2 & T > T_C \end{cases} \tag{1.10}$$

1.6.2   Stability criterion for cables and tapes

The appearance of a local normal zone in a superconducting wire can be recovered if the heat generated on it, can be removed faster than it is generated. In this case, the local temperature decreases, and the normal zone will reduce until it disappears. In composite superconducting wires, the heat generation is largely dumped by the presence of copper. In fact, in the presence of copper, the current of the normal zone of disturbance will be shared between the copper and the superconductor. Because the superconductor has a higher resistivity than copper, in the normal state this current will flow mainly in the copper matrix, where it generates heat that is transferred quickly and efficiently to the coolant. In any case, the superconductor will be able to recover only if the heat removed exceeds the heat generated. On the contrary, due to the increase of the temperature, the whole superconductor will fall in the normal state. The critical power dissipation can be obtained by choosing the total current I_T equal to $I_C(T_0)$. In this condition, the sharing process will start at T_0 and continue up to T_C. With the choice of $I_T = I_{C0}$ and as a consequence $T_{CS} = T_0$ the Eq.1.09 will be modified as follows.

$$G_J(T) = \frac{\rho_M}{A_M} \, I_{C0}^2 \left(\frac{T - T_0}{T_C - T_0}\right) \tag{1.11}$$

Where the metallic resistivity per unit length $\rho_M = R_M A_M$, have been introduced. Similarly, $\rho_{cd} = R_{cd} A_{cd}$ and $J_{cd} = I_{cd}/A_{cd}$ so that, the Joule heating $G_J(T) = R_{cd}(T) I_{cd}^2$ can be obtained by multiplying the Joule heating density $\rho_{cd}(T) J_{cd}^2$ with composite cross-section A_{cd}. On the other hand, by using $\rho_{cd}(T) J_{cd}^2 = R_{cd}(T) I_{cd}^2/A_{cd} = G_J(T)/A_{cd}$. It is possible to obtain from Eq.1.11 the unit length Joule heating density.

$$\rho_{cd}(T) J_{cd}^2 = \frac{\rho_M}{A_{cd} \, A_M} \, I_{C0}^2 \left(\frac{T - T_0}{T_C - T_0}\right) \tag{1.12}$$

The Eq.1.12 represents the Joule heating dissipation into the composite with a current $I_T = I_{C0}$ within the temperature range $[T_0, T_C]$.

The Eq.1.12 can be placed in Eq.1.03 of the unit length power equation.

$$C_{cd}(T)\frac{\partial T}{\partial t} = \frac{\rho_M}{A_{cd}\,A_M}\,I_{C0}^2\left(\frac{T-T_0}{T_C-T_0}\right) - \left(\frac{f_p\,P_D}{A_{cd}}\right)h_q\,(T-T_0) \qquad (1.13)$$

In Eq.1.13, when the cooling capability, represented by the last term, is greater than Joule heating, on the second term, the time derivative of the temperature is negative and the temperature decreases until the stable equilibrium condition at $T = T_0$ is reached. On the contrary, when this time derivative is positive, the temperature increases until reaches and exceeds the critical temperature T_C. The system stability requires that the heat removed exceed the heat generated or that time derivative of the temperature is negative. This is equivalent to the following inequality:

$$\frac{\rho_M\,I_{C0}^2}{A_M(T_C-T_0)} \leq f_p\,P_D\,h_q \qquad (1.14)$$

To guarantee the thermal stability of a cryogenic system Stekly decided to introduce a parameter α as the ratio of the two-member of Eq.1.14.

$$\alpha = \frac{\rho_M\,I_{C0}^2}{A_M\,f_p\,P_D\,h_q(T_C-T_0)} \qquad (1.15)$$

The Stekly stability parameter in Eq.1.15 is a dimensionless number. By using this criterion, a cryogenic system can be considered stable when $\alpha \leq 1$ where the heat removal is larger than its generation. [WL02 p92] [WS99]

Besides the Joule heating thermal instabilities, there is another source of instability known as the Flux Jumping. The mechanism of this instability is not well understood and happens in the presence of shielding currents induced by an external magnetic field. In a superconductor, the increase of the magnetic field on the superconducting surface will increase the shielding currents. When the value of these shielding currents overcome J_C the shielding does not

increase anymore and allows the penetration of some magnetic flux until the magnetic field on the surface reduces to a value that can be shielded by shielding currents with magnitude J_C. The penetrated magnetic flux while moving generates some heat until is trapped by the pinning centers and, contributes to the shielding. The Critical-State model is based on this penetration and trap mechanism. Within the model, the shielding currents are only either J_C or zero and the penetrated magnetic field linearly decreases in the superconductor region where the shielding currents have the J_C value. A small heat pulse may create a locally increase of the temperature and, as a consequence, a local reduction of the temperature-dependent critical current $J_C(T)$. The reduction of $J_C(T)$, forces the reduction of the shielding currents, with further penetration of the magnetic field, which improves dissipative effects. This penetration mechanism has positive feedback that may be enhanced when the newly entered flux quanta can free some pinned flux and generate an avalanche of flux quanta with remarkable heat production. The value of the total heat generated can be computed for a thermally isolated slab within the critical state model [WL02]. From here, the effective value of the specific heat C_E of the superconductor with the shielding current contribution will be:

$$\gamma C_E = \gamma C_{cd} - \frac{\mu_0 J_C^2 a^2}{3(T_C - T_0)} \tag{1.16}$$

Where γ is the density, C_{cd} the specific heat and a is the slab half-width. The equation clearly shows that the energy of the shielding currents leads to a reduced value of the specific heat C_E and, for any given heat increase it will also enhance the temperature increase. A high instability occurs when the shielding current term in the Eq.1.16 equates γC_{cd}. In this case, the effective specific heat becomes zero and, even the smallest heat pulse, because of the previously positive feedback mechanism, will cause an unlimited increase of the temperature or a Flux Jump [WL02]. A condition for the avoidance of this

Flux Jump condition can be obtained by imposing in the Eq.1.16 the condition for a positive effective specific heat or $\gamma C_E > 0$

$$\beta = \frac{\mu_0 J_C^2 \, a^2}{\gamma C_{cd}(T_C - T_0)} < 3 \tag{1.17}$$

The parameter β has been defined as the stability parameter and because the condition obtained in Eq.1.17 has been obtained without any heat exchange, the condition $\beta < 3$ is also called the adiabatic stability condition. It is worth noting that, even if the adiabatic stability condition is respected, any significant reduction of C_E leaves the superconductor into a very sensitive condition to the other disturbances. For this reason, a reduced β value, at least half of the critical value, is advisable. The stability improves with the temperature because the value of temperature-dependent specific heat $C_{cd}(T)$ increases with the temperature and, therefore, more heat is required for a temperature increase. In some conditions, it may happen that, the increment of $C_{cd}(T)$ arrests the flux jumping. This behavior is called partial flux jump phenomena. The Eq.1.17 can be used to estimate the value of the half-width a for a superconductor that fulfills the adiabatic stability condition. As an example, a $NbTi$ wire with $J_C(4.2) = 1.5 \cdot 10^9 \, A/m^2$, $\gamma = 6.2 \cdot 10^3 \, kg/m^3$, $C_{cd}(4.2) = 0.89 \, J/kg$, and $T_C = 6.5 \, K$ designed to work at $4.2 \, K$ with a magnetic field of $6 \, T$ fulfills the adiabatic stability condition only if the value of $a < 116 \, \mu m$. Thicker wires will be unusable because they will be subject to spontaneous flux jumping. Thinner wires with $a \approx 60 \, \mu m$ will ensure better stability and immunity to other disturbances. [WL02]

The current sharing mechanisms, widely adopted by the commercial production of superconducting composite offers also the advantage of limiting the current flowing in the superconducting element by sharing part of the total current in the normal metal during the transition to the normal state. The reduction of the $J_C(T)$ during the transition may be considered within the model of Fig.1.09, as an increase of the resistance R_S. Within this model, the

application of the current partition it is possible to write the currents I_S flowing in the superconducting branch as

$$I_S = \frac{R_M \, I_T}{R_M + R_S} \qquad (1.18)$$

Assuming that the value of R_M is current-independent and the current behavior of R_S spans, with a non-linearly sharp transition, from zero to a very high resistance value, it is possible to obtain, in agreement with Eq.1.18, that the current I_S in the superconductor is $I_S = I_T$ for $R_S = 0$ and $I_S \approx 0$ for $R_S \to \infty$. The power dissipation $G_S(R_S)$ due to the fictitious behavior of the R_S of the model, according to Eq.1.18 can be written as follows:

$$G_S(R_S) = R_S I_S^2 = \frac{R_S \, R_M^2 \, I^2}{(R_S + R_M)^2} \qquad (1.19)$$

The value of $G_S(R_S)$ is always positive for all values of R_S in the interval of $R_S \in [0, +\infty[$, without any dissipative effect at both interval boundaries, i.e. $G_S(0) = G_S(+\infty) = 0$. A study of Eq.1.19 shows a monotonic increase from zero up to a maximum value $G_S(R_S)_{Max}$ and then an asymptotic decrease to zero. The value of the maximum dissipation is obtained for $R_S = R_M$ where the value of $G_S(R_S)_{Max}$ assumes the following value.

$$G_S(R_S)_{Max} = \frac{1}{4} R_M \, I^2 \qquad (1.20)$$

The Eq.1.20 shows that, in the model, the presence of the normal resistance R_M limits the dissipation of R_S with a maximum dissipation depending on the value of the resistance R_M of the model, which represents the normal metal matrix resistance.

1.7   Superconducting wires characterization

The dc electrical characterization of wires and cables starts with the measure of critical temperature T_C. The measure of the critical current I_C is done for different values of both temperature and magnetic field. Besides the electrical characterizations, there are also several types of measures for magnetic characterization. The most common is the magnetic field and temperature dependence of magnetization and ac magnetic susceptibility. [CR01] [SR19] The magnetic characterization of multifilamentary wires is also an important tool in order to measure the filament coupling loss of the composite conductor. [FB09] [FB13] [GR16] [NN16] [CR01]

In the following, we summarize the measure of both T_C and I_C , the basic quantities used in designing superconducting magnets, our experimental apparatus are shown in Fig.1.11 and different techniques that can be used.
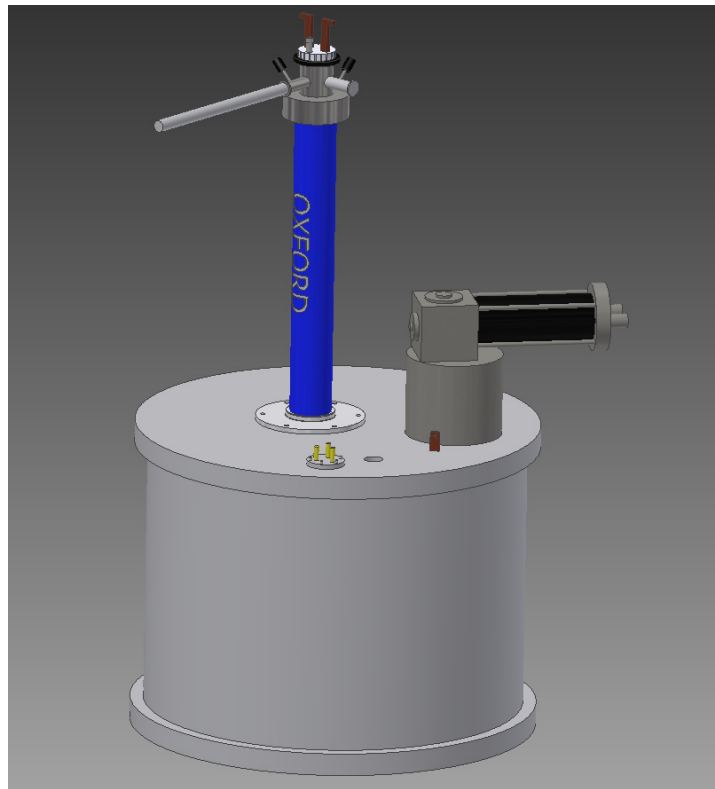

Fig.1.11 The experimental apparatus used in our laboratory for the measures of T_C and I_C . The blue cylinder is the Oxford flux cryostat, the gray tank contains the cryogen-free $12\,T$ magnet with, in black, its own cryocooler.

45

1.7.1   Critical temperature measurements

The critical temperature T_C can be measured electrically or magnetically. In the first case, the electrical resistance of a sample is measured at a fixed current as a function of the temperature until the phase transition from the normal to the superconducting state is observed. With the electrical method, T_C is the value of the temperature at which the first superconducting path, able to carry the bias current, between the voltage probes, appears. Both methods require an experimental apparatus where the temperature can be kept under control and changed during the measurements.

The temperature may be changed in several ways. A simple method consists of putting the sample and a cryogenic thermometer into a liquid helium Dewar and dipping both within the thermal gradient of the cold gas spanning from the temperature of the cryogenic liquid surface to almost room temperature on the top of the Dewar. The sample to be measured, and the cryogenic thermometer are both in close contact with a bulk metallic support. Alternatively, the metallic support may be fixed on the cold finger of a cryocooler, whose temperature is controlled by a small heater. Temperatures slightly under the liquid phase of $4.2\ K$ for helium and $77\ K$ for nitrogen at the atmospheric pressure may be reached by reducing the pressure above the liquid. This technique allows measurements up to about $2\ K$ for helium and $63\ K$ for nitrogen. [KN06]

The values of T_C measured in our laboratory, are obtained by using an Oxford® gas flow cryostat. Within this cryostat, the liquid helium enters through a needle valve and vaporizes by cooling the surrounding environment. A heater, around the helium orifice, modifies the temperature of the helium gas. An ITC 503 Oxford® temperature controller keeps the operating temperature adjusting the power heater on the helium inlet gas. Above the helium gas orifice, there is a region where the temperature is uniform. In order to place the sample in this zone, several inserts, one for each specific

application has to be realized. The insert for measuring T_C in its simplest form is a stainless steel can with a sample holder on its extremity. The can length is computed in a way that permits the positioning of the sample holder in the measurement zone of the cryostat. The samples to be measured and a calibrated Cernox® thermometer are mounted on a sample holder. Taking care that the sample and the thermometer are in good thermal contact, the value of the temperature of the cryogenic sensor is also the temperature of the sample. The T_C is a measurement of the temperature dependence of the sample resistance with the four points method. A 2440 Keithley Sourcemeter power supply feeds the sample with a constant bias current and a 2002 Keithley Nanovoltmeter is used for reading the voltage across it. The currents flowing in the sample have to be chosen with some care. The value of the bias current influences T_C and should be kept as low as possible. On the other hand, because of the Ohm law, samples with small resistance return voltages too small to be detected. Our samples, because of their low resistance values, are measured with bias currents in the range of $1 \div 5\,A$ obtaining in return voltages of tens of microvolts. At these low voltages, the presence of the thermoelectric voltages may modify the voltages read by the nano-voltmeter. It is possible to avoid this problem by reversing the bias current and making an average of the positive and negative voltages. A measure of T_C of a $NbTi$ sample obtained with our experimental apparatus is shown in Fig.1.12.

The measure is made with a bias bi-polar current of $\pm 5\,A$ on a $50\,mm$ long sample, welded straight on the top of a bulk copper sample holder with the voltage taps $19\,mm$ apart. Because the $NbTi$ resistivity is much larger than the copper, the resistance values measured on the normal state is essentially the copper sample holder resistivity. The temperature hysteresis, shown in Fig.1.12, between values taken in the cool-down (dashed red line) and warm-up (dotted blue line) can be further reduced with a slower temperature variation rate. In this case, the rate was $0.3\,K/min$. Because of the hysteresis,

the value of T_C is set to $9.12\ K$ taken as the average of the half transition value between the two curves.
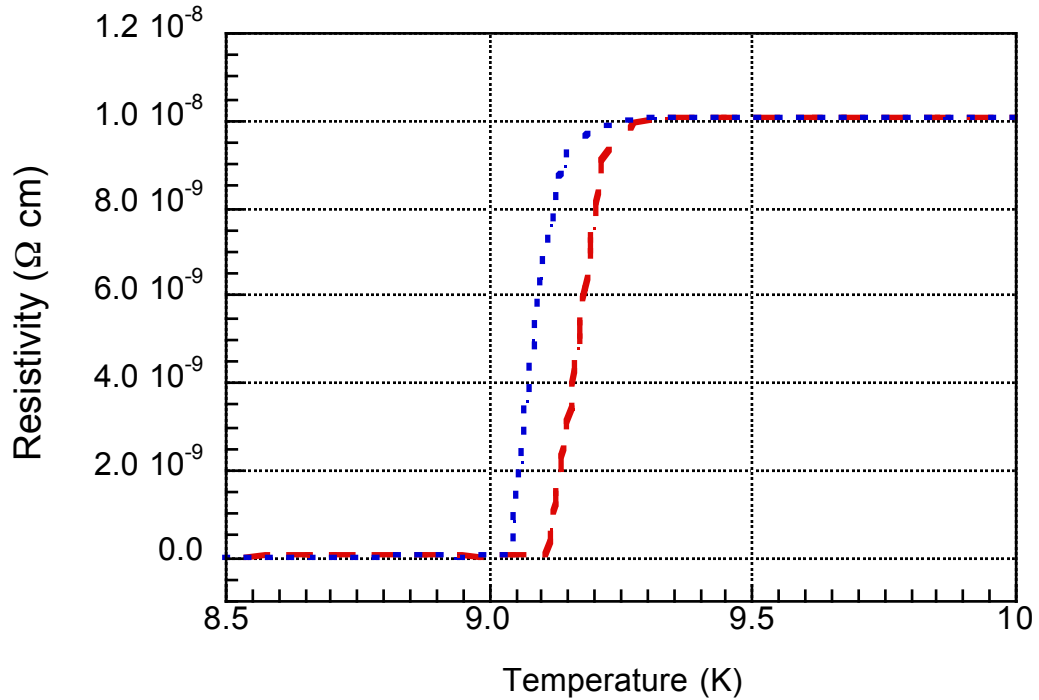

Fig.1.12 Measure of T_C of a $NbTi$ wire. The resistivity is measured in the cool-down (red dashed line) and warm-up (blue dotted line). The temperature variations rate both in cool-down and warm-up is 0.3 K/min.

The previous measure was obtained without any external applied magnetic field. The measures of T_C with an external magnetic field can be done in our laboratory because, as shown in Fig.1.11, the Oxford® gas flow cryostat can fit within the warm bore of our cryogen-free superconducting magnet. This magnet can reach a maximum magnetic field of 12 Tesla. The magnet is feed with an Oxford IPS120 power supply with a maximum current is $103\ A$.

The influence of an external magnetic field on the measures of T_C can be observed on the measure on a sample of the commercial tape HTS superconductor HCN04150 produced by SuNAM©. This measure of T_C was done as a first characterization before the investigation on the quench propagation velocity of the normal zone along with these tapes. The measures have been done, by using a bias bi-polar current of $\pm 1\ A$, with the procedure

already described. Looking at Fig.1.13 it could be noticed that on this tape, the transition regions, as shown in the inset of the figure, are strongly dependent on the magnetic field.
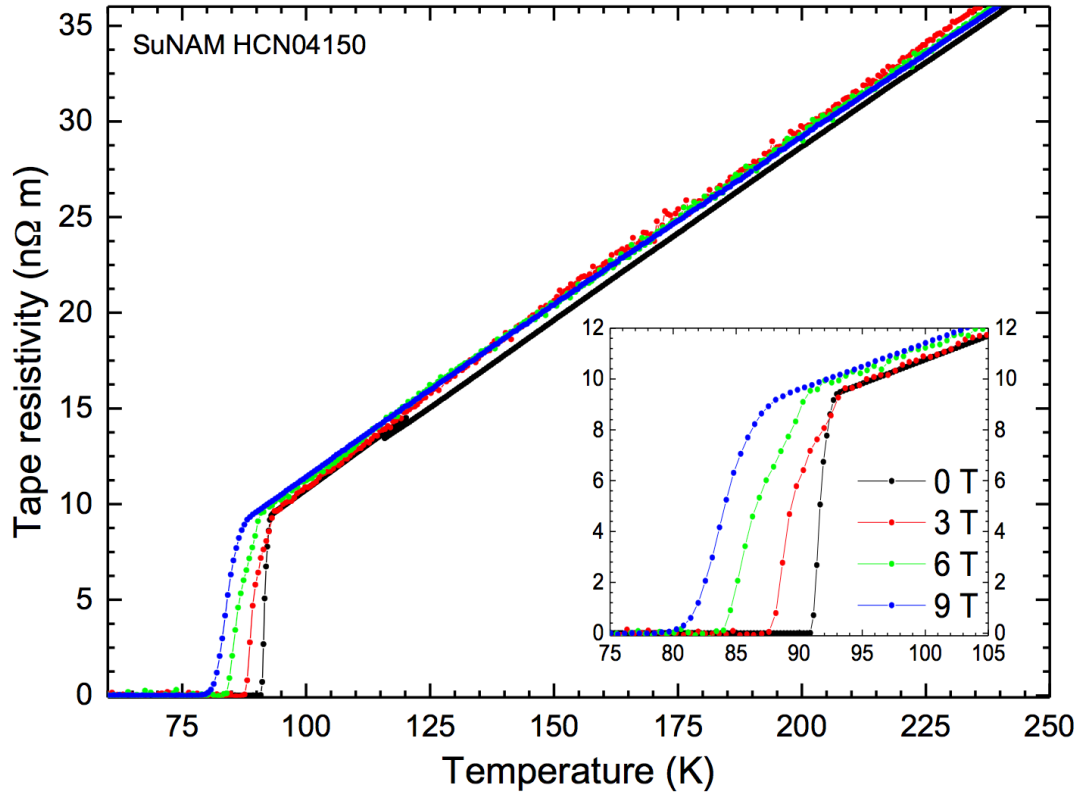

Fig.1.13 Measures of T_C for different values of the applied magnetic field.

Indeed, without an applied field, the transition to the superconducting state is sharp and the temperature at which the resistivity approaches zero is above $90\ K$. Increasing the applied magnetic field, T_C reduces and the transition becomes broader. At $9\ T$, the superconducting state is reached at about $80\ K$. Similar results were obtained on the SuperPower© tapes.

Another measure of T_C has been done on a $25\ cm$ long sample of the *SuperPower©* tape $SP4050AP$ with a bias current of $I_T = 1\ A$. The resistances, shown on the top of Fig.1.14, are obtained by dividing the measured voltages $V(T)$ for the current I_T. Likewise, the dissipated power can be obtained by multiplying the same values of $V(T)$ with I_T. Since the current I_T is kept

constant for the whole measure, the power dissipated by the superconductor will be proportional to the resistances and the curve is shown on top of Fig.1.14, with a change of units and a suitable scale factor, it is also a representation of the power dissipated by the superconductor. In particular, for this measure, $I_T = 1\,A$ and the scale factor is one.
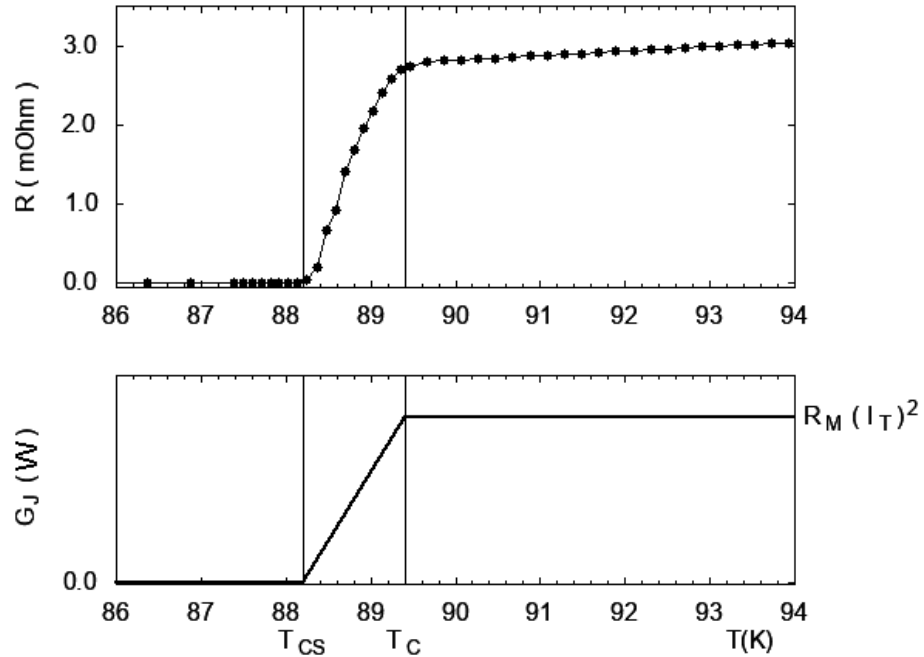

Fig.1.14 The HTS measure of T_C (up) and the comparison with Eq.1.10 (down).

The dissipation of a composite has been investigated within the current sharing model. The final result of Eq.1.10 of the energy loss for this model is reported on the bottom of Fig.1.14. With this model, it is possible to identify the beginning of the transition as the temperature T_{CS} where the current sharing starts and the usual value of T_C where the superconductor is normal.

The comparison between these two curves shows the differences between the model and the measure in the temperature region $\Delta T = T_C - T_{CS}$ in LTS composite superconductors the temperature interval ΔT is small and, the linear behavior obtained by using the current sharing model, can be considered accurate. On the other hand on the HTS superconductors $\Delta T \approx 1\,K$

50

and often, strong nonlinearities are observed. In these cases, the predicted linear behavior cannot be considered accurate and the curve experimentally obtained should replace the sharing model results.

These measurements of T_C will be used later during the measurements of the quench propagation. In particular, the measured values of I_C will be used for the accurate determination of the I_0/I_C ratio with the bias current I_0. [NG08]

1.7.2   Critical current measurements

The experimental determination of the critical current $I_C(T, B)$ in this thesis was done by the four-points transport method, but it can be also measured magnetically. During the measurements, the temperature is kept constant by either, immersing the sample into a cryogenic liquid or, by using a cryostat with a temperature controller able to keeps the temperature constant during the acquisition of the whole $I - V$ characteristic. The measurements at $77\ K$, on HTS superconductors, are usually made, by using a liquid nitrogen bath. This simple method, do not require thermal stabilization and, guarantees a high grade of thermal stability. Measurements on LTS superconductors or, at temperatures below the temperature of $77\ K$, require the use of liquid helium and a cryostat able to keep the temperature constant. The measurements of I_C on composite wires and tapes, with I_C of the order of hundreds of Ampere, beside the need for a current source able to supply such currents, requires current leads able to transport these currents from the power supply at room temperature, down to the sample in the cryogenic environment. The choice of optimized current leads is obtained by minimizing both, the current generated heat and the thermal conduction. This optimization may be greatly improved with extra cooling, obtained by forcing the escape of the cold cryogenic gas through the current leads. The electrical resistance of joints, between current leads and the superconductor, should be as small as possible because, the Joule heating generated in these zones, reaches the superconductor and creates thermal gradients and instabilities on the temperature control.

In the ideal case, the voltage V on the $I - V$ characteristic is zero for all current values under I_C with a sharp rising at I_C. In real cases, the $I - V$ characteristic is smoother, with a rapid increase of the voltage V near the I_C value. This behavior of the $V(I)$ on the $I - V$ characteristic near the I_C value may be analytically described by the following phenomenological equation.

$$V(I) = V_C \left(\frac{I}{I_C} \right)^n \tag{1.21}$$

Where, the superconducting voltage V_C is obtained by the product of a specified unit length voltage criterion, with the distance of voltage probes on the superconductor. The constant n is called superconductor index and cannot be theoretically predicted but, low values of this superconducting index, are found on defective or poor quality superconductors. [WS99 p370]

In our laboratory, the measurements of I_C are done with the same apparatus used for measuring T_C, with the usage for the sample current bias a 6680 Agilent power supply with a maximum current of $875\ A$. These currents, usually of the order of hundreds Ampere are accurately read by using a Danfysik DCCT flux gate [CG15] [CR15]. The current leads of our measurements are two brass cans counter flux cooled by the helium gas flow used by the cryostat for cooling the sample. These current leads have been optimized for the steady transport current of $200\ A$ [SS06]. On the cold side of this current leads there are two copper blocks where, as shown in Fig.1.15, small samples of superconducting tapes can be mounted in two different positions in order to measure its I_C on both parallel and orthogonal magnetic field.
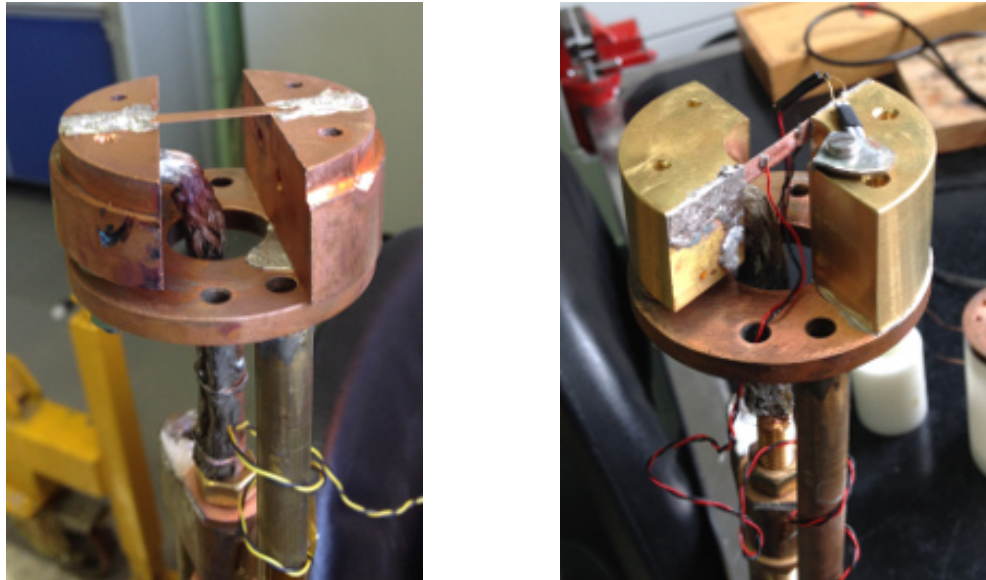

Fig.1.15 The sample holder with a $ReBCO$ tape ready for I_C measurements. The tape is orthogonal (left) and parallel (right) to the magnetic field.

The experimental determination of I_C is shown in Fig.1.16. This figure shows the $I - V$ characteristic of a sample, of HCN04150 tape produced by SuNAM© and measured at the temperature of $77\ K$ in self-field.
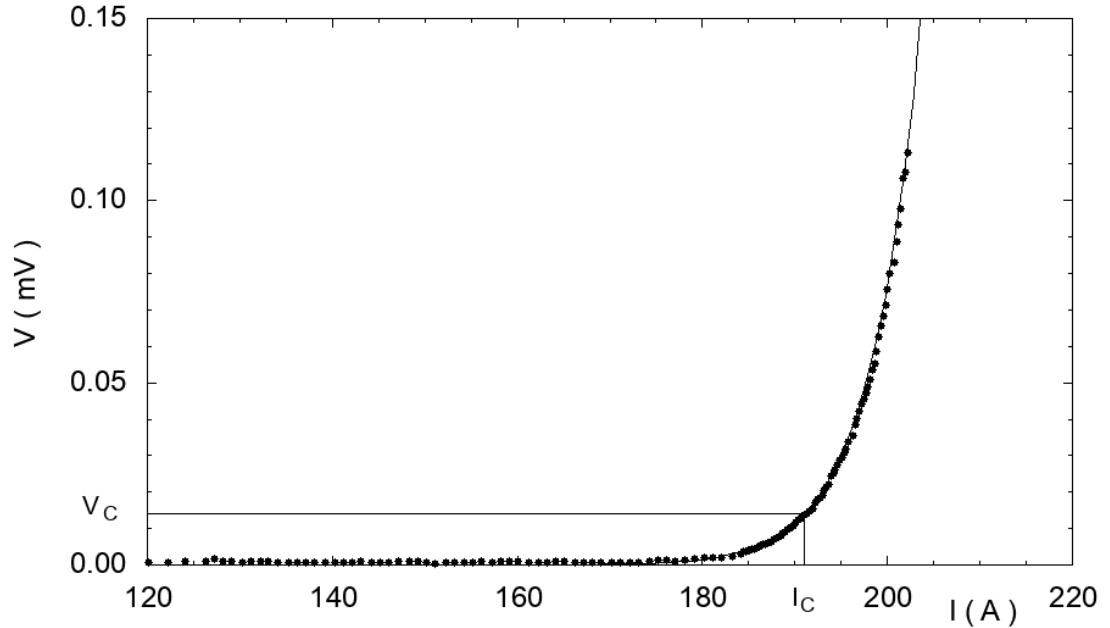

Fig.1.16 An $I - V$ characteristic with $I_C = 191\ A$. Data points (dots) are fitted with Eq.1.21 (line) with $V_C = 14\ \mu V$ and the index $n = 37$.

The sample with a length of $25\ cm$ has been joined to the current leads with two brass clamps. The voltage probes were soldered, with a low melting point alloy, on the copper above the superconducting side of the tape. The room temperature resistance was $R_{300} = 14.3\ m\Omega$, measured by setting a current of $7\ A$ and reading a voltage of $100\ mV$ across the voltage probes. The value of V_C has been determined by using the unit length voltage criterion of $1\ \mu V/cm$. The use of this generally adopted criterion, with the voltage probes, placed $14\ cm$ apart, makes $V_C = 14\ \mu V$. In Fig.1.16 the horizontal line at the voltage V_C crosses the $I - V$ characteristic on the point $I_C \approx 190\ A$. A better determination of I_C can be obtained by a numerical fit of Eq.1.21. The fit of the data shown in Fig.1.16 with the Eq.1.21 gives $I_C = 191\ A$ and a value of the index $n = 37$.

Composite wires and tapes fabricated for magnet windings, such as $NbTi$, Nb_3Sn, and coated conductor on $ReBCO$ tapes have values of n from ~30 to ~80 for the LTS and from ~10 to ~40 for HTS. The determination of the n index value is one of the ways to detect defective and damaged samples, in fact, the value on n may reduce after permanent damages.

The measurements of I_C require fast reader of both the currents and voltages because, as shown in Fig.1.16 above I_C the voltage increases exponentially. To avoid excessive dissipations on this range of the bias currents, the voltages have to be read, as fast as possible and above a certain value, the bias current has to be interrupted. In our laboratory, a computer continuously acquires currents and voltages and when a dangerous dissipation is reached the bias current is automatically interrupted. This protection mechanism sometimes fails and the dissipation goes well above its limit. In these cases, the sample damages, and as shown in Fig.1.17, the tape burns.
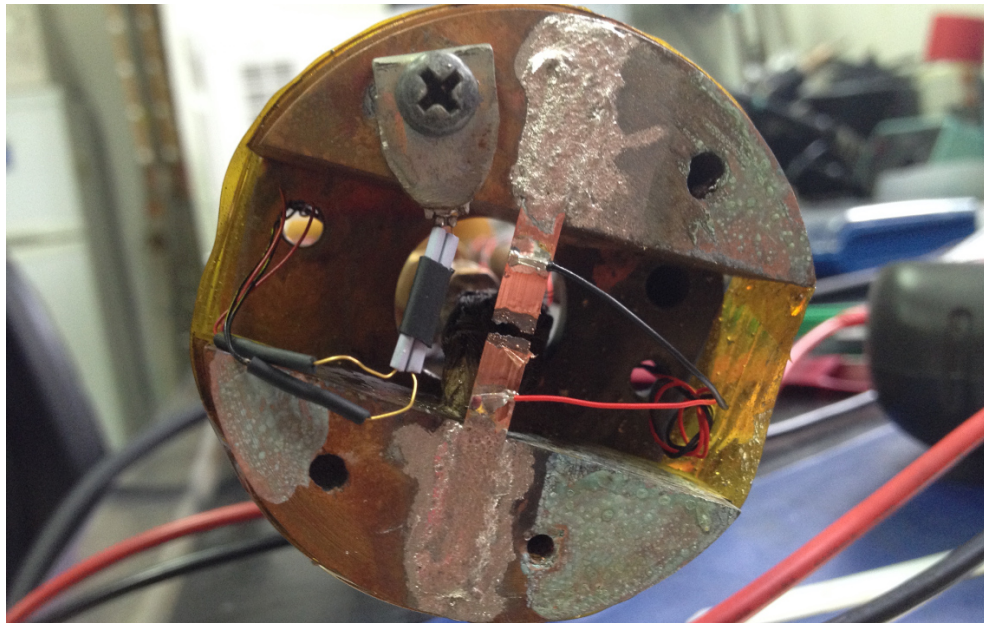

Fig.1.17 Consequences of an overheating during the measure of I_C on a $4\ mm$ wide HTS tape. Excessive dissipation generates a large amount of heat raising the temperature high enough to destroy the sample.

The measurements of I_C requires also the thermal stabilization of the sample during the data acquisition. This is not an easy task because, on both

the current leads and the sample, the high values of the current generate extra heating that have to be removed. The temperature control, for measurements in a liquid-gas bath, is less significant because the liquid cryogen bath can remove the amount of extra heating and keep the temperature stable. On the contrary, during the measures of I_C in a gas flow environment needs much more care. The generated extra heating becomes a constraint on the choice of the current ramp to be used during the acquisition of the $I-V$ characteristic. Another key point for an accurate determination of I_C is the measurement of the voltages down to a few μV. This requires a reduction of the noise and, the use of a voltmeter having adequate sensitivity.

We performed I_C measurements as a first characterization of the HTS tape HCN04150 produced by SuNAM© and SCS4050AP produced by SuperPower©. The data collected during these measurements of $I_C(B,T)$ are used in the next chapter during the measurements of the quench propagation velocity in these tapes.

The measurements of critical currents as a function of the magnetic field and temperature $I_C(B,T)$ for both tapes were done with the apparatus previously shown in Fig.1.11. The magnetic field was applied parallel and orthogonal to the tape as shown in Fig.1.15. A summary of all relevant results is reported, for the SuNAM© tapes in Fig.1.18 a) and b) and for the SuperPower© tapes in Fig.1.19 a) and b). In all figures, the solid lines with full symbols refer to a magnetic field applied parallel to the tape. Open symbols and dashed lines refer to a magnetic field applied perpendicularly to the tapes.
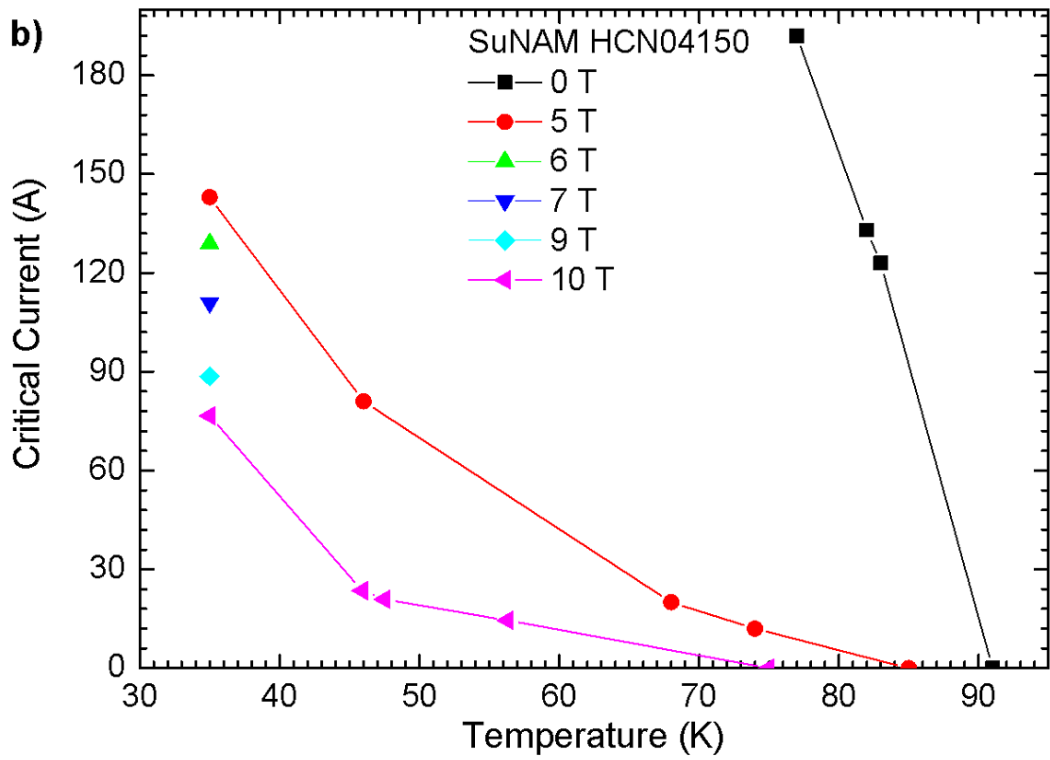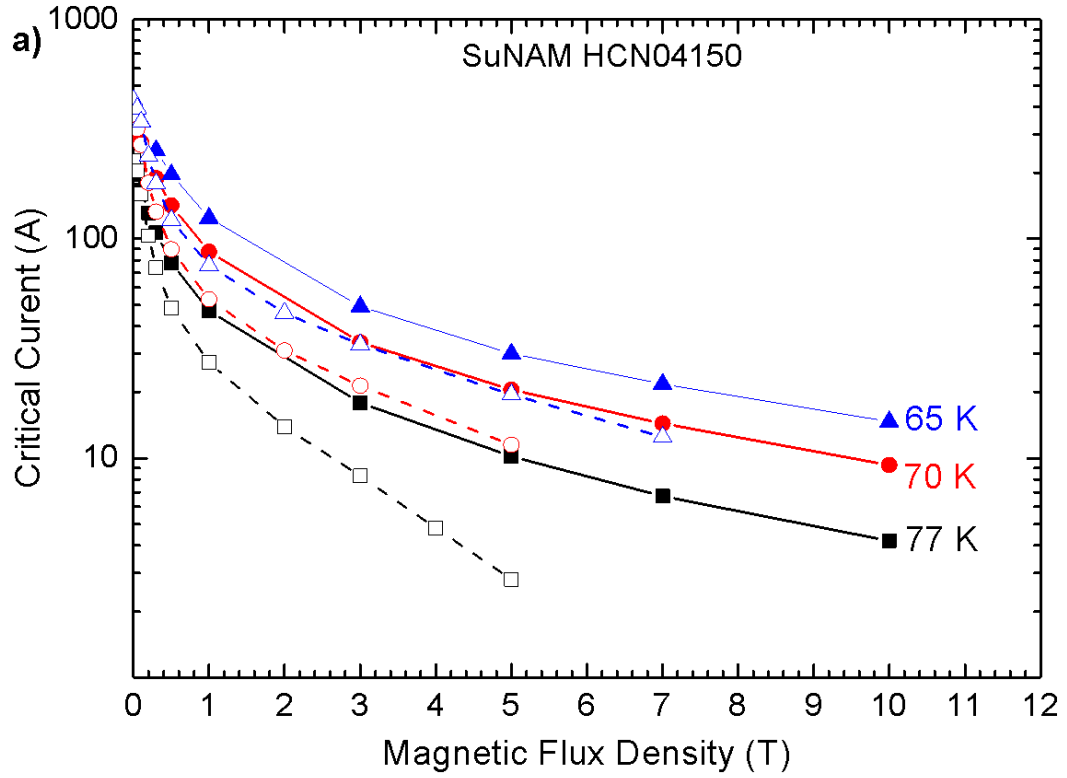
Fig.1.18 Measurements of $I_C(B,T)$ for the SuNAM© HCN04150 tapes as a function of the applied magnetic field a) and the temperature b). With the magnetic field parallel (solid lines) and perpendicular (dashed lines).

Fig.1.19 Measurements of $I_C(B,T)$ for SuperPower© SCS4050AP tapes as a function of the applied magnetic field a) and the temperature b). With the magnetic field parallel (solid lines) and perpendicular (dashed lines).
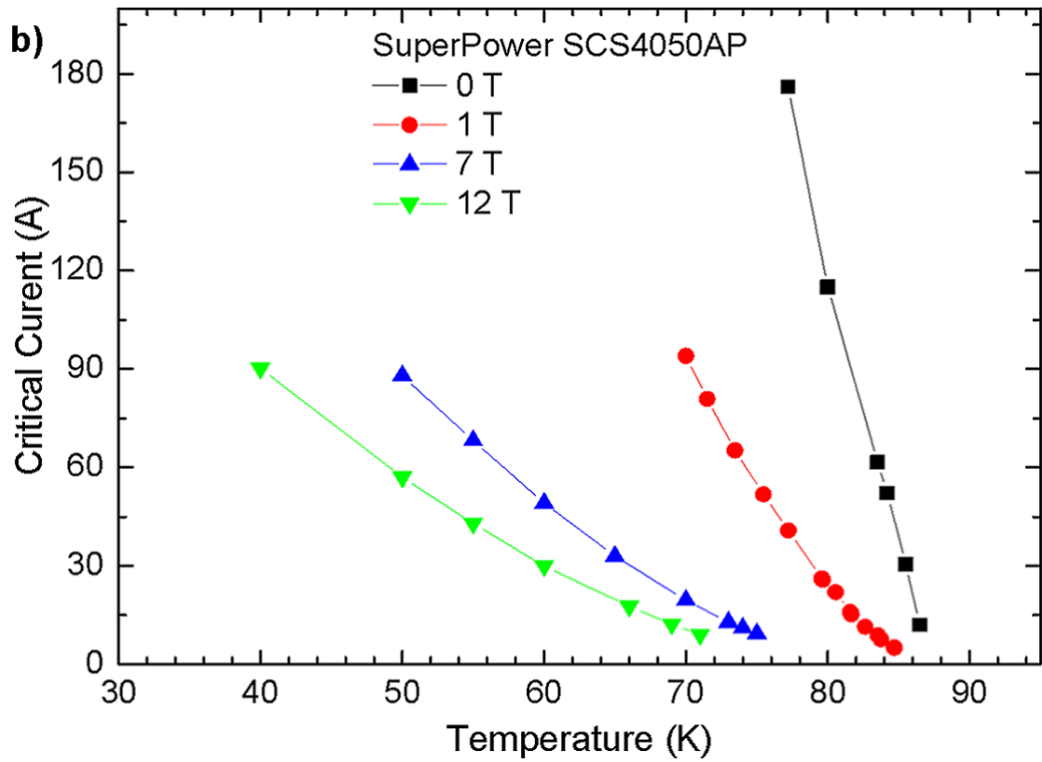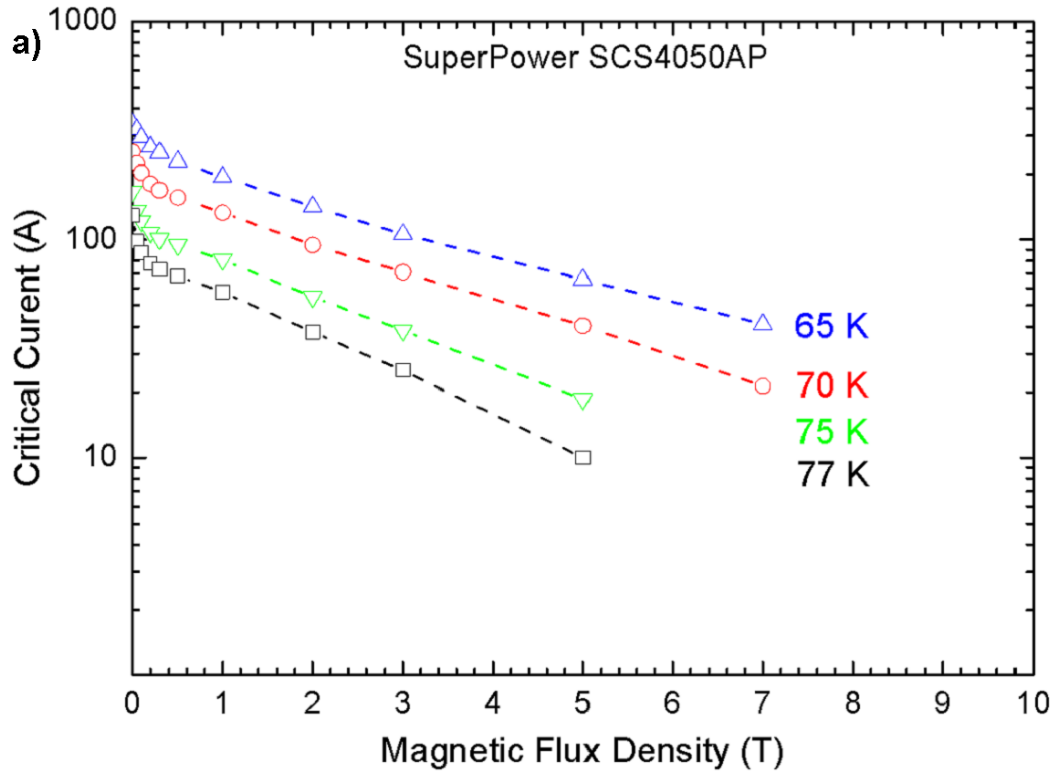
As shown in the Fig.1.18 the SuNAM© tapes show a value of the $I_C(77K) = 190\,A$ in the self-field. This critical current reduces to $I_C(35K) = 80\,A$ under the application of a magnetic field of $10\,T$. In Fig.1.19, the measurements on the SuperPower© tapes in the self-field is $I_C(77K) = 180\,A$ and $I_C(40K) = 90\,A$, under the application of a magnetic field of $12\,T$. The measurements have been done on $6\,cm$ samples, though cut from the same tape batch of the samples used for the measurements of $NZPV$.

All tapes were measured using the same experimental apparatus. All the other experimental conditions were kept unchanged in order to improve the repeatability and reproducibility.

Critical currents on small coils: In this section, a model that permits to cancel the coil inductive voltages is presented. This voltage is always present during the measures of the critical current with the application of time-dependent currents. The measurements of I_C on a superconducting coil with a current ramp presents a voltage offset caused by the coil inductance. This voltage, proportional to the current ramp rate K_R can be reduced and almost canceled by increasing very slowly the currents during the measure of I_C. Unfortunately, current rates that can be as slow as 0.01 A/s, do not completely cancel this effect and, still, some tiny voltage can be seen.

The presence of this voltage offset plus a slowly linear increasing voltage makes difficult the choice of V_C and, as a consequence, increases the error on the determination of I_C. A very slow increase in the current is not a suitable choice. In fact, slow rates are not suitable for the measurement of the large values of I_C on composite conductors because large currents generate high dissipation in the resistive joints. This time-dependent heat is difficult to control and the thermal stability becomes difficult to maintain for a long time. Furthermore, slow rates, in the dissipative part of the I-V characteristic, cause a

59

rapid increase of the temperature that is difficult to keep under control, and a quench which leads to a tape rupture, like the one shown in Fig.1.17, may happen more frequently. For this reason, as a rule of thumb, rapid measurements are always preferred.

With the aim to find an analytic expression for this time-dependent voltage $V(t)$ and the desire to understand this phenomenon, an equivalent circuit model of a composite superconductor developed to facilitate the calculation of ac dissipation was considered. [GR03] The circuit, with discrete components, shown in Fig.1.20, is a simplified version of the original circuit model and can be used only for currents $I_T(t) < I_C$. [SS03]
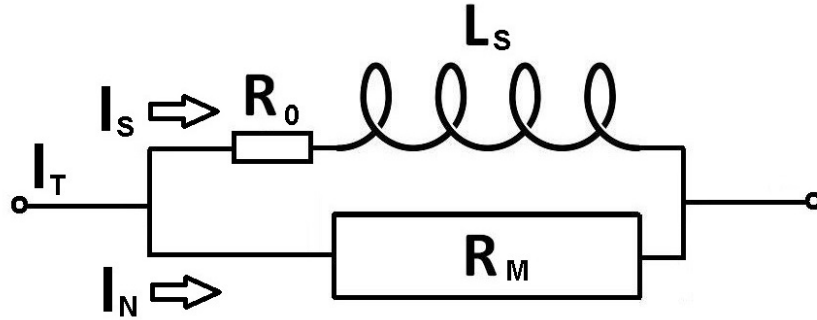

Fig.1.20 Equivalent circuit for a coil made with a composite superconductor.

In the original circuit the current dependent $R_S(I_S)$, which takes into account the superconductor losses, is taken as the sum of a residual resistance R_0 with the ratio $V_S(I_S)/I_S$. In this model, by using Eq.1.21 with an index $n > 20$, it follows that for all currents $I_S(t) \leq I_T(t) < I_C$, the resistance $R_S(I_S) \approx R_0$.

$$R_S(I_S) = R_0 + \frac{V_S(I_S)}{I_S} = R_0 + \frac{V_C}{I_S}\left(\frac{I_S}{I_C}\right)^n = R_0 + \frac{V_C}{I_C}\left(\frac{I_S}{I_C}\right)^{n-1} \approx R_0 \qquad (1.22)$$

The other two components of the circuit model shown in Fig.1.20 are the Inductance L_S of the coil and, the resistance R_M of the metallic matrix. Moreover, the inductive coupling between the normal and the superconducting material present in the original circuit has not been considered.

On the circuit of Fig.1.20, as in the usual measure of I_C, a time-dependent current is applied and, the voltage $V(t)$ across the superconducting coil is unknown. In order to obtain $V(t)$, the analytic expressions of the same voltage drop, i.e. the voltage across the normal and the superconducting branches, are equated:

$$R_M I_N(t) = R_0 I_S(t) + L_S \frac{d}{dt} I_S(t) \tag{1.23}$$

Where $I_N(t)$ and $I_S(t)$ are respectively the currents in the normal and superconductive branch. For these currents, the Kirchhoff law, always valid, allows writing $I_T(t) = I_N(t) + I_S(t)$ where $I_T(t)$ is the external current fed into the coil. For a current ramp with constant rate K_R, the time-dependent external current can be written as $I_T(t) = K_R t$. Putting all these conditions in Eq.1.23, and rearranging the terms, it is possible to obtain the following equation:

$$\frac{d}{dt} I_N(t) + \frac{(R_M + R_0)}{L_S} I_N(t) = K_R + \frac{R_0}{L_S} K_R t \tag{1.24}$$

This ODE shown in Eq.1.24 can be analytically solved. The solution obtained using the Wolfram Mathematica© package is the following.

$$I_N(t) = \frac{R_M L_S}{(R_M + R_0)^2} K_R \left(1 - \exp\left(-\frac{R_M + R_0}{L_S} t\right)\right) + \frac{R_0}{R_M + R_0} K_R t \tag{1.25}$$

The calculation of the voltage $V(t)$, due to the coil impedance, can be computed by using the expression of $I_N(t)$ obtained Eq.1.25 and the Ohm law applied on the normal branch of the model, $V(t) = R_M I_N(t)$.

$$V(t) = \frac{R_M^2 L_S}{(R_M + R_0)^2} K_R \left(1 - \exp\left(-\frac{R_M + R_0}{L_S} t\right)\right) + \frac{R_M R_0}{R_M + R_0} K_R t \tag{1.26}$$

In the limit of negligible losses when $R_0 \to 0$ the Eq.1.26 reduces to

$$V(t) = L_S K_R \left(1 - \exp\left(-\frac{R_M}{L_S} t\right)\right) \tag{1.27}$$

The Eq.1.26 is made of two terms. The exponential on the first term will lead to a rapid increase of the voltage that will saturate to a constant value with the time constant τ given by the ratio $\tau = L_S/(R_M + R_0)$. The second term is a linear increase of the voltage depending mainly by the dissipation of the superconductors represented in the model by R_0. In fact, in the condition $R_0 \rightarrow 0$, the Eq.1.26 becomes the Eq.1.27 that is made of only one term with the rapid increase that saturates to the constant voltage value $V(t) = L_S K_R$.

In Fig.1.21, both Eq.1.26 and Eq.1.27 have been compared to the $I - V$ characteristic taken from a measure of the I_C on a superconducting coil.
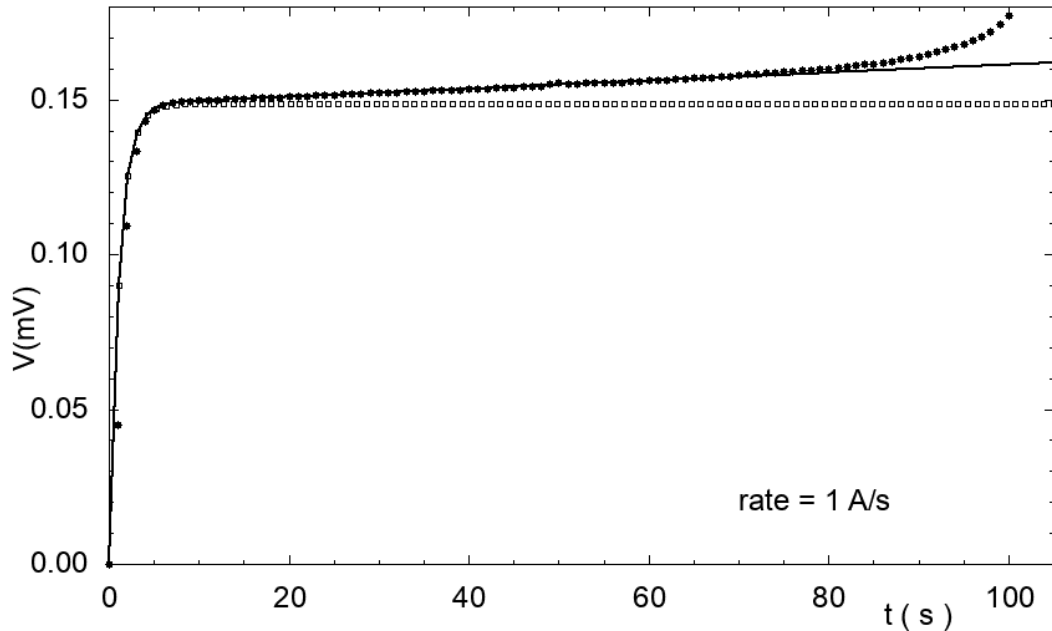

Fig.1.21 Time-dependent voltages for an HTS superconducting coil at $77\ K$ with a current ramp of $1\ A/s$. The experimental data (dots) are superimposed to the best fit of Eq.1.26 (line). The best fit with the Eq.1.27 where $R_0 = 0$ is also drawn (open circles).

The coil used for these measurements was obtained by winding, on a 40 mm diameter, plastic reel, 24 turns of SuNAM© HCN04150-16277-02 HTS tape. The winding was insulated with a thin Kapton insulation layer. The ends of the tape were soldered on the copper current leads by using a low-temperature alloy for a length of about half turn. The voltage readings were taken near the coil extremity within the current leads contacts. The temperature stability was

62

granted putting the coil on a liquid nitrogen bath. The voltages obtained by the measurements were done by applying a current ramp with a rate of $1\ A/s$ for about $100\ s$. Because of this particular rate choice, the time scale of the x-axis of Fig.1.21 is the same for both the times in seconds, and the currents in Amperes. In other cases, with different values of the rate, a scale factor $I(A) = K_R(A/s)\ t(s)$ should be applied. On both Eq.1.26 and Eq.1.27, shown in Fig.1.21, the values of the resistance $R_M = 0.13\ m\Omega$, the coil inductance $L_S = 0.1486\ mH$ and the resistance $R_0 = 0.13\ \mu\Omega$ that represents the superconductive loss, have been found by applying the best fit to the measured data. In Fig.1.21, besides the experimental data, shown with black points, it is possible to observe the agreement with the Eq.1.26, shown with a continuous line. This agreement is valid up to the time $t = 85\ s$ or $I = 85\ A$ where the condition $I < I_C$ is satisfied. Above this value, the nonlinear behavior of $R_S(I_S)$ shown in Eq.1.22 should be considered. Again in the Fig.1.21, the Eq.1.27 is shown with open dots. The agreement, until $t = 10\ s$, of the Eq.1.27 with both the experimental data and Eq.1.26, is not a surprise. In fact, up to this time, on Eq.1.26, the increase of the voltage on the second term, is small compared to the exponential jump of the first term where, the value of R_0, in the sum $R_M + R_0$, can be neglected since R_0 has been found to be three orders of magnitude smaller than R_M. The attribution of special physical meaning to the components of this model is out of the purpose of this work, even if the value of L_S found by the best fit of the experimental data is very close to the value of $0.144\ mH$ expected for the inductance of this coil. The main scope of this model is to eliminate, from the measures, the unpleasant voltage offset caused by the coil inductance and allows an easier and more accurate determination of the coil critical current $I_C(T)$. The enhancement of the critical current once the inductive voltage has been neglected is shown in Fig.1.22 where the Eq.1.26 with the fit parameters is subtracted from the experimental data. The voltages of the $I - V$ characteristic shown in Fig.1.22 have been obtained from the time-dependent voltages to

the dependence of the current by using the relation $I(A) = K_R(A/s)\,t(s)$. The numbers on the scales are unchanged because in this lucky case the rate is $1\,A/s$.
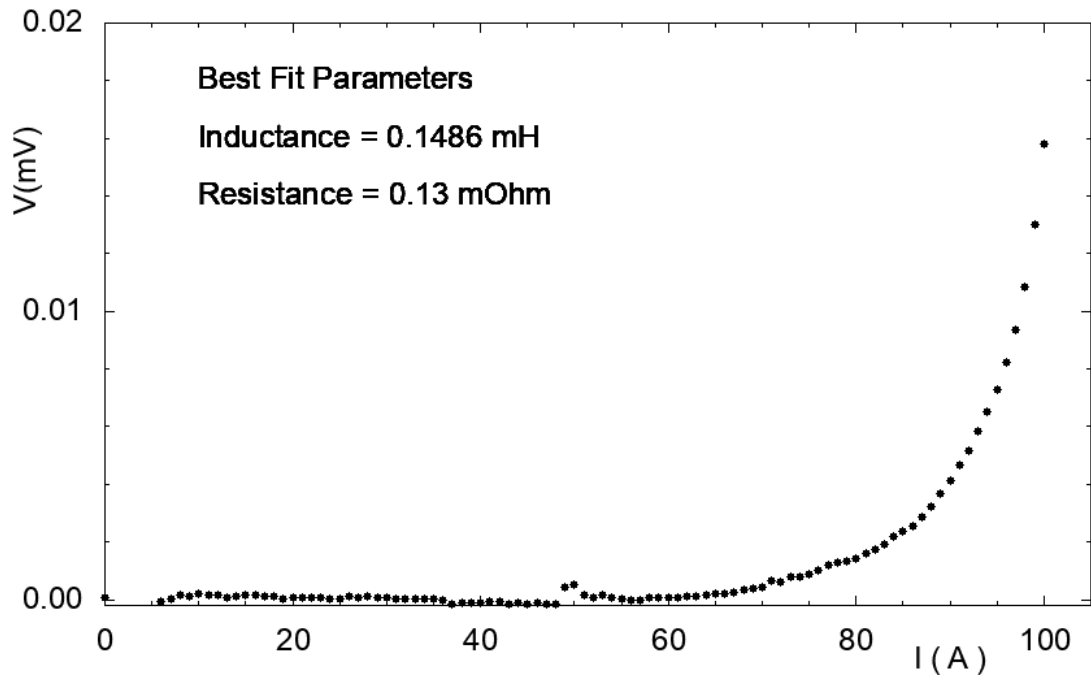
Fig.1.22 The $I - V$ characteristic of the HTS superconducting coil at $77\,K$ once the inductive voltages have been removed. The voltages as a function of time have been reported as a function of the current by using the constant rate of $1\ A/s$ and the relation $I(A) = K_R(A/s)\,t(s)$

In conclusion, the usage of this model, valid only for linear current ramps, allows the elimination of the inductive voltage and makes a better comparison of the $I - V$ characteristic between measurements on coil and wires.

2

THE QUENCH PROPAGATION PHENOMENA

2.1 A phenomenological description

The cryo-stability analysis has been carried out in section 1.6.2 and stability criteria have been defined. In this part, the reaction of a composite superconductor to the presence of an external disturbance, and the quench phenomena seen as a consequence of a local disturbance, will be experimentally investigated on two $ReBCO$ commercial tapes. [GR18] [BL94]

Even for a magnet with the best stabilization, there is a not negligible probability to have one or more quenches. The superconductive quench represents a serious problem for high field magnets. Despite the presence of a protection system, which turns down the bias current, there is the stored energy that must be discharged. This energy is converted in heat that causes damages to the winding if the magnet is not adequately protected. Therefore all commercially available superconducting magnets have quench protections. The damage of the winding generally occurs when the heat generated during the quench process concentrates on a small length of the wire. In this case, the temperature of the conductor will become high enough to permanently destroy part of it. On the contrary, if the heating generated during a quench is spread out along the conductor, the local temperature remains under the destructive threshold.

The quench phenomena likewise any avalanche effect, needs a small amount of energy to ignite. To determine the approximate order of magnitude of the minimum amount of energy required to start the quench, an approximate calculation can be performed. In Fig.2.01 a piece of superconducting wire with section A, carrying a current I_C at a temperature T_0 is shown. When it is affected by a point disturbance over a length L, the local temperature can rise above T_C. In this case, the superconductivity is locally suppressed.
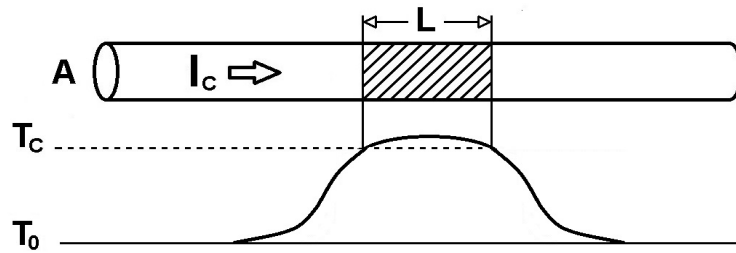

Fig.2.01 Point disturbance with a normal zone of length L on a wire with section A carrying a current I_C (top) and the temperature profile of the wire (bottom).

The Joule effect, due to the current flowing into the normal conductor of length L, generates some heat that is spread along the conductor by thermal conduction. In the normal zone, where $T = T_C$, the heat generated can be determined as $R_N I_C^2 = \rho_N L A J_C^2$, here ρ_N, R_N are the wire resistivity and resistance in the normal state, respectively. The generated heat will propagate along the wire. This propagation will be proportional to the temperature gradient that can be approximated as $(T_C - T_0)/L$ so that the propagating heat will be $2 k A (T_C - T_0)/L$ where k is the wire thermal conductivity and factor 2 considers the heat propagation on both sides. In the equilibrium condition, the heat generated in the normal zone is equal to the heat that propagates. In this condition it is possible to compare these two terms:

$$\rho_N L A J_C^2 = 2 k A \frac{(T_C - T_0)}{L} \tag{2.01}$$

Once the other quantities have been set, the length L that satisfies the equilibrium condition can be determined by solving the Eq.2.01 as follows.

$$L_{MPZ} = \frac{1}{J_C} \sqrt{\frac{2\,k}{\rho_N} (T_C - T_0)} \qquad (2.02)$$

The length L_{MPZ}, called Minimum Propagation Zone or MPZ represents an unstable equilibrium state, generating the propagation of the normal zone. If the length of the normal zone is shorter than MPZ, the term of the heat generation is smaller than the heat propagation. In this case, the heat generated at the disturbance point will spread along with the wire and Joule heating effect will not be able to sustain the quench avalanche. The wire cools down and the thermal disturbance disappears. On the contrary, a normal zone longer than MPZ will have the heat generation term larger than the heat propagation one. In this case, the Joule heating effect sustains the quench and normal zone propagates along the wire.

The value of MPZ can be computed for composite superconductors. By using the same approximation used before, the equilibrium condition obtained on Eq.2.01 can be written into a slightly modified form. In the normal zone, the thermal conductivity k of the superconductor can be substituted by the normal metal thermal conductivity k_M of the metal layer of the composite and, for the Joule dissipation, the result obtained by using the Eq.1.10 for $T > T_C$ with $I_T = I_{C0}$ and the metal resistance $R_M = \rho_M\,L/A_M$, where ρ_M and A_M are the resistivity and the section of the metal. With these changes, and assuming that the whole current will flow only in the normal metal, so that $I_{C0} = J_{C0}\,A_M$, the comparison between the propagation and generation terms for a composite conductor becomes the following:

$$\rho_M\, L\, A_M\, J_{C0}^2 = 2\, k_M\, A_M\, \frac{(T_C - T_0)}{L} \qquad (2.03)$$

The section A_M takes into account only the metal layer since, in the normal state, the contribution of the superconductor to the electrical heating

and thermal conductivity is negligible compared to the metal matrix. As before, the length L_{MPZ} that satisfies the equilibrium condition can be determined by solving Eq.2.03.

$$L_{MPZ} = \frac{1}{J_{C0}} \sqrt{\frac{2\,k_M}{\rho_M}(T_C - T_0)} \qquad (2.04)$$

The Eq.2.02 and Eq.2.04 are formally identical, but numerical results can be dramatically different. The thermal conductivity of normal metal is much larger than in the superconductors especially when the normal metal is copper. On the other hand, the electrical resistivity of the normal metal is smaller than in the superconductor. It turns out that k/ρ ratios, allows the composite to have much longer MPZ, since $k_M/\rho_M \gg k/\rho_N$. As an example, on the LTS wires such as the $NbTi$ wire at $4.2\,K$, the Eq.2.01 gives an MPZ length less than a micron. A similar calculation done with Eq.2.04 on a copper-based composite with a factor $k_M/\rho_M \approx 7.5 \cdot 10^6$ times higher makes the length of the MPZ of few millimeters. The composites, based on HTS, have a longer MPZ since the difference $T_C - T_0$ is much larger. It means that a composite superconductor is more stable because it needs a larger heat disturbance spot to ignite the quench. The disturbance energy needed to create a normal zone with length MPZ is called Minimum Quench Energy or MQE and its value is proportional to the length MPZ depending on both the temperature T_0 and the current density J_{C0}. Pure superconducting wires, with their small values of MQE, have a high grade of instability and, for this reason, are unusable in all the applications that require the transport of high currents, also in the presence of high magnetic fields. HTS coated conductors, with their higher MQE values are more stable and seem suitable for technological applications.

Another aspect to be considered is the propagation speed of the normal zone. This parameter, called Normal Zone Propagation Velocity or $NZPV$ is a measure of the propagation speed of the normal zone along the whole composite wire after the occurrence of a local quench. High values of $NZPV$ allow a fast distribution of the thermal energy generated by the discharging

currents, thus limiting the damages that can occur as a consequence of the rise of the temperature. [LC14][LC17] In particular, LTS composite wires have $NZPV$ in the *m/s* range. On the other side, HTS wires and tapes have higher MQE due to their high T_C , but $NZPV$ in the *cm/s* range. The full characterization of a composite that will be used for the construction of a superconducting coil requires the knowledge of the $NZPV$ at the working temperature, magnetic field, and bias current.

2.2　　　Quench analytical models

The models able to describe the propagation of the normal zone in superconducting wires and tapes, and the calculation of the $NZPV$ have been developed since 1960 by many researchers. Nowadays a popular model is due to N.M.Wilson [WL02]. In this model, the profile of the normal zone wavefront propagating along on the superconductor is shown on the left of Fig.2.02.
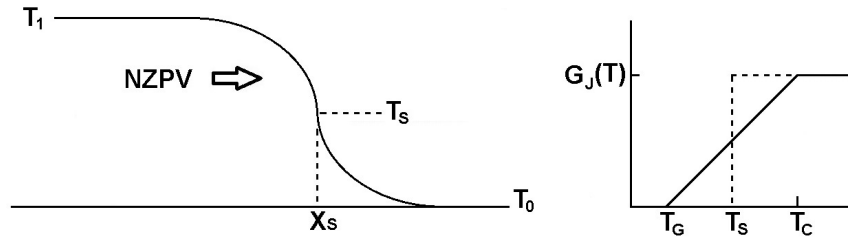
Fig.2.02 (Left) Temperature profile of the normal zone wavefront propagating with velocity $NZPV$. (Right) Current sharing Joule dissipation and, shown by dashed lines, the N.M.Wilson approximation with the transition at T_S .

This wavefront profile moves from left to right with constant velocity $NZPV$. The superconductor in contact with the cryogenic coolant and without any dissipation is at the temperature $T_0 < T_1$. On the other side, far from the wavefront, the superconductor is in the normal state. Its temperature T_1 is obtained by the equilibrium between heat generation and cooling $f_p P_D h_q (T_1 - T_0) = G_J A_{cd}$. [WS99] The computation of the power density general equation Eq.1.03, applied to the case of a one-dimensional conductor, with the approximation of the heat transfer h_q, thermal conductivity k_{cd} and specific heat C_{cd} constant, become.

$$C_{cd} \frac{\partial T}{\partial t} = \frac{\partial}{\partial x}\left(k_{cd}\frac{\partial T}{\partial x}\right) + G_J(x) - \left(\frac{f_p P_D}{A_{cd}}\right) h_q(T - T_0) \tag{2.05}$$

The joule dissipation $G_J(x)$ in this model is shown by the dashed line in the right part of Fig.2.02 and, is approximated by a sharp transition from zero for all $T \leq T_S$ to the value $\rho_{cd} J_{cd}^2$ for all $T > T_S$. The position x_S , as shown on

the left of Fig.2.02, corresponds to the value on the wavefront profile corresponding to the temperature value T_S that, in this model, is chosen as:

$$T_S = \left(\frac{T_C + T_G}{2}\right) \tag{2.06}$$

With all these approximations the Eq.2.05 can be divided into two parts in contact at the point x_S considered the origin of a new coordinate system moving with the wavefront velocity $NZPV$. In this framework the solution of the Eq.2.05 in the approximation of an adiabatic, *i.e.* not externally cooled, propagation velocity is then:

$$NZPV = \frac{J_{cd}}{C_{cd}}\sqrt{\frac{\rho_{cd}\,k_{cd}}{T_S - T_0}} \tag{2.07}$$

The usage of the temperature-dependent $C_{cd}\,(T)$, $\rho_{cd}(T)$ and $k_{cd}\,(T)$, instead of their constant values, can improve the accuracy of the model. In particular, the use of constant values in a wide range of temperature constitutes a severe approximation.

Moreover, the choice of the temperature T_S on Eq.2.06 appears to be reasonable for LTS, where the transition amplitude $\Delta T = T_C - T_G$ is a few tenths of a degree and, a linear behavior of the resistivity seems to be adequate. However, in the HTS composite, where the transition amplitude ΔT can be several degrees and the resistivity behavior is strongly non-linear, a different choice may be taken. Recently, an alternative to the linear behavior has been proposed with the introduction of a new temperature-dependent shielding resistivity $\rho_{sh}(T)$ that modifies the current sharing in the temperature interval between T_G and T_C. [CL15] This shielding resistivity is zero for $T < T_G$, equal to the normal state resistivity ρ_{cd} for $T > T_G$ and, in the range $T_G \leq T \leq T_C$, is given by the expression:

$$\rho_{sh}(T) = \rho_{cd}\left(\frac{T - T_G}{T_C - T_G}\right)^m \tag{2.08}$$

where the exponent m is a parameter that could be related to the value of the n-index of the $I - V$ characteristic, in the phenomenological Eq.1.21. With this choice, the value $m = 1$ of the exponent reproduces the linear behavior of the original model. In the top of Fig.2.03, it is shown how the m exponent affects the $NZPV$ value for fixed temperature and bias current. [CL15]
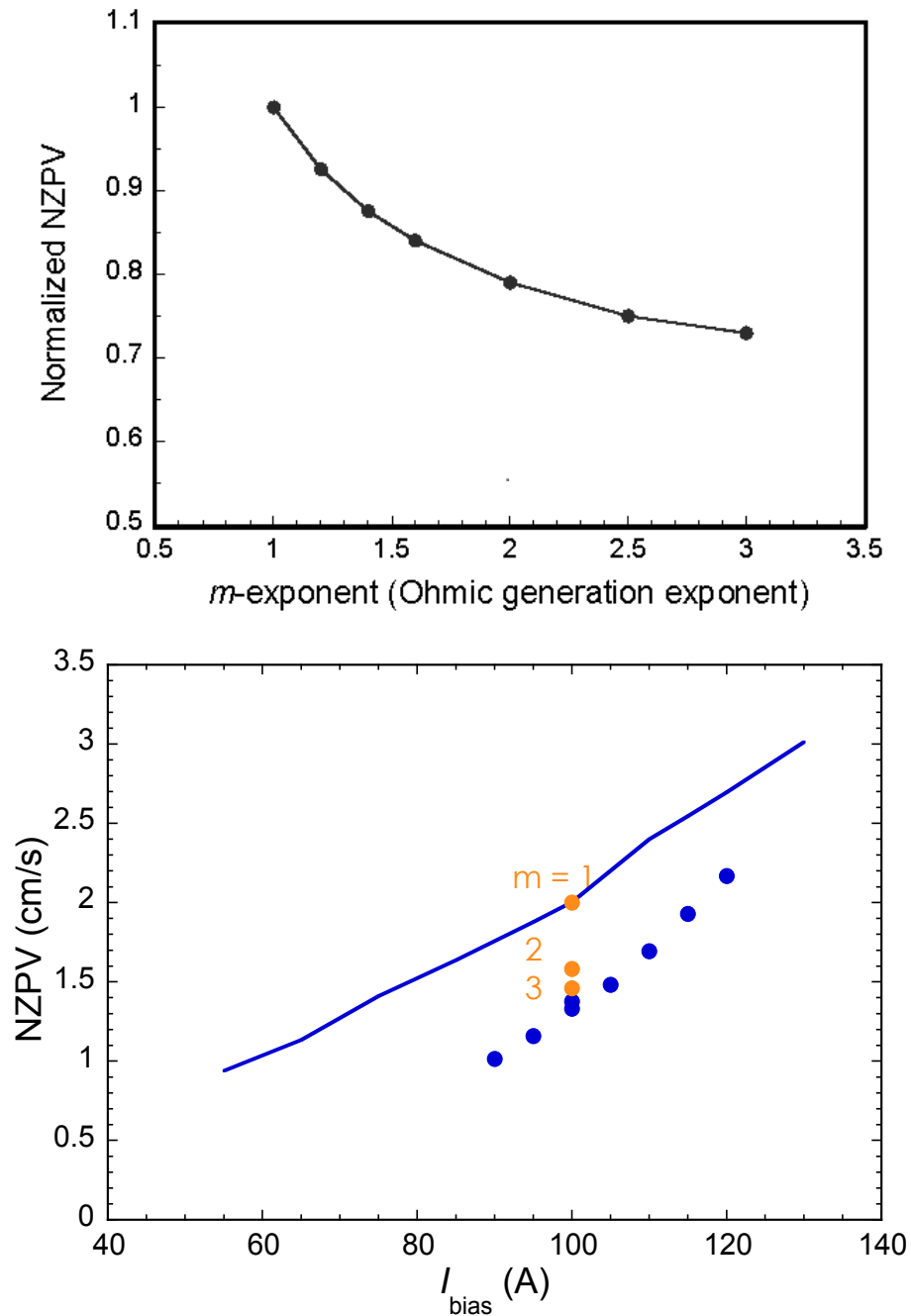

Fig.2.03 (Top) $NZPV$ reduction by increasing the m-exponents. (Bottom) The Eq.2.07 with $m = 3$ provides a better agreement with experimental data.

In the bottom of the Fig.2.03 solid line represents Eq.2.07 with $m = 1$ and dots are the experimental measurements of $NZPV$. In the same figure it is reported, just as one point of bias current, how the analytical curve shifts towards the experimental data as *m* increases. [CL15]

In 1999, *Y.Iwasa* proposed a model for the computation of the $NZPV$, without the constraints of the usage of constant C_{cd}, ρ_{cd}, and k_{cd}. [WS99] The model assumes that a constant current density J_{cd} flows into a conductor and $x = 0$ is the place where the thermal wavefront separates the normal and the superconducting state. [ZH91] The steady-state equations in one-dimensional form, that describe both the normal and superconducting zones, is written as follows:

$$C_N(T) \frac{\partial T_N}{\partial t} = \frac{\partial}{\partial x} \left(k_N(T) \frac{\partial T_N}{\partial x} \right) + \rho_N(T) J_{cd}^2$$

(2.09)

$$C_S(T) \frac{\partial T_S}{\partial t} = \frac{\partial}{\partial x} \left(k_S(T) \frac{\partial T_S}{\partial x} \right)$$

Where, in the first row of Eq.2.09, $C_N(T)$, $k_N(T)$, and $\rho_N(T)$ are the temperature-dependent heat capacity, the thermal conductivity, and the electrical resistivity, in the normal state, respectively. Likewise, in the second row of Eq.2.09, $C_S(T)$ and $k_S(T)$ represent the temperature-dependent heat capacity and the thermal conductivity in the superconducting state, respectively. It is possible to notice that the Joule heating has been removed from the equation of the superconducting part on the second row of Eq.2.09. On this conductor, the wavefront, at the separation between the normal and the superconducting zones, moves with constant velocity $NZPV$. The Eq.2.09 are solved, with a moving coordinate system. The boundary condition at the origin requires the temperature profile and its derivative to be continuous in the origin. After a mathematical computation, the solution with the determination of the value of the $NZPV$ is the following equation:

73

$$NZPV = J_{cd} \sqrt{\frac{\rho_N(T_T)\, k_N(T_T)}{\left[C_N(T_T) - \frac{1}{K_N(T_T)}\frac{dK_N}{dT}\Big|_{T=T_T}\, \int_{T_0}^{T_T} C_S(T)dT\right]\, \int_{T_0}^{T_T} C_S(T)dT}} \qquad (2.10)$$

The temperature T_T is the transition temperature for a superconductor carrying a current I and corresponds to the value of the tape temperature at $x = 0$. The Eq.2.10 can be simplified by considering the derivative of $k_N(T)$ at the temperature T_T negligible respect to the value of $C_N(T_T)$. [BN16] With this approximation the $NZPV$ can be written into the following simplified version.

$$NZPV = J_{cd} \sqrt{\frac{\rho_N(T_T)\, k_N(T_T)}{C_N(T_T)\, \int_{T_0}^{T_T} C_S(T)dT}} \qquad (2.11)$$

This approximation can be done in $YBCO$ because for this material the derivative of $k_N(T)$ near T_T is strongly reduced by the magnetic field. The error due to this approximation reduces by increasing the magnetic field and at $19\,T$ is always smaller than 7%. [BN16]

The Eq.2.11 can be further simplified for materials with temperature-independent properties and can be written into a more simple form.

$$NZPV = J_{cd} \sqrt{\frac{\rho_N\, k_N}{C_N C_S\,(T_T - T_0)}} \qquad (2.12)$$

It is worth to notice that $NZPV$ is proportional to the geometric average of the heat capacities in the normal and superconducting regions. The Eq.2.12 is valid for a bare superconductor under adiabatic condition. In the condition of $(T_T - T_0)/T_0 \ll 1$ generally applicable to LTS and in case of $C_N = C_S = C_{cd}$ Eq.2.12 can be written with the temperature dependence of C_{cd}, ρ_N, and k_N.

$$NZPV = \frac{J_{cd}}{C_{cd}(T_\mu)} \sqrt{\frac{\rho_N(T_\mu)\, k_N(T_\mu)}{(T_T - T_0)}} \qquad (2.13)$$

Where is $T_\mu = (T_T + T_0)/2$. For composite superconductors with the cross-section A_M of the normal metal matrix, the current density to be used is J_M and with $T_T = T_S$ and the approximation of $C_{cd}(T_\mu) \approx C_M(T_\mu)$, it is also obtained.

$$NZPV = \frac{J_{cd}}{C_M(T_\mu)} \sqrt{\frac{\rho_M(T_\mu)\, k_M(T_\mu)}{(T_T - T_0)}} \qquad (2.14)$$

In Eq.2.14, the metallic matrix resistivity ρ_M is much smaller and in parallel with ρ_N may replace it. Similarly, the matrix thermal conductivity k_M is much larger than k_N and may also replace it. The Eq.2.13 with $T_T = T_S$ and the approximation of the resistivity ρ_M, thermal conductivity k_{cd}, and specific heat C_M independent from the temperature become equal to Eq.2.07.

The Eq.2.13 describes the quench propagation process assuming that the system is perfectly adiabatic. It has been experimentally observed that exists a minimum value of the current $I_m(T)$ that below which the normal zone does not propagate even when an overcurrent pulse, with an energy value that exceeds the stability margin, has been applied to the superconductor. [GB03].

The existence of a value of the minimum current $I_m(T)$ or, equivalently a minimum current density $J_m(T) = I_m(T)/A$, was not considered in the development of the models for the computation of $NZPV$. This problem, in cases of experimental environments not perfectly adiabatic, has to be taken into account. This correction to Eq.2.07 applied to the Wilson model leads to:

$$NZPV = \frac{J_{cd} - J_m(T_0)}{C_{cd}} \sqrt{\frac{\rho_{cd}\, k_{cd}}{T_S - T_0}} \qquad (2.15)$$

The same correction may be applied to Eq.2.10 and its derivations up to Eq.2.14. In all these equations it is possible to take into account the minimum current $I_m(T)$ in the computation of $NZPV$ by replacing the current density J_{cd} with the difference $J_{cd} - J_m(T_0)$.

2.3 Experimental measurements of quench propagation

The measure of the $NZPV$ is usually performed into a variable temperature cryostat. [LU02] It is possible to measure $NZPV$ also in the presence of a magnetic field B. Different thermal conditions can be used for the measurements of $NZPV$. In the case of conductive cooling, the composite is kept under vacuum and cooled by thermal conduction only from the two extremities. [GM07] Conversely, with conductive and convective cooling, besides the cooling through the two ends, part of the surfaces is exposed to a coolant fluid. Depending on the space available, the composite superconductor may be placed straight or wound around to the insulating support. A resistive heater, needed to generate the point disturbance, is usually glued on the center of the superconducting wire. Along its length, at measured distances, several voltage taps are added. The measurement of the $NZPV$ requires the knowledge of both T_C and $I_C(T, B)$ that are measured on samples cut from the same batch, or on the same sample before starting the $NZPV$ measurements. [CL09] [TR03]

In Fig.2.04 a sample of HTS tape is shown before its placement inside the cryostat with a short description of the heater and the voltage tap placement.
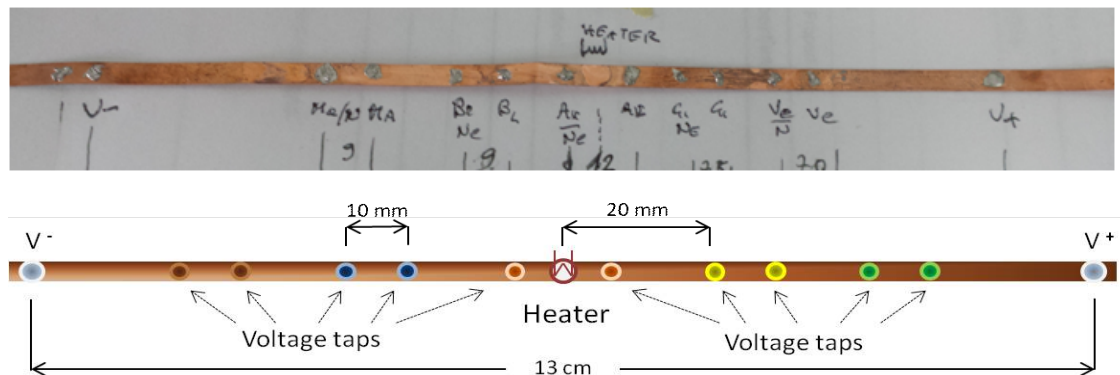

Fig.2.04 2G-HTS SCS4050 from SuperPower© with several voltage taps placed on it. On the center, there is some room for the heater used as Hot Spot. From left to right the color of voltage taps are: Brown and Blue on the left. Orange in the center. Yellow and Green on the right side of the tape.

76

In Fig.2.04, the first and the last dots are the connections of the voltage readout across the whole tape. These readouts are connected to the protection circuit that shuts down the bias current when the safety threshold is reached. A simplified scheme of the electrical connections and instruments is shown in Fig.2.05.
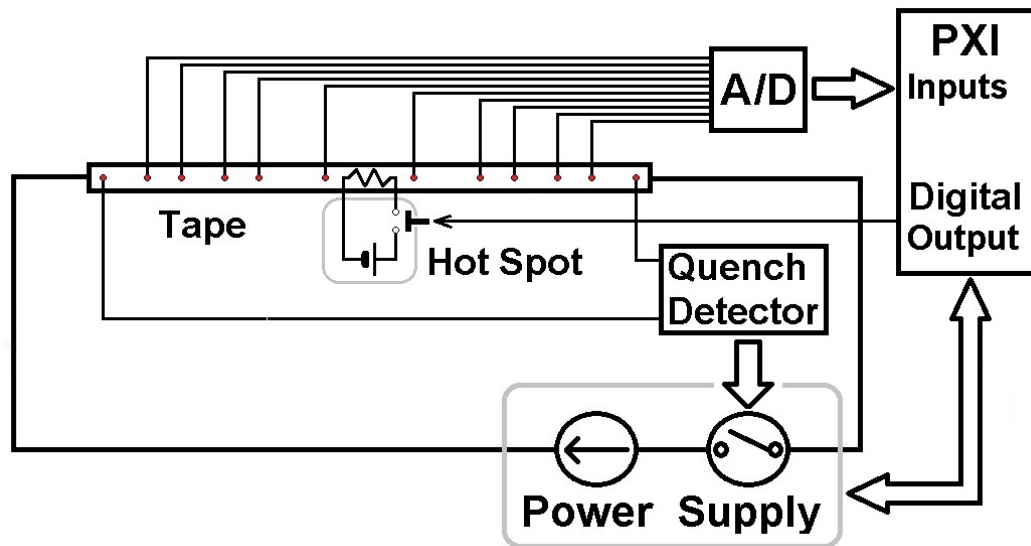

Fig.2.05 A simplified scheme of the $NZPV$ measurement apparatus. A Computer-controlled Power Supply feeds the tape. The resistor triggers the quench and its propagation is detected by recording the voltages on the measure taps. When the voltage measured on the outer readouts becomes higher than the threshold level the current is switched off.

In Fig.2.05 the superconducting tape, with an active length of around $10\ cm$, is connected with two copper blocks to the current-controlled power supply. On the tape, all the voltage taps are connected to a multichannel input differential voltage card. The voltages were acquired at a rate of 100 readings per second. Each voltage was obtained by averaging 200 readings acquired at 20 kHz with an 18 bit-ADC card, controlled by a National Instruments© PXI computer. The noise signal of a few microvolts is observed on the tape in the superconducting state. Near both extremities of the tape, the other two taps are connected to a nanovoltmeter that acts, as a quench detector switching off the bias current anytime, the measured voltage is above a threshold value. The

SMD resistor acts as a heater generating the hot spot that triggers the start of the measurements. It is glued on the tape center and is connected to a computer-controlled current generator. [TR05]

The tape, as shown in Fig.2.06, has been mounted on the fiberglass support and soldered at about $80\,°C$ with a low-temperature indium-based solder alloy. Once the tape is inserted into the flux cryostat and is thermally stabilized at the set temperature T_0 below T_C, it is connected to the power supply and fed with the desired constant transport current I_T.
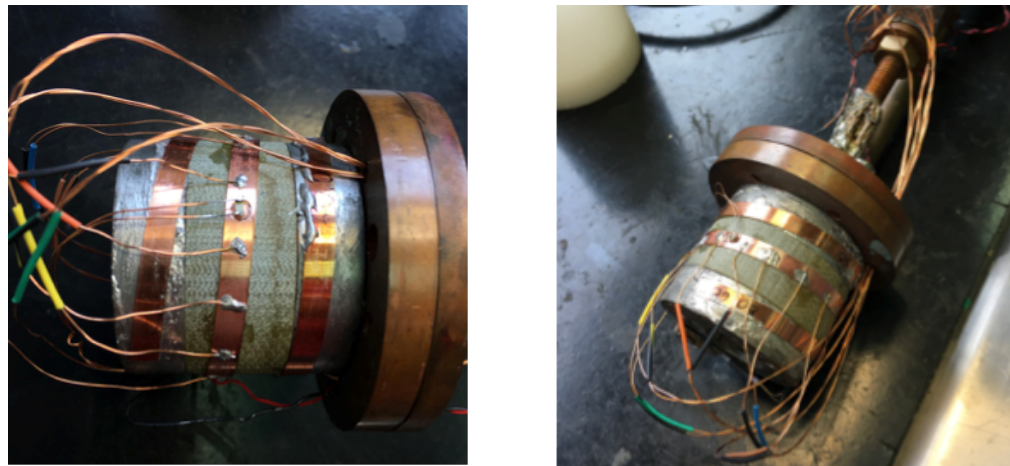

Fig.2.06 The 2G-HTS tape, mounted on the fiberglass support before measures.

After the temperature controller has stabilized the temperature, a small current pulse is sent to the heater to generate the hot spot on the tape.

The thermal effect caused by the hot spot is the same as those described in Fig.2.01. In Fig.2.07, generated voltage values are reported versus the time. In the beginning, the values of the voltages across all couples of taps are zero because the whole tape is in the superconducting state. During the current pulse, the thermal disturbance raises the temperature T of the tape underneath the heater. If this temperature is larger than T_{CS} (see Fig.1.10) a voltage is immediately observed on the first orange taps placed just across the heater. If, after a small transient, all voltages read by the taps return to zero it means that the energy of the hot spot was insufficient for the quench propagation. In this case, the energy of the impulse is increased a little bit and

the measure is repeated until the voltage read on the first orange taps will continuously grow and a voltage will appear also on the second yellow and the third blue couples of voltage taps on both sides of the heater. Such an occurrence is shown in Fig.2.07. The quench continues to propagate along with the tape with the appearance of a voltage also in the brown and green couples of taps placed near the end of the tape. Finally in Fig.2.07 at the time $t = 7.55\ s$ it is shown that all curves together fall to zero. This decay is due to the activation of the quench protection that shuts down the bias current before overheating. The Fig.2.07 with a solid black line, reports only part of the $75\ mA$ current pulse that lasts $3.5\ s$. The pulse, that generates this quench, was recorded by acquiring the voltage across a $100\ \Omega$ current shunt.
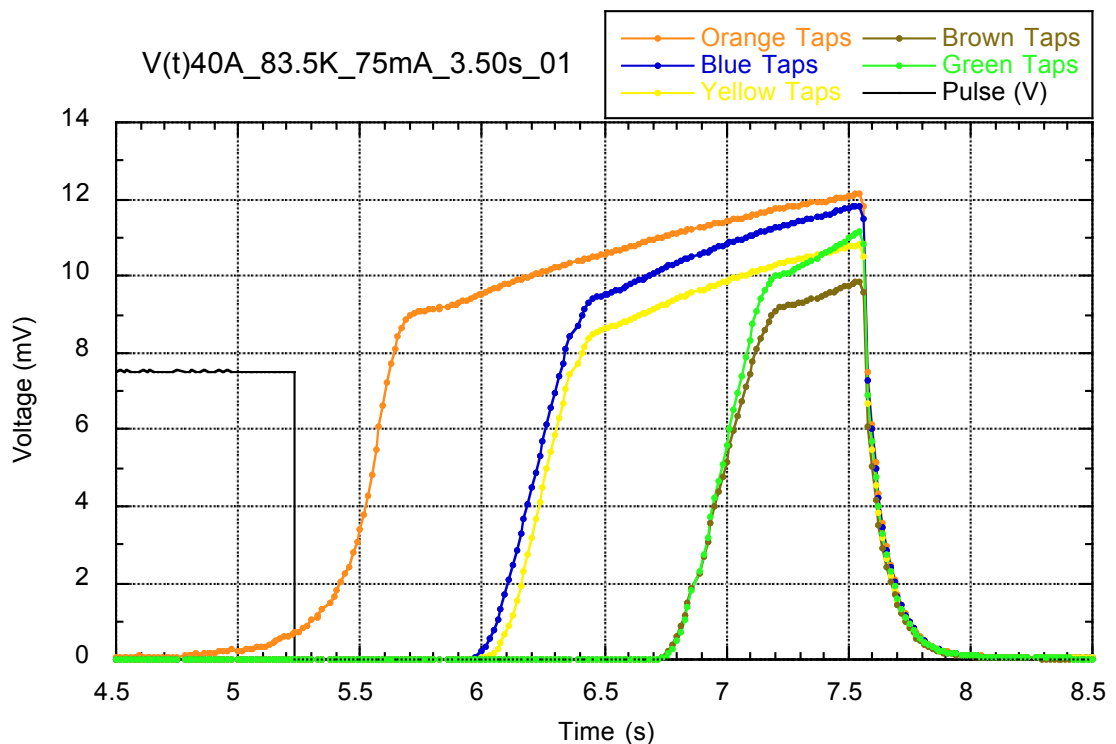
Fig.2.07 Voltages read across the taps on the SuperPower© SCS4050AP tape at $T_0 = 83.5\ K$, $I_0 = 40\ A$, and self-field. Starting on the left the first curve is the voltage across the heater. Next curves are the voltages read on the right (yellow and green) and on the left side (blue and brown).

This method does not allow us to a direct measurement of the MQE value, but as the measurement is repeated starting with a current pulse not

79

giving rise to any propagation, we achieve the MQE value. All voltage curves recorded in Fig.2.07 show two different slopes. The first slope from zero to about $9\ mV$ is due to the propagation of the normal zone between the voltage taps, and the second is due to the increase of the resistance of the normal metal caused by the increase of the local temperature. It is possible to determine the $NZPV$ by measuring the ratio of the distance between the voltage taps and the time shift between the corresponding curves to reach a fixed voltage value. We set this voltage at 100 μV, which is well above the noise level. From the curves shown in Fig.2.07, it is possible to obtain four values of $NZPV$ by considering also the first orange curve combined with all the aforementioned voltage curves. However, the velocity values obtained by using the orange curve are not considered because the initial heat transient affects the value of the $NZPV$. In fact, only away from the point of disturbance $NZPV$ has been found to be constant. [NN19] The measure shown in Fig.2.07 was performed on a sample of SuperPower© HTS SCS4050AP tape, without any external applied magnetic field at temperature $T_0 = 83.5\ K$, and bias current $I_0 = 40\ A$. During the measure the helium gas flow in the cryostat was a $50\ \ l/min$ in Standard Temperature and Pressure, STP conditions. The heat pulse that started the quench process was generated by a constant current pulse of $75\ mA$ lasted $3.5\ s$ on the $100\ \Omega$ SMD heater resistor, equivalent to an energy of about $1.97\ J$.

2.4   The NZPV analysis on some commercial samples

In the following, we focus on the $NZPV$ measurements on two different $ReBCO$ tapes commercially available: the HCN04150 produced by SuNAM© Co. Ltd. a South Korea factory, and the SCS4050AP produced by SuperPower© Inc. in the USA, now owned by Furukawa. Nowadays, both companies may be defined as world leaders in the market in the production of 2G HTS wires, and these tapes represent a sample of their commercially available products. Both tapes are employed for the realization of high field magnets and in many other superconducting power applications. The characterization of their features, further than standard superconducting properties, is mandatory for designing devices based on this technology. [CL13]

The first characterization performed on these tapes was the measure of $T_C(B)$ and $I_C(B, T)$, both reported in section 1.7.1 and 1.7.2, respectively.

The knowledge of the values of $I_C(B, T)$ is important during the measures of $NZPV$ for the accurate determination of the ratios I_0/I_C. [NG08]

The values of the $NZPV$ measured, following the procedure described in Section 2.3, for the SuNAM© tapes and the SuperPower© tapes are shown in Fig.2.08, and in Fig.2.09, respectively.

During the measurements, the $NZPV$ values were computed from the quench propagation curves, as shown in the example of Fig.2.07 by choosing a fixed voltage criterion of $100\ \mu V$ for the determination of the differences in time. This threshold value was significantly above the background noise. Different choices of this voltage criterion do not significantly affect the computed $NZPV$ values. The errors on these $NZPV$ values are evaluated to be smaller than 10% and are due mainly to the uncertainty on the determination of distances from the positions of the voltage taps on the tape.

As expected, the measures of $NZPV$ show in both Fig.2.08 and Fig.2.09 report a linear behavior and become faster while the temperature increases.
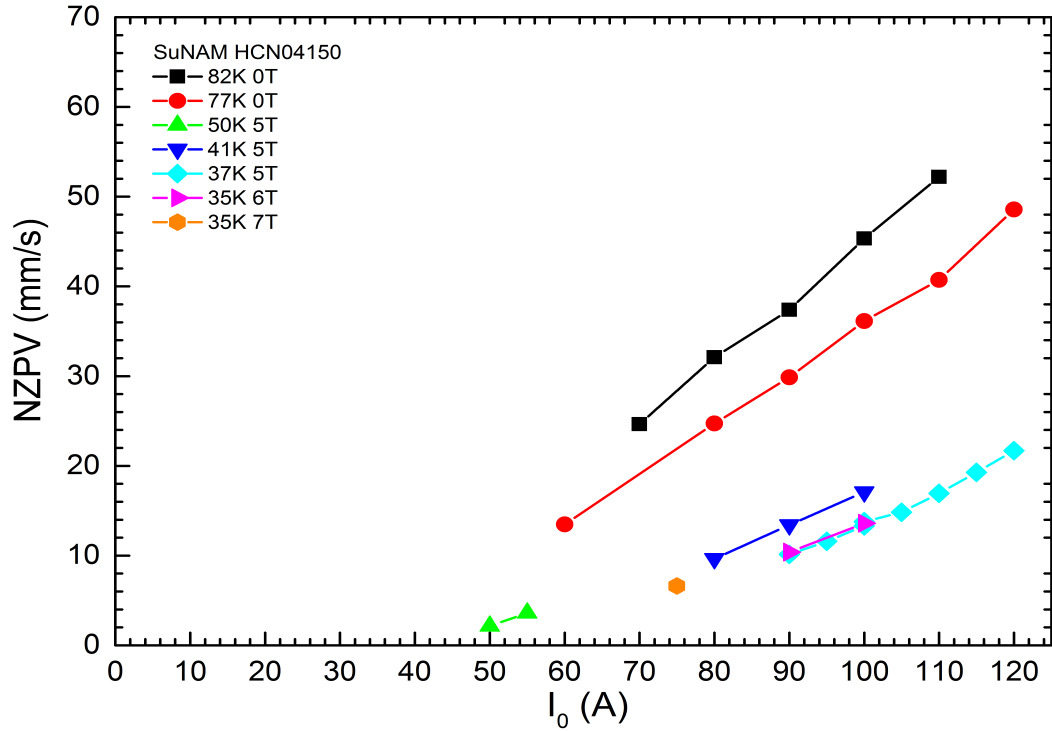
Fig.2.08 Measured $NZPV$ values on SuNAM© HTS HCN04150 tapes as a function of the bias current for various temperatures and applied magnetic field.

In particular, the data taken from the SuNAM© tapes reported in Fig.2.08 show that at $T = 82\ K$ the values of the $NZPV$ are ranging from $26\ mm/s$ for $I_0 = 70\ A$ to $54\ mm/s$ for $I_0 = 110\ A$.

For a similar value of the temperature the SuperPower© tapes reported in Fig.2.09 show at $T = 82.5\ K$ the values of the $NZPV$ are ranging from $8\ mm/s$ for $I_0 = 30\ A$ to $53\ mm/s$ for $I_0 = 54\ A$. In order to quickly compare all $NZPV$ values, the data reported on Fig.2.08 and on Fig.2.09, are drawn by using the same scales. From this comparison, it is evident that the SuperPower© tape has higher values of $NZPV$. In fact, the maximum speed of $67\ mm/s$, obtained at $81.5\ K$ and current bias of $80\ A$ in the Superpower tape, is larger than the value of $52\ mm/s$ measured in almost the same conditions on the SuNAM© tape.
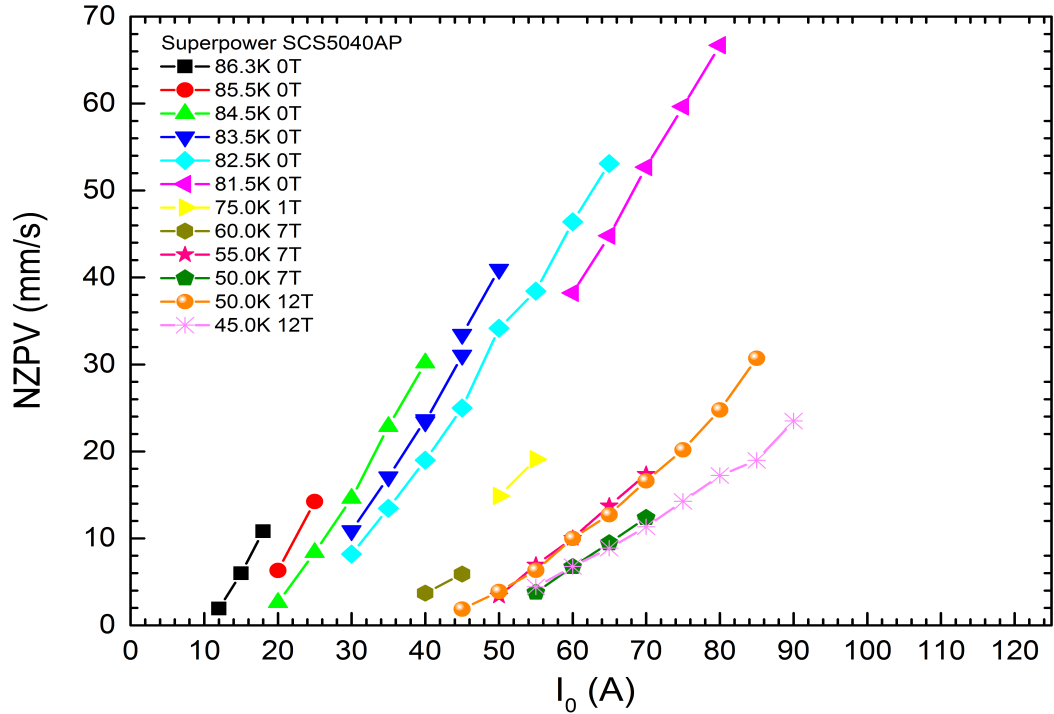
Fig.2.09 Measured $NZPV$ values on SuperPower© HTS SCS4050AP tapes as a function of the bias current for various temperatures and applied magnetic field.

Using Eq.2.07 a first quantitative analysis of $NZPV$ was carried out. The Fig.2.10 shows, as a function of the I_{BIAS}, the experimental data (star symbol), measured on the SuperPower© tape taken at T=50 K and 12 T. Above these experimental points the solid line reports the values computed with Eq.2.07.

The presence of a shift between the experimental values and the value computed with Eq.2.07 is evident. This anomalous shift can be explained by the reduced adiabatic behavior of the experimental environment that can be taken into account as due to the presence of the minimum propagation current I_m phenomenologically observed. [GB03], [NG15] The presence of this current was already added to the widely used $NZPV$ models as a reduction of the bias current. The value of the minimum propagation current I_m can also be estimated by extrapolating the $NZPV$ data to its zero value, *i.e.* the intercept on the I_{BIAS} axis where the velocity is zero. [GB03]
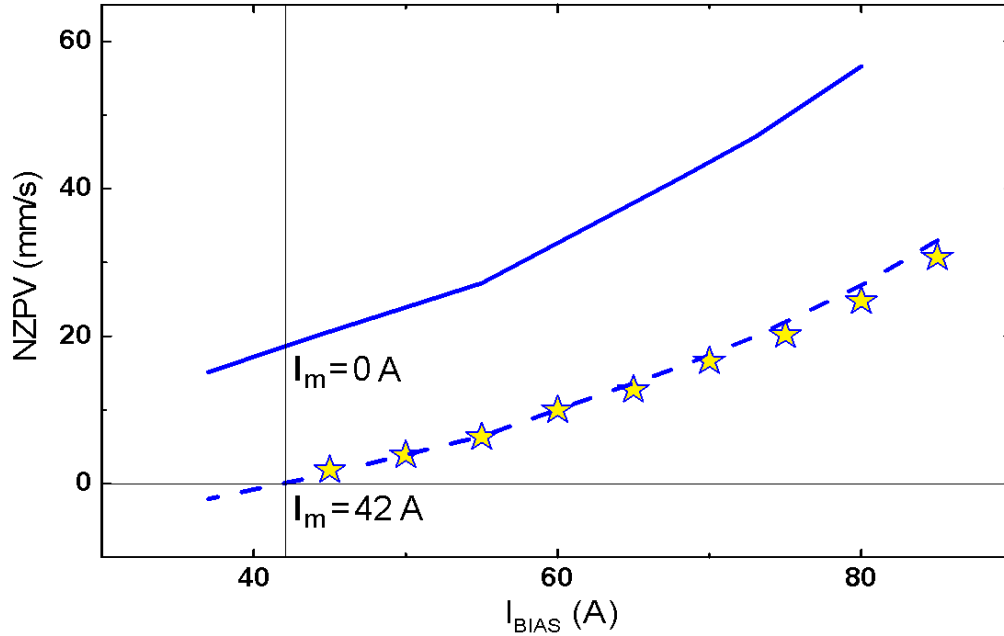
Fig.2.10 Measurements of $NZPV$ on the SuperPower© tape at $50\,K$ and $12\,T$. The experimental values (stars) are compared with both the Eq.2.07 (solid line) and Eq.2.15 with $I_m(T) = 42\,A$ (dashed line).

By using this criterion, the estimated value of $I_m = 42\,A$ is obtained from the data displayed in Fig.2.10. The dashed line, drawn on the same figure, reports the $NZPV$ values computed by using Eq.2.15 that takes into account the presence of the estimated value of I_m. As can be seen in this case there is a good agreement between the experimental data and the model.

A selected ensemble of $NZPV$ values is reported with colored symbols in Fig.2.11 together with their calculated dashed curves computed with Eq.2.15 and the proper value of the minimum propagation current I_m. The Fig.2.12 and Fig.2.13 report a selected values subset chosen among the $NZPV$ values in the SuNAM and SuperPower tapes, respectively, obtained from measurements at an applied magnetic field higher than $5\,T$ and the temperatures lower than $50\,K$. On both figures, the graphic uses log-log scales because it has been shown that all bias current dependent $NZPV$ curves, obtained on a SuperPower© tape at low temperatures and high magnetic fields, follow a power-law behavior with an exponent of about 1.5. [NG12]

84
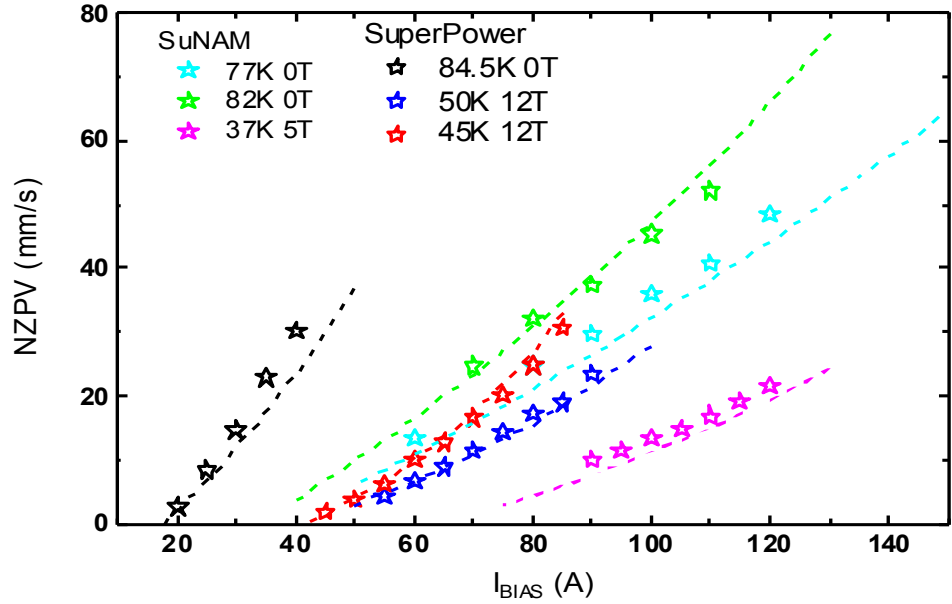
Fig.2.11 Measurements of $NZPV$ on SuNAM and HTS tapes (symbols) for different temperatures and applied magnetic field. The curves report the values computed with Eq.2.15 and its own $I_m(T)$ value (dashed lines).

Fig.2.12 $NZPV$ measurement of the data shown in Fig.2.08 reported on a Log-Log scale (symbols) and their linear-fit with an exponent of 2.5 (dashed line). The power-law obtained on a SuperPower© tape with the exponent of 1.5 is shown for comparison (solid line). [NG12]

The *NZPV* values, shown in Fig.2.12, and measured on a SuNAM© tape, well agree to a power-law dependence because are effectively well distributed on a straight line. The best-fit slope, reported in Fig.2.12 as a dotted line, has a slope of about 2.5.

This value is different from the previously reported value of 1.5 in SuperPower© tapes, reported for comparison with a solid line on the same figure. This difference however can be ascribed to the different manufacturing processes between these tapes.

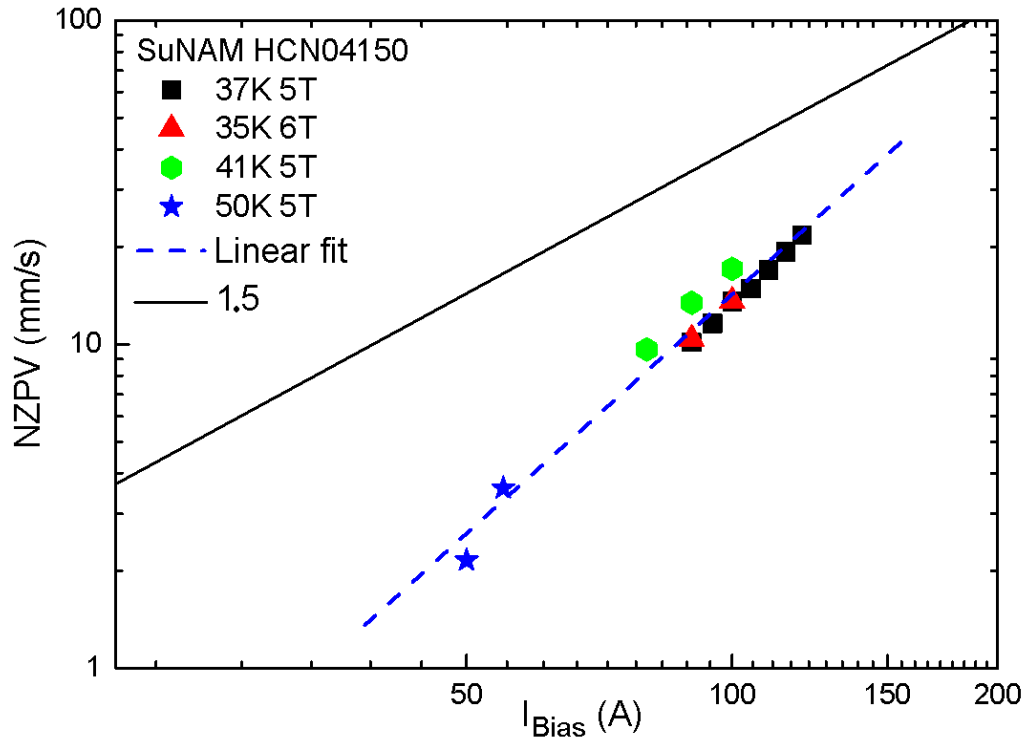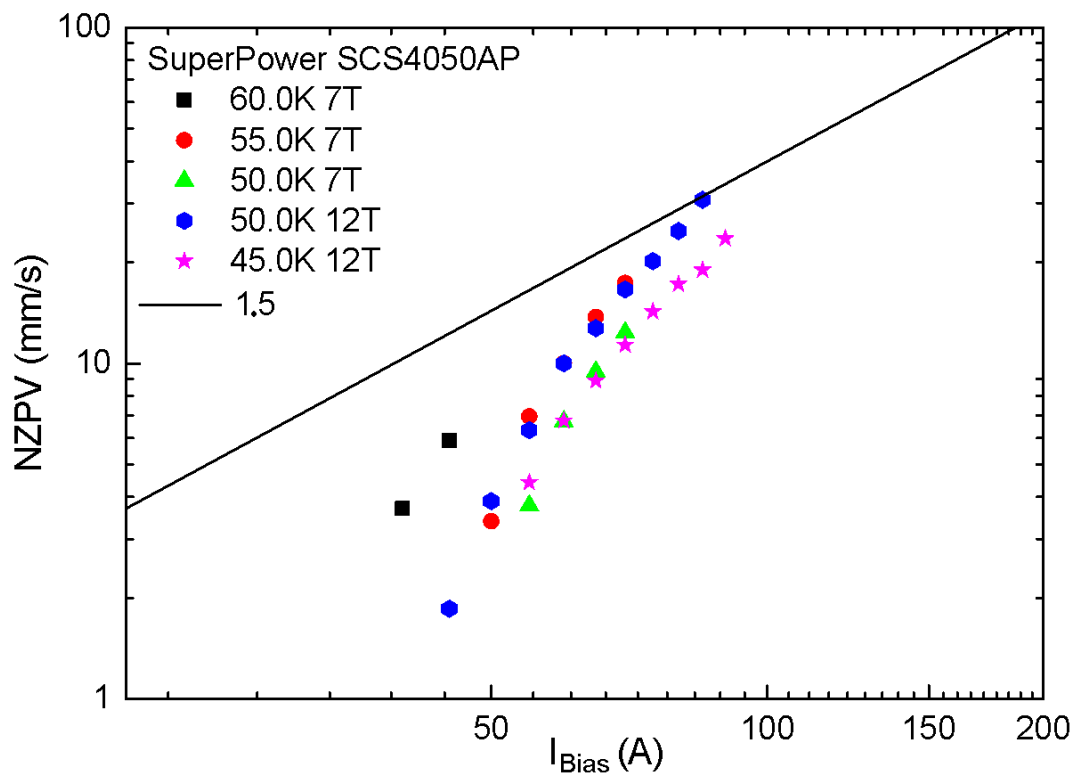Fig.2.13 Measurements of *NZPV* of the data shown on Fig.2.09 reported on a Log-Log scale (symbols) The power-law obtained on a SuperPower© tape with the exponent of 1.5 is shown for comparison (solid line). [NG12]

In Fig.2.13 the experimental *NZPV* data concerning the SuperPower tape are shown. In this sample, we have not observed the power-law behavior as previously reported in this kind of tape. The behavior seems only approaching the expected power-law behavior represented by the solid line.

The power-law behavior in the high magnetic field and low temperatures has been extensively discussed and a suitable model able to explain the physical origin of this experimental finding was proposed. [BN16] This model is based on the specific thermal and electrical conductivity properties, of the copper coating of HTS tapes when exposed to a high magnetic field. [BN15]

Within the model, at low temperatures, the magnetic field, analogously to the disorder, reduces the electron mean free path, and consequently the thermal conductivity. This effect becomes less important at temperatures higher than $50\,K$, where the electron-phonon scattering starts to be more relevant respect to the electron like scattering in determining the heat conduction. As a consequence, the thermal conductivity curves associated with different values of B approach each other and in the temperature range, up to $50\,K$, the derivative of $k_{cu}(T)$ is strongly reduced by the increase of the magnetic field. These findings were applied to the development of a simplified expression for the computation of $NZPV$ suitable for 2G HTS. Data reported into a log-log scale follow a power-law dependence of $NZPV$ on the bias current that is almost independent of either the temperature or the magnetic field. [BN16]

This behavior has not been observed on LTS materials where $NZPV$ shows a clear dependence on B. [WH65] A reason that may explain the different behavior of our experimental findings respect to the power-law predicted by this model is the fact that we are not exactly in the parameter range where this effect dominates. And this is mainly due to the special SuperPower tape we used for the analysis: the SCS4050AP is, in fact, the Advanced Pinning type tape, designed with improved performances just at a high magnetic field. Other reasons may also be due to differences in the experimental apparatus or the experimental condition during the measurements.

2.5   Quench numerical analysis

A simplified one-dimensional equation can be numerically studied with any programming languages available. [KR09] Numerical library, available in Fortran and also in C Language, may help in the usage of the needed mathematical algorithms. [PR92] The numerical analysis is useful because in this way it is possible to consider the role played by the dependencies of the thermal and electrical properties of the materials that, in analytical solutions, are assumed to be constant or taken in a simplified analytical approximation. A better description and a quantitative analysis of the phenomena need to consider also the role that is played by the geometry and the boundary conditions of the environment surrounding the quench phenomena. The Finite Element Analysis FEA is usually adopted by the engineers for the solution to this kind of problem. This computation method is based on the reduction of a Partial Derivative Equations PDE continuous problem, into the application, on a discrete computation mask, of an algebraic equations system. The numerical computation methods allow us to find solutions to analytically untreatable problems defined on complex geometries and with particular boundary conditions. The computer simulations are particularly useful for investigations as they avoid a large number of experimental tests, allowing also investigating on parameters not so easy to be realized. Drawbacks related to the usage of FEA computation, are the errors due to the extensive use of numerical computation and the difficulty in the management of huge and tiny numerical quantities together. The critical point on the usage of the FEA method is the choice of the computation mesh. Usually, the FEA programs are clever enough to propose a triangular mesh that is optimized for most of the engineering problems. Unfortunately, the computing time optimization of the simulation sometimes requires a different mesh structure where the number of cells and their dimension has to be carefully chosen. Moreover, Comsol Multiphysics© allows a conventional physics-based user interface and is accompanied with many ready to use application modules. For these reasons, we decided to

consider the use of an FEA numerical analysis for a more accurate description of the quench. The first step for an effective FEA investigation is the construction of a framework similar to the real experimental apparatus. [CH09][CH10][PL16][ZH06]

The model adopted in the simulation is based on a 260 mm long 2G-HTS $ReBCO$ straight tape. The rectangular section had a width of $4\,mm$ and a thickness of $100\,\mu m$. The lattice mesh, shown in Fig.2.14 has been simplified respect to the structure of the real tape shown on Fig.1.05, in order to improve the computation speed. [LV10]
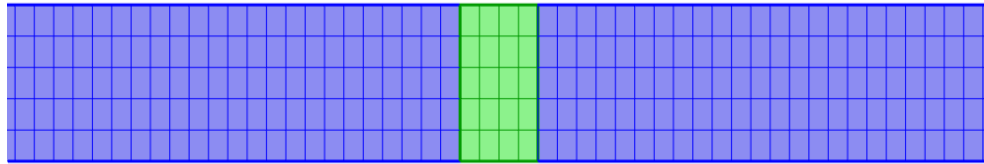
Fig.2.14 Central part of the tape model chosen for the FEA computation. The rectangular mesh superseded the default to better adapt to the tape symmetry. The green band on the center simulates the hot spot.

A bidimensional model was used with the appropriate thickness, even if the quench dynamics in a single HTS tape evolves naturally in one dimension.

Our analysis started by considering a simplified model for the tape. As a first step, assuming a homogeneous conductor, we do not consider the thermal properties of the buffer and superconducting layer. Those layers are thin and their contributions to thermal properties are negligible with respect to the thicker copper layer. So that we model the whole tape as a single material layer with the thermal proprieties of $C_{Cu}(T)$ and $k_{Cu}(T)$ of the copper, and the resistivity $\rho_{Cu}(T)$ that behaves as a superconductor below T_C and as normal copper above T_C.

Because of the symmetry of the tape, a more computational efficient rectangular lattice superseded the default triangular lattice mesh. The computational optimal value for the mesh size has been found by reducing the

89

starting cells until further refinements do not affect anymore the simulation outputs. At the end of the refinement, there are about 2500 elements, and each simulation lasts about 3 hours. The values of $\rho_{Cu}(T)$, $k_{Cu}(T)$ and $C_{Cu}(T)$ of copper, and their dependence on the resistivity ratio and magnetic field, were taken from the tables available in ref. [HS84][NG12]. The curves of $T_C(I)$ and $I_C(T)$ were taken from on the experiments. The hot spot has a finite size, negligible with respect to the tape longitudinal dimension. We defined the heat pulse as a square pulse term with a fixed duration, $\Delta T = 0.05\ s$. Concerning the electrical resistivity $\rho(T)$, in the sharing regime, we propose the following expression to describe the current sharing between T_G and T_C:

$$\rho(T) = \begin{cases} 0 & T < T_G \\ \rho_{sh}(T) & T_G < T < T_C \\ \rho_{Cu}(T) & T > T_C \end{cases}$$

(2.16)

$$with \quad \rho_{sh}(T) = \rho_{Cu}(T_C) \left(\frac{T - T_G}{T_C - T_G} \right)^m$$

When $T < T_G$ all the current flows through the tape that is in the fully superconducting state. Between T_G and T_C , the current is shared in the conducting elements of the tape, and we can assume a temperature-dependent total resistivity $\rho_{sh}(T)$ for our system as shown in Eq.2.16. Finally, when $T > T_C$ the tape is in its normal state and all the current flows through its conducting elements with the normal copper resistivity $\rho_{Cu}(T)$.

The *m*-value in Eq.2.16 significantly affects the quench dynamic. In this simulation, we set *m* = 1, in order to reproduce the linear transition of the sharing current from the full superconducting state below T$_G$ and the normal state above T$_C$.

The voltage values, caused by the quench propagation, are read introducing virtual probes, likewise to the real experiment, equally spaced of $2\ mm$ along the whole length of the tape. An example of the output from the model is shown in Fig.2.15.
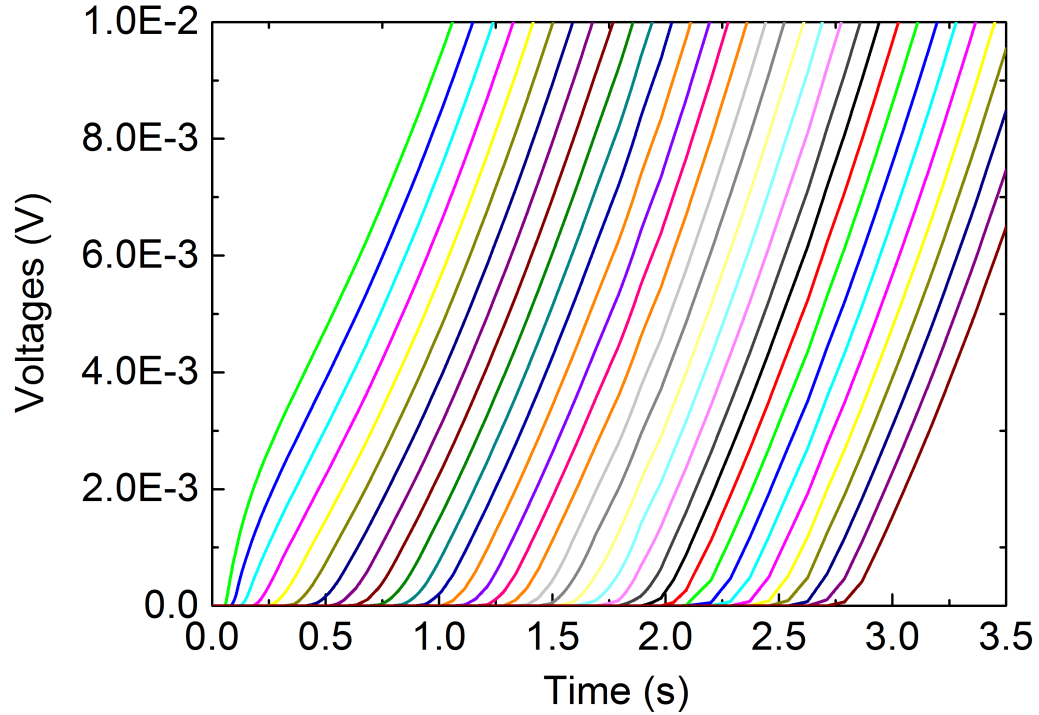
Fig.2.15 Quench propagation on the FEA model of the superconducting tape.

In this FEA model, the values of the $NZPV$ are computed from the continuously time-dependent voltages recorded on the virtual taps. As in the experimental work, a threshold voltage of $100\ \mu V$ was chosen and the $NZPV$ are calculated. In order to validate the results of our model, we compared the $NZPV$ values computed with the analytical expression of Eq.2.10 shown as continuous lines, with the points obtained by the FEA model at different temperatures and applied fields. The results are shown in Fig.2.16.

The analytical computations of Eq.2.10 were carried out with Mathematica© by using the polynomial interpolated values of $\rho_{Cu}(T)$, $k_{Cu}(T)$, and $C_{Cu}(T)$ tables used into the FEA model. The analytical result of Eq.2.07 only provides one $NZPV$ value, while the FEA model is able to follow the full $NZPV$ dynamics along with the tape, even in the zones, which are affected by the heat disturbance. The comparison reported in Fig.2.16 is made with the asymptotic value of the FEA model and the analytical formula.
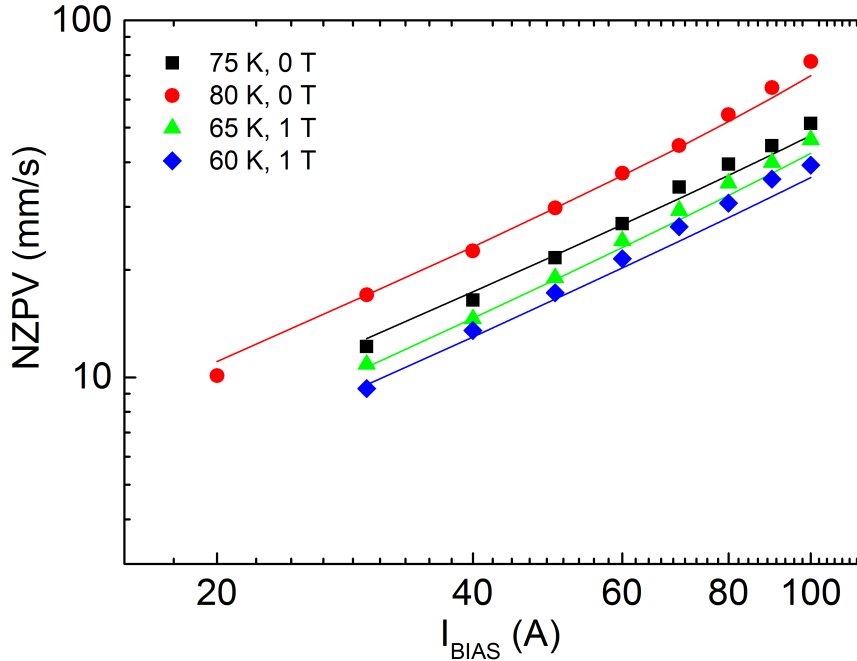
Fig.2.16 Comparison of the $NZPV$ values computed with Eq.2.10 (continuous lines) with some results obtained by using the numerical model (dots).

Due to the good agreement, we can validate the FEA model. Additional features, which are provided by the FEA is the local tape temperature evolution during a quench. A three-dimensional graph of the temperature profile during the quench is shown in Fig.2.17 for $T_0 = 75\ K$, a bias current of $50\ A$, and the hot spot energy of $462\ mJ$.

The measurement of the temperature profile, and its time evolution during the quench is hard to obtain. In fact, the experimental determination of the temperature profile requires the installation of too many thermometers on the tape. These thermometers have to be fast, able to give a response in times on the order of a tenth of second or even less in order to follow the rapid temperature evolution during the quench and do not have to affect the dynamic of the process. Instead, these temperature values are easily available from the time evolution of the output of the FEA computation. In the simulation of Fig.2.17, the heater dimensions were always taken smaller then MPZ. At the beginning of the process, a temperature peak on the center of the tape shows the point where the hot spot has generated the disturbance.

92
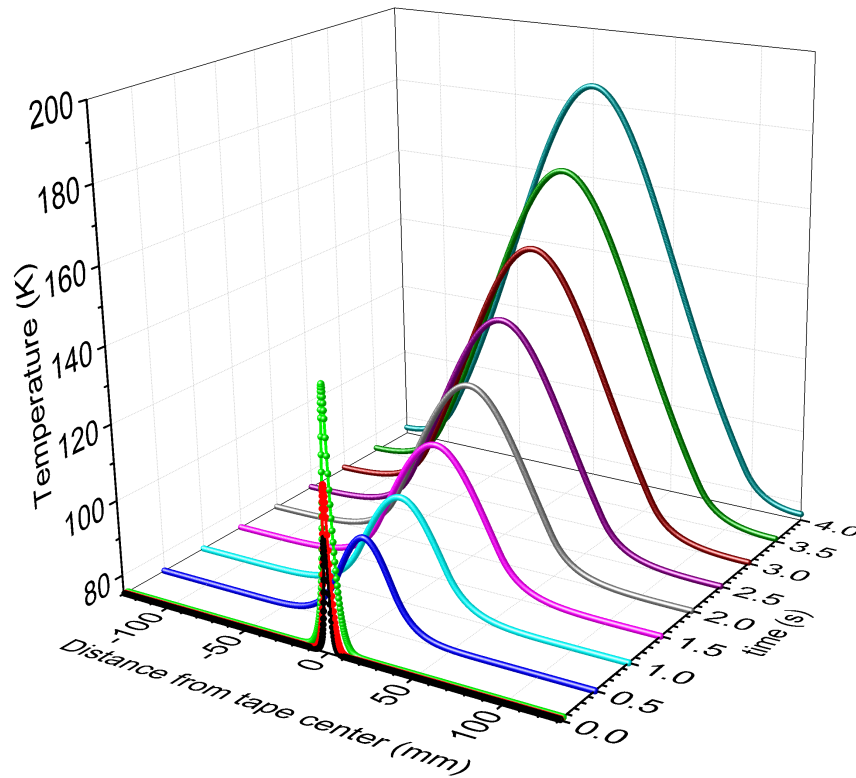
Fig.2.17 Temperature profiles along with the tape during the quench propagation.

The narrow temperature peak with more energy than the MQE reduces and creates on the tape a normal zone that starts to dissipate and ignites the quench. As time goes on, the normal zone continues to dissipate and the temperature steadily increases. Another interesting feature obtainable by the usage of the FEA computation is the investigation of the dependence of the $NZPV$ on the distance from the quench starting point. The simulation shown in Fig.2.18 reports the values of the $NZPV$ as a function of the distance from the hot spot at different values of the generated thermal disturbance, and the value analytically computed. [NN19] [HR15]

The simulation of Fig.2.18 has been obtained with the initial temperature $T_0 = 75\ K$ and a bias current of $50\ A$ without any external magnetic field. The simulated pulse energy values are in the range of $240 \div 460\ mJ$.
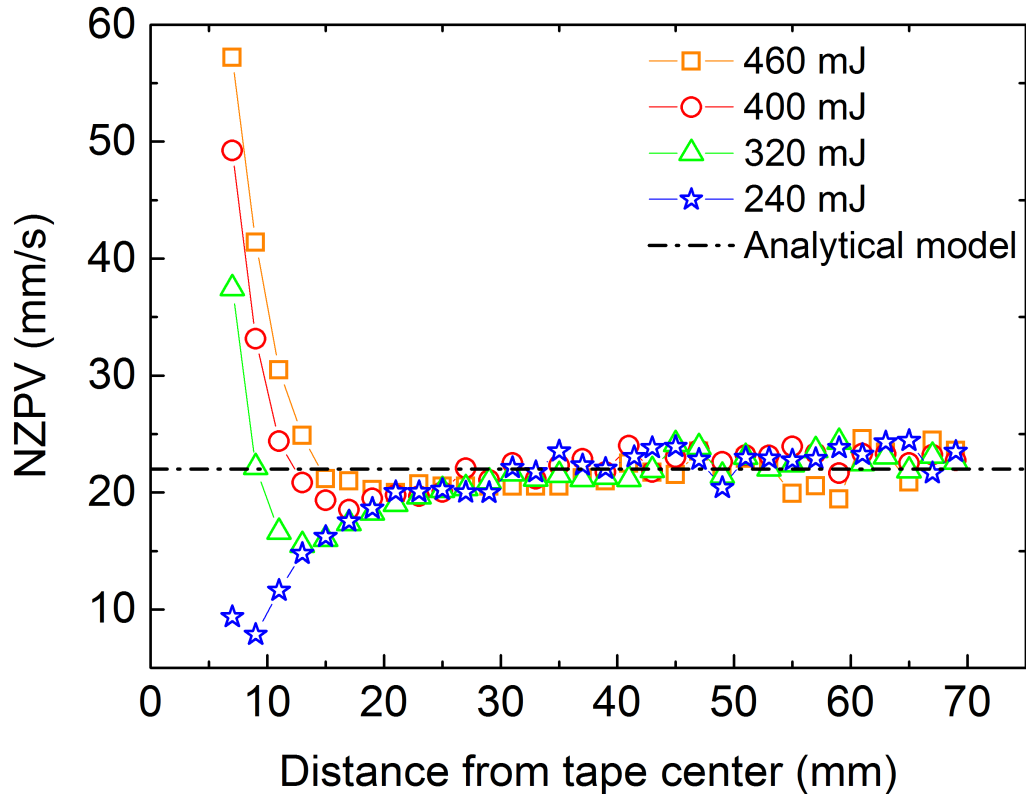
Fig.2.18 Computed $NZPV$ values as a function of the distance from the hot spot for different values of the excitation energy, compared with the horizontal line of the asymptotic $NZPV$ value computed with Eq.2.10.

As expected, the $NZPV$ near the heater is influenced by the hot spot. The asymptotic $NZPV$ value of $22\,mm/s$, shown as the horizontal dot-dash line in Fig.2.18, is achieved over lengths of about $25\,mm$.

Unfortunately, this result is hard to be experimentally verified with the voltage taps technique, as the experiment would require the usage of a large number of voltage-taps. But the number of points, where to place the voltage taps, is really limited, either for the space needed to solder the wires of the voltage taps, or for the limited amount of tape length that can withstand full normal state before overheating during a quench. The FEA computation instead, having none of the experimental constraints, can put an unlimited number of voltage taps and reproduce the experimental method for the measure of the values on the $NZPV$ at any point of the superconducting tape.

2.6   A simple approach to the quench in isolated wire/tape

The majority of quench propagation models are based on the differential heat balance (Eq.1.01) or a simplified version of it. [BN16] [DR79] Here we focus only on the determination of time t_u before the tape temperature reaches the value T_{MAX} that may damage the conductor. Once this value is known with the help of any propagation model it is possible to make a prevision about the maximum distance safely traveled by the quench wave. As seen in the simulation in Fig.2.16 it is evident that the highest temperature on the wire is always where the quench begins. For this reason, our investigation considers only the neighbor where the quench starts. The knowledge of T_{MAX} in a simulated model is one of the program outputs, as well as the time t_u required to reach this temperature. The knowledge of the relationship between T_{MAX} and t_u for any temperature and time can also be obtained from the simulation output data. The values of the maximum temperature, from the simulation output, were taken from the data at the center of the simulated tape. Fig.2.19, reports the values of T_{MAX} , taken from several runs at different temperatures, as a function of their simulation time. All these values, reported in Fig.2.19 are shown as black dots and are taken from the program output used to generate Fig.2.17. As can be seen, the values of T_{MAX} as a function of t_u shown in Fig.2.19 have a parabolic behavior. This feature can be usefully exploited by a parabolic interpolation as shown by the solid red line. This quadratic function can be also extrapolated outside the range of investigated values and permits to know at what time a certain value of temperature is reached. As an example, suppose that the measure of $NZPV$ is done on a $ReBCO$ tape, and for the safety of the tape, we decide to remain under the maximum allowable temperature value of $T_{MAX} = 400\ K$, with the help of the second degree polynomial of the curve shown in Fig.2.19 it is possible to extrapolate the value of the useful time $t_u = 7.70\ s$.
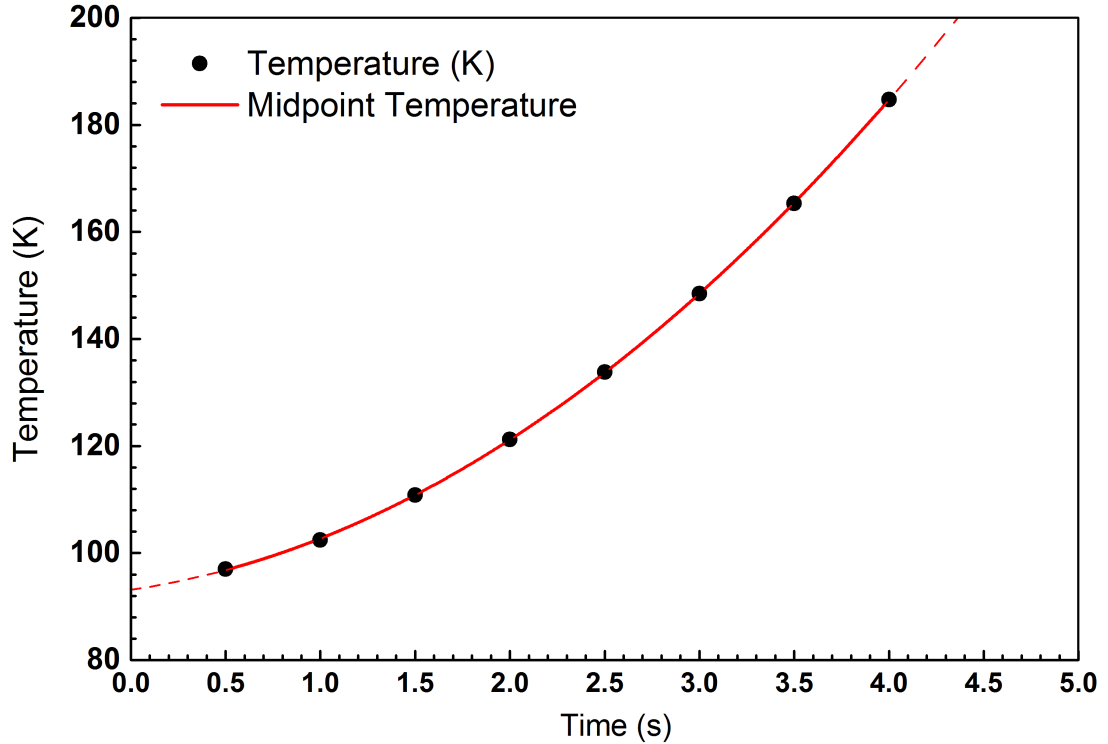
Fig.2.19 Temperatures taken from the top of the midpoint on each curve of the computer simulation shown in Fig.2.17 as a function of time (Black dots). Parabolic interpolation of these data points (solid line).

On the other side of the polynomial curve, the extrapolation to $t = 0$ the value of the temperature is $93.6\,K$. This temperature is higher than the environment temperature of $T_0 = 75\,K$ and can be explained by considering the heat delivered by the simulated hot spot in Fig.2.17 that reaches a peak value of the temperature above $140\,K$ followed by a rapid decrease after the beginning of the quench process. [NN20]

In the following, we would like to present an easy approach to the determination of the time t_u once the temperature T_{MAX} is known, by using a simple model and some measurements of voltages acquired during the quench. The model considers the experimental values of the voltages recorded on the part of the superconductor between the two taps. This segment of the conductor before the quench is superconducting at the environment temperature T_0 and the voltages read by taps surrounding this segment

$V(t, I_0)$, neglecting the electric noise, is zero. When the temperature rises, following the normal zone wavefront, it will happen that a fraction of tape will turn from superconducting to normal state, through the current sharing regime. Thus the quench process proceeds along the rest of the tape while the current bias is flowing in the tape.

In this condition, further increases of the temperature are mainly due to the Joule heating of the normal matrix $E_J(t) = V(t, I_0) \, u_I I_0 \, t$. In conductors, in an isolated environment, the joule heating energy produces a temperature variation in the tape fraction according to $E_J(t) = c_p \, m \, \Delta T(t)$. If during this exchange the energy is not lost, these two energies may be equated:

$$V(t, I_0) \, u_I I_0 \, t = c_p \, m \, \Delta T(t) \tag{2.17}$$

where, beside the voltage $V(t, I_0)$, u_I indicates the current unit (*i.e.* $u_I = 1 \, A$), c_p is the averaged specific heat that is assumed constant, m the mass of the conductor segment, $\Delta T(t) = T(t) - T_0$ the time-dependent temperature variation, caused by the dissipated energy, and T_0 the temperature of the environment. It is important to note that, in this section, I_0 obtained by the ratio of $I_0 = I_B / u_I$. With this assumption, the number I_0 represents the numeric value of the currents in units of Amperes.

The general dependence of $V(t, I_0)$ is quite complex and difficult to analyze. The main purpose of this model is to focalize on the behavior of the voltage $V(t, I_0)$ only after the complete transition of the whole segment in the normal state. The beginning of this condition is easily recognizable on the curves of the voltage tap as a function of time. The voltage $V(t, I_0)$ on the tape segment between the couple of voltage tap is shown in Fig.2.20. In this figure, the dashed straight black line represents the voltage values corresponding to the transition from the superconducting to the normal state. Further increases of the voltages above $11 \, mV$ are due to the heating of the sample that is already in the normal state. This is evidenced by the change of the slope in $V(t, I_0)$ as shown in Fig.2.20 where, the continuous straight red line, lays on

97

the voltage values measured after the complete transition in the normal state and during the sample heating. The observation of the normal state voltage behavior on the normal segment, both from the observation of the experimental curves and the FEA computations, shown in Fig.2.15, can be approximated to a linear function of time. In the proposed phenomenological model, besides the linear dependence on time, it is also considered a power-law dependence of $V(t, I_0)$ on the current I_0.

$$V(t, I_0) = K_V \, I_0^\alpha \, t + V_0 \tag{2.18}$$

Where α is the numerical exponent of the I_0, K_V is a suitable proportionality coefficient, and V_0 is the voltage value at which the linear dependence due to the heating begins. The voltage V_0 can be identified in Fig.2.20 as the crossing point between the two straight lines.
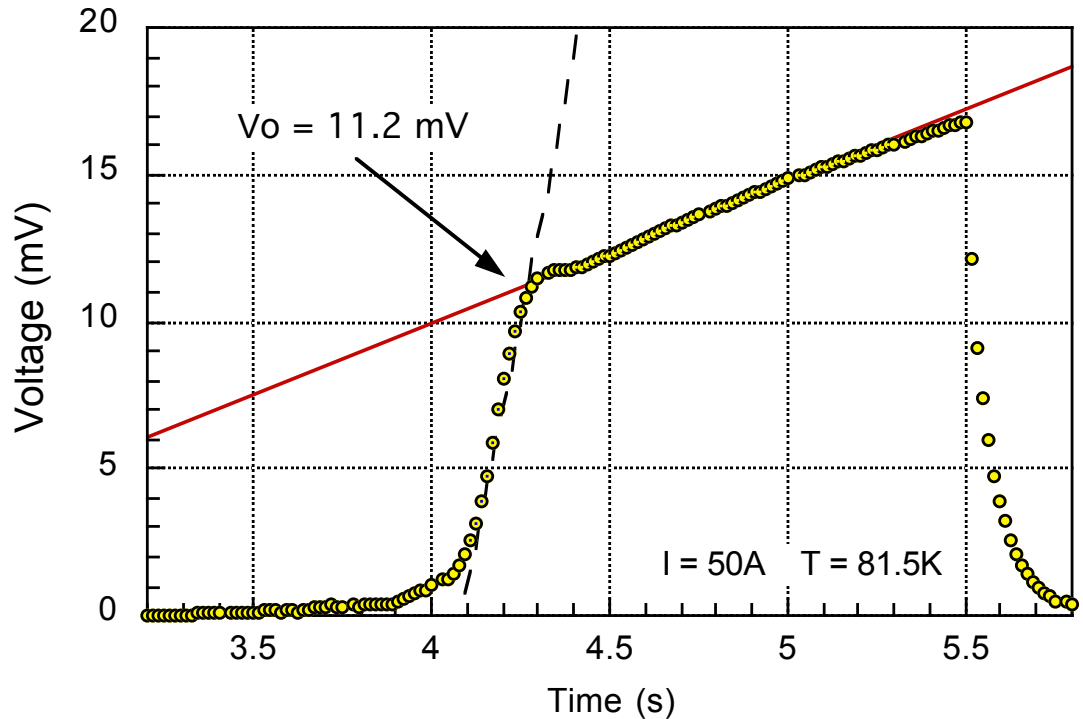

Fig.2.20 The voltage $V(t, I_0)$ during the transition from the superconducting to the normal state (dashed black line) and during the sample heating when is already in the normal state (continuous red line). The crossing point between these two straight lines allows the definition of the value of V_0.

In the following of this model we retain V_0 because the case $V_0 \approx 0$ has been already treated. [DG20] The Eq.2.18 can be substituted in the Eq.2.17 and then solved with respect to the temperature variation $T(t)$.

$$T(t) = \frac{K_V \, u_I I_0^{\alpha+1}}{c_p \, m} t^2 + \frac{V_0 \, u_I I_0}{c_p \, m} t + T_0 \tag{2.19}$$

This phenomenological model does not consider the time dependence of the heat diffusion along with the tape. The experimental verification of the accuracy of the result obtained on Eq.2.19 is not easy because it requires the usage of fast and accurate cryogenic thermometers that do not perturb the measure.

During the quench evolution, the measurement time for $NZPV$ is limited by the value of the maximum acceptable temperature T_{MAX} that can be safely achieved by the conductor. The Eq.2.19 can be used to link the maximum allowed temperature T_{MAX} on the conductor to the value of the maximum useful time t_u for measuring the quench phenomena.

$$T_{MAX} = \frac{K_V \, u_I I_0^{\alpha+1}}{c_p \, m} t_u^2 + \frac{V_0 \, u_I I_0}{c_p \, m} t_u + T_0 \tag{2.20}$$

The value of T_{MAX} is determined by the material and fabrication process of the superconductor to be measured. Anyhow, once the value of T_{MAX} is chosen, it is possible to solve Eq.2.20 and determine the time t_u :

$$t_u = \frac{-V_0 \, u_I I_0 + \sqrt{(V_0 \, u_I I_0)^2 + 4 \, K_V \, u_I I_0^{\alpha+1} \, (T_{MAX} - T_0) \, c_p \, m}}{2 \, K_V \, u_I I_0^{\alpha+1}} \tag{2.21}$$

The knowledge of the time t_u can be used to estimate the value of the length ΔS_u traveled by the quench propagation wavefront when the temperature in the origin of the quench reaches T_{MAX}. This estimation can be done because, in agreement with Eq.2.07 and Eq.2.10, it is possible to consider the linear dependence of the $NZPV$ on the current I_0 . More explicitly the front velocity of the $NZPV$ may be written as $NZPV = K_{NZ} I_0$, where K_{NZ} takes into account all the current independent factors. K_{NZ} may also be taken from

data experimentally observed or the numerical computations. The constant value of $NZPV$, its dependence on I_0 and the Eq.2.21 can be brought together to compute the maximum length ΔS_u as follows:

$$\Delta S_u = NZPV\, t_u = K_{NZ}\, I_0\, t_u \tag{2.22}$$

A determination of the useful time t_u and the maximum length ΔS_u is made using our experimental apparatus. The measures were done without any external applied magnetic field on a single 2G-HTS tape SCS4050AP assembled as shown in Fig.2.06. The environment temperature was $T_0 = 81.5\ K$.

The values of the exponent α, the constant K_V, and the offset voltage V_0 required by the Eq.2.18 can all be determined from the values of the time-dependent voltages when the chosen segment is completely normal. One of the $V_0(I_0)$ values, as shown in Fig.2.20 for $I_0 = 50\ A$ is $V_0(50A) = 11.2\ mV$. The value of V_0 depends on the bias current and on the distances between the voltages taps. The voltage $V_0(I_0)$ is constant if all taps couples share the same width. On the considered sample, voltage taps are placed with a width of about $10\ mm$. According to the Ohm law the voltage $V_0(I_0) = R_0\, I_0$ is a linear function of I_0 and, as shown in Fig. 2.21, a linear fit of $V_0(I_0)$ as a function of I_0 allows the determination of the tape normal resistance $R_0 = 0.228\ m\Omega$.
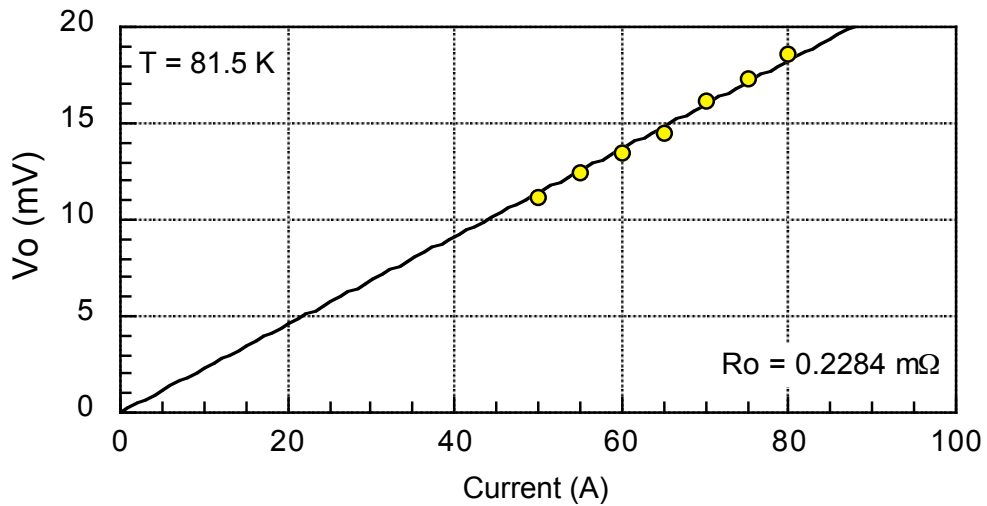
Fig.2.21 The voltage $V_0(I_0)$ as a function of I_0. This linear behavior permits to compute the value of the normal resistance $R_0 = 0.228\ m\Omega$. [RC19]

100

The values of α and K_V may be obtained more simply from the experimental data shown in Fig.2.22 and R_0.
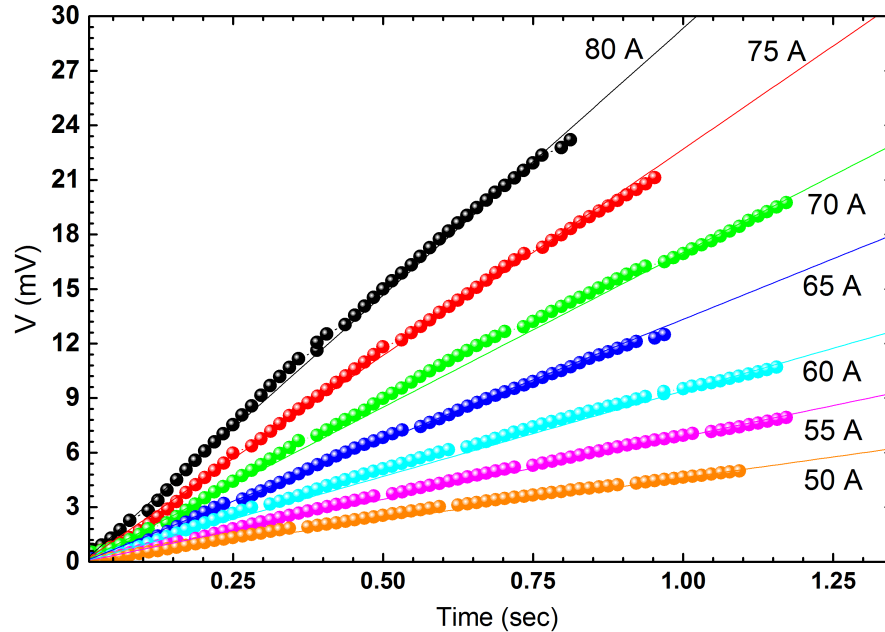
Fig.2.22 Time dependence of the measured voltages $V = V(t, I_0) - V_0(I_0)$ at T=81.5K for different values of the current I_0. All curves are shifted to a common origin at the time when the tape fraction is in the normal state.

The point series shown in Fig.2.22 are obtained from the measurements of $V(t, I_0)$ during the quench propagation. These voltages were acquired on the same tape segment from all quench curves, repeated at several values of the bias current I_0. Each point set, reports only the voltages acquired after the time t_0 corresponding to the complete transition to the normal state of the considered tape segment. These starting times t_0, which are different for each curve, are all translated to a common origin at $t_0 = 0$, and the values of the voltages V are shifted to zero by setting $V = V(t, I_0) - V_0(I_0)$. These two shifts, both in time and voltage, make all the curves of Fig.2.22 starting from the axis origin and do not modify the value of the slope $K_V I_0^\alpha$. The value of the slope is determined with a linear fit on each data set, as shown in the Fig.2.22. The observed linear behavior is in agreement with Eq.2.18 of the proposed

101

model. For these lines, the increase with time of the voltage is solely due to the Joule heating, while the quench is still propagating along the remaining part of the superconductor. Within this model, Eq.2.18 proposes a functional dependence between this slope and the power-law dependence $K_V I_0^\alpha$ so that, it is possible to find its value from the experimentally determined slopes. Once the values of $K_V I_0^\alpha$ are known for each I_0, it is possible to obtain the value of the parameters α and K_V from a power-law best fit of these data. This has been done in Fig.2.23 where, on a log-log graph, the slopes $K_V I_0^\alpha$, obtained from the data shown in Fig.2.22, are reported as a function of the current I_0.
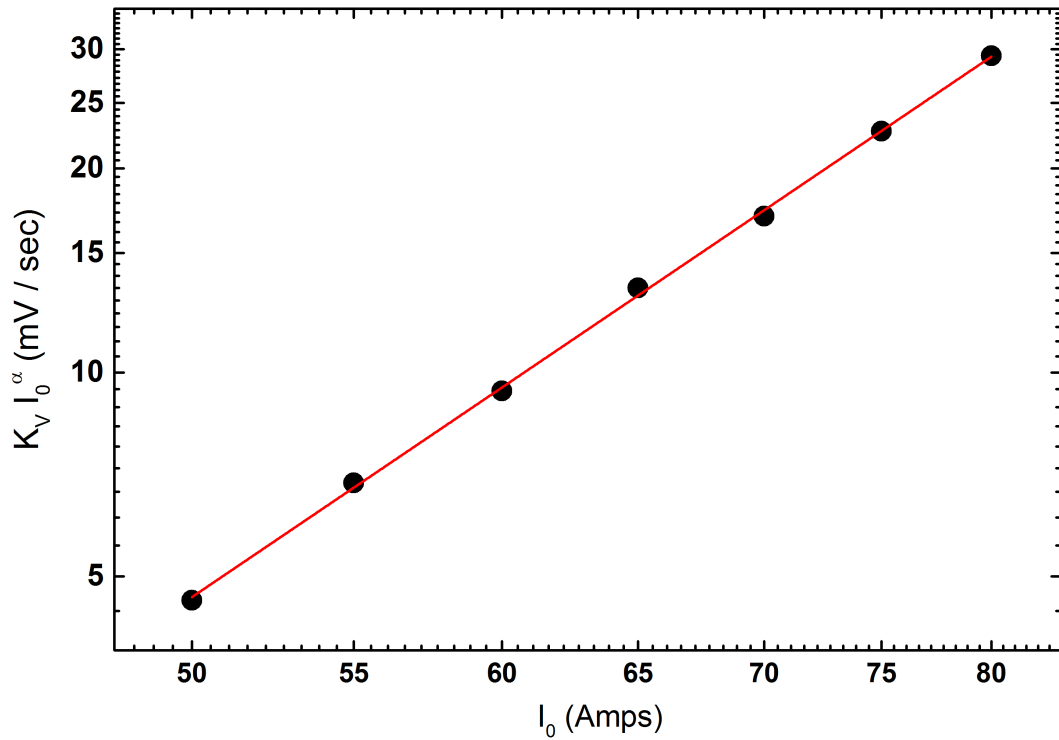
Fig.2.23 The slope coefficients of the time-dependent linear increase of the voltages shown in Fig.2.19 as a function of the bias current.

On this figure, the straight line, drawn on the experimental point, is the numerical best power fit of the experimental data. This best fit is obtained with the value of $\alpha = 3.90$ and $K_V = 1.0715 \cdot 10^{-8}$ (V/s). The good agreement of the experimental values with the power-law fitting line justifies the phenomenological model proposed by Eq.2.17. The values α, K_V, and $V_0(I_0)$ with averaged copper specific heat $c_p = 250$ $(J/Kg\ K)$ and $m = 1 \cdot 10^{-4}$ Kg

102

can be used in Eq.2.21 for the determination of the time t_u. As an example, the useful time determined in adiabatic condition with the Eq.2.21 by using the previous values of α and K_V, with a bias current of $I_0 = 50\ A$, a voltage $V_0(50A) = 11.2\ mV$, and a temperature $T_{MAX} = 400\ K$ is $t_u = 1.75\ s$. This value drops to $t_u = 0.56\ s$ for a bias current increase to $I_0 = 80\ A$.

The computation of the values of the useful length ΔS_u was obtained by using the Eq.2.22 from the already computed values of t_u. In our measures, the knowledge of the values of the $NZPV$, and its proportionality to the bias current I_0 leads to the value $K_{NZ} = (1.528\ mm/A\ s)$. Finally, the value of ΔS_u computed with a bias current of $I_0 = 50\ A$ is $\Delta S_u = 134\ mm$. This value drops to $\Delta S_u = 68.6\ mm$ for a bias current increase to $I_0 = 80\ A$. During the computation of both t_u and ΔS_u we noticed the high sensitivity of Eq.2.21 respect to the value of the parameter α. In the Fig.2.24 the behavior of ΔS_u, computed with Eq.2.21, is reported as a function of I_0 for three values of α.
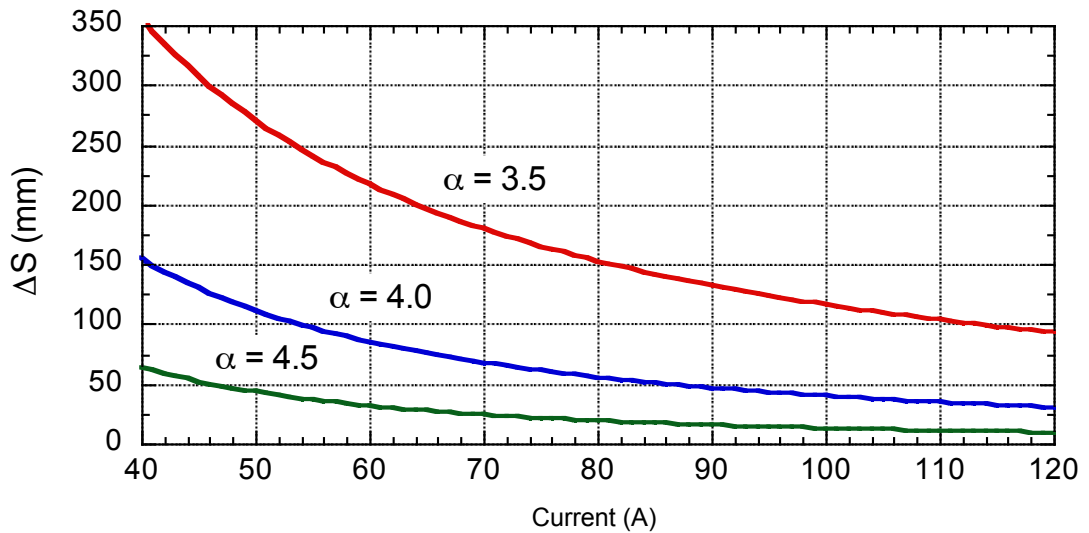
Fig.2.24 The behavior of the length ΔS_u computed with Eq.2.21 is reported as a function of the current I_0 for three different values of α. On the top, there is $\alpha = 3.5$, in the center $\alpha = 4.0$, and on the bottom $\alpha = 4.5$.

The values of the parameter α for the three curves have been chosen around the value of $\alpha = 3.90$ obtained from our measures. Observing Fig.2.24, it is possible to note that the useful length ΔS_u decreases when the current

increases. Moreover, at bias current $I_0 = 40\,A$, an increase of α from $\alpha = 3.5$ to $\alpha = 4.0$, halves the useful length ΔS_u from about $300\,mm$ to $150\,mm$. This reduction further increases at higher current values. At $I_0 = 120\,A$ the value of ΔS_u drops from $93.2\,mm$ to $30.6\,mm$ for the same increase of α.

The value ΔS_u is the length that the wavefront can propagates before the temperature at the generation point to achieve T_{MAX}. The voltage taps placed at distances longer than the ΔS_u value are useless because, if the tape has to be kept safe for the next measurements, these regions of the tape will never be reached by the normal zone wavefront. Within the region limited by the value of ΔS_u the position and the number of couples of voltage taps can be optimized by choosing the right combination of the voltage tap separation and their number. Another implication of the ΔS_u is that under particular circumstances, the $NZPV$ asymptotic value [NN19] may occur at distances longer than ΔS_u, and is practically not measurable.

This model offers a way to estimate the value of the useful length ΔS_u, and the parameter α. The values of ΔS_u computed with Eq.2.21 and shown in Fig.2.24 by using the measurements taken from our apparatus do not allow an easy way to measure the $NZPV$ for bias currents higher than $100\,A$. In fact, when $\alpha > 4$ and $I_0 > 100\,A$, it is easy to burn the tape during the measurements of $NZPV$.

This chapter shows that the superconducting length that can be used for placement of the voltage taps is limited and in an ideal adiabatic environment is strongly dependent on the value of the bias current. The knowledge of this limit can be usefully used before the measurements for the optimal choice of the voltage taps position.

2.7   Superconducting magnet protection

The quench process always begins on a single point and then propagates on the whole magnet winding. The resistive behavior of the superconducting conductor, in the normal state, causes heating due to the Joule effect. This heating may destroy the insulation or, break the conductor like a fuse, with contemporary destruction of the magnet. In the previous chapter the Fig.2.17, of our FEM model, shows that the point that mostly suffers during the quench process is the quench starting point. This is generally true because, at that point, there is the highest temperature rise due to the longest time of the Joule heating. Moreover, because of the large magnetic energy stored on the coil inductance, large voltages could be generated with amplitudes high enough to break the insulation among turns. In order to avoid coil damages either the magnet can be designed to withstand these, heat and voltage peaks or, various protections can be installed on it. On small laboratory magnets, quench protection can be obtained by the installation, on the magnet winding terminals, of a voltage detector able to continuously read the quench induced voltage and open a switch to exclude the power supply. In this way, the discharge current is diverted on an external dump resistor R_E. A scheme of this protection, applied on a coil with inductance L, is shown in Fig.2.25 during the quench phase.
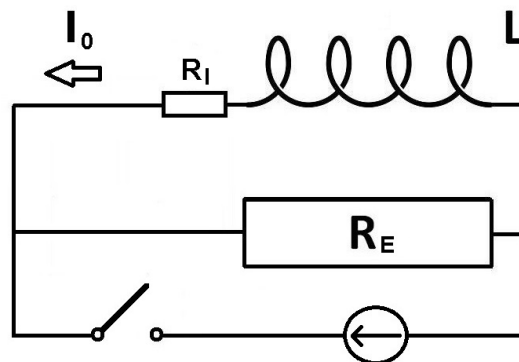

Fig.2.25 Scheme of protection for a superconducting coil L with internal quench resistance R_I. During the quench phase, the switch is open so that the current can discharge through the external dump resistor R_E.

Many power supplies devoted to feeding superconducting magnets have this kind of protection already built inside. With the choice of $R_E \gg R_I$, where R_I is the internal quench resistance, the decay of the coil current $I(t)$ can be obtained by neglecting R_I from the current decay on the usual LR circuits with the condition $I(0) = I_0$:

$$I(t) = I_0 \, Exp\left(-\frac{R_E}{L} \, t\right) = I_0 \, Exp\left(-\frac{t}{\tau_E}\right) \tag{2.23}$$

Where $\tau_E = L/R_E$ is the time constant of the current decay. During the time required by the current $I(t)$ to discharge the magnet, according to Eq.2.19, the temperature increases. In order to limit the temperature rise, in Eq.2.23 small values of τ_E are preferred. Small τ_E values can be obtained by increasing the resistance value of the external discharge resistor R_E as much as possible. However, the resistance R_E must be not too large because the current I_0 at the beginning of the discharge would generate on the resistor R_E a voltage $V = R_E \, I_0$ that can generate insulation problems on all the circuits. Usually, the value of R_E is chosen in order to have voltages in the 1 kV range. A more direct way to estimate this discharge voltage is to consider the coil inductance as a function of the energy E_M stored in the magnet [WS99]:

$$E_M = \frac{1}{2} \, L \, I_0^2 \quad \Longrightarrow \quad L = \frac{2 \, E_M}{I_0^2} \tag{2.24}$$

A superconductive magnetic coil-like any common inductor develops on its termination a voltage difference V is given by Eq.2.24 and the Lenz's law:

$$V = L \, \frac{d\,I}{d\,t} = \frac{2 \, E_M}{I_0^2} \, \frac{d\,I}{d\,t} \tag{2.25}$$

At the end of the discharge the total current variation ΔI can be equated to the current I_0 so that Eq.2.25 for a complete energy discharge can be expressed as

$$V = \frac{2 \, E_M}{I_0^2} \, \frac{\Delta I}{\Delta t} \approx \frac{2 \, E_M}{I_0 \, \Delta t} \tag{2.26}$$

Since the time interval Δt is limited by the temperature variation, then Eq.2.26 affirms that the overvoltage protection becomes a serious problem for those magnets with stored energies above $100 \; kJ$.

For these magnets, as shown in Fig.2.26, the coil can be divided into several sections each of them with its external discharge resistor R_{Ei} and only one R_I on the quenched section.
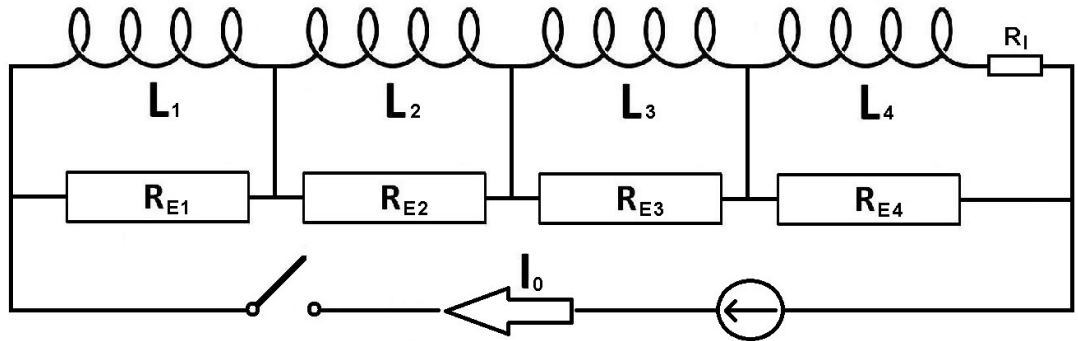
Fig.2.26 Scheme of protection for a large superconducting coil L divided into 4 independent sections each with its own external discharge resistor R_E .

When one of the coil sections quenches, as into section 4 of Fig.2.26, the coil resistance R_I appears but the current I_0 will continue to flow through R_{E4} and all the other coils. In this case, the decay of the current, in section four, depends only on the inductance L_4, which is about a quarter of the total inductance of the magnet. As a consequence, there is a reduction of quench time, temperature, and peak voltage during the quench of that section. Moreover, the fall of the current through the coil with inductance L_4 because of the presence of the mutual inductance among the coils will increase the current on the other coils. With the choice of a current I_0 close to the coils critical current, if the quench starts on one of the sections, then the increase of the current on the other section is sufficient to spread the quench in each of the other sections. This propagation speed can be increased by using the resistors as a coil heater by placing them in good thermal contact with the coil winding. The switches, in both Fig.2.25 and Fig.2.26, have to be designed to open the circuit with currents I_0 of the orders of thousands of Amperes,

107

without any damage. Because of the high voltages involved in the quench process, the mechanical switches have to be provided even with a mechanism for extinguishing the arc. The usage of the external dump resistor permits a heating reduction into the cryogenic environment, as a large proportion of the stored magnetic energy is brought to the external resistor. The presence of less heating, reduce the liquid helium loss and lowers the danger of overpressures, caused by the rapid boiling of the cryogenic fluid. A disadvantage of the usage of the external dump resistor occurs while charging the magnet. In this phase, there is a current split between the coil inductance L and the resistor R_E. A disadvantage that may occur in the subdivision with not well adapted dump resistor. In this case, during the magnet charging process, the coupling between sections can give rise to transient currents in the individual loops, causing a quench in some sections, before the critical current is reached in others. [SM63] This problem may be reduced with slow charging rates. Nowadays the development of power semiconductors devices permits to resolve these problems by replacing the external dump resistors with the usage of high current diodes. These diodes, act as non-linear resistances, with high impedance for low voltages up to $0.8 \div 1\ V$ and act like a normal resistor at much higher voltages. [AN18] The usage of a dozen of these diodes in series permits to have a nonlinear dump device with high resistance for voltages up to tens of volts and then a low resistance at higher voltages. The high resistance allows an easier magnet charging process and the low resistance allows the reduction of the induced voltage generated by the coil at the beginning of the quench process. Another way to extract the magnetic energy from a superconducting coil with a reduction of the heating is the placement close to the primary coil of a coupled secondary coil connected to an external dump resistor. These two coils will act as a transformer with a coupling coefficient $k \leq 1$. At the beginning of the quench, the current on the secondary is negligible and the primary winding behaves as a coil with reduced inductance $L_P = L(1 - k^2)$. As a side advantage of this method, if the

secondary winding is in good thermal contact with the primary winding, it is possible to transfer the heat generated into the secondary coil on the primary coil and accelerate the quench speed. In general, coils windings made with LTS superconductors, with their high values of $NZPV$, spread the normal zone very quickly. Consequently, the thermal heating is dissipated on a longer length, lowering the temperature peak. This better thermal energy distribution along the conductors permits the use of all the passive protections as described above. On the contrary, on HTS tapes the slowness of $NZPV$ allows the heat generated to remain concentrated longer on the small quench region so that active protections must be used. These protections are called active in the sense that, as soon as a non-recoverable quench is recognized their active intervention generally forces the discharge of the magnet.

A simple circuit of this kind, applied on a two coils magnet, is shown in Fig.2.27. This model works as well for a single-coil divided into two parts. The mutual inductance between the two coils can be added to the self-inductance because are connected in series.
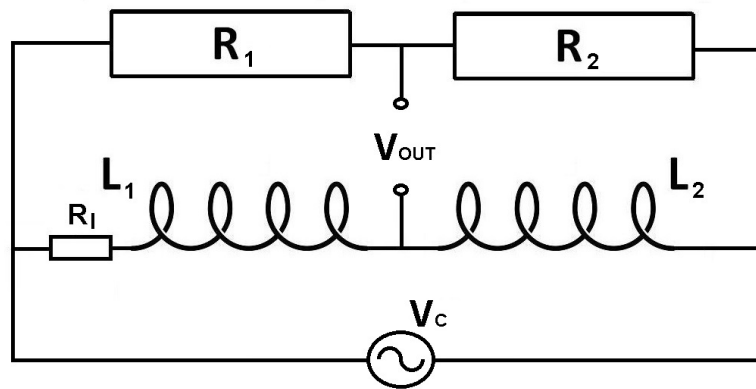
Fig.2.27 Scheme of active quench protection for two superconducting coils. The bridge scheme is unbalanced because of the quench in the L_1 coil.

As usual, the small resistance R_I appears near the coil L_1 where the quench process is starting. The scheme, in Fig.2.27, shows two branches, and the elements are connected into a bridge configuration with the voltage $V_{OUT}(t)$ taken as the signal output. All circuit elements of this model are

considered constant and, it is also assumed that the values of R_1 and R_2 are sufficiently large for not perturbing the signal on the bridge. In this condition it is possible to compute the voltage across the two coils branch $V_c(t)$ as follows:

$$V_c(t) = R_I \, I(t) + (L_1 + L_2) \frac{d \, I(t)}{d \, t} \tag{2.27}$$

The current $I_R(t)$ flowing on the two resistors R_1 and R_2 is the following

$$I_R(t) = \frac{V_c(t)}{R_1 + R_2} \tag{2.28}$$

On the other hands, the output voltage $V_{OUT}(t)$ can be obtained as the following voltage differences taken from the two branches

$$V_{OUT}(t) = L_1 \frac{d \, I(t)}{d \, t} + R_I \, I(t) - R_1 \, I_R(t) \tag{2.29}$$

The Eq.2.27 and Eq.2.28 can be combined and substituted in Eq.2.29.

$$V_{OUT}(t) = \left(\frac{R_2}{R_1 + R_2}\right) L_1 \frac{d \, I(t)}{d \, t} - \left(\frac{R_1}{R_1 + R_2}\right) L_2 \frac{d \, I(t)}{d \, t} + \left(\frac{R_2}{R_1 + R_2}\right) R_I \, I(t) \tag{2.30}$$

An output voltage $V_{OUT}(t)$ proportional only to $R_I \, I(t)$ requires that the first two terms of the Eq.2.30 have to be equal, verifying the following condition.

$$\left(\frac{R_2}{R_1 + R_2}\right) L_1 \frac{d \, I(t)}{d \, t} = \left(\frac{R_1}{R_1 + R_2}\right) L_2 \frac{d \, I(t)}{d \, t} \tag{2.31}$$

The condition of Eq.2.31 is equivalent to the request of the bridge balance condition $R_2 \, L_1 = R_1 \, L_2$ obtained during the normal operations with $R_I = 0$ or in the absence of any running quench. The simplified version of Eq.2.30 is finally.

$$V_{OUT}(t) = \left(\frac{R_2}{R_1 + R_2}\right) R_I \, I(t) \tag{2.32}$$

This quench detection circuit despite his simple description presents some practical issues as the equilibrium condition required by Eq.2.31 needs

the independence of $I(t)$ and $\mathrm{dI/dt}$. The presence of high voltages in the quenching coil can be avoided by adopting two separate coils electrically insulated from the main superconducting coil. [TK17] In case of fast ramped magnets the insulated pickup coils can be inductively coupled to the two main superconducting coils and the signal difference applied directly to the quench detection electronics. [ZH19]

<div style="text-align: right; font-size: 3em;">3</div>

THE CRYOGENIC CURRENT LEADS

3.1   Normal metal current leads

The current links are the components employed for the energy transmission and distribution, from a high current power generator to the final device. Typically the links have to withstand the prescribed values of isolation and heat dissipations depending on the device in use.

In all cryogenic high current applications, with hundreds of Ampere or more, current leads are needed to transfer the current from a generator, at room temperature, into the low-temperature region, where the device is placed. In its simplest form, the current leads may be made of a copper metal bar with a suitable shape. In addition, a current link for cryogenic applications needs to be optimized in order to reduce the thermal energy that will arrive on the cold side. This is because cryogenic refrigeration is expensive, and because the heat delivered at low temperatures may be dangerous for the cold device operations as in the case of superconducting devices. The current leads provide two heat sources that contribute to the heating of the cryogenic devices linked to them. The first heat source is the heat generated by the Joule effect, due to the current flowing into the current leads, $W_J = \rho(L/A)\, I^2$, where ρ is the resistivity of the metal, L is the current lead length between the

room temperature T_A and the cold connection at T_0, and A is its cross-sectional area.

The second heat contribution is the heat conduction through the current leads from the external room temperature T_A toward the other side at the colder temperature T_0. This power $\dot{Q}$ may be estimated by using the Fourier thermal conduction equation $\dot{Q} = k\,(A/L)\,(T_A - T_0)$ where k is the value of the metal thermal conductivity coefficient. [LN19]

In a standard design the current I and the length L, have been assigned, as well as the resistivity ρ, and the thermal conductivity k of the metal. The Joule dissipated power W_J, could be minimized, by increasing the current lead sectional area, but on the other hand, the heat flux $\dot{Q}$ could be minimized by reducing the cross-sectional area. In the current leads made for cryogenic applications, the cross-sectional area plays two antagonistic roles that have to be both balanced: the optimization requires a value of the cross-sectional area that minimizes both these effects. This value of A is dependent on the current design value, so that, each current lead can be optimized only for one specific bias value.

Assuming adiabatic conditions, it is possible to compute the optimized value of the minimal cross-sectional area at a fixed value of the current I, by requiring that the heat flow toward the low-temperature region is minimum. Let us consider a current lead made of a metallic rod with length L and constant cross-sectional A, as shown on Fig.3.01. This bar extends from the point $x = 0$, corresponding to its cold side at a temperature T_0 , to the point $x = L$, corresponding to the warm side at the temperature T_A . At a generic point x between 0 and L, in the thermal equilibrium condition, we consider a thin slice of the current lead with thickness dx.
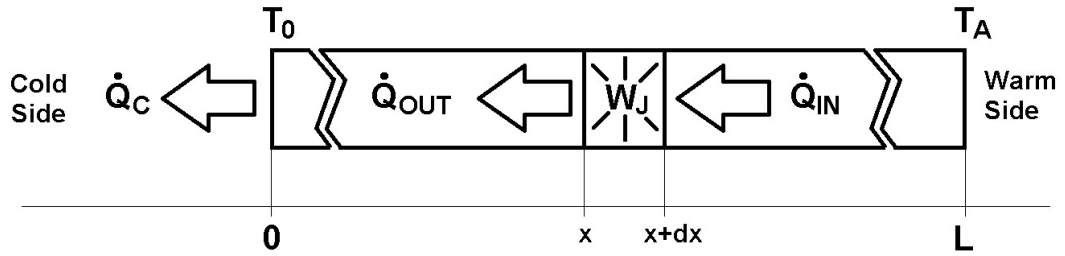
Fig.3.01 Scheme of heat fluxes in an adiabatic current lead: the heat conduction occurs from the warm side at the temperature T_A to the cold side at T_0 ; the heat W_J is generated in the tiny volume $A\,dx$.

At the point $x + dx$, there is the incoming heat flux $\dot{Q}_{IN}$, at the point x, there is $\dot{Q}_{OUT}$, which leaves this region and flows toward the cryogenic temperature T_0 . Within the tiny volume $A\,dx$ the Joule effect generates a dissipation power $W_J = \rho(dx/A)\,I^2$.

In thermal equilibrium condition, within the volume $A\,dx$ it is possible to write the conservation energy condition as $\dot{Q}_{IN} - \dot{Q}_{OUT} + W_J = 0$. By using the Fourier heat conduction law, the previous condition can be explicitly written as:

$$k(T)\,A\frac{dT}{dx}\bigg]_{x+dx} - k(T)\,A\frac{dT}{dx}\bigg]_{x} + \rho(T)\frac{dx}{A}I^2 = 0 \tag{3.01}$$

Where the computation of the derivatives is done at the points x and $x + dx$. In this way, the Eq.3.01 can be written explicitly in the following differential form.

$$\frac{d}{dx}\left(k(T)\frac{dT}{dx}\right) + \rho(T)\,J^2 = 0 \tag{3.02}$$

Where the current density $J = I/A$ has been used to replace the current I allowing the elimination of the cross-sectional A from Eq.3.02. A way to solve Eq.3.02 is based on the introduction of a new function S defined as follows.

$$S = k(T)\,\frac{dT}{dx} \qquad \Rightarrow \qquad S = \frac{\dot{Q}}{A} \qquad\qquad (3.03)$$

Where the second definition of S has been taken in agreement with the Fourier heat conduction law $\dot{Q} = k(T)\,A\,dT/dx$. By substituting the equation on the left side of Eq.3.03 in the Eq.3.02 it is possible to obtain:

$$\frac{dS}{dx} + \rho(T)\,J^2 = 0 \qquad \Rightarrow \qquad \frac{dS}{dT}\frac{dT}{dx} + \rho(T)\,J^2 = 0 \qquad\qquad (3.04)$$

The term dT/dx in the Eq.3.04 can be expressed in terms of this new function S by using again the left side of Eq.3.03 and, then multiplying for $k(T)$.

$$\frac{S}{k(T)}\frac{dS}{dT} + \rho(T)\,J^2 = 0 \qquad \Rightarrow \qquad S\,dS + k(T)\,\rho(T)\,J^2 dT = 0 \qquad\qquad (3.05)$$

It is now possible to return to the heat flux $\dot{Q}$ by using the equation on the right side of Eq.3.03 in the Eq.3.05, obtaining the following equation.

$$\dot{Q}\,d\dot{Q} \;+\; k(T)\,\rho(T)\,I^2 dT = 0 \qquad\qquad (3.06)$$

The Eq.3.06 is a differential equation to be integrated along the whole length of the current lead from the cold side up to the warm side. According to Fig.3.01, the integration extremes for the heat flux $\dot{Q}$, span from the heat flux exiting from the cold side $\dot{Q}_C$ up to the heat flux entering from the warm side $\dot{Q}_A$. In the same manner, the values of the temperature integration extremes span from cold side temperature T_0 up to the room temperature T_A on the warm side of the current lead.

$$\int_{\dot{Q}_C}^{\dot{Q}_A} \dot{Q}\,d\dot{Q} \;=\; -\int_{T_0}^{T_A} k(T)\,\rho(T)\,I^2 dT \qquad\qquad (3.07)$$

The current lead optimization then requires a minimum heat flux to the cold side at the cryogenic cold region $\dot{Q}_C = \dot{Q}_C(min)$ and the absence of heat flux entering from the warm side of the current lead or $\dot{Q}_A = 0$. With these

115

conditions on the integration extremes, the minimum heat flux $\dot{Q}_C(min)$ can be obtained by the integration of Eq.3.07, leading to the following result.

$$\dot{Q}_C(min) = I \sqrt{2 \int_{T_0}^{T_A} k(T)\, \rho(T)\, dT} \qquad (3.08)$$

By using the Fourier heat conduction law, $\dot{Q}_C(min)$ in Eq.3.08 can be substituted by its expression for the condition of the minimum heat flow at T_0.

$$\left(k(T)\, A\, \frac{dT_0}{dx} \right)_{min} = I \sqrt{2 \int_{T_0}^{T_A} k(T)\, \rho(T)\, dT} \qquad (3.09)$$

The temperature T_0 in Eq.3.09 can be considered as the new variable T^* and, without any loss of generality, allows the determination of dx as follows.

$$dx = \frac{k(T)\, A\, dT^*}{I \sqrt{2 \int_{T_*}^{T_A} k(T)\, \rho(T)\, dT}} \qquad (3.10)$$

The Eq.3.10 can be integrated over the whole length from 0 to L and from temperature T_0 up to T_A.

$$\frac{L}{A} = \int_{T_0}^{T_A} \frac{k(T)\, dT^*}{I \sqrt{2 \int_{T_*}^{T_A} k(T)\, \rho(T)\, dT}} \qquad (3.11)$$

The ratio L/A computed on Eq.3.11 represents the optimized form factor for the current lead. Its value can be numerically computed by using Eq.3.11, once $k(T)$ and $\rho(T)$ are known. [HM09]

Approximated computation: The computation of the minimum heat flux $\dot{Q}_C(min)$ obtained on Eq.3.08 can be analytically estimated by using the Sommerfeld theory of metal in the free electron gas approximation for the product of $k(T)$ and $\rho(T)$. [SH17]

$$k(T)\rho(T) = l_0\, T \qquad (3.12)$$

116

The Eq.3.12 is known as the Wiedermann-Franz law and affirms that good electrical conductors, with low resistivity, have a high thermal conductivity. The value of the constant l_0 is known as the Lorentz number and its value is $2.44 \cdot 10^{-8} \ W \ \Omega \ K^{-2}$. The Wiedermann-Franz law is fairly accurate for the major part of metals when the electronic components of both thermal and electrical conductivity dominate. [SH17]

The approximation of Eq.3.12 can be substituted in the Eq.3.08 and the integral can be evaluated by obtaining the following value for $\dot{Q}_C(min)$.

$$\dot{Q}_C(min) = I \sqrt{l_0 \ (T_A^2 - T_0^2)} \tag{3.13}$$

Usually, in the normal metals, the resistivity $\rho(T)$ can be linearized as $\rho(T) = \alpha \ T$. [CR99] In these cases, the Wiedermann-Franz law of Eq.3.12, leads to a temperature-independent thermal conductivity $k(T) = l_0/\alpha$. This result and Eq.3.12 can be substituted in Eq.3.10 obtaining this approximated expression.

$$dx = \frac{l_0 \ A \ dT^*}{\alpha \ I \sqrt{l_0 \ (T_A^2 - T^{*2})}} \tag{3.14}$$

The Eq.3.14 can be integrated over the whole current lead length from 0 to L and from the temperatures from cold side temperature T_0 up to T_A .

$$\frac{L}{A} = \frac{\sqrt{l_0}}{\alpha \ I} \left(\frac{\pi}{2} - \sin^{-1} \frac{T_0}{T_A} \right) \tag{3.15}$$

The Eq.3.15 represents the optimized geometrical ratio L/A of the current lead in the Wiedermann-Franz and linearized resistivity approximation. The Eq.3.15 proves that once a certain current value I has been assigned, exists an optimized ratio L/A, which is independent of the adopted material.

Another analytical result in this framework is the temperature profile along with the current lead. Neglecting the temperature dependence of the resistivity $\rho(T) = \rho_0$ and the thermal conductivity value $k(T) = k$ the eq.3.02 by considering the product $k \ \rho_0$ constant can be simplified as follows:

$$k \frac{d^2}{dx^2} T(x) + \rho_0 J^2 = 0 \tag{3.16}$$

The general solution of this second-order differential equation, with constant coefficients, is made with the following terms.

$$T(x) = -\frac{\rho_0 J^2}{2k} x^2 + c_1 x + c_2 \tag{3.17}$$

The arbitrary constants c_1 and c_2 can be determined by using, as boundary conditions, the values of the temperature T_0 at $x = 0$ and T_A at $x = L$ on both extremity of the current lead. [SS06]

$$T(x) = -\frac{\rho_0 I^2}{2k} \left(\frac{x}{A}\right)^2 + \frac{T_A - T_0 + \frac{\rho_0 I^2}{2k}\left(\frac{L}{A}\right)^2}{\left(\frac{L}{A}\right)} \left(\frac{x}{A}\right) + T_0 \tag{3.18}$$

Finally, Eq.3.18 shows the temperature profile along with the current lead for the optimal L/A ratio and Fig.3.02 report this profile for the optimized current and for larger and lower current values respect to the optimized one.
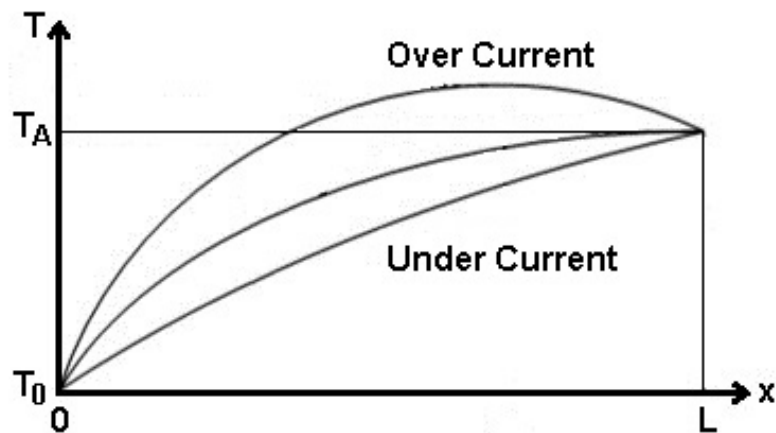
Fig.3.02 The temperature profile of the current lead for the optimized value of the current. Profiles for currents larger and smaller than the optimized value are shown respectively as Over Current and Under Current.

A more realistic example: the thermal leakage through the current leads and other thermal leaks, as well as the dissipation of the cryogenic devices, need a continuous cooling to maintain the environment constantly at the

118

cryogenic working temperature T_0. Often the latent heat of evaporation is used to this purpose. In order to save cryogenic bath consumption, or generally to reduce the refrigeration power load, it is possible to fully utilize the available cooling capacitance of the evaporated gas too. In the ideal case, it would be advisable that the cryogenic fluid would leave its whole cooling power in the cryostat, leaving the cryogenic system with temperatures, as close as possible, to the room temperature. As an example, within a liquid helium bath, the dissipation of only $1\,J$ produces $48\,mg$ of 4.2K helium gas. This cold helium vapors can adsorb $74\,J$ before reaching room temperature. Since one of the largest contributions to the thermal losses is due to the current leads, it is convenient to make the current leads to behave as heat exchangers in which the cold helium gas is used to cool the current leads. In this way, a large amount of heat is absorbed by the gas stream and removed from the cryogenic system before reaching the liquid helium bath.

An image of a current lead with the counter flux cooling is shown in Fig.3.03. The main difference from the Fig.3.01 is the presence of a pipe that surrounds the current where a mass flow $\dot{m}\,(kg/s)$ of the boiled off liquid helium absorbs the heat W_J generated by the Joule heating in the volume $A\,dx$.

The heat leak minimization, as well as the dissipated power W_J can be minimized in the thermal equilibrium by using the Eq.3.01 with the addition of a term H that considers the rate of the heat transferred to the coolant. [WL02]

$$k(T)\,A\left.\frac{dT}{dx}\right]_{x+dx} - k(T)\,A\left.\frac{dT}{dx}\right]_x - H + \rho(T)\frac{dx}{A}I^2 = 0 \qquad (3.19)$$

The solution of Eq.3.19, likewise Eq.3.01 can be numerically computed.
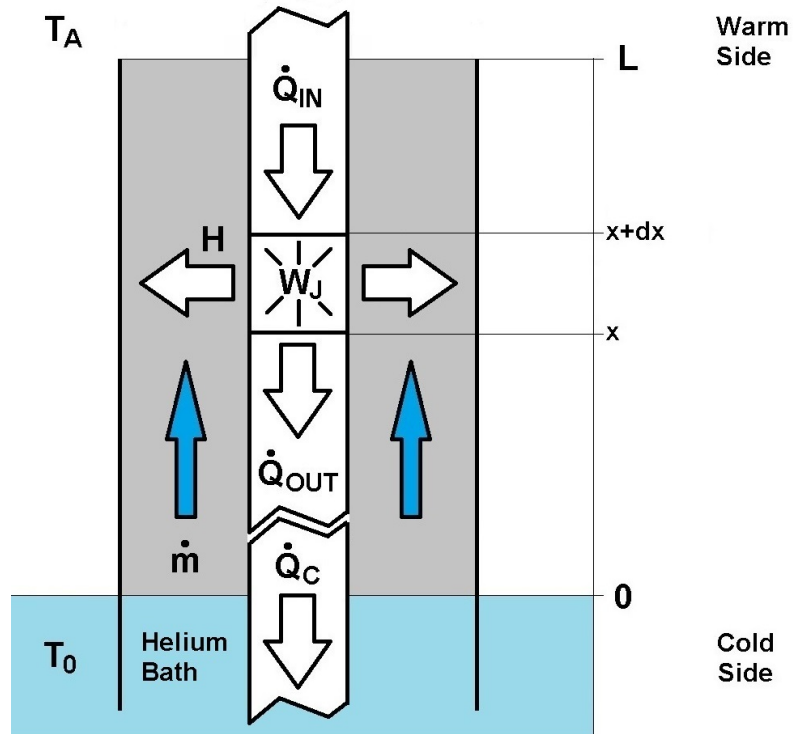
Fig.3.03 Scheme of a counter flux cooled current lead. The vapor flow coming from the boiled off liquid bath partially absorbs both the heat from the warm side at T_0 and the heat power W_J generated by the Joule heating.

However, *M.N.Wilson* was able to find an analytic solution by taking into account some approximations. [FF67][WL02]

Generally speaking, respect to the adiabatic current leads, the heat removal of the counter flow cooled current leads, permits to improve the L/A geometrical ratio. In these current leads, the optimized transport current requires a smaller cross-sectional area A. However, the best results require the optimization of the heat transfer efficiency that is obtained by the optimization of the heat exchange surfaces and the gas flow, nearly to the laminar regime. The optimization of the design that considers all these aspects is part of a complicated design problem demanding numerical solutions.

3.2 Superconducting HTS current leads

The progress in HTS technology over the past years, made possible the realization of current leads that incorporate HTS sections able to transport very high currents. This development was highly stimulated by the request of a high heat load reduction, of the high currents needed to feed superconducting magnets for particle accelerators and nuclear fusion plants. [RB18] [BL07]

The usage of HTS current leads allows the separation of the heat link in two different thermal loads. The normal metal, with its own Joule effect dissipation and thermal conductivity, takes care of the first part from room temperature to liquid nitrogen temperature. The second part, from liquid nitrogen temperature to around $4\,K$, where it is possible to use the HTS materials and take advantage that the Joule dissipation is absent [HL11] [HL19]. Moreover, the thermal conduction can be widely reduced because the metallic holders of the HTS tapes are made of low thermal conductivity materials. This new cryogenic link technology has got a significant development, especially where a large delivery of power into the cryogenic environment is required. In these conditions with the usage of HTS current leads, a remarkable amount of cryogenic cooling energy can be saved. [HL93]

In Switzerland the CERN, European Organization for Nuclear Research, with the request of more than 3000 current lead for the superconducting magnets of the LHC, Large Hadron Collider, in the year 1995 began to evaluate the convenience of using a new generation of current leads for its magnets [RS04]. With the goal of minimizing the heat load to about $4\,kW$ dissipated into the cryogenic environment by the already optimized normal metal current leads, the CERN started to evaluate, for the transport of a current altogether of about $3 \cdot 10^6\,A$, the usage of superconducting HTS current leads for its current leads ranging from 60 up to $13000\,A$ [BL99]. It has been found that the usage of HTS material on the bottom part of the normal metal leads, makes a significant reduction of about a factor 10 on the heat load of the cryogenic

bath with important savings in liquefaction power respect to conventional leads. [BL02] [BL08] [BR17] [HL18] [ZH16]

Among all, the most important superconducting HTS current lead is the one optimized for the highest current of $13\ kA$, shown in Fig.3.04.
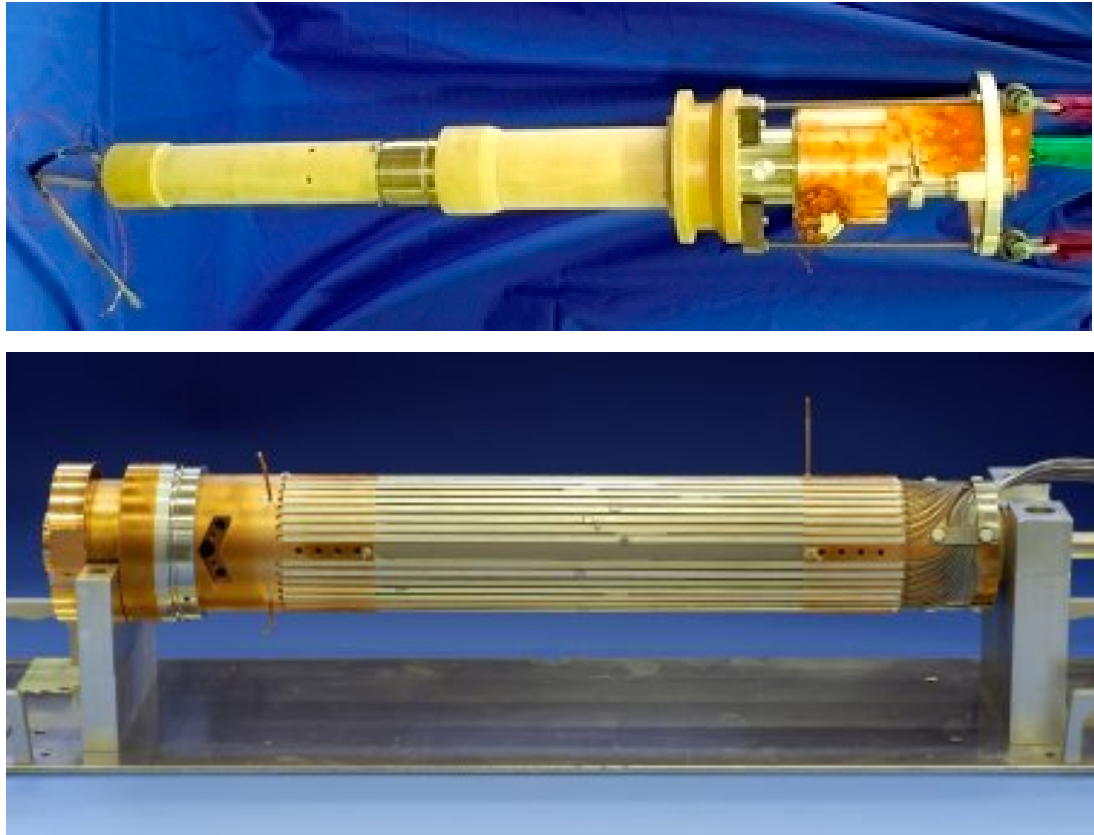
Fig.3.04 Superconducting HTS current lead optimized for $I = 13\ kA$ (Top) and a particular of the superconducting part with the HTS tapes (Bottom).

Another large-scale application of the superconducting HTS current leads can be found in the International Thermonuclear Experimental Reactor, ITER it is being built in France. Both the central solenoid and the toroidal field coil use the Nb_3Sn cable in conduit windings, with currents that are as high as $68\ kA$. The connections between the room temperature power supply and the magnets are realized by using high capacity superconducting HTS current leads, designed and built for currents of $70\ kA$. [HL05] These superconducting HTS current leads are shown on the top of Fig.3.05. On the bottom of the same figure, the two main parts of these current leads are visible. The resistive part

is mainly a copper heat exchanger with a cooling circuit with a helium gas inlet at the temperature of $50\ K$ and a pressure of $0.3\ MPa$. This part has been modeled for working between 65 K and room temperature. [RZ13]

Fig.3.05 A view of the 68 kA HTS current lead developed for the ITER toroidal field coils. (Top). The same current lead with its parts (Bottom). [HL05]

3.3 Our development of high current leads

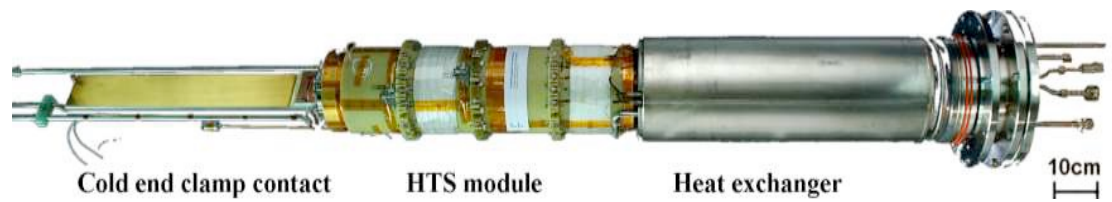In Salerno, the Italian National Institute for Nuclear Physics, INFN, in a joint project with the University of Salerno, created a laboratory for the power application of superconductivity. In this laboratory, a dedicated test area was created for testing superconducting both magnets and cables for high current applications. In order to fulfill testing lines needs, is required a $10\,kA$ and a $20\,kA$ current leads. So, we decided to design a versatile couple of leads capable of working at both currents, just changing the cooling conditions. The facilities will be cooled, alternatively, with a cryogenic refrigerator able to supply up to $15\,g/s$ helium gas stream at $4.6\,K$. More details on the facility will be given in the next chapter.

The chosen solution is the usage of superconducting HTS current leads. The superconducting HTS current leads have been optimized for a counter flow helium mass flow rate of $0.6\,g/s$ at a current of $10\,kA$. The addition of liquid nitrogen cooling is foreseen when the current leads have to operate at $20\,kA$. The Fig.3.06 shows a schematic design of this HTS current lead.

The design shown in Fig.3.06 has been divided into two parts: the gray color thinner part represents the superconducting lead made by several stacks of 2G-HTS composite tapes, surrounding a thin stainless steel mechanical support. The brown-colored thicker part, of the same cylinder, represents the normal copper heat exchanger. Around this latter part, there is a ring-shaped cryogenic liquid reservoir that, with its independent heat exchanger, adds some extra cooling for the optimized operation at the higher current of $20\,kA$. In Fig.3.06 are also visible, on both extremities, the two copper current blocks, the first is located near the top insulating flange with the room temperature joint to the power supply, and the second on the bottom with the cold joint for the superconducting magnet.
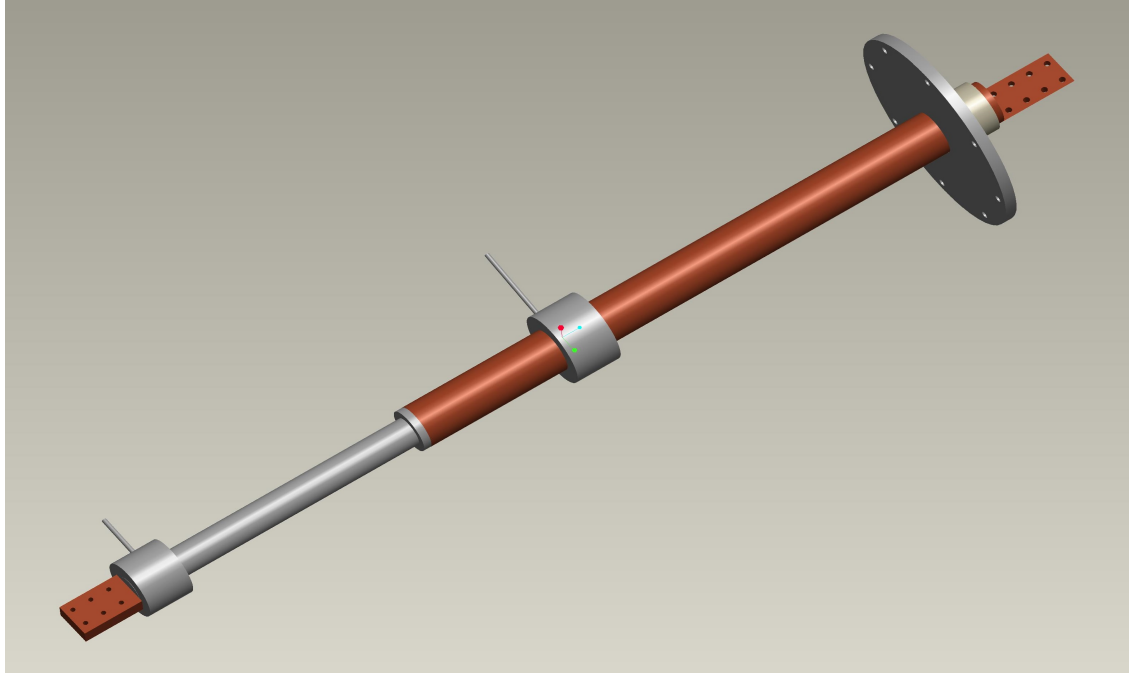
Fig.3.06 Superconducting HTS current lead design. The gray part of the cylinder is the superconducting lead and, the brown part, the copper heat exchanger. The gray ring, on the brown part, is a liquid nitrogen reservoir for an extra cooling to be used in the high current regime.

In Fig.3.07 the gas flow path is shown. The 4.5K helium gas stream enters into the bottom of the superconducting HTS current lead, cools down both the superconducting and the normal metal resistive parts, and leaves the copper block at room temperature. This cooling is sufficient for operating the current lead at 10 kA. The liquid nitrogen with its independent heat exchanger absorbs the extra heat generated at 20 *kA* into the copper resistive part. Furthermore, a temperature-controlled electrical heater ensures that the top copper electrical block remains at room temperature. In this way, the formation of moisture and humidity is avoided in both working conditions.

The optimization was done by considering the maximum available helium mass flow rate of $\dot{m} = 0.6 \, g/s$ at the temperature of $4.6 \, K$, and by using the Eq.3.20 as a general equation describing the physical situation. [SG15]

$$\frac{\rho(T)}{A} I^2 + \frac{d}{dx}\left(A\, k(T) \frac{dT}{dx}\right) - \eta\, \dot{m}\, C_P\, \frac{dT}{dx} = 0 \qquad\qquad (3.20)$$
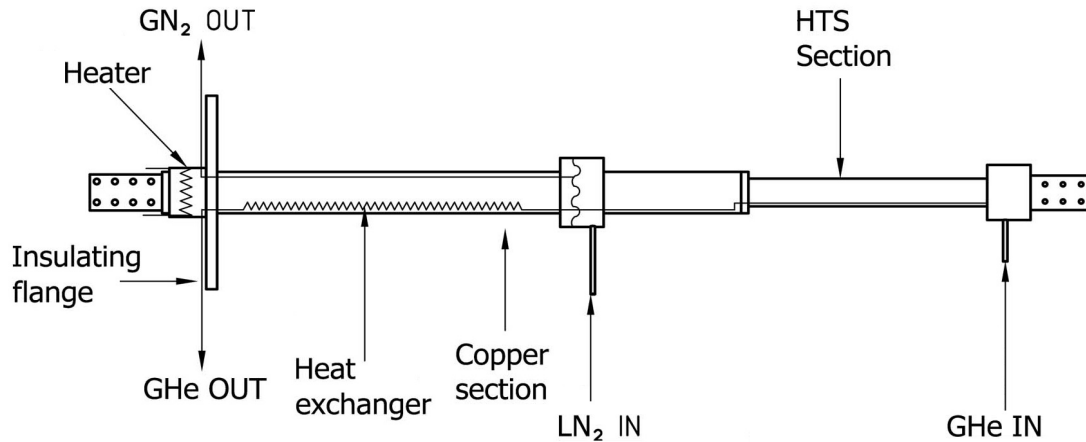
Fig.3.07 Design concept of the superconducting HTS current lead of Fig.3.06 with the indication of the cryogenic cooling inputs and outputs and the small heater needed to avoid the formation of moisture and humidity.

Where, apart from the other symbols already defined, I is the current flowing into the lead, η the heater exchanger efficiency and C_P the gas at the constant pressure specific heat. The Eq.3.20 has been solved by using the software Comsol Multiphysics© numerical FEA, Finite Element Analysis. The numerical analysis considers just the normal conducting part. A constant dissipation value of $50W$, comprehensive of all dissipations, has been assumed. This value takes into account the joint electrical resistance of the order of $100\ n\Omega$ at the current top value of $20\ kA$. Because of this heat load the helium gas flow, entering on the superconducting parts at $4.6\ K$ it is assumed that would raise its temperature leaving the superconducting part with an expected maximum value of $20\ K$. Moreover, the maximum allowed temperature on the top of the superconducting part has been limited to $60\ K$. This temperature value ensures that at the current of 20 kA, there is still a large safety margin, i.e. the critical current of the HTS tapes at $60\ K$ is

$I_C(60\,K) \gg 20\,kA$. The numerical optimization started by considering a copper cylindrical bar with a resistivity ratio $RRR = 100$ and the corresponding temperature-dependent resistivity $\rho(T)$ and thermal conductivity $k(T)$ taken from the CryoComp©5.2 database and, inserted in the model as tabulated values [CR99]. The computation started by considering a copper bar with length $L = 600\,mm$ and a diameter $\phi = 40\,mm$. These values lead to the ratio $L/A = 4.77\,cm^{-1}$ corresponding to a conduction-cooled lead, optimized for a current of $I = 7.2\,kA$ in case of the adiabatic condition without helium cooling. The heat exchange between the helium gas flow inlet, coming from the superconducting part at the temperature $20\,K$, and the cylindrical copper bar, was modeled with the introduction of 196 tiny cylindrical virtual copper thermal flux-tubes, each of them with a diameter of $\phi = 2\,mm$ for a total heat exchange surface of about $0.74\,m^2$. All simulations were done by keeping the top extremity of the copper cylindrical bar at room temperature and leaving the cold extremity free to stabilize. The steady-state thermal profiles at different bias currents are shown in Fig.3.08.
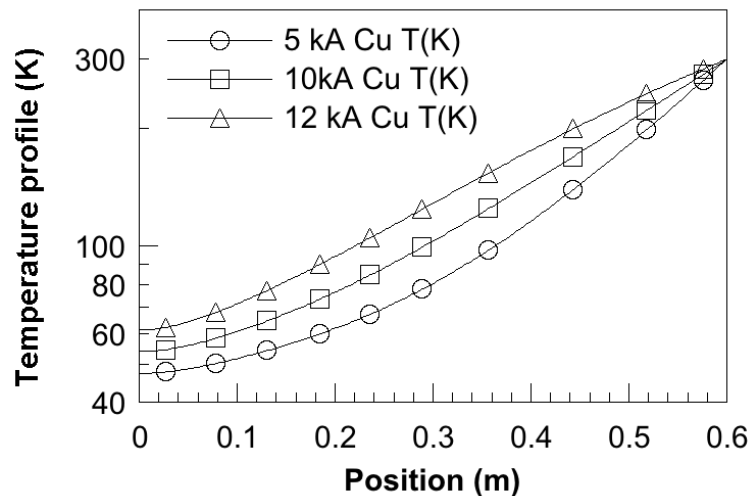
Fig.3.08 Copper exchanger temperature profile with 0.6 g/s of 20K inlet gas stream at three values of current: $5\,kA$ (Circles), $10\,kA$ (Squares), and $12\,kA$ (Triangles). No liquid nitrogen addition. In all cases, the temperature remains under $T = 60\,K$.

For all the currents with an inlet gas flow of 0.6 g/s at 20 K, the bottom temperature of the copper bar is lower than 60 K, indicating a good working point for the HTS stack.

The computation has been done with the same cold He gas flow and the addition of the liquid nitrogen in the reservoir. The computed thermal profiles are shown in Fig.3.09.
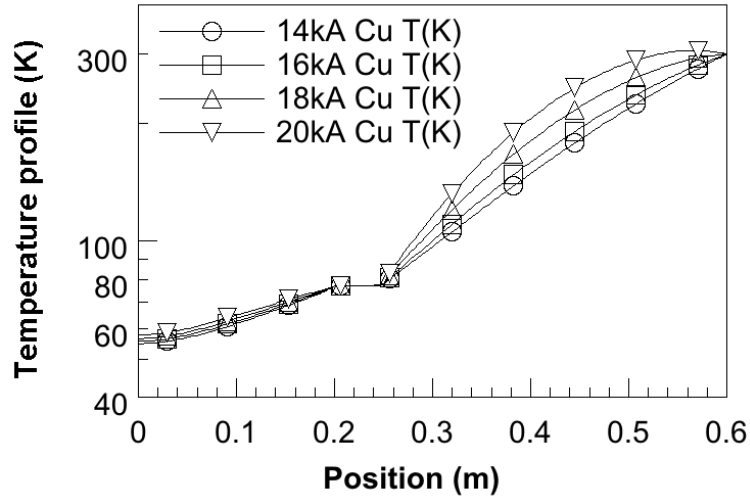
Fig.3.09 Temperature profile of the copper exchanger with the reservoir filled with liquid nitrogen for different values of the current flow: $14\,kA$ (Circles), $16\,kA$ (Squares), $18\,kA$ (Triangles), and $20\,kA$ (upside-down triangles). In all profiles, the temperature remains under $T = 60\,K$.

The ring-shaped reservoir, filled with liquid nitrogen at $77\,K$, as shown by a common horizontal segment in Fig.3.09, with its $5\,cm$ height, was placed at a distance of $20\,cm$ far from the cold extremity of the normal part. This distance has been chosen, by observing in the previous simulation that at $10\,kA$, the value of the temperature in this region is about $70\,K$. In this way, the helium gas flow would not freeze the liquid nitrogen. Also in this case the lower side of the copper bar is kept below 60 K.

In Fig.3.10, the 3D-Comsol© graphics of the computed surface colored temperatures map are shown on the left for a $10\,kA$ current with only He counter-flow, and on the right for the maximum current value of $20\,kA$, with He counter-flow and liquid nitrogen.
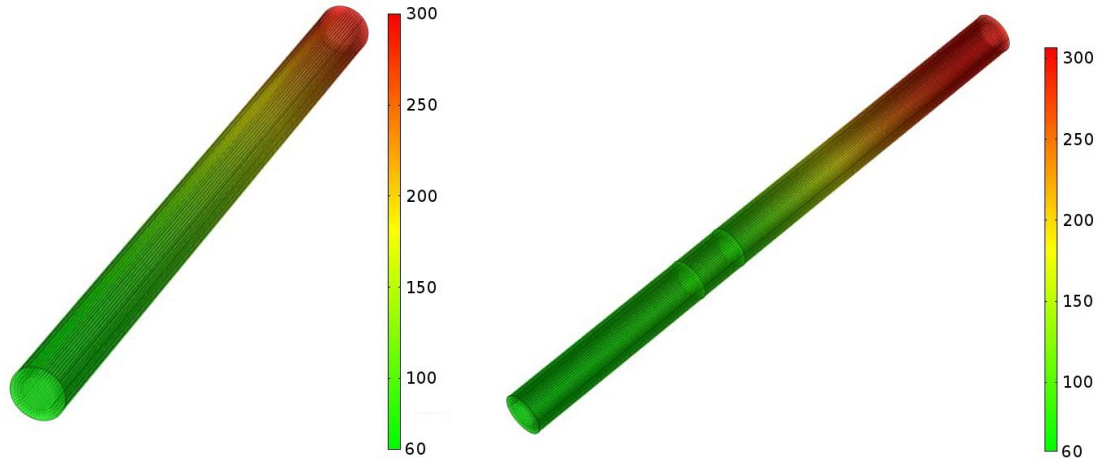
Fig.3.10 3D-Comsol© graphics temperatures map with a current flow of $10\ kA$ and helium cooling (Left). The same temperature map with a current flow of $20\ kA$ and the addition of liquid nitrogen cooling (right). The lengths are the same but the image on the right has been rotated in order to enhance the position of the liquid nitrogen reservoir.

In the picture shown on the right of Fig.3.10, it is possible to notice the position of the liquid nitrogen reservoir from the constant temperature region.

In Fig.3.09, thanks to the presence of the liquid nitrogen reservoir, the normal part of the current leads can be used with currents up to $20\ kA$ without affecting the temperature of the bottom of the copper normal part and, for these current values, the top side of the part is well cooled with only a negligible overheating at the current value of $20\ kA$. A careful observation of the temperature profile in Fig.3.08 shows, near the top side of the part, that the temperature appears not properly optimized. This problem may be overcome either by using temperature-controlled electrical heaters on these leads or by fine adjustment of the gas flow. The liquid nitrogen consumption was also evaluated by using the thermal gradient near the liquid nitrogen reservoir for the computation of the heat flow. The results from this computation are reported on the graphic shown on Fig.3.11.
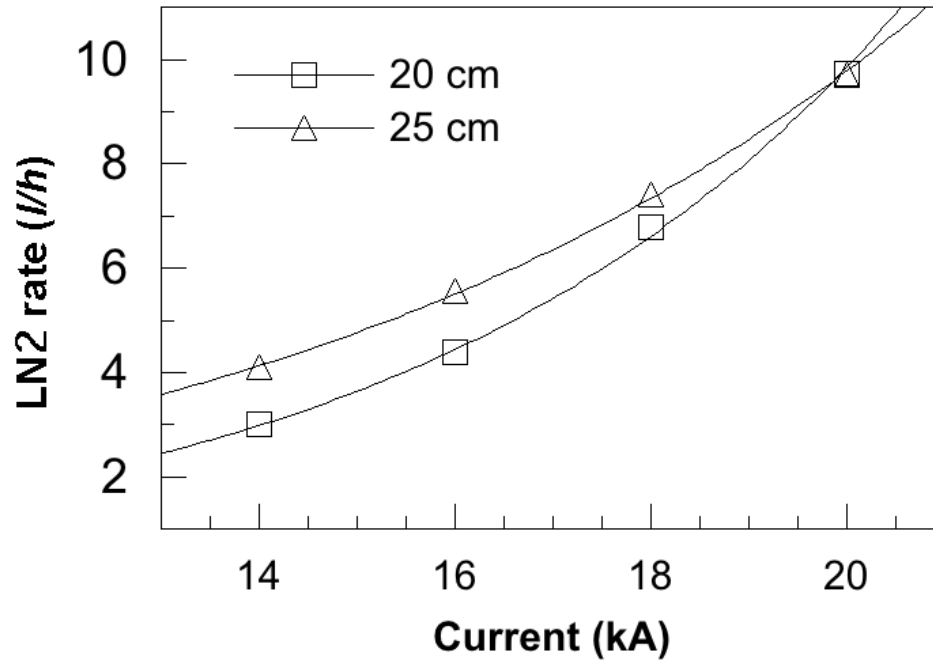
Fig.3.11 Values of the liquid nitrogen consumption obtained from the numerical computation as a function of the current for two different positions of the liquid nitrogen reservoir. The two lines are only a guide for the eyes.

The values shown in Fig.3.11 show that the estimated evaporation rate, computed with the current flow of $20\,kA$, is about $10\,l/h$. This value reduces monotonically up to $3\,l/h$ for a current of $14\,kA$. Raising the position of the liquid nitrogen reservoir of $5\,cm$ increases the liquid nitrogen consumption for all currents lower than $20\,kA$. This indicates that the position of the reservoir is optimized because shorter distances may lead to a possible liquid nitrogen freeze and longer distances would increase the liquid nitrogen consumption.

The results of these simulations were sent to a factory specialized in the realization of such devices. A team of mechanical engineers with cryogenic expertise, following our project, manufactured a double current optimization by making the design shown in Fig.3.06. The design obtained at the end of the development process is shown in Fig.3.12. In this figure, it is clearly visible, in gray color the superconducting section where the HTS superconducting strips are allocated.

Fig.3.12 CAD design of the complete HTS current lead with its superconducting part, shown by the gray-colored zone under the yellow line with its two copper clamps. The Liquid nitrogen input pipe to the reservoir is also visible. The overall length of the current lead is about 1.7 meters.

In this figure, it is also visible the pipe for the liquid nitrogen reservoir filling, the insulation flange, and the top feedthrough with the copper blocks. On the bottom of the figure, a similar copper joint delivers the current to the coil windings. The HTS current lead partially built in its main parts during the assembly phase is shown in Fig.3.12 where, on the bottom of the image, the copper heat exchangers are clearly visible. These exchangers are made with a spiraling copper foil that forces, the cold gas flow, to rotate around the copper bar, in an empty channel left for the heat exchange. During its path toward the exit, the He gas warms up by absorbing the heat, generated within the copper metal and coming from the top side of the current lead at room temperature. On the top of Fig.3.13 are also visible the two superconducting HTS parts. Each part is made with two cylindrical copper ends that provide the transfer of the current from the other copper parts to the superconductor. The resistive joints are made by engraving, on the surface of the copper cylinders, a dozen of grooves. A non-twisted stack of superconducting tapes is soldered on each groove. The contacts between the stacks of the superconducting tapes and the copper terminations are made employing a soft soldering alloy, usually using the EutecRod© 157 or similar product [TC00][TC08].

Fig.3.13 Picture of the main parts of the two HTS current leads before the final assembly. The superconducting parts with their soft soldered (2G) $ReBCO$ superconducting strips (Top). The copper made, gas exchangers showing the cooling path of the cold nitrogen gas obtained from the evaporation of the liquid nitrogen of the reservoir (Bottom).

In the final version of the HTS current leads, tapes of (2G) $ReBCO$ biaxial textured film produced by SuNAM©, have been used. [SN00] This choice is due to the superior flexibility of the thinner $ReBCO$ tape and higher in field current density at elevated temperatures. The chosen tapes have a width of $12\ mm$ and a thickness of $140\ \mu m$. The averaged value of critical currents on the tape wound on the reel of $100\ m$ bought by Criotec, Chivasso (TO), oscillate from a minimum of $612\ A$ and a maximum of $760\ A$, both well above of the specification values of $500\ A$. [SN00] With these tapes, 60 strips distributed in a dozen of stacks can transport up to $30\ kA$. This value is above the requested value of $20\ kA$.

One of these current leads is shown in Fig.3.14 completed with all the accessories mounted on it and ready to be used.

Fig.3.14 Picture of one of the HTS current leads with a total length of 1700 mm.

Presently these HTS current leads optimized for both $10\ kA$ and $20\ kA$, manufactured by Criotec, Chivasso (TO), were shipped to the INFN Laboratory in Salerno and mounted on their temporary support. The two current lead, shorted with a copper bar mounted on the cold side, will be mounted on a box under vacuum and cooled down to $4\ K$ by using our cryogenic refrigerator. After being leak tested, the current leads will be connected to a power converter, available in the laboratory and a current up to $20\ kA$, will be used to feed these current leads for the experimental validation and a future usage within the experimental activities of the laboratory.

4

TESTS ON SIS100 QUADRUPOLE MODULES

4.1 Introduction

The GSI *(Gesellschaft für Schwerionenforschung), a Helmholtz Centre for Heavy Ion Research* laboratory performs basic and applied research in physics and related natural science disciplines. Since 2010, in cooperation with 10 international partners, involving 3000 researchers from 50 countries, an international research structure named FAIR, *Facility for Antiproton and Ion Research,* was established at GSI. The site construction started in 2017. [WE00]

The main difference between the FAIR accelerator facility and the other accelerators, like LHC (Large Hadron Collider) built at CERN in Genève (Switzerland), is its design that allows the possibility of accelerating a variety of ions of all the natural elements in the periodic table, as well as protons. The advantage of FAIR is also the possibility to execute several parallel experiments on different targets since the detectors are placed on beam branches and not directly on the accelerator ring as in the CERN experiments.

The physics investigated with FAIR is wide and several fields will be explored. The SIS100 ring accelerator will be the largest ring of the FAIR laboratory. Its relevant impact of this development of the FAIR laboratory can be better understood in Fig.4.01 where, the SIS100 accelerator ring, together

with the other new planned facilities are shown with red lines together with their connection to the already existing facilities shown with blue lines.
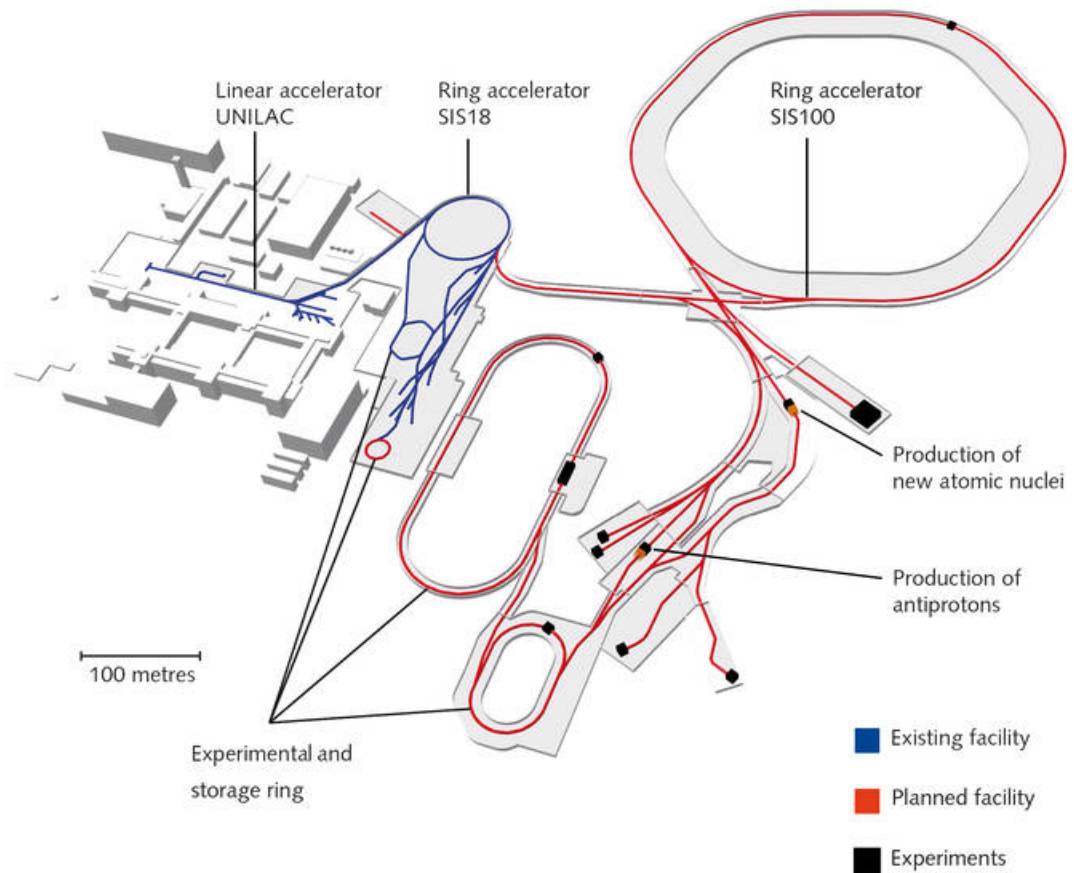
Fig.4.01 The schematic map of the existing facilities are reported with blue lines. The new SIS100 ring accelerator and its related experimental infrastructures are shown with red lines.

The project of the SIS100 ring accelerator is very complex and based on many different technologies in several fields of engineering and physics. A schematic representation of its structure is shown in Fig.4.02.

The superconducting magnets of the SIS100 ring are into a cryostat with vacuum insulation and cryogenic cooling. In each dipole, the superconducting magnet bends the particle beam into a circular path. [RX18] Further to the dipole magnets there are the quadrupole modules. These modules provide the necessary focusing and defocusing the particle beam. [FS17]
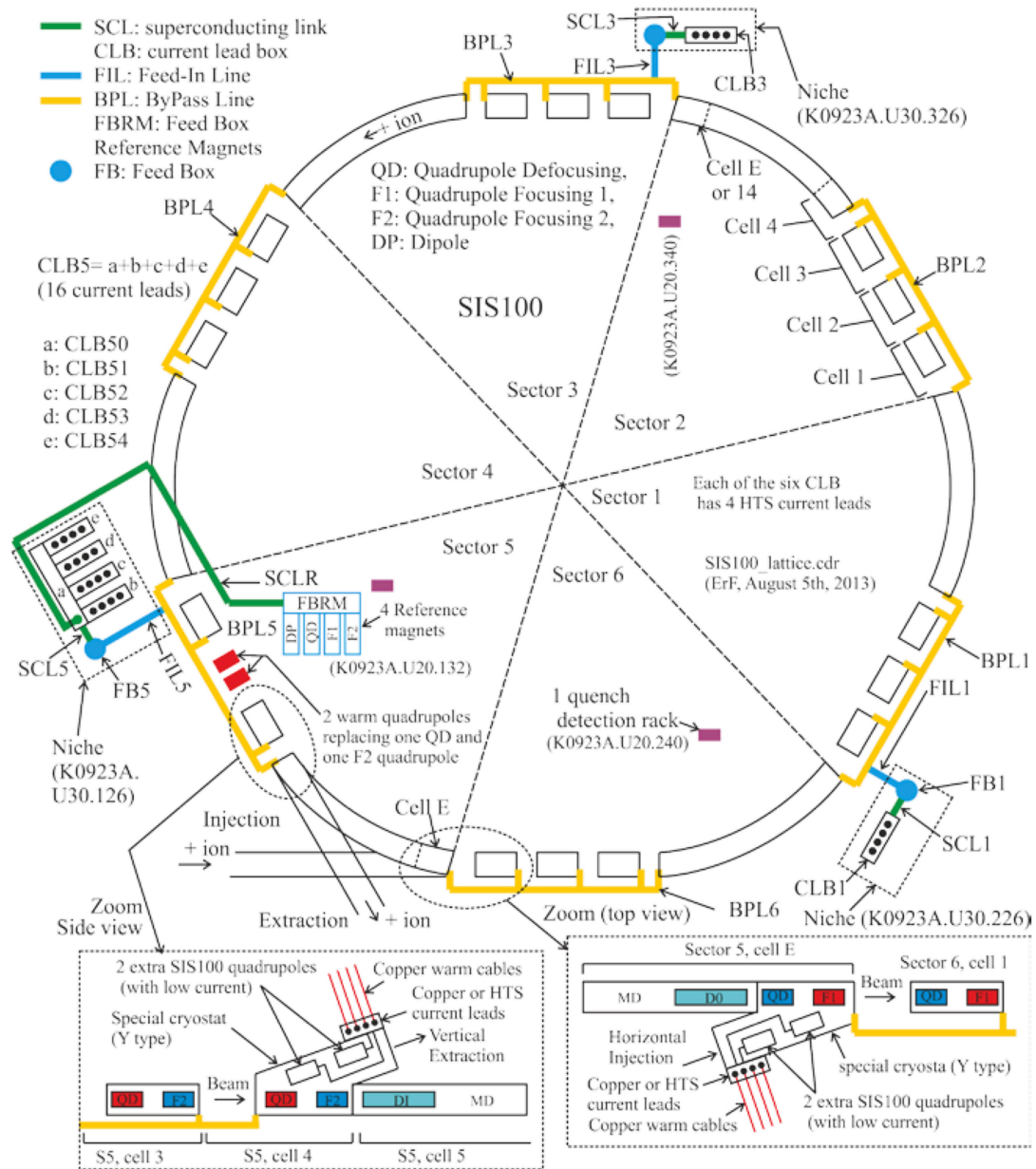
Fig.4.02 Schematic representation of the complex structure of the SIS100 ring accelerator. On the bottom, there is the enlargement of some modules.

The superconducting magnets within the quadrupole modules are produced at the JINR *Joint Institute for Nuclear Research* located in Dubna, Russia, and shipped to Bilfinger Noell in Germany for the installation into a cryostat with the addition of all the other parts needed by their usage. Once the modules are ready and before their final destination on the SIS100 ring accelerator, they have to be tested. The dipole magnets are tested at the GSI

laboratory while the quadrupole modules will be tested in the framework of collaboration between the GSI, INFN, and the University of Salerno. In this framework the THOR, *Test in HORizontal*, facility was set up in the campus area of the University of Salerno.

In the following of this chapter it will be described the verification activities and the test measurements on the dipole modules, carried at the GSI in Darmstadt, and the preparatory work is done in the Salerno laboratory, for setting up the experimental apparatus able to take the test required for the final verification of the integrity of the quadrupoles. [GM19]

The content of this chapter comes from two different experiences. The preliminary work at the Salerno laboratory, and during the first visit to the GSI laboratory, where I had the opportunity to collaborate with the technical staff of the cryogenic laboratory while doing the characterization of the dipole modules. Both experiences were useful for setting up the experimental apparatus able to take the test required for the final verification of the integrity of the quadrupoles. [GM19]

4.2   Testing of dipoles and the QDM at GSI

The SIS100 requires the presence of 108 dipoles and 83 quadrupole modules built with the superferric technology. All the superconducting magnets installed in the accelerator ring are used to control the beam trajectory. The role of dipole magnets is the bending of the particle bunches of particles into a circular trajectory. [SC14] [MR16] The quadrupole magnets are arranged in modules, the QDM, containing two main quadrupole magnets and other high order correction magnets. The role of these magnets is to correct and focus the beam. [ZL02] More details on the QDM modules will be reported in the following section.

The dipole bending is not constant because, while the beam particles circulate, the beam energy increases, and the dipole bending forces have to increase accordingly to the energy growth of the particles, to keep a stable trajectory. The dipole magnets generate a bending magnetic field that spans from $0.253\,T$, when the particle beam enters the ring, up to $1.9\,T$ when the beam energy reaches its maximum value. The maximum ramp rate is $4\,T/s$. The maximum current needed for reaching the maximum magnetic field is $13.2\,kA$. This current is fed into the superconducting coil with $0.56\,mH$ of inductance. Other relevant parameters of the dipole can be found in the following table [MR19]. An image of the internal structure of the dipole during the room temperature tests is shown in Fig.4.03.

SIS100 Basic Dipole Magnets Parameters		
Magnets Technology		Superferric
Number of magnets		110
Effective magnetic length	m	3.062
Radius of curvature	m	52.632
Bending angle	deg	3 1/3
Good field region (hor. x ver.)	mm x mm	115 x 60

SIS100 Basic Dipole Magnets Parameters (cont.)		
Nominal current	kA	13.2
Magnetic field strength	T	1.9
Magnetic field homogeneity		$< \pm 6 \cdot 10^{-4}$
Cycling rate	T/s	4
Inductance	mH	0.56
Mass	kg	1850
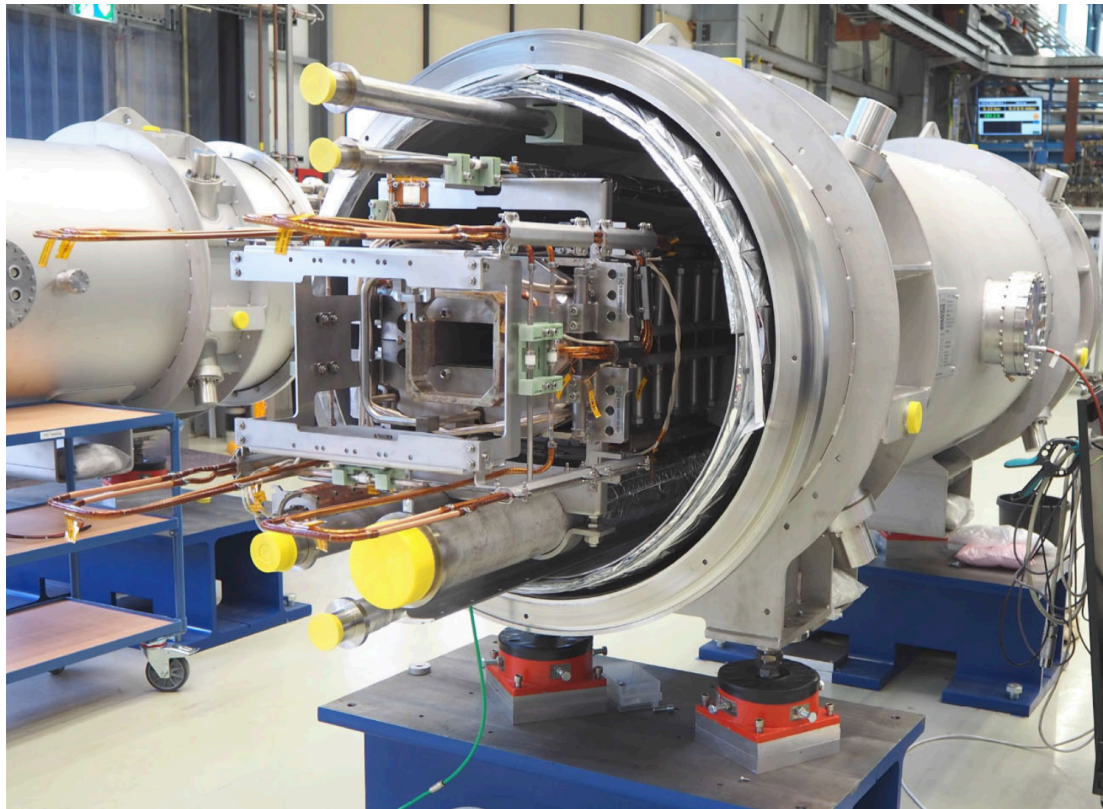
Fig.4.03 Dipole of the SIS100 series at the GSI test facility. The superconducting coil used in this dipole is a special Nuclotron conductor developed to be suitable for high currents in the presence of ac loss. [MR19]

The type of Nuclotron cable adopted was specially developed to be suitable for a high ac loss application. The conductor is shown in Fig.4.04.
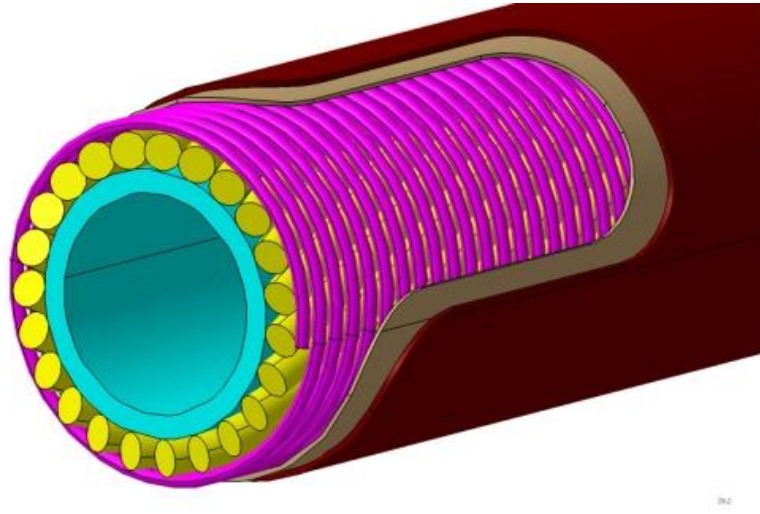
Fig.4.04 Picture of the Nuclotron cable witch highlights its main features. The $CuNi\,30$ tube with 4 mm diameter is surrounded by the $NbTi$ strands with the $CrNi$ fixation wire and wrapped with polyimide insulation.

It is made of 23 superconducting strands spirally wound on a $CuNi\,30$ tubes with a cross-section of $8.168\,mm^2$. Each strand is made of $NbTi$ filaments with a diameter of $2.9\,\mu m$. The total $NbTi$ cross-section is $0.2096\,mm^2$ with a copper cross-section of $0.2026\,mm^2$ and an overall cross-section of $CuMn$ filament barrier of $0.0905\,mm^2$. These values sum up to a strand diameter of $0.8\,mm$ and make a normal metal to the superconducting ratio of 1.4 with a copper resistivity ratio value of $RRR = 125.5$. The layer of $NbTi$ strands, surrounding the $CuNi\,30$ tube, is placed between two polyimide insulation layers and bounded by a spirally wound $CrNi$ fixation wire. The whole cable is finally covered with another insulation layer for a comprehensive insulation cross-section of $6.0696\,mm^2$. The $CuNi\,30$ alloy has been chosen to keep a balance between low ac loss and sufficient thermal conductivity.

The use of the Nuclotron cable has the advantage of a low hydraulic resistance provided by the $CuNi\,30$ tubes, around which the superconductor strands are wound.

The $NZPV$ values for this cable have been computed with a one-dimensional cable model and found in agreement with the experimental findings. The $NZPV$ behavior has been already fully characterized and found proportional to the current with a maximum speed under $30\ m/s$ for a current $I_0 = 14\ kA$. The dipole coil current decay has been already simulated with a current of $I_0 = 13.2\ kA$ and connected to its external resistive current dump with $R_d = 5.4\ m\Omega$, and a complete current decay under $300\ ms$ with a final temperature value of about $T \approx 330\ K$ has been computed. In these conditions, the maximum length of the quenched coil conductor would be less than $9\ m$ on each side. [SZ19]

This quenched length, compared to the typical dipole winding length of about $50\ m$, and permits to affirm that the quenching process would remain confined into a single dipole.

4.2.1   Vacuum and helium pressure tests

The dipoles, as well as the quadrupole modules, are cooled by mean of liquid helium that circulates on three main cooling circuits: the beam pipe chamber, the cold mass elements, and the external radiation shield. A schematic view and a CAD design of the position of these pipes, corresponding to each circuit is shown in Fig.4.05 with a short explanation of their role.
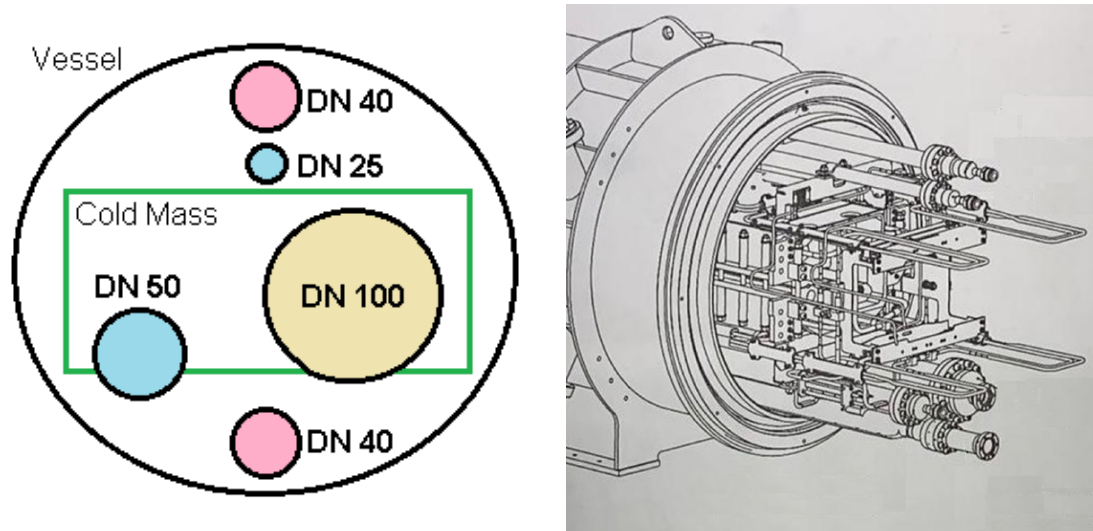
Fig.4.05 Schematic view of the cooling pipes of the dipoles and the QDM (Left).

A CAD design of the gas pipes entrance side, as seen on a dipole (Right).

The pipes shown in Fig.4.05 can be easily recognized based on their dimensions and position inside the vacuum vessels. The DN25 pipe is the cold gas input of the cooling circuit of the beam pipe. The cooling of the beam pipe is very important and requires a cooling circuit by itself. The DN50 pipe is another cold gas input that is used for cooling the superconducting coils with the forced flow of two-phase helium. The Nuclotron windings are cooled in parallel through the $4\ mm$ conductor tube shown in Fig.4.04. Then this helium stream will be brought back with a larger pipe diameter into the iron cold mass of the magnet to absorb the heat released there by the eddy currents. Both helium gas flows from the DN25 and DN50 pipes exit through the larger DN100

pipe. The two DN40 pipes are part of an independent circuit used to keep cool the thermal radiation shield.

Before starting the tests all these pipes are connected into the gas circuit as shown in Fig.4.06. The circuit connects through three valves the pipes with a helium gas bottle, a differential pressure gas meter, and a gas flow meter.
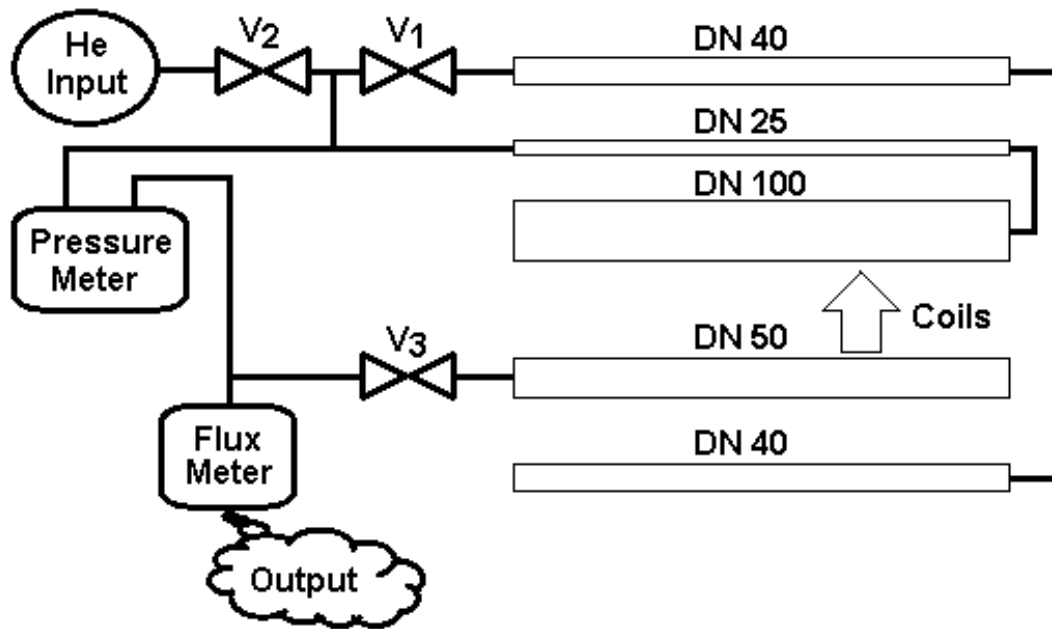
Fig.4.06 Schematic of the pipes used for the pressure and leak tests. The Pressure meter measures the differential pressure on the two inputs. The helium gas flows through the Nucletron coils from DN50 to DN100 pipes.

With these connections, all module pipes are connected in series and can be tested at the same time. A first test, on the module pipes, is done with the valve V_1 open and V_2, V_3 closed. The pipes are all pumped down through a leak detector, not shown in Fig.4.06, connected to the DN100 pipe. The small volumes should allow a fast pumping and a vacuum in the range of $10^{-7} \, mbar$ can be reached in a few hours. Once the vacuum limit is reached then the leak search can start. The search is done as usual with a portable helium bottle by spraying some helium gas on the flanges and the other connections. Once this test is passed the leak detector is disconnected and the pressure test can start.

As shown in the scheme of Fig.4.06 the pipes are filled with helium gas by closing the valve V_3 and leaving open the valves V_1, V_2 until the pressure of $20 \, bar$ is read on the differential pressure meter a GE Sensing Druck DPI 800/802. Once the value of $20 \, bar$ is reached the valve V_2 is also closed, the piping circuit is isolated and the pressure test can start. Usually, at the beginning of the pressure test, a reduction of the pressure within the circuit is observed. This initial reduction is due to the plastic deformation of the metallic piping and usually stabilizes in $3 \div 4 \, h$. After $12 \, h$ the test may be considered passed if the observed pressure drop from the pressure measured after the mechanical stabilization and the actual value is less or equal to $1 \, \%_0$. During the pressure test, it is possible to check the pipe flanges with a helium sniffer for ensuring the effective absence of leaks. Once the test is over, by opening the valve V_3 the lines can be depressurized. During this phase, it is possible to take advantage of the gas output for measuring the differential pressure through the circuit DN25, DN100, Nuclotron windings, and the DN50 pipe. The gas output goes through the gas flux meter, and its flow rate can be easily measured contemporary to the differential pressure. This measure of pressures and gas flow rates are essentially used for the measurement of flow impedance in the superconducting windings. This because, the measured value of the pressure drop on the gas circuit, is essentially due to the impedance of the Nuclotron windings because the other pipes of this series circuit have negligible impedance respect to the thin and long pipe inside the Nuclotron wire. The measure is not really accurate because while emptying, both the pressure and the flow rate changes. By closing the valve V_1 and opening the valves V_2, V_3 it is possible to do a more stable measure of the gas impedance. In fact, the pressure on the helium input could be regulated to any given value leading to a constant flow rate value that can be read more accurately. Typical couples of pressure drop and gas flow values measured on QDM windings are $\Delta p = 3 \, mbar$ and flow rate of $0.32 \, g/s$ or $\Delta p = 1 \, mbar$ and $0.14 \, g/s$.

The measure of the leaks of the beam pipe is very important for the accelerator and has to be in the range of $10^{-10}\,mbar\,l/s$ [FS14]. In order to keep its cleanliness, the beam pipe is pumped with a separate oil-free pumping system. If the limit vacuum is not satisfying then a suspicious of a leak arises. The leak tests on the beam pipe mounted on the QDM cannot be done as usual, because in this case the most parts of the beam pipe and many of its flanges are not easily reachable. In this case, an integral test is required. The integral test is done, by closing with a plastic bag, both sides of the vessel, and putting some helium gas inside. If a leak is present a leak detector placed on one of the beam pipe terminations will detect it.

4.2.2   Voltage tests on windings and other devices

The dipoles and the quadrupole modules besides the main superconducting coils contain many other devices such as thermometers, heaters, vacuum gauges, cryocatcher, and beam control devices. All these devices are needed for the correct module management and monitoring and all of them have to be tested. There are three different types of tests that have to be done on each device. The first is the continuity test, which ensures that the device is effectively connected to the plug from which the signals are taken. The second is the insulation test, which verifies that the devices are insulated respect to ground, and the third is the control that the device is effectively working as expected.

The order of execution of the tests is important. The insulation tests have to be made after the continuity tests because the measure of the insulation respect to the ground makes sense only if the device is effectively connected to its output. Otherwise, the tests, made on an open connection, would be correct even if the device were in contact with the ground. The functioning test has to be as the last test because it is necessary to control that the device is still correctly working after the application of the high voltages during the Insulation tests. In fact, a not correctly applied high voltage may cause severe damages to the device under test.

All devices are tested individually and, especially during the insulation test, in order to improve safety and avoid damages all the other devices, not involved with the device under test, all the other connections are grounded.

The technical staff, at the GSI laboratory, usually executes these tests by connecting the termination of all the signals with some ad hoc cable whose termination is selected by hand and connected to the instruments required for the execution of the test. An example of this methodology is shown in Fig.4.07 during the preparation of an insulation test. In this figure, it is possible to see several cables plugged on the access port of the module and, on the other side,

147

inserted into a box and then connected to the ground. The red and black cables ending with Crocodile Clips are connected to the Megger® S1-568 Insulation Resistance Tester, not shown in Fig.4.07. The black cable from the negative pole is connected to the ground on the vessel while the red cable from the positive lies on the cart waiting to be connected to the device to be tested. All the devices have to be tested and for each test, the cabling of the wires shown in Fig.4.07 has to be manually adapted to the required measure.
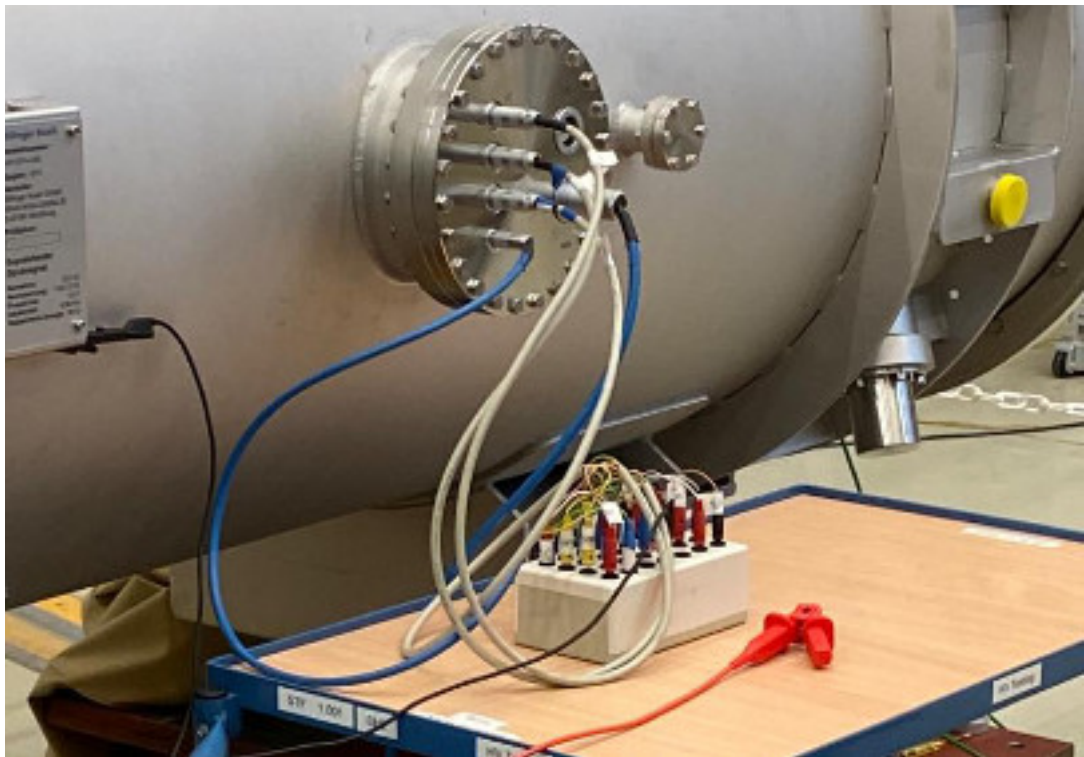
Fig.4.07 Insulation tests done with manual cabling method on a dipole. The black clip of the Megger® S1-568 Insulation Resistance Tester, not shown in the figure, is grounded on the module vessel. The red crocodile clip lies on the cart waiting to be connected. All the other devices are plugged into the gray box and grounded together.

In the following, these three types of tests are presented in some details for each type of device to be analyzed.

Bus bar and coils continuity test: This test aims to verify the electrical connection of the voltage taps on the bus bars and to the dipole or quadrupole coils connected to it. This test requires also the verification of the absence of

inversions of the voltage taps position on magnets. The test starts by connecting, with external jumpers, all the bus bars in series to a low voltage power supply. Voltages of about 5 V and few amperes do not hurt the Nuclotron cable even at room temperature. All voltages are read respect to the negative pole of the low voltage power supply and will increase as the position of the taps moves away from the negative pole. A position inversion of the voltage taps is detected by observing a not monotone increase in the increasing sequence of measures. At the end of the measure, the bus bar connections and the low voltage power supply have to be removed.

Current leads and corrector coils continuity test: This test is required only on QDM modules where these coils are mounted. Like the one previously described, the test needs a connection to a low voltage power supply for checking the correct assignment of voltage taps. However, in this case, no jumpers are needed since the QDM corrector coil and its current leads are already connected. The voltages have to be read in the order of increasing distances from the negative pole and the values have to be all monotonically increasing. The test must be repeated for each coil and the MID connection of the QDM module, usually less than five.

Two wires devices continuity test: The test, reads the electrical resistance across the two contact devices as PT1000 thermometers, thermocouples, and heaters. On a PT1000 thermometer, this value should be a little over $1\ k\Omega$ and thermocouples should behave as a short circuit, and only the resistance of the copper wiring should be measured. Like the PT1000, the values of the electrical resistance of the heaters have to be a little higher than their reference values.

Four wires devices continuity test: The test cannot simply measure the electrical resistance because these semiconducting thermometers do not return a predictable value of their resistance and the measure could damage them. The best that can be done is to plug the thermometer on its reader and only if the measure is incorrect, then act with further investigations, like the

measure and comparison of the resistances of the wiring couples V^+I^+ and V^-I^-. These connections join together their terminations on the thermometer, and the measuring currents do no affects the semiconductor.

Bus bar and main coils, high voltage insulation tests: This test, verifies the insulation of each bus bar respect to ground. The tests verify also the insulation of the dipole or quadrupole coils connected to the bus bars. The test is done by connecting the bus bar voltage tap to the positive output of a Megger® S1-568 Insulation Resistance Tester with its negative grounded together with all the other wires. An increasing sequence of voltages is applied in three steps of $600\,V$, $1500\,V$, and $3000\,V$. The voltages are applied for 2 minutes for each value. The detection of a leak at lower voltage interrupts the insulation test procedure. During the application of the voltages, the Megger® autonomously measures and stores the values of both the insulation resistance and the leakage current. This test must be repeated, one at a time, for all eight bus bars of the dipoles and QDM modules, and is considered passed if all the final insulation resistances are above $1\,G\Omega$.

Current leads and corrector coils, middle voltage insulation tests: This test is required only on the QDM modules and is similar to the previous insulation test and done in the same way. The only difference is the increasing sequence of voltages, which in this case is applied in steps of $200\,V$, $500\,V$, and $1100\,V$. Also in this case the voltages are applied for two minutes for each value, and both the insulation resistance and the leakage current measured by the Megger® are recorded and stored. Because of the internal connections, only one measure for testing the insulation of each corrector coil circuit is needed. Another measure is needed for the MID connection of each coil.

Two and four wires low voltage insulation tests: This test aims to verify the insulation respect to the ground of both the two and four wires devices. Before starting the test, in order to avoid damages, all wires of the device under test are joined together. The positive pole of the Megger® Insulation Resistance Tester is connected to the device under test and the negative pole,

as usual, is grounded with all the other devices. The voltages are applied by the Megger® for one minute to the device under test. The value of the applied voltage depends on the device to be tested, and in particular, is $50\ V$ for all the thermometers and thermocouples and $100\ V$ for the heaters. In both cases, only the final value of the insulation resistance and the leakage current is recorded. The test is considered passed if for each device the insulation resistance is above the value of $100\ M\Omega$.

Final control tests: This test is a repetition of all the continuity tests exactly as described above with the addition of the functionality test for the temperature-controlled heaters. In fact, these heaters can be well insulated and perfectly functioning but mechanically disconnected from the device they should warm-up. This anomaly is checked by visual inspection where this is possible. Otherwise, the way to test the functioning of these devices at room temperature is to apply to the heater about 10% of their nominal electrical dissipation power and to observe the expected temperature increase on the thermometer thermally linked to this heater. If the temperature increase is not observed, then the applied power can be further increased before the unavoidable visual inspection, even if the heater has been installed into an inaccessible location.

The strategy of the test sequence on the dipoles and the description of selected measurement systems are presented here [MR19].

4.3   The quadrupole modules

The SIS100 ring quadrupole magnets are built with the superferric technology. On any single magnet, the maximum current is $8000\,A$, its inductance is $0.91\,mH$ and a total ac loss, per cycle of $32.3\,J$.

Other relevant parameters of the quadrupole magnets can be found in the following table, while a design of a quadrupole module, containing two quadrupole magnets and other corrector magnets is shown in Fig.4.08.

SIS100 Basic Quadrupole Magnets Parameters		
Magnets Technology		Superferric
Number of quadrupole magnets		168
Magnetic Field Gradient	T/m	32
Maximum Ramp Rate	T/m/s	61
Current	A	8000
Inductance	mH	0.91
Total $a.c.$ loss per cycle	J	32.3
Effective field length	m	1.1
Pole Aperture	mm	100
Mechanical length (iron/cold mass)	m	2.686
Vacuum chamber aperture (h/v)	mm^2	130 x 65

The quadrupole modules are made of two quadrupoles unit and up to five multipolar magnets, all integrated into one cryostat by Bilfinger Noell.

The Nuclotron cables used on the quadrupole windings are similar to the one used for the dipoles, with 28 strands instead of 23. A more detailed design of this cable structure is reported in Fig.4.09 with all the other relevant dimensions.

During one of my visits to the GSI laboratory, the First of a Series quadrupole module arrived at the GSI laboratory. In the following days, this module was unpacked and mounted with its supports on the track guide of the cryogenic test station for the room temperature preliminary tests.
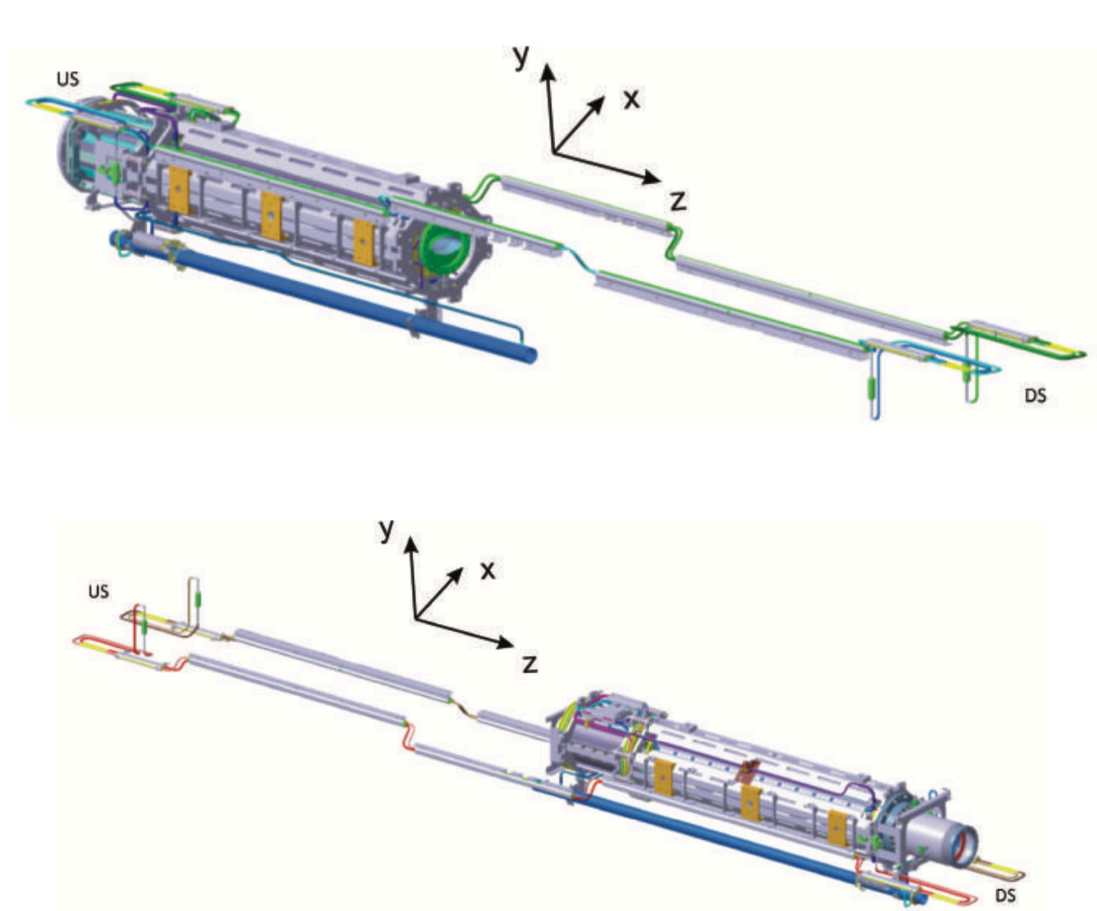
Fig.4.08 The two quadrupole units on the module, containing two quadrupole magnets and up to five other high order corrector magnets. The module image has been divided into two parts for improving its clearness.

On this occasion, I participated in the continuity and insulation tests of the superconducting windings and all the other accessories, such as thermometers, and heaters, already installed into the quadrupole module.
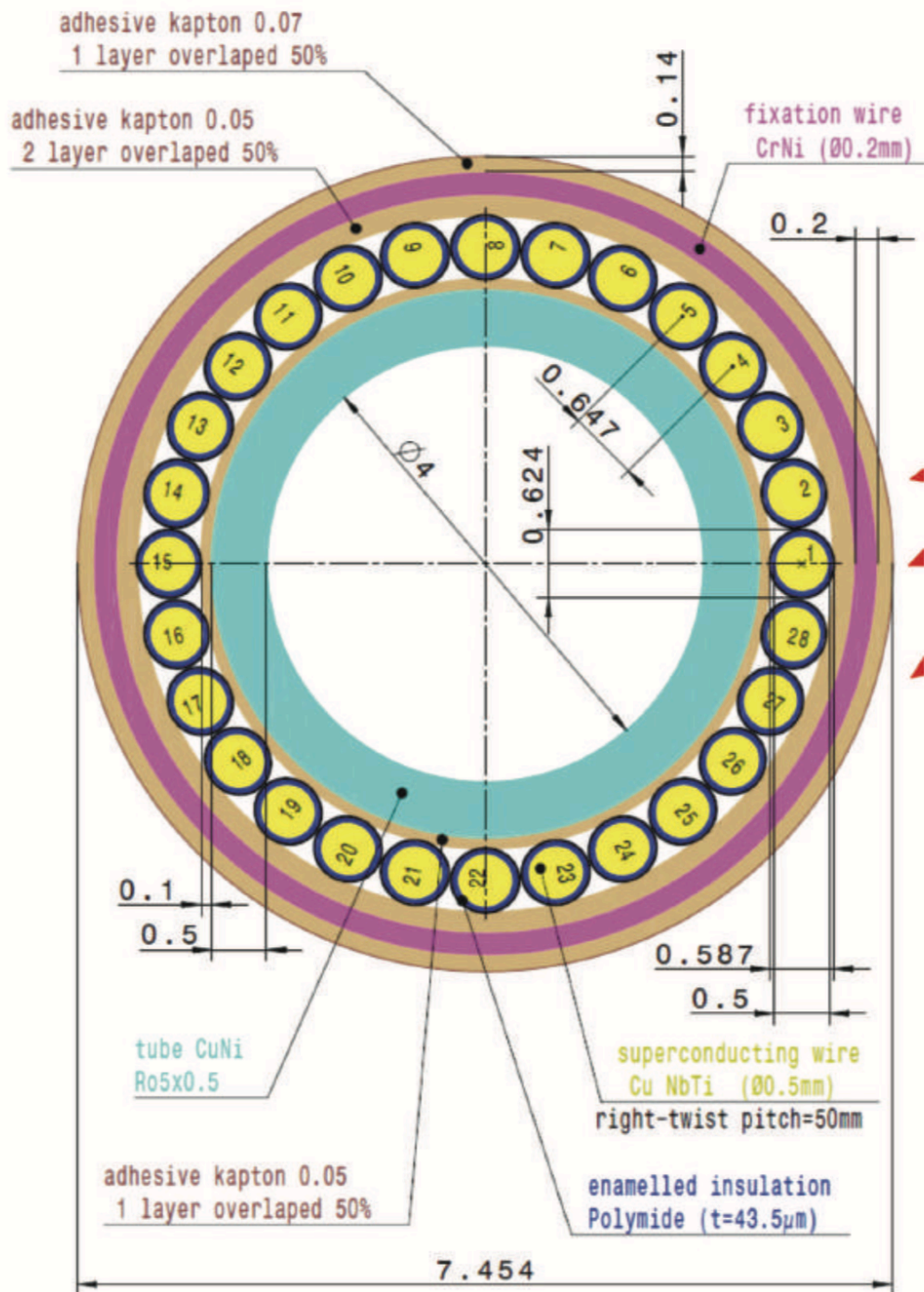
Fig.4.09 Special Nuclotron cable for corrector magnets with 28 insulated strands. In the chromaticity sextupole, steering magnet (vertical and horizontal coil) and multipole corrector (quadrupole coil, sextupole coil, and octupole coil), one strand, out of 28 coil strands, is reserved for quench detection. Other details can be found on page 24 of ref. [QM16]

154

The first test was a continuity test of all wirings. This simple test, performed with a laboratory Ohmmeter is important because it permits to detect, in advance, one or more disconnections that could cause anomalies. Thanks to this preliminary test, a few devices were found unplugged and then fixed.

The four-wire thermometers connection, have been functionally tested by plugging them on their readers. Since all thermometers reported the room temperature value, the test was considered passed. On the other two-wire devices the test was considered passed because the measured resistances were found to be compatible with the expected values.

The following low voltage insulation tests have done by connecting the Megger® S1-568 Insulation Resistance Tester to all electronic devices as described in the previous section. This test was considered passed because the resistance toward the ground was higher than $100\ M\Omega$.

The high voltage insulation tests were applied only to the taps on superconducting coils and bus bars. As described in the previous section after the recording of the environmental temperature and humidity, a high voltage was applied on each tap. The test was considered passed because, at the end of the test, the insulation resistance was greater than 1 Giga Ohm for any voltage step.

In the end, the continuity check was repeated for ensuring the absence of eventual damages caused during the insulation tests.

4.4   The QDM planned test procedures

The agreement between GSI and the INFN Sezione di Napoli (Gruppo Collegato di Salerno) provides the verification of 81 QDMs. This test will be considered as a final test prior to the installation into the SIS100 accelerator. The QDMs are not all identical but can be divided into groups of QDMs with identical characteristics and many similarities with the elements of the other groups. The following table reports the names of the QDM groups with the number of units appertaining to these groups. The first digit in the short name denotes the type of focusing quadrupole, either 1 or 2. The characters after the decimal point denote the cell numbers in the ion optical lattice of the SIS100. The SIS100 ring consists of 6 sectors with 14 cells in each sector. The cells are numbered from 1 to E according to the hexadecimal notation. The meaning of the detailed long names can be found on Ref. [MR14].

QDM Identification Name		
Detailed Long Name	Short	Quantity
VQD-CR-SF2B	2.5	6
VQD-CR-SF1B	1.7B	12
BQD-C-SF1H	1.6A	12
BQD-C-SF2H	2.8C	12
BQD-CR-SF2J	2.9D	12
QDBb-T-SF2Mb	2.4	5
MQDb-C-SF1Bd	1.E	5
QD*B-TRP-SF1*/2*	2.123	14
QD*Bs-TRP-SF2*s	2.13s	3

The main purpose of the test will be the check at warm, cold, and again at warm temperatures, the electrical and mechanical integrity of each module, its leak tightness, the test of the cryocatcher, and beam position monitor

functionality. The testing program does not include the power test of the superconducting quadrupoles because the single magnet units have been already tested at the JINR laboratory in Dubna before the integration in the module. The tests on the other corrector magnets are limited to the power test of the corrector magnets and their HTS current leads.

The standard test sequence on each QDM listed above is part of the agreement between GSI and the INFN unit in Salerno. Each module has to be tested following a well-specified procedure that provides the following steps:

Step 1: The cryostat is on the bench: open, warm, and unplugged
1. Protection removal and Incoming inspection of the QDM
   a) Visual inspection and check of shock indicators
   b) Download of the accelerometers data
   c) Accelerometers data verification
   d) Check the completeness and CID numbers
   e) Check the delivered FAT documentation for completeness
   f) Unload the QDM from the truck and second visual inspection
2. Check of the mechanical interfaces with mechanical templates
3. Room temperature preliminary electrical tests
   a) Electrical continuity and voltage tap sequence verification
   b) Sensor integrity and electrical resistance measurements
   c) Integrity of heaters circuits
4. Pressure leak test of the helium processing lines
5. Test of the mass flow rate within the QDM units and the beam tube cooling lines
6. Electrical tests on the Beam Position Monitor
7. Electrical tests on the cryocatcher
8. Mounting on the test bench and hydraulic and UHV connections

In this first step, the QDM arrives at SAT, and before the unloading procedure, the visual inspections verify the presence of damages due to the delivery. Then the first electrical tests are done at room temperature.

Step 2: The cryostat is on the bench: open, warm, with hydraulic and vacuum-plugged
1. Electrical insulation tests (1)
   a) High Voltage insulation tests on the quadrupole coils
   b) Medium Voltage insulation tests on corrector magnets

      c)   Visual Low Voltage insulation tests on sensors and heaters
      b)   Insulation test with cross check among some selected circuits
2.   Continuity test of sensor wires and duplicate voltage taps
3.   Vacuum leak test of the helium process line connections
4.   Pumping, vacuum leak test, and Residual Gas Analysis, RGA on the beam tube
5.   Connection to feed & end box and start pumping the insulation vacuum

      In this second step, the QDM is mounted on the test bench and the electrical tests can begin. During the insulation tests the QDM, because of the presence of high voltages, a security procedure is applied and some barriers have to be installed to avoid accidental dangerous contacts.

Step 3: The cryostat is on the bench: closed, warm, and under UHV vacuum
1.   Electrical insulation tests (2)
      a)   High Voltage insulation tests on the quadrupole coils
      b)   Medium Voltage insulation tests on corrector magnets
      c)   Visual Low Voltage insulation tests on sensors and heaters
      b)   Insulation test with cross check among some selected circuits
2.   Test of the instrumentation
3.   Leak test & RGA of the cryostat vessel with He lines evacuated
4.   RGA of the cryostat vessel with He lines under pressure
5.   RGA of the UHV beam tube during operations
6.   Start the cool-down operations

      The electrical insulation tests are repeated under vacuum conditions. The pressure values have to be accurately verified in order to avoid electrical discharges that can compromise the quality of the magnet insulation.

Step 4: The cryostat is on the bench: closed, cold, and under UHV vacuum
1.   Analysis of temperature & vacuum behavior during the cool-down
2.   RGA monitoring of the cryostat vessel (pumped up to 40K)
3.   RGA monitoring of the beam tube (pumped up to 20 K)
4.   Powering current leads heaters, measure the power consumption with coils off
5.   Electrical insulation tests (3)
      a)   High Voltage insulation tests on the quadrupole coils
      b)   Medium Voltage insulation tests on corrector magnets
      c)   Visual Low Voltage insulation tests on sensors and heaters
      b)   Insulation test with cross check among some selected circuits
6.   Test of the instrumentation

7. Safety test of quadrupole and interlocks before powering corrector magnets
8. Checking current leads voltages while corrector magnets are powered
9. Activation of γ-t magnet powering
10. Test of the cryocatcher integrity and check of its heater
11. Beam Position Monitor integrity test
12. Flow measurements and in/out temperature measurement at cold steady state
13. Start warm-up operations
14. Leak test of beam tube at cold during natural warm-up

This is the most important step of the whole testing procedure. The QDM is under vacuum and also at cryogenic temperature and the corrector magnet may be energized. In this condition, many tests are requested and the stability of both the vacuum as well as the temperature has to be monitored.

Step 5: The cryostat is on the bench: closed, warm, and under UHV vacuum
1. Continuous monitoring RGA in the isolation vacuum and beam tube vacuum
2. Electrical insulation tests (4)
    a) High Voltage insulation tests on the quadrupole coils
    b) Medium Voltage insulation tests on corrector magnets
    c) Visual Low Voltage insulation tests on sensors and heaters
    b) Insulation test with cross check among some selected circuits
3. Vacuum leak test of the helium process line
4. Pumping and vacuum leak test and RGA analysis of the UHV beam tube
5. Disconnection from feed & end box and hydraulic and UHV connections
6. Electrical insulation tests (5)
    a) High Voltage insulation tests on the quadrupole coils
    b) Medium Voltage insulation tests on corrector magnets
    c) Visual Low Voltage insulation tests on sensors and heaters
    b) Insulation test with cross check among some selected circuits

The refrigeration was switched off at the end of step 4 but the QDM and in particular its magnets are still cold and the status of the quadrupole has to be monitored because anything can happen, the thermal stress inside the magnets could have caused damages that have to be revealed soon.

Step 6: The cryostat is on the bench: open, warm, and unplugged
1. Travel preparation of the QDM for shipment
2. Final controls of the SAT documentation
3. Load QDM on truck

The electrical insulation tests are repeated five times both in the worm and in cold conditions. The availability of an automatic measurement system for the electrical insulation measures would be a great help during the measures, especially when the QDM is cold and many other instruments and parameters have to be controlled.

4.5 The INFN test facility laboratory

The brand new INFN test facility laboratory has its own building realized in the campus area at the University of Salerno. The structure was available from February 2015, after the building commissioning.

The laboratory spans over a length of $30\,m$, a width of $15\,m$, and a height of $10\,m$, with an indoor available surface of $450\,m^2$. Besides this area, two additional side rooms, each one, with $3\,m$ height and a surface of about $40\,m^2$, are also available. In addition to the main access, there is a front gate entrance large enough to allow truck access. A side view of this laboratory is shown in Fig.4.10.

Fig.4.10 External view of the INFN Laboratory built on the University campus. On the right the water-cooling tower and the helium and nitrogen tanks. Besides the laboratory, there is also the $196\,kW$ screw compressor.

The laboratory is equipped with a 20 tons crane with $9\,m$ clearance under the hook. The standard fast and slow movements are compatible with the safe operation modes for delicate instruments. The crane can operate on about 95% of the indoor available laboratory surface. This crane will be used to load and unload the quadrupole modules from tracks, directly inside the laboratory.

On the backside external area of the shed, partially shown on the right of Fig.4.10, some technical services have been installed. There is a $300\,kW$

evaporation tower that provides the cooling water for the $200\ kW$ helium screw compressor placed under the sheet metal roof, the $30\ m^3$ helium gas storage tank, the liquid nitrogen cryogenic reservoir, and the dry air compressor. Large spaces around the shed are still available for further expansions.

A dedicated $16\ kV$ medium voltage electric substation provides a power of $1.2\ MW$ for the scientific activities. This electric power may be upgraded up to 2.5 MW. The indoor installations cover less than half of the surface, allowing enough room for activities in the other half.

4.6   The cryogenic refrigeration plant

The laboratory is equipped with the largest helium standard cryogenic refrigeration plant, LR208R, manufactured by Linde Kryotechnik. Its configuration is customized for the widest range of applications. The actual configuration includes a helium sub-cooler stage for supercritical He, a separate Joule-Thomson liquid port, an internal gas purifier, and an $80\,K$ absorber. Recently an external liquid nitrogen trap has been introduced to easy the purification process of processed gas.

In the refrigeration mode, the cryogenic plant can deliver a single-phase stream of supercritical helium gas at $4.5\,K$ and pressures up to $7\,bar$ with a maximum gas flow of about $15\,g/s$, thus the refrigerator can deliver an isobaric power of $200\,W$ at $4.5\,K \div 6\,K$, plus an additional $500\,W$ of shield flow at $60\,K \div 80\,K$, while also providing a cold $1.5\,g/s$ helium flow at $4.6\,K$, returned to the refrigerator at room temperature. This latter stream will be used if needed to cool down the current leads returning the helium gas directly to the warm side low-pressure suction, instead of passing through the internal heat exchangers.

In liquefaction mode, with the purifier, the Cold-Box can operatively produce up to $120\,l/h$ of liquid helium.

The whole refrigeration plant is controlled and monitored with a Linde standard controller based on a dedicated computer running the SCADA Supervisory Control And Data Acquisition SIMATIC WINCC from Siemens.

An image of the cryogenic refrigerator is shown in Fig.4.11 with a transfer line to a Test-Box.

The available helium stock is stored in the external helium storage vessel, whose capacity is $30\,m^3$ at the pressure of $10\,bar$ for a total volume of $300\,m^3$ of 5.5 purity grade helium gas. In addition, 40 high-pressure cylinders, at $200\,bar$, provide additional $400\,m^3$ of pure helium backup gas.

Fig.4.11 The LR280R cryogenic refrigerator, produced by Linde Kryotechnik, is connected to the Cold-Box through the cryogenic transfer pipe.

The $196\ kW$ SFC screw compressor, with the full speed of $1500\ rpm$ can provide about $70\ g/s$ of gas flow at a maximum pressure of $11\ bar$. The SFC (Static Frequency Converter) electronic controls the gas flow through the compressor speed. The speed can be dropped up to $750\ rpm$ reducing the input power to about 50%.

On the helium process pipes, during the purging procedures, the external liquid nitrogen absorber speeds up the gas contamination removal. A dedicated gas analyser and Multi-Component Detector of nitrogen and moisture, provide the contaminants monitoring in 5 selectable zones of the helium refrigerator.

Further performance improvements were obtained by the liquid nitrogen transfer-line connected to the liquid nitrogen tank.

4.7 The laboratory mechanical interface for QDM tests

The quadrupole magnets are fixed into one horizontal cryostat and they have to be connected to the cryogenic refrigeration plant through a Feed-Box, and a cryogenic transfer line. On the other side of the horizontal cryostat, there is an End-Box containing all the needed cryogenic bypass lines that will close the module cryostat. In Fig.4.12 it is shown the final design of the full test facility.

The Feed-Box cryostat is where the hydraulic and electrical connections pass through to get to the cryogenic environment. On the Feed-Box top flange, two high current leads could be fitted, to deliver the electrical power at low temperature, as well as valves, electrical, vacuum, and gas feedthrough.

We adopted in the test line design similar to the STF cryogenic boxes designed at the GSI by C.Schroeder and H.Kollmus [SC19]. The wide side accesses in the Feed-Box and the End-Box will allow a comfortable mechanical assembly between the Feed-Box and the QDM. The Feed-Box will also provide the vacuum pumping system and analysis, and will also contain the cold flow meters.
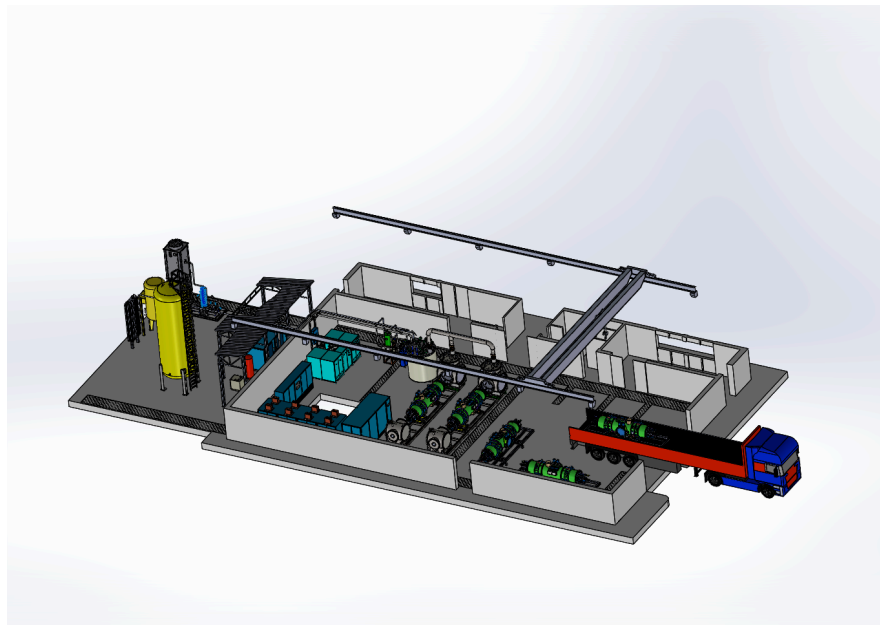

Fig.4.12 The 3D view design of the laboratory installations layout.

The complete cooling scheme, connecting the QDM to the Cold-Box through the Feed-Box and capped with the End-Box is reported in Fig.4.13. In the Feed-Box the forward 4.5K flow is split into cold mass and beam pipe flows. Two mass flow meters are installed on this line in order to measure the actual mass flow rate. The Coriolis measure the magnets circuit flow and WekaSense® the beam pipe flow. The V5 and V6 valves are for having a suitable path in the warmup cycles.
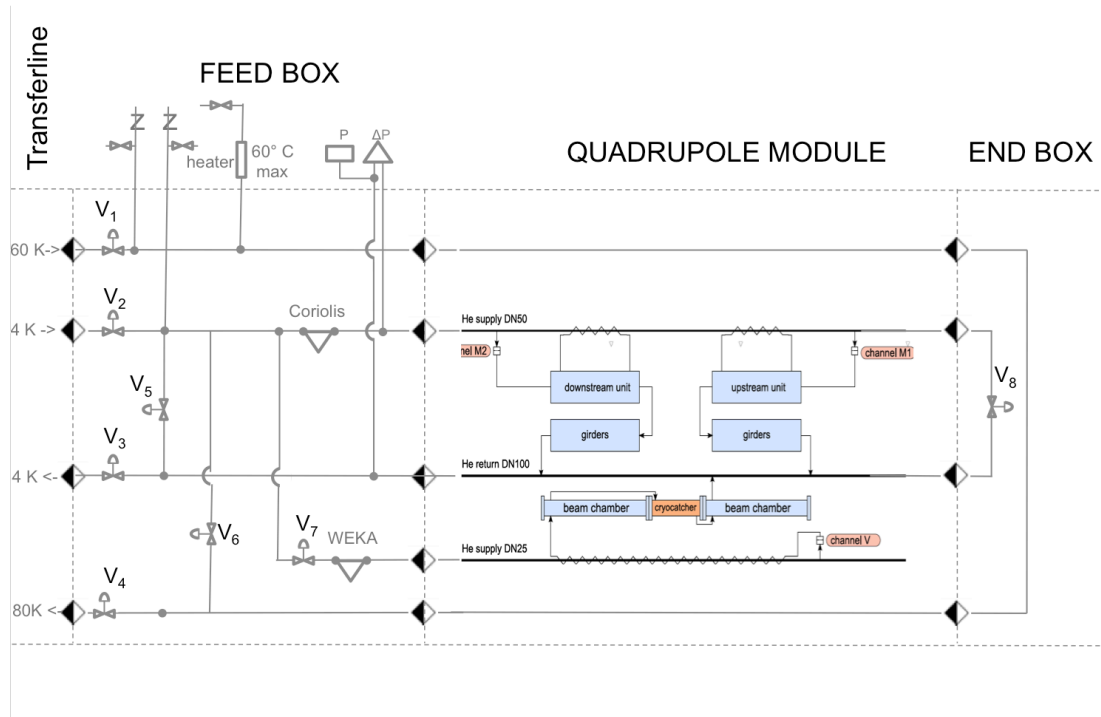
Fig.4.13 The complete scheme of the cooling piping connection of the QDM to Cold-Box through the Feed-Box and capped with the End-Box.

One of the needs of the test program is to keep the scheduled timeframe of the FAIR program. In order to speed up the testing time, it is planned to set up a second test line. However our Cold-Box cannot support independent cool-down and warm-up of two testing lines, but only a parallel operation is possible, thus the operational features of the facility are not improved of the same factor. Even with this limitation, the addition of a second line can significantly improve the test rate.

Pumping system on insulation vacuum. The QDM modules share the vacuum with the Feed-Box and the End-Box. The Feed-Box is equipped with a pumping system made of an oil-free Agilent IDP-15 scroll pump with a pumping speed of 15 m^3/h, an oil-free Leybold Dryvac screw pump with pumping speed of 100 m^3/h, and an Agilent V551 TMP, Turbo Molecular Pump, with a pumping speed of 600 l/s. The End-Box is equipped with TwisTorr 304FS TMP with a pumping speed of 300 l/s and an oil-free Agilent IDP-7 scroll pump. The screw pump is first used to pump down the system from normal pressure to a few $mbar$, and the TMP will then be started with its foreline scroll pump. At this stage, the screw pump will be switched off.

The layout of the pumping system is sketched in Fig.4.14. The standard foreline and pumping line are controlled with electro-pneumatic valves, an ISO F 160 gate valve on the TMP, and a 90° KF40 valve on the foreline.
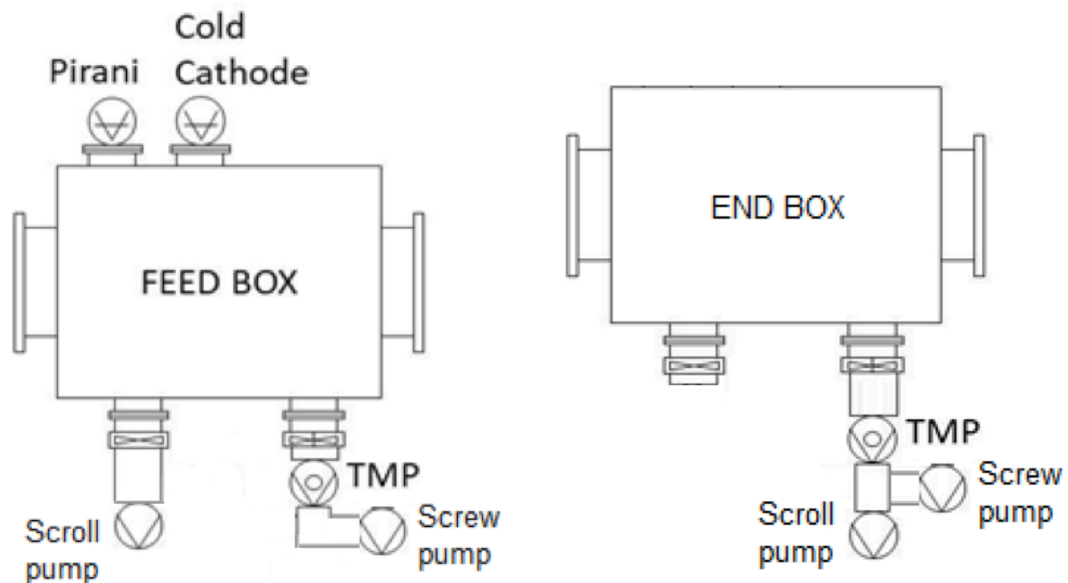

Fig.4.14 The pumping system with all the pumps and the pressure gauges used in the Feed-Box (left) and the End-Box (right) isolation vacuum.

The Agilent XGS-600 vacuum reader and controller manage the automatic switch between the valves. There is a ConvecTorr by Agilent Pirani gauge on the foreline, and, on the top flange of the Feed-Box, another

ConvecTorr by Agilent Pirani gauge with an IMG 100 Agilent cold ionization gauge. The vacuum meter holds the setpoint pressures to switch the valves and safely operate the ionization gauge. [FR99]

The test of the insulation vacuum tightness, as well as the monitoring of the residual gases, will be performed according to the GSI prescriptions.

The vacuum quality control is achieved by using an RGA Residual Gas Analyzer (Stanford Research System RGA 100, with faraday cup). This device works from 1 to 100 amu Atomic Mass Units with a resolution better than $0.5\ amu$ at 10% peak height. As the RGA starts operating from about $10^{-5}\ mbar$ we put a differential vacuum system to perform a residual gas analysis starting from higher pressures. The End-Box vacuum is connected to RGA through a needle valve. The differential RGA pumping system is made of an oil-free pumping system (Dry Scroll IDP-3 and 74FS Turbo Pumps and a Multi-range gauge FR700 all provided by Agilent).

Pumping system on the beam pipe: The test of the beam pipe vacuum tightness as well as the monitoring of the residual gases will also be performed according to the GSI prescriptions. The Ultra High Vacuum, UHV is foreseen in the beam pipe in order to achieve a good beam lifetime and to avoid ion trapping. Due to specific requirements, this pumping system must be completely oil-free. The sealings and the fittings of this component will be made of metal gaskets on the CF ConFlat® flange type. We will put an Agilent Twist Torr 304 TMP, with a CF100 flange, followed by an Agilent IDP 15 dry scroll pump with a pumping speed of 15 m^3/h. During the leak tests, an oil-free helium leak detector must be connected to the TMP exhaust. The pumping layout system on the beam pipe is reported in Fig.4.15. The pressure is measured by an MKS cold cathode 422, integrated on the beam pipe, and read by the controller 937B already used for the insulation vacuum.
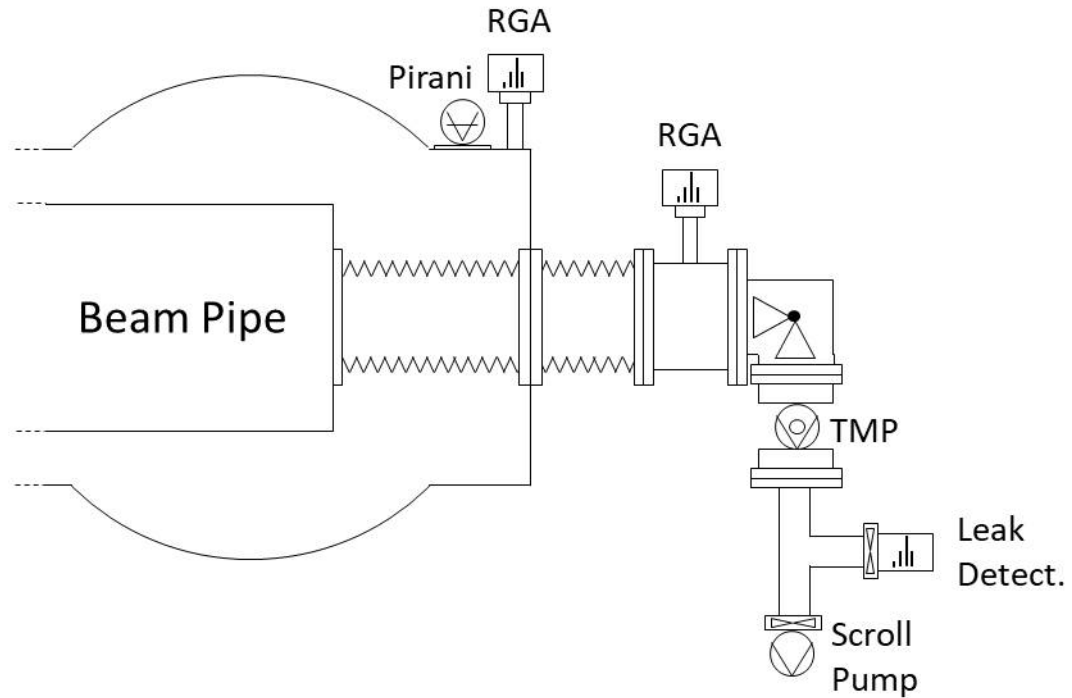
Fig.4.15 The pumping system to be used in the beam pipe isolation vacuum.

The residual gas in the beam pipe will be monitored using another Stanford Research System RGA 100 with a Secondary Electron Multiplier, SEM. The analysis will run continuously on the warm side connection of the beam pipe, including the cool-down phase. The SEM detector improves the minimum detectable partial pressure up to $5 \cdot 10^{-14} \, mbar$. The TMP valve will be kept closed as long as the beam pipe temperature is below 20K.

Other devices to be used for the QDM tests. According to the GSI requests, during laboratory tests, as shown in Fig.4.13, two cryogenic mass flow meters were installed on the $4.5 \, K$ cold flows of supercritical helium entrance. The CMF025 Coriolis manufactured by Emerson and the WEKA Sense® manufactured by Weka AG.

The Coriolis meter is based on the principles of motion dynamics. When the process fluid enters the sensor, it is split. During the operations, a drive coil

stimulates the tubes to oscillate at the natural resonant frequency. As the tubes oscillate, a sine wave signal is generated on two pickup coils. These signals indicate the motion of one tube relative to the other. In the absence of flow, the two signals are in phase. The phase shift between the two sine waves is directly proportional to the mass flow rate. The phase shift signal is processed by the electronic and the firmware included on this instrument. The mass flow rate value is displayed on the instrument and is also available on its RS485 standard computer interface. Many parameters can be tuned through the computer access on this interface. The maximum mass flow rate of our device is $25\,g/s$. The mass and volume flow accuracy for liquid is $\pm 0.10\%$ of the rate while the mass flow accuracy for gas reduces to $\pm 0.35\%$ of the rate.

The WEKA SENSE is a self-calibrating thermal mass flow meter, also known as a calorimetric flow meter. It consists of an external electronic unit and a compact sensor that is integrated into the helium cold line. Measurement range is up to $12\,g/s$ in the temperature range between 3K and 100K. Measurement accuracy, under stable operating conditions, is better than 1% of the actual flow rate. [GR14]

Within the standard cold tests program, agreed with GSI, is includes the powering of corrector magnets, in dc mode, to test their $250\,A$ HTS Local Current Leads, LCL. To perform these tests, we procured from CRYOGENIC Ltd. a reversible superconducting magnet power supply. This four-quadrant power supply, with an output of $\pm\,320A$, and a compliance voltage of $10\,V$ has thermal output stability better than $5\,ppm/K$ with a 20-bit resolution. This instrument can be operated manually via the front panel or under computer control by using one of the two USB or RS232 available interfaces. A quench detection system is built into the power supply firmware and an additional quench detection system may be used. For the safety of LCL, we will use the

Danfysik four-channel board Quench Detector System, connecting the corrector coil and its two LCL at the same time.

Another important device installed on the quadrupole modules is the cryogenic BPM Beam Position monitor. The BPM is a non-intercepting device that provides a sensitive online control of the beam center of mass. The closed orbit feedback uses the beam position readings from all 84 BPMs to calculate magnetic corrector settings on the ms time scale. The integrity tests of the BPMs and the Cryo-catchers, installed in each QDM, require a Network Analyzer with Time Resolved Domain feature.

This type of measure will be repeated at the INFN laboratory in Salerno by using a Rohde&Schwarz R&S®ZNB 4 Vector Network Analyzer. This instrument with a frequency range from $9\,kHz$ up to $4.5\,GHz$ and dynamic range up to 140 dB has four input channels with two independent generators and typical temperature stability of $0.01\,dB/°C$. The included time domain reflectometry option will be used to check the QDM integrity of the components under test.

On each quadrupole module, there are up to five high order corrector coils. These coils winding are feed through LCL. As discussed in Sec. 3.1, each of them is equipped with two heaters and a PT1000 platinum resistive thermometer. The GSI requires an analogic control of the heaters current, and the registration of the heaters dissipated power when the top LCL temperature is below the room temperature. The Institut für Luft und Kältetechnik gGmbH - ILK Dresden, developed a compact eight-channel thermostat card, able to continuously change the value of the electrical power. The ILK card is fully programmable through an RS485 standard interface, so all the available values can be accessed by our PXI computer.

QDM insulation tests are also sensitive to room temperature and humidity. In the INFN laboratory, an LKM-455 a Thermo Hygrometric probe, provided by LKM Electronics GmbH will be installed. This hybrid instrument will continuously measure the environmental parameters and can be used to log both temperature and humidity during the QDM tests. The temperature sensor covers the temperature range of from $-20 \div +80\,°C$ with a sensitivity of $0.5°C$, while the humidity probe can measure the relative humidity of the air in the $0 \div 95$ % range with an uncertainty better than $3\%\,RH$.

4.8 The Paschen effect

The measures of leakage currents in the insulation tests when performed in a vacuum environment have some critical aspects. Namely, there is the possibility of having a leakage current by the air ionization. This effect is generated when there is a voltage difference between two electrodes in a volume filled with specific gas pressure. In both cases, the presence of the voltage creates and accelerates free electrons. If the energy gained by these free electrons is larger than the ionization energy, it begins an avalanche effect. The discharge inception voltage depends on the gas ionization energy, its pressure, and the distance between the electrodes. In fact, for a given gas, in a high vacuum, the scattering probability is small unless there are very long distances to be traveled before a successful scattering. On the opposite, if the gas pressure is high, the mean free path of the free electrons is small and they do not get enough ionization energy from the voltage unless this voltage is not very large. A German physicist, Louis Carl Heinrich Friedrich Paschen, known for his work on electrical discharges, discovered the now widely used Paschen curves. In particular, he found that there is a product of the gas pressure P and the distance d between the electrodes, which minimizes the discharge inception voltage V_B. His analytic expression is reported in Eq.4.01. [WK00]

$$V_B = \frac{B\,P\,d}{\ln(A\,P\,d) - \ln\left[\ln\left(1 + \frac{1}{\gamma}\right)\right]}$$

(4.01)

The product Pd can be seen as a measure of the number of collisions an electron makes by traveling through the space between the electrodes. The constants A, B, and γ are gas-dependent coefficients found experimentally. The values of these constants for some gas are reported in the next table and the graphic of the voltages V_B versus Pd for these gases is shown in Fig.4.16.

The Eq.4.01 was developed under normal conditions of pressure and temperature $T_A = 20°C$, $P_A = 760\,Torr$, and absolute humidity of $11\,g/m^3$ [SL11].

Paschen coefficients for some selected gas			
Element	$A\ (m^{-1}Pa^{-1})$	$B\ (V\ m^{-1}Pa^{-1})$	γ
Helium	2.1	58	0.16
Neon	3.3	83.3	0.14
Argon	8.63	132	0.07
Hydrogen	3.6	102	0.015
Nitrogen	8.85	243.8	0.00093
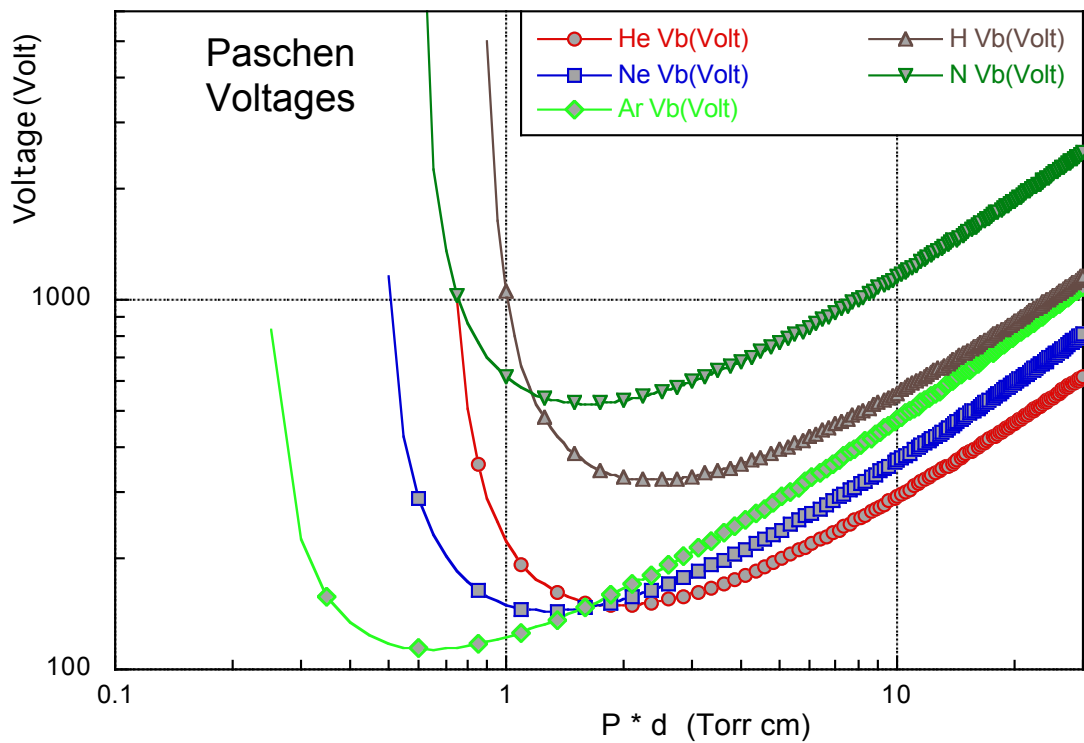
Fig.4.16 The Paschen voltage breakdown V_B as a function of the product Pd computed with the constants A, B, and γ of the previous table. [WK00]

In dry air at the normal pressure, voltages of the order of kV are safe. Care must be taken when high voltages are applied under specific pressure ranges of residual gas. In these conditions, as shown in Fig.4.16, the insulation test may incur in an undesired discharge. In order to avoid damages or incorrect results, the PXI computer must inhibit the high voltage test continuously checking the computed voltage V_B.

4.9   Automated QDM continuity and insulation tests

In the design stage, we decided to realize an Automated Monitor and Control System in order to increase reliability and repeatability as well as speed-up the test procedure.

This computer-controlled system automatically connects the devices and automatically executes all the tests. Moreover, it will be faster and does not require manpower during its execution. The hardware of the automated test system is shown in Fig.4.17. These switch boxes contain the relays with all the circuits necessary to enable the connection with two Multimeters and two Lake Shore model 224 temperature monitors for continuity tests, and a Megger® S1-568 Insulation Resistance Tester, for the insulation tests.

Fig.4.17 The automatic QDM test system front (left) and back view (right). Under the last switch box on the bottom of both figures, there is a PXI computer that manages the switch boxes and all the other instruments.

The switch boxes software has been realized in collaboration with Vitrociset, an external company with experience in the field of control systems.

The circuits on the four switch boxes are divided by type of tests and the devices under control. The first switch box from the top is devoted to high and middle voltages insulation tests on bus bars and coils. The second is used for the continuity tests on the voltage taps. The third is used for continuity and insulation tests on two-terminal devices, such as PT1000 thermometers, thermocouples, and the heathers. The fourth is used for the insulation tests on the cryogenic thermometers with four wires. Under the last switch box, there is the $PXIe$ 8880 computer that manages all the switch boxes as well as other instruments. The switch boxes are all connected with a bus cable, as sketched in Fig.4.18. The arrows on this bus indicate the signal direction among the switch boxes. Three PXI-6512 Digital Output 64 channel source cards, mounted on the $PXIe$ 8880, are connected to the switch boxes digital inputs as indicated by arrows with labels (A), (B), and (C). It has to be noticed that the connection sequence among the switch boxes is unique and cannot be changed.

The internal view of two switch boxes is shown in Fig.4.19 while mounting the wires. The high voltage box, on the left side of this figure, shows the high voltage insulated silicon wires already connected to the high voltage reed relays DAT 72410 from Cynergy3 and the HM 24-1A83-03 from Meder, both having more than $15\,kV$ insulation voltage and switching capability, guaranteed up to $7\,kV$. Only on this switch box, the status of all relays is displayed on the front panel with an array of led lights that continuously show the status of the connections of each relay. This is a safeguard measure due to the high voltages involved. The PCB design of these cards has been made considering the usage with high voltages. The upper side of the PCB has been reserved for the high voltage connections, leaving the $24\,V$ relays excitation traces on the other side. The minimum distance between high voltage copper traces is $1\,cm$ and an insulating varnish film was sprayed on the surfaces.
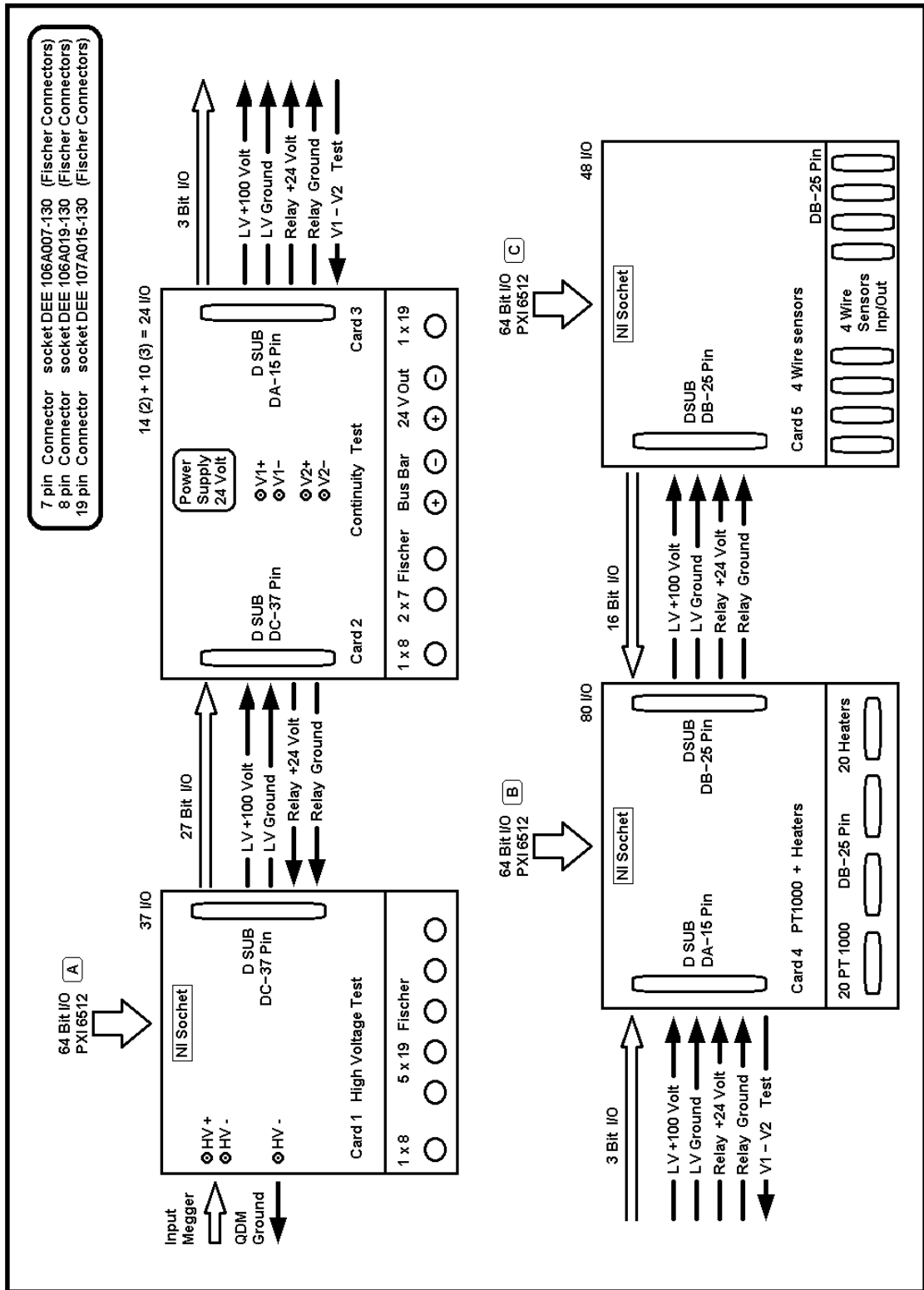
Fig.4.18 Schematic block connections with the bus cable carrying the digital signals and voltages exchanged between the boxes. The three inputs with labels (A), (B) and (C) are the digital output lines of the three PXI-6512 cards of the PXI computer that manages the relays and the instruments.

The insulation of the printed circuit of the high voltage insulation box, because of the high voltages involved, has been verified before the assembly.

The insulation measure has been done with the same Megger® S1-568 Insulation Resistance Tester that will be used for the insulation tests. A voltage ramp of $1000\,V/min$ was applied for $10\,min$ on the fiberglass PCB. The DAR, Dielectric Adsorption Ratio, defined as the IR, Insulation Resistance, ratio $IR(60\,s)/IR(30\,s)$, was computed by the instrument. At the voltage of $5000\,V$, the Insulation Resistance Tester reported an insulation resistance value of $2.85\,T\Omega$ that corresponds to a leakage current of $1.79\,nA$ and a measure of $DAR = 1.10$. This DAR value is considered as *acceptable*.

On the right side of Fig.4.19 the SMD, Surface Mounted Device, low profile relay, model TX2SA-24 from Jameco®, and TQ2SA from Panasonic®, are partially mounted on the PCB, Printed Circuit board.
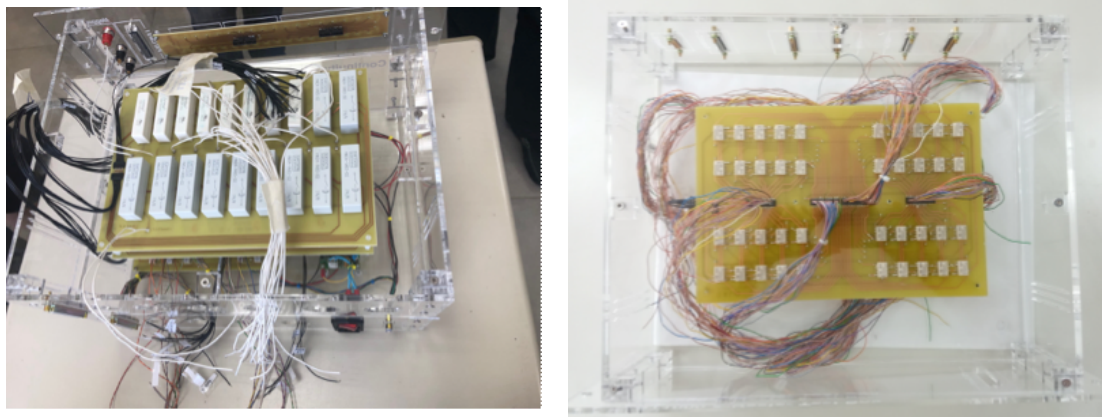
Fig.4.19 Insulation box for high and middle voltage tests on a QDM (left) and a box for low voltage measures (right). The large high insulation relays for the high and middle voltage tests are clearly recognizable (left picture). A Large number of SMD relays can fit into a single PCB card (right picture).

The high voltage from the Megger® S1-568 Insulation Resistance Tester, as shown in Fig.4.20, is applied as input to the high voltage switch box and connected directly to the devices that have to be tested with voltages up to $3000\,V$. A high voltage reed relays isolate the other switch boxes from the

Megger® when voltages above $100\ V$ are generated. This HV Test relays will be closed only during the insulation tests on the other devices where voltages up to $100\ V$, are required, a value less dangerous and easier to manage.

In the following part of this section, a brief explanation of the tests and how are carried out within these switch boxes is presented in detail. In particular, are shown the high and middle voltage insulation tests and the two and four wires low voltage continuity and insulation tests.

High and Medium Voltage insulation tests: these high and middle voltage insulation tests are applied on quadrupole and bus bars while the middle voltage insulation tests are applied on the MID and the other corrector coils. The high voltage test is done as specified in section 4.2.2 of this chapter.

The computer-controlled relays on high and medium insulation board, apply the sequence of test voltages on each input in a predefined sequence. A partial electrical scheme for these measures is shown in Fig.4.20.
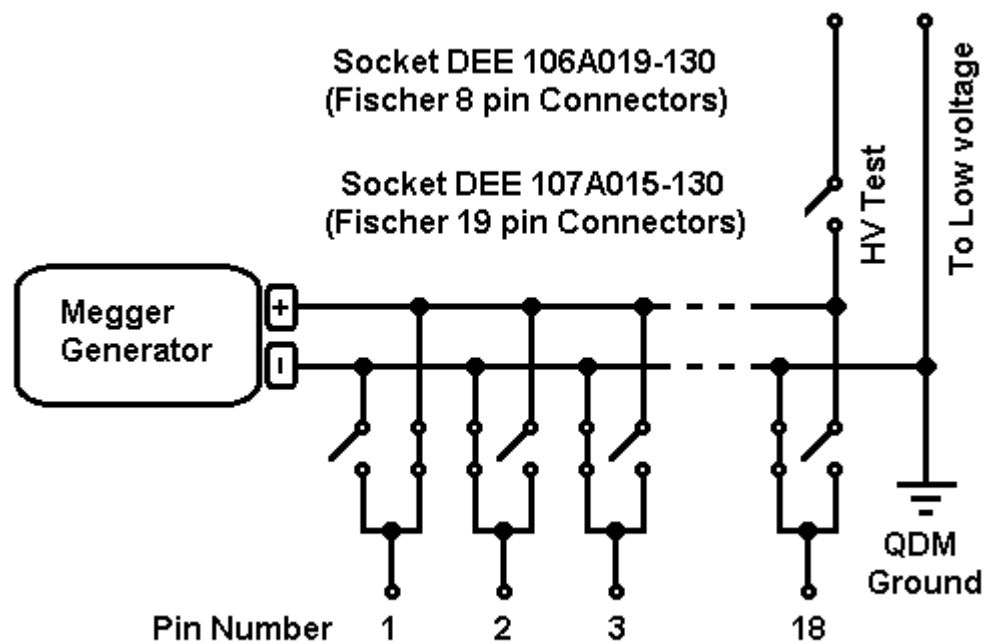

Fig.4.20 Electrical scheme for the High and Middle Voltage box. The bus bar on pin 1 is under test and the others are grounded. The HV output is open.

Because of the usage of reed relays type SPST Single Pole Single throw, for each test line two reed relays have to be used to emulate a switch type SPDT Single pole Double Throw are difficult to purchase as high voltage relays. This choice, forced by this unavailability, may offer the advantage of a more flexible analysis when multiple leaks are detected. On the scheme of Fig.4.20, the voltage tap attached to pin 1 is connected to the positive pole of the Megger® S1-568 Insulation Resistance Tester, and all the other pins are grounded. In this configuration, the test of the bus bar can be executed on this voltage tap attached to pin 1. With an analogous configuration, the tests can be done on all voltage taps attached to the other pins.

High and Medium Voltage continuity tests: these continuity tests ensure the electric connection of the voltage taps with bus bars and coils. First, a circuit is made with electrical jumpers and joins all the bus bar into a loop. Corrector coils do not need these jumpers since the coil and current leads are already connected. The test on the bus bar and quadrupole coils are done in two parts. During the first part, the computer-controlled relays on this box, simply connect, once at a time, the many couples of voltage taps that have to be continuity tested. For each couple, the Multimeters acquires the values of the resistance. These resistance values are compared with the expected values. Usually for a good, all-metal circuit, the resistance values are less than $10\ \Omega$ Ohms, while a weak contact or an open circuit shows the value of the resistance above $10\ k\Omega$.

In the second part of this continuity test, the voltage taps inversion is verified. For this test, on loops extremities, a current generator or voltage generator limited to a maximum output current of about $5\ A$ is plugged. Also in this part, the relays on this switch box connect the voltage taps to the Multimeters and the voltages are automatically acquired. As explained in section 4.2.2 a crescent series of voltages is expected. If it is not so, a voltage tap position inversion is automatically detected and reported.

At the end of the measure, the bus bar jumper connections have to be removed. For this reason, the second part of this test cannot be done on the bus bar at cryogenic temperature, because it is not possible to gain the access to the bus bars, inside the module. After all, they are closed under vacuum inside the vessel. However, this would not be a problem since once fixed the voltage taps are not going to change position.

Continuity and low voltage insulation tests on two-wires devices: these low voltage continuity and insulation tests are applied on the two-wire PT1000 thermometers, heater resistances, and few thermocouples by using the same switch box. On each input, channel the computer-controlled relays, apply the test voltages during the insulation tests, and read both voltages and resistances on the continuity test. A partial electrical scheme, for only one channel, is shown in Fig.4.21, all the other channels are connected in parallel to the lines where the Megger® and two multimeters are connected.
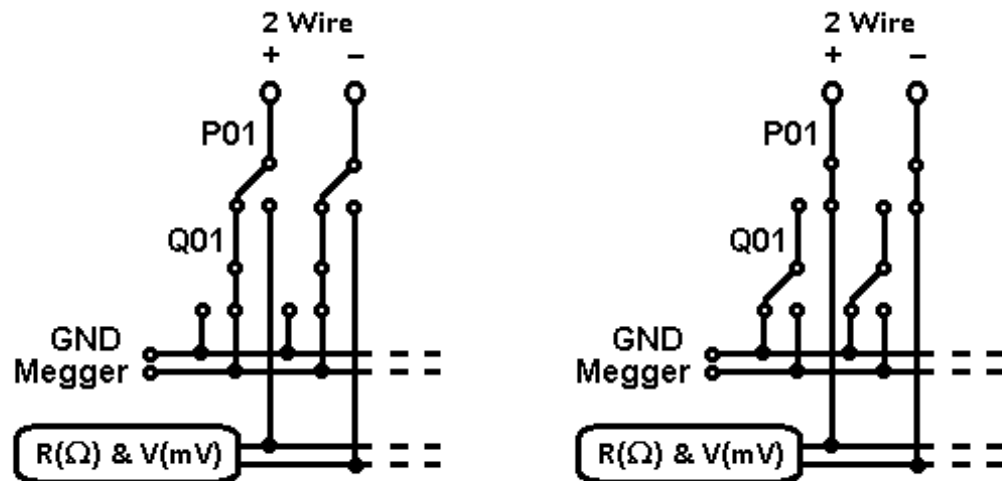

Fig.4.21 Electrical scheme for channel 01 of the two wires devices. On the left during the insulation test, relay P01 is open and relay Q01 closed. On the right during the continuity test, relay P01 is closed and relay Q01 is open.

The scheme on the left part of Fig.4.21 shows the relays during the insulation tests. In this configuration, on channel one, the relay P01 is open,

and the relay Q01 is closed, so that the two wires device, with the termination, joined together, is connected to the Megger®. On all the other channels, the relays P0[n] and Q0[n] are both open and the device[n] is shorted to ground as required by the GSI test procedures. During the insulation test, the Megger® applies, for one minute the voltage of $50\,V$, on the thermocouple or the PT1000 thermometer, and $100\,V$ on the heater. The Megger® automatically acquires the final value of the insulation resistance. The scheme on the right part of Fig.4.21 shows the relays during the continuity tests. In this configuration, on channel one, the relay P01 is closed, the relay Q01 is open, and the two wires device is connected to the multimeter. On all the other channels the relays P0[n] and Q0[n] are both open and the device[n] is disconnected from the multimeter and shorted to ground. During the continuity test, the value of the resistance is automatically acquired and compared with the expected value. The use in the circuit of DPDT, Double Pole Double Throw, relays permits to execute all needed commutation on a single channel with two relays and two channels of the PXI output card.

Thermometers low voltage insulation tests: these low voltage insulation tests are applied on the four-wire semiconducting thermometers. On each input, the computer-controlled by relays apply the test voltages during the insulation tests and connect the thermometers to the LakeShore® LS224 temperature monitors during the continuity test. A partial electrical scheme, for only one channel, is shown in Fig.4.21, all the other channels are connected in parallel on the lines where the Megger® is connected.

The scheme on the left part of Fig.4.22 shows the relays during the insulation tests. In this configuration, on channel one, the twin relays T01 and the relay W01 are closed, so that the four wires device, with the termination, joined together, is connected to the Megger®. On all the other channels, the twin relays T0[n] are closed, the W0[n] relays are open, and the device[n] is shorted to ground as required by the GSI test procedures.
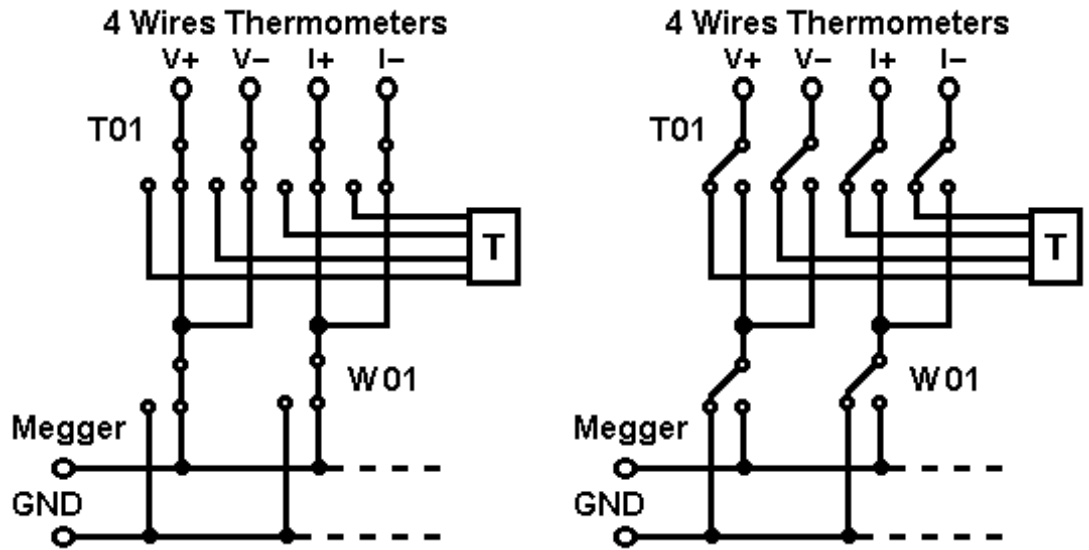
182

Fig.4.22 Electrical scheme for channel 01 of the four wires devices. On the left relay T01 is closed and relay W01 now open, will close during the insulation test on this channel. On the right relay T01 and W01 are both open and the thermometer is connected on the temperature reader.

During the insulation test, the Megger® applies, for one minute the voltage of $50\,V$, on all termination of the four-wire thermometer. The Megger® automatically acquires the final value of the insulation resistance. The scheme on the right part of Fig.4.21 shows the relays during regular usage. In this configuration, all relays are open, and the four wires thermometer, are all connected to each input channel of the temperature monitors. Also, in this case, the use in the circuit of DPDT relays permits to execute all needed commutation on a single channel with three relays, and because two of them are twin relays, only two channels of the PXI output card are needed.

The continuity and functionality tests for these four-wire semiconducting thermometers are obtained from the usage of the temperature monitor. The electrical connection status can be verified by reading the temperatures on all thermometers. On LakeShore® LS224 temperature monitors, the wrong or open connections, are reported as an error. At the same time, the availability of both the sensor resistance and the corresponding computed value of the

temperature allows the verification of the correctness of the conversion curves stored in memory.

All four wire thermometers needed for testing the QDM modules are connected to LakeShore® LS224 temperature monitors. There are two instruments available. Each instrument can read up to 12 thermometers and store all the calibration temperatures needed to correctly convert the voltage values in the current temperature value. Both instruments have IEEE-488, USB, and Ethernet interfaces. Another reader can be used if more than 24 thermometers have to be monitored.

4.9.1   QDM data collection and Master & Control System

The electrical insulation tests as reported in Section 4.4 are repeated five times both in the worm and in cold conditions. The availability of an automatic measurement system for the electrical insulation measures is a great help during the measures, especially when the QDM is cold and many other instruments and parameters have to be controlled.

The tests on 81 QDMs raise the problem of repeatability not only on the electrical tests but also on the whole test procedure of the QDM. This problem is enhanced at the INFN test facility laboratory by the reduced number of technical staff and the time allowed for each test that requires a short working cycle for each QDM. With this idea in mind, the automatic electrical tests philosophy has been expanded, by including the electrical tests into a more general computer management procedure. A draft of a computer diagram network, for the project of management of all the instruments involved in the QDM tests, is shown in Fig.4.23. This project has been called M&CS, Master & Control System, and is under development in collaboration Vitrociset.
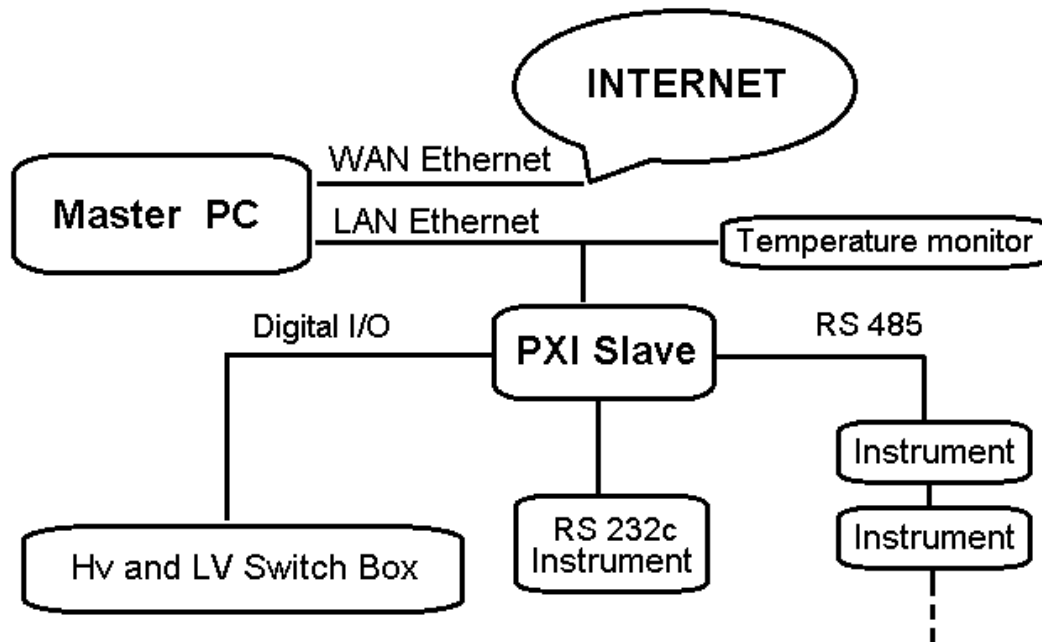

Fig.4.23 A diagram network of the management of all devices in the QDM tests.

The M&CS is a software and hardware environment realized for the multiprotocol connection and management of all instrument connection with the ability of control and data collection. The M&CS is based on the assumption that the devices can be remotely controlled, and it is possible to access the devices and read the process variables in real-time. The M&CS software will consist of a suite of programs able to automatically record the variations of the instruments outputs. This software is installed on two computers. The choice, of using two separate computers, has been done mainly for security reasons. In fact, as shown in the diagram network of Fig.4.23, the master PC is equipped with two Ethernet cards. The first card is connected to the INFN network through the university campus WAN, Wide Area Network, and is accessible from everywhere. The second card is part of a separate LAN, Local Area Network, that involves the connection only to the $PXIe\ 8880$ Computer and the three LakeShore® LS224 temperature monitors. Both computers on the LAN can access the LakeShore® LS224 temperature monitors for two different activities. The master PC will download and update for each QDM the new thermometers calibration curves and the $PXIe\ 8880$ computer will read the temperature values anytime they are requested.

The heart of the M&CS is the $PXIe\ 8880$ Computer with its ability to manage all the connections and have the access to the instruments by using the RS232, RS485, USB, and Ethernet protocols. On this computer, some programs will be dedicated by keeping under control some critical process variables. A special program will monitor the environment condition and will react properly in case of anomalous events or erroneous commands from the operator. The suite of programs of M&CS is under development. The Vitrociset has already realized part of the operator front-end of one of its programs and two screenshots are shown in Fig.4.24. In the first image, on the top of Fig.4.24, a window with five graphic panels reports the data recorded during the leak tests from five different instruments.
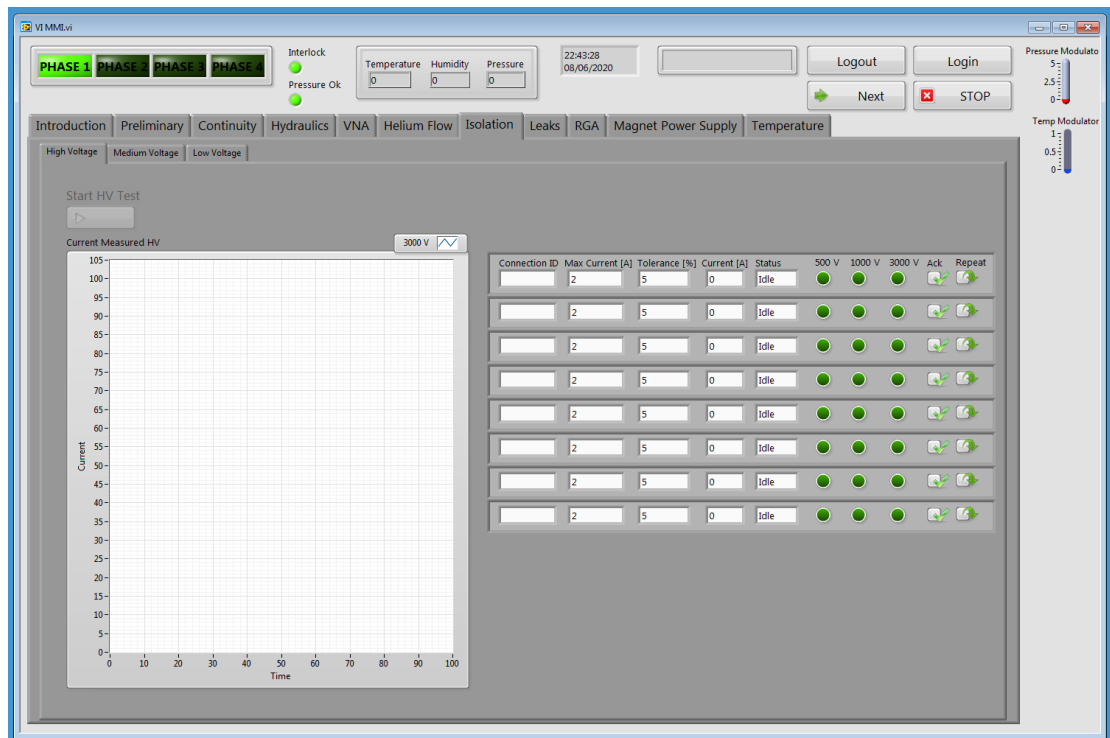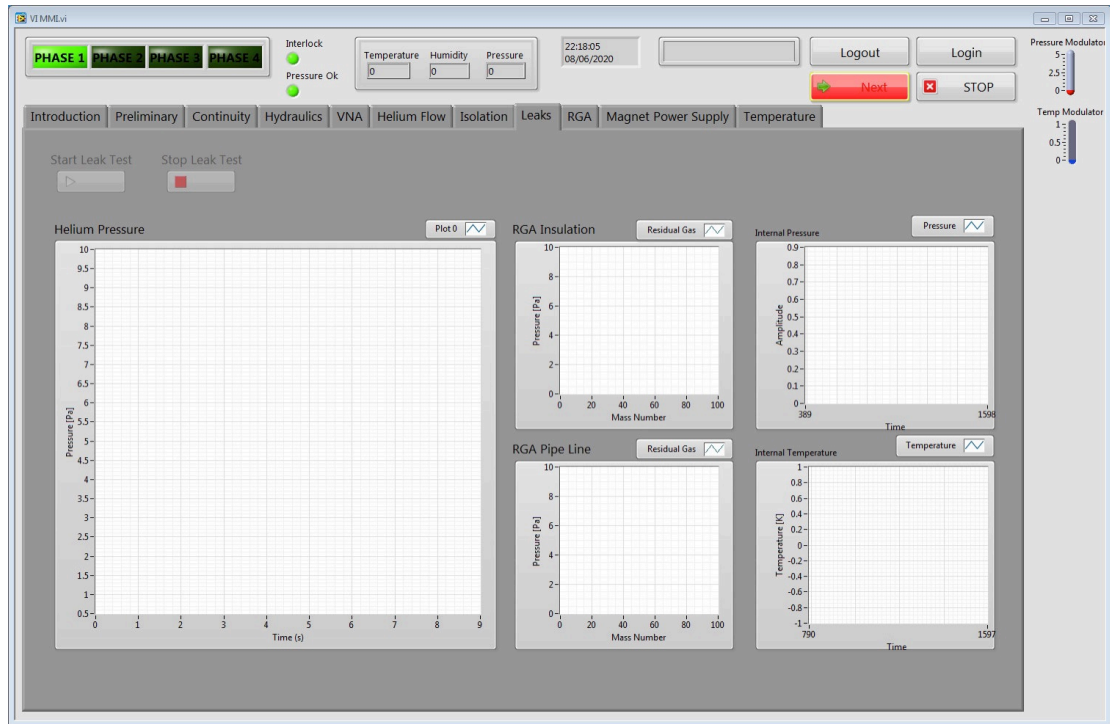
Fig.4.24 Two screenshots of the M&CS software. The first panel shows the graphic displays of the pressure monitoring sub-system (top). The second panel shows the high voltage insulation test output with the graphic display of the time-dependent leakage currents and a display of the insulation test status (bottom).

The second image, on the bottom of Fig.24, is an image of the insulation test panel. The left side of this figure, shows the leakage current as a function of time, read directly from the Megger® S1-568 Insulation Resistance Tester, during the high voltage insulation test. On the right side of the same figure, a matrix with both indicators and numerical values reports the insulation values and the status of the running tests. For each QDM test, the *PXIe* 8880 computer will acquire and store, all the required data.

The test results, with a summary of the most significant measures, have to be collected into a report and shipped together with the QDM to the GSI. In the planned test procedures, the master computer under the control of the M&CS will help the operator during the selection of the significant measures from all the acquired measures while preparing the final report.

The M&CS suite of programs is under development under the LabView© graphical IDE, Integrate Design Environment. This graphic language, developed for the management of instruments in the industrial environment, has been chosen for its management capability of managing the connections of the instruments and built-in functions for network communications.

This idea, of an instrumentation network, will never be definitive because of its intrinsic flexibility. This could be an advantage because, in case of modifications underway of part of the test procedure, the system can be adapted to the new needs.

Conclusions and Outlook

The applications of superconductivity are spread in many fields also outside the research laboratory. In this thesis, the attention has been focused on the high current application of superconducting wires and tapes, with particular attention on their transport properties. To introduce the subject, we first describe the measures carried out in our laboratory, with particular attention devoted to the investigation of the instabilities and the quench propagation on novel high-temperature superconductors tapes based on the rare earth compounds. This is because these tapes are now widely used in HTS current leads, allowing saving a large amount of cryogenic power in large-scale applications. In addition, HTS tapes represent the most promising solution in the manufacture of very high field magnets (higher than 25 Tesla). The realization of higher energy particle accelerators, beyond Hi-Lumi LHC, will require this kind of magnets, thus investigations on these tapes are being more and more interesting for their applications. We limited our work to the experimental features of some commercial tapes, and in this framework also discuss the limits of the investigations we found by using the tools widely used in this kind of experiment.

We then discuss the typical use of HTS in a high current leads we had to realize for a local experiment: an optimized $10\,kA$ current lead with the possibility of working also at $20\,kA$. In fact, our $20\,kA$ power converter was designed for 2 current levels: $10\,kA$ up to $50\,V$, or $20\,kA$ up to $25\,V$, for two different experiments. We then studied the possibility of using just one pair of current leads with two cooling systems, thus nearly optimized for the two current levels. These current leads have been designed and realized.

The final part of this work is connected to the construction of the SIS100 particle accelerator ring at the GSI in Darmstadt (D). The INFN set a collaboration agreement with GSI to establish in Salerno a new laboratory where to perform the final tests on the quadrupole modules of SIS100. The verification tests on the manufactured superconducting dipoles for this accelerator are done in Darmstadt, where also the preliminary test on the first of the series quadrupoles module is carried out. We first introduce these new challenging, "fast ramped" dipoles and

quadrupoles, where fast means up to 4 T/s. The verification tests of dipoles are performed at the Serial Test Facility of GSI in Darmstadt. Presently the manufacture of the first of series quadrupole module, give rise to the first test of this new module at GSI, and we take the opportunity to attend to these tests, which will define the verification tests that have to be performed on the serial production at the INFN laboratory in Salerno. Further to this training activity, a large part of the work is also devoted to the build-up of the facilities in the Salerno laboratory: in the 4th chapter, the cryogenic and electric environments are discussed with some improvements on the methods for testing these quadrupole modules. The aspects related to the creation of a computer-controlled instrument network, with automatic test procedures, and the perspective of a full-automatized system closes this thesis.

Before the end of this year, we will be able to receive the First of Series quadrupole module in our test line in Salerno. Then the full commissioning of the laboratory will take place and all our designs will be tested in the real field. After this, the continuous verification activity at low temperatures on the 81 modules will start. This work will last for three years or more and will qualify the laboratory as a European center where large-scale superconductivity program could be developed.

The Bibliography

[AN18]   AN1829 Application Note Revision B, Power Diode datasheet Notation, Microsemi Power Matters, (2018), Figure on page 6. https://www.microsemi.com/document-portal/doc_download/14695-defining-diode-data-sheet-parameters

[BD09]   R.A.Badcock, N.J.Long, M.Mulholland, S.Hellmann, A.Wright, and A.Hamilton, "Progress in the Manufacture of Long Length YBCORoebel Cables", IEEE Transaction on Applied Superconductivity, 19, (2009), 3244-3247. https://doi.org/10.1109/TASC.2009.2019065

[BL02]   A.Ballarino, "HTS current leads for the LHC magnet powering system", Physica C, 372–376, (2002), 1413–1418. https://doi.org/10.1016/S0921-4534(02)01042-0

[BL07]   A.Ballarino, L.Martini, S.Mathot, T.Taylor, and R.Brambilla, "Large Scale Assembly and Characterization of Bi-2223 HTS Conductors", IEEE Transaction on Applied Superconductivity, 17, (2007), 3121. https://doi.org/10.1109/TASC.2007.900043

[BL08]   A.Ballarino, "Large-capacity current leads", Physica C, 468, (2008), 2143–2148. https://doi.org/10.1016/j.physc.2008.05.217

[BL94]   R.H.Bellis and Y.Iwasa, "Quench Propagation in High Tc Superconductors", Cryogenics, 34, (1994), 129-144. https://doi.org/10.1016/0011-2275(94)90036-1

[BL99]   A.Ballarino, "High Temperature Superconducting Current Leads for the Large Hadron Collider", IEEE Transaction on Applied Superconductivity, 9, (1999), 523-526. https://doi.org/10.1109/77.783350

[BN15]   M.Bonura and C.Senatore, "High-Field Transport properties of ReBCO coated Conductors", Superconductor Science and Technology, 28, (2015), 025001. https://doi.org/10.1088/0953-2048/28/2/025001

[BN16]   M.Bonura and C.Senatore, "An Equation for the Quench Propagation Velocity valid for High Field Magnet Use of ReBCO Coated Conductors", Applied Physics Letters, 108 (2016), 242602. https://doi.org/10.1063/1.4954165

[BR17]   P.Bruzzone, R.Wesche, D.Uglietti, and N.Bykovsky, "High temperature superconductors for fusion at the Swiss Plasma Center", Nuclear Fusion, 57, (2017), 085002. https://doi.org/10.1088/1741-4326/aa7bab

[BR61]   T.G.Berlincourt, R.R.Hake, and D.H.Leslie, "Superconductivity at High Magnetic Fields and Current Densities in Some Nb-Zr Alloys", Physical Review Letters, 6, (1961), 671-674. https://doi.org/10.1103/PhysRevLett.6.671

[BT82]   P.A.Bottomley, "NMR imaging technique and applications: A review", Review of Scientific Instruments. 53, (1982), 1319-1337. https://doi.org/10.1063/1.1137180

[CG15]   L.Callegaro, C.Cassiago, and E.Gasparotto, "On the Calibration of Direct-Current Current Transformers (DCCT)", IEEE Transactions on Instrumentation and Measurement, 64, (2015), 723-727. https://doi.org/10.1109/TIM.2014.2359812

[CH09]   W.K.Chan, P.J. Masson, C.A. Luongo, and J.Schwartz, "Influence of Inter-Layer Contact Resistances on Quench Propagation in YBa2Cu3Ox Coated Conductors", IEEE Transaction on Applied Superconductivity, 19, (2009), 2490-2495. https://doi.org/10.1109/TASC.2009.2018514

[CH10]   W.K.Chan, P.J.Masson, C.Luongo, and J.Schwartz, "Three-Dimensional Micrometer-Scale Modeling of Quenching in High-Aspect-Ratio YBa2Cu3O7−δ Coated Conductor Tapes—Part I: Model Development and Validation", ", IEEE Transaction on Applied Superconductivity, 20, (2010), 2370-2380. https://doi.org/10.1109/TASC.2010.2072956

[CL09]   G.Celentano, G.M.Polli, A.Angrisani Armenio, A.Augieri, V.Galluzzi, A.Mancini, A.Rufoloni, A.Vannozzi, U.Gambardella, A.Saggese, and S.Pace, "Hot Spot Stimulated Transition in YBCO Coated Conductors: Experiments and Simulations", IEEE Transaction on Applied Superconductivity, 19, (2009), 2486-2489. https://doi.org/10.1109/TASC.2009.2017916

[CL13]   G.Celentano, G.Messina, A.Angrisani Armenio, A.Augieri, F.Fabbri, V.Galluzzi, A.Mancini, F.Rizzo, A.Rufoloni, A.Vannozzi, U.Gambardella, A.Saggese, G.Iannone, and P.Sabatino, "Quench Behavior of a Conduction Coated $Y_1Ba_2Cu_3O_{7-x}$ Tape Pancake Coil", IEEE Transaction on Applied Superconductivity, 23, (2013), 4600704. https://doi.org/10.1109/TASC.2012.2234334

[CL15]   G.Celentano, U.Gambardella, G.Iannone, and A.Saggese, "A Low Temperature Behavior Investigation of ReBCO Coated Conductors", 24th International Conference on Magnet Technology (MT-24)", Seoul, Korea, October 18-23, 2015, unpublished.

[CR01]   W.J.Carr, "A.C. Loss and Macroscopic Theory of Superconductors", 2nd edition, CRC Press, (2001). ISBN 0-415-26797-8 https://www.abebooks.it/servlet/BookDetailsPL?bi=22221275270

[CR15]   M.Cerqueira Bastos, "High Precision Current Measurement for Power Converters", Published by CERN in the Proceedings of the CAS-CERN Accelerator School: Power Converters, Baden, Switzerland, 7–14 May 2014, edited by R. Bailey, CERN-2015-003 CERN, Geneva, (2015). https://arxiv.org/pdf/1607.01584.pdf

[CR99]   Cryocomp and Metalpack, Computer Properties Packages, Version 5.30, Published by Cryodata Software inc., (1999), Available from Eckels Engineering Inc. http://www.eckelsengineering.com

[DG20]   D.D'Agostino, U.Gambardella, G.Iannone, and A.Saggese, "Critical aspects in the measure of the quench propagation velocities on HTS tapes", 10th Young Researcher Meeting, 18-21 June 2019, Proceeding of the Conference by IOP Conf. Series: Journal of Physics, 1548, (2020), 012029. https://doi.org/10.1088/1742-6596/1548/1/012029

[DM16]   G.De Marzi, N.C.Allen, L.Chiesa, G.Celentano, M.Takayasu, G.Tomassetti, A.Augieri, and A. della Corte, "Bending Tests of HTS Cable-In-Conduit Conductors for High-Field Magnet Applications", IEEE Transaction on Applied Superconductivity, 26, (2016) 4801607. https://doi.org/10.1109/TASC.2016.2528501

[DR79]   L.Dresner, "Analytic Solution for the Propagation Velocity in Superconducting Composites", IEEE Transaction on Magnetics, 15, (1979), 328-330. https://doi.org/10.1109/TMAG.1979.1060268

[DV04]   A.Devred, "Practical Low-Temperature Superconductors for Electromagnets", CERN Yellow Reports: Monographs, CERN-2004-006, Geneva: CERN, (2004), 87 p. https://cds.cern.ch/record/796105 ISBN-10 9290832274, ISBN-13 9789290832270 https://doi.org/10.5170/CERN-2004-006

[FB09]   P.Fabbricatore, S.Farinon, S.Incardone, U.Gambardella, A.Saggese, and G.Volpini, "The transverse resistivity in S/C multifilament wires studied through ac susceptibility measurements", Journal of Applied Physics, 106, (2009), 083905. https://doi.org/10.1063/1.3234378

[FB13]   P.Fabricatore, S.Farinon, V.Corato, G.De Marzi, T.Spina, U.Gambardella, and A.Saggese, "Experimental investigation of the transverse resistivity in Nb3Sn wires through ac susceptibility", Superconductor Science and Technology, 26, (2013), 085001. https://doi.org/10.1088/0953-2048/26/8/085001

[FF67]   K.R.Efferson, "Helium Vapour Cooled Leads", The review of Scientific Instruments", 38, (1967), 1776-1779. https://doi.org/10.1063/1.1720670

[FR18]   J.H.Fournier-Lupien, C.Lacroix, S.Hellmann, J.Huh, K.Pfeiffer, and F.Sirois, "Use of the buffer layers as a current flow diverter in 2G HTS coated conductors", Superconductor Science and Technology, 31, (2018), 125019. https://doi.org/10.1088/1361-6668/aae2cd

[FR99]   B.Ferrario, "Introduzione alla Technologia del Vuoto", 2nd Ed., Revision by A.Calcatelli, Patron Editore Bologna, 1999. ISBN 88-555-2510-7 https://www.abebooks.it/servlet/BookDetailsPL?bi=30508606720

[FS14]   E.Fischer, P.Schnizer, A.Mierau, K.Sugita, J.P.Meier, A.Bleile, H.Müller, H.Leibrock, and J.Macavei, "Status of the Superconducting Magnets for FAIR", IEEE Transaction on Applied Superconductivity, 24, (2014), 4004007. https://doi.org/10.1109/TASC.2013.2289960

[FS17]   E.Fischer, A.Bleile, J.C.Velasco, V.Datskov, F.Kaether, J.P.Meier, A.Mierau, H.Mueller, C.Roux, P.J.Spiller, and K.Sugita, "Superconducting Magnets at FAIR", WEOCB2, Proceedings of the 8th International Particle Accelerator Conference, IPAC2017, Copenhagen, Denmark, Section 07 Accelerator Technology, Sub-Section T10 Superconducting Magnets, V.RW Schaa, G.Arduini, J.Pranke, M.Seidel, and M.Lindroos Editors, Publisher JACoW, Geneva CH, (2017), 2546-2549, ISBN 978-3-95450-182-3. https://doi.org/10.18429/JACoW-IPAC2017-WEOCB2

[GA96]   B.J.Gao, M.D.Bird, S.Bole, Y.M.Eyssa, and H.J.Schneider-Muntau, "Design of a 20 T, 200 mm Bore Resistive Magnet", IEEE Transaction on Magnetics, 32, (1996), 2562-2565. https://doi.org/10.1109/20.511396

[GB03]   R.Grabovickic, J.W.Lue, M.J.Gouge, J.A.Demko, and R.C.Duckworth, "Measurement of Temperature Dependence of the Stability and Quench Propagation of a 20-cm long RaBiTS Y-Ba-Cu-O Tape", IEEE Transaction on Applied Superconductivity, 13, (2003), 1726-1730. https://doi.org/10.1109/TASC.2003.812874

[GM07]   U.Gambardella, A.Saggese, P.Sessa, A.Guarino, S.Pace, G.Masullo, A Matrone, E.Petrillo, and R.Quarantiniello, "Stability measurement in multifilamentary MgB_2 Tapes", IEEE Transaction on Applied Superconductivity, 17, (2007), 2937-2940. https://doi.org/10.1109/TASC.2007.900009

[GM19]   U.Gambardella, G.Iannone, and A.Saggese, "The build up of a test station facility for the SIS100 superconducting modules", 9th Young Researcher Meeting, IOP Conf. Series: Journal of Physics: Conference Series, 1226, (2019), 012017. https://10.1088/1742-6596/1226/1/012017

[GR03]   F.Grilli, S.Stavrev, B.Dutoit, and S.Spreafico, "Numerical Modeling of a HTS Cable", IEEE Transaction on Applied Superconductivity, 13, (2003), 1886-1889. https://doi.org/10.1109/TASC.2003.812940

[GR14]   S.Grohmann, "A new method for flow measurement in cryogenic systems", Cryogenics, 60, (2014), 9. http://doi.org/10.1016/j.cryogenics.2014.01.004

[GR16]   F.Grilli and A.Kario, "How filaments can reduce AC losses in HTS coated conductors: a review", Superconductor Science and Technology, 29 (2016) 083002. https://doi.org/10.1088/0953-2048/29/8/083002

[GR18]   R.Gyuráki, F.Sirois, and F.Grilli, "High-speed fluorescent thermal imaging of quench propagation in high temperature superconductor tapes", Superconductor Science and Technology, 31, (2018), 034003. https://doi.org/10.1088/1361-6668/aaa703

[HL05]   R.Heller, S.M.Darweschsad, G.Dittrich, W.H.Fietz, S.Fink, W.Herz, F.Hurd, A.Kienzler, A.Lingor, I.Meyer, G.Nother, M.Susser, V.L.Tanna, A.Vostner, R.Wesche, F.Wuchner, and G. Zahn, "Experimental Results of a 70 kA High Temperature Superconductor Current Lead Demonstrator for the ITER Magnet System", IEEE Transaction on Applied Superconductivity, 15, (2005), 1496-1499. https://doi.org/10.1109/TASC.2005.849145

[HL11]   R.Heller, W.H.Fietz, A.Kienzler, and R.Lietzow, "High temperature superconductor current leads for fusion machines", Fusion Engineering and Design, 86, (2011), 1422–1426. https://doi.org/10.1016/j.fusengdes.2010.12.077

[HL18]   R.Heller, N.Bagrets, W.H.Fietz, F.Groner, A.Kienzler, C.Lange, and M.J.Wolf, "Towards a 20kA high temperature superconductor current lead module using REBCO tapes", Superconductor Science and Technology, 31, (2018) 015021. https://doi.org/10.1088/1361-6668/aa9b09

[HL19]   R.Heller, W.H.Fietz, F.Groner, M.Heiduk, M.Hollik, C.Lange, and R.Lietzow, "Test results of a 20 kA high temperature superconductor current lead using REBCO tapes", Superconductor Science and Technology, 31, (2018), 055014. https://doi.org/10.1088/1361-6668/aab5f9

[HL93]   J.R.Hull, "High-Temperature Superconducting Current Leads", IEEE Transaction on Applied Superconductivity, 3, (1993), 869-875. https://doi.org/10.1109/77.233839

[HM09]   H.M.Chang and M.J.Kim, "Optimization of conduction-cooled current leads with unsteady operating current", Cryogenics, 49, (2009), 210-216. https://doi.org/10.1016/j.cryogenics.2009.01.006

[HR15]   E.Haro, J.Jarvela, and A.Stenvall, "Variation of Quench Propagation Velocities in YBCO Cables", Journal of Superconductivity and Novel Magnetism, 28, (2015), 1705–1710. https://doi.org/10.1007/s10948-015-2976-y

[HS84]   J.G.Hust and A.B.Lankford, "Thermal Conductivity of Aluminum, Copper, Iron, and Tungsten for Temperatures from 1 K to the Melting Point", Technical Report PB-84-235878 NBSIR-84/3007, National Bureau of Standards, Boulder, CO (USA). Chemical Engineering Science Division, (1984), https://www.osti.gov/biblio/6225458

[KH05]   H.G.Khodzhibagiyan, E.Fischer, A.D.Kovalenko, G.Moritz, L.V.Potanina, A.K. Shikov, and G.P.Vedernikov, "Design and Test of a Hollow Superconducting Cable Based on Keystoned NbTi Composite Wires", IEEE Transaction on Applied Superconductivity, 15, (2005), 1529-1532. https://doi.org/10.1109/TASC.2005.849157

[KL06]   S.S.Kalsi, B.B.Gamble, G.Snitchler, and S.O.Ige, "The status of HTS ship propulsion motor developments", 2006 Power Engineering Society, IEEE General Meeting. https://doi.org/10.1109/PES.2006.1709643

[KN06]   J.W.Ekin, "Experimental Techniques for Low-Temperature Measurements Cryostat Design, Material Properties, and Superconductor Critical-Current Testing", Oxford University Press, (2006). ISBN-10 0-19-857054-6, ISBN-13 978-0-19-857054-7 https://www.abebooks.it/servlet/BookDetailsPL?bi=30564849093

[KN61]   J.E.Kunzler, "Superconductivity in High Magnetic Field at High Current densities", Reviews of Modern Physics", 33, (1961), 501-509. https://doi.org/10.1103/RevModPhys.33.501

[KN77]   J.W.Ekin, F.R.Fickett, and A.F.Clark, "Effect of Stress on the Critical Current of the Critical Current of NbTi Multifilamentary Composite Wire", Proceedings First International Cryogenic Materials Conference, Kingston, Ontario, Canada, July 22-25, 1975, Paper I-1 in: Advances in Cryogenic Engineering, K.D.Timmerhous, R.P.Reed, A.F.Clark (eds), Vol.22, 449-452, Springer, Boston, MA, 1977. ISBN 978-1-4613-9852-3 https://doi.org/10.1007/978-1-4613-9850-9_54

[KR09]   H.A.Kartmann, "Big Practical Guide to Computer Simulation" 2nd Ed., World Scientific, 2009. ISBN 978-981-4571-77-7 https://www.abebooks.it/servlet/BookDetailsPL?bi=30571566490

[KS09]   V.V.Kashikhin, R.Bossert, G.Chlachidze, M.Lamm, I.Novitski, and A.V. Zlobin, "Quench Margin Measurement in Nb3Sn Quadrupole Magnet", IEEE Transaction on Applied Superconductivity, 19, (2009), 2454-2457. FERMILAB-CONF-08-481-TD, Ref. 3LPH10. https://doi.org/10.1109/TASC.2009.2019290

[KY97]   T.Kiyoshi, K.Inoue, M.Kosuge, H.Wada, and H.Maeda, "Current Decay Evaluation of Closed HTS Coil Circuits", IEEE Transaction on Applied Superconductivity, 7, (1997), 877-880. https://doi.org/10.1109/77.614643

[LC14]   C.Lacroix and F.Sirois, "Concept of a current flow diverter for accelerating the normal zone propagation velocity in 2G HTS coated conductors", Superconductor Science and Technology, 27, (2014), 035003. http://doi.org/10.1088/0953-2048/27/3/035003 Corrigendum, 27, (2014), 129501. http://doi.org/10.1088/0953-2048/27/12/129501

[LC17]   C.Lacroix, F.Sirois, and J-H.Fournier Lupien, "Engineering of second generation HTS coated conductor architecture to enhance the normal zone propagation velocity in various operating conditions", Superconductor Science and Technology, 30, (2017), 064004. https://doi.org/10.1088/1361-6668/aa684f

[LN08]   N.J.Long, R.Badcock, P.Beck, M.Mulholland, N.Ross, M.Staines, H.Sun, J.Hamilton, and R.G.Buckley, "Narrow strand YBCO Roebel cable for lowered AC loss", Journal of Physics: Conference Series 97 (2008) 012280.
https://doi.org/10.1088/1742-6596/97/1/012280

[LN19]   A.A.Ilin, I.A.Kovalev, S.L.Kruglov, A.V.Polyakov, V.I.Shcherbakov, and D.I. Shutova, "Current caring capacity of bare REBCO tapes at high ramp rates at 77 K and 4.2 K", Physica C: Superconductivity and its applications, 566, (2019), 1353524.
https://doi.org/10.1016/j.physc.2019.1353524

[LU02]   J.W.Lue, M.J.Gouge, R.C.Duckworth, D.F.Lee, D.M.Kroeger, and J.M.Pfotenhauer, "Quench test of a 20 cm-long RaBiTS YBCO Tape", AIP Conference Proceedings, 613, (2002), 457. https://doi.org/10.1063/1.1472054

[LV10]   G.A.Levin, K.A.Novak, and P.N.Barnes, "The effects of superconductor–stabilizer interfacial resistance on the quench of a current-carrying coated conductor", Superconductor Science and Technology, 23, (2010), 014021.
http://doi.org/10.1088/0953-2048/23/1/014021

[MN16]   A.Morandi, M.Fabbri, B.Gholizad, F.Grilli, F.Sirois, and V.M.R.Zermeno, "Design and Comparison of a 1-MW/5-s HTS SMES With Toroidal and Solenoidal Geometry", IEEE Transaction on Applied Superconductivity, 26, (2016), 5700606.
https://doi.org/10.1109/TASC.2016.2535271

[MR14]   J.P.Meier, A.Bleile, E.Fischer, G.Hess, J.Macavei, and P.Spiller, "Cryo-technical Design Aspects of the Superconducting SIS100 Quadrupole Doublet Modules", Advances in Cryogenic Engineering, AIP Conference Proceedings 1573, (2014), 1519-1526.
https://doi.org/10.1063/1.4860887

[MR16]   A.Mierau, P.Schnizer, E.Fischer, H.Mueller, H.Khodzhibagiyan, S.Kostromin, L.Serio, S.Russenschuck, and O.Dunkel, "Testing of the Superconducting Magnets for the FAIR Project", IEEE Transaction on Applied Superconductivity, 26, (2016), 4401605.
https://doi.org/10.1109/TASC.2016.2539152

[MR19]   A.Mierau, C.Roux, P.A.Bartolome, F.Kaether, G.Golluccio, P.Kosek, P.Szwangruber, W.Freisleben, G.J.Ketter, K.Sugita, A.Warth, F.Marzouki, and E.Fischer, "Testing of Series Superconducting Dipole Magnets for the SIS100 Synchrotron", IEEE Transaction on Applied Superconductivity, 29, (2019), 4003907.
https://doi.org/10.1109/TASC.2019.2904693

[MS33]   W.Meissner and R.Ochsenfeld, "Ein neuer Effekt bei Eintritt der Supraleitfahigkeit", Naturwissenschaften, 21, (1933), 787-788. https://doi.org/10.1007/BF01504252

[MY14] Y.Miyoshi, H.Kitaguchi, X.Chaud, F.Debray, G.Nishijima, and Y.Tsuchiya, "Homogeneous performance and strain tolerance of long Bi-2223 HTS conductors under hoop stress", Superconductor Science and Technology, 27, (2014), 025003. http://doi.org/10.1088/0953-2048/27/2/025003

[NG08] A.Angrisani Armenio, A.Augieri, G.Celentano, V.Galluzzi, A.Mancini, A.Rufoloni, A.Vannozzi, U.Gambardella, A.Saggese, P.Sessa, and S.Pace, "Stability measurement in YBCO Coated Conductors", IEEE Transaction on Applied Superconductivity, 18, (2008), 1293-1296. https://doi.org/10.1109/TASC.2008.920835

[NG12] J.Van Nugteren, "Normal Zone Propagation in a YBCO Superconducting Tape Measurement and Analysis of Quasi-Adiabatic Normal Zone Propagation in a YBCO Coated Conductor", A technical report performed within the framework of a graduation assignment as part of the Applied Physics Master of Science programme, September 20, 2012. https://essay.utwente.nl/62096/1/MSc_J_van_Nugteren.pdf

[NG15] J.van Nugteren, M.Dhallé, S.Wessela, E.Krooshoopa, A.Nijhuisa, and H.ten Katea, "Measurement and analysis of normal zone propagation in a ReBCO coated conductor at temperatures below 50 K", 25th International Cryogenic Engineering Conference and International Cryogenic Materials Conference, ICEC 25–ICMC 2014, Physics Procedia 67 (2015) 945-951. https://doi.org/10.1016/j.phpro.2015.06.159

[NN16] G.Iannone, F.Quero, U.Gambardella, P.Fabbricatore, S.Farinon, and G.Volpini, "Composite superconducting wires for fast ramped magnets", Composites Part B, 90, (2016), p.133-140. https://doi.org/10.1016/j.compositesb.2015.12.023

[NN19] G.Iannone, A.Saggese, D.D'Agostino, G.Celentano, and U.Gambardella, "Numerical Model for Quench Propagation in Composite HTS Tapes", IEEE Transaction on Applied Superconductivity, 29, (2019), 4901305. https://doi.org/10.1109/TASC.2019.2899462

[NN20] G.Iannone, D.D'Agostino, A.Saggese, G.Celentano, and U.Gambardella, "Quench Propagation in Commercial ReBCO Composite Tapes", To be published on Cryogenics

[PL16] C.Poole, T.Baig, R.J.Deissler, D.Doll, M.Tomsic, and M.Martens, "Numerical study on the quench propagation in a 1.5T MgB2 MRI magnet design with varied wire compositions", Superconductor Science and Technology, 29, (2016), 044003. http://doi.org/10.1088/0953-2048/29/4/044003

[PN08] V.Pantsyrny, A.Shikov, and A.Vorobieva, "Nb3Sn material development in Russia", Cryogenics, 48, (2008), 354–370. https://doi.org/10.1016/j.cryogenics.2008.04.006

[PR92] W.H.Press, B.P.Flannery, S.A.Teukolsky, and W.T.Vetterling, "Numerical Recipes in C: The Art of Scientific Computing", 2nd edition, Cambridge University Press, (1992). ISBN-10 0-521-43108-5, ISBN-13 978-0521431088 https://www.abebooks.it/servlet/BookDetailsPL?bi=30465897114

[QM16]   Quality Management GSI, "Bus-Bars and Voltage Taps in the SIS100 Quadrupole Modules", Document number: F-DS-MT-80e, Date: 20.06.2016. Original file name: F-DS-MT-80e_SIS100_Bus-Bars_and_Voltage_Taps_in_SIS100_QDMs_v7.0.pdf

[RB18]   C.Rubbia, "The role of elementary particle accelerators", International Journal of Modern Physics A, 33, (2018), 1844010. http://doi.org/10.1142/S0217751X18440104

[RC19]   S.Richard, F.Sirois, and C.Lacroix, "Post-processing method for extracting the resistivity of Rare-Earth Barium Copper Oxide (REBCO) coated conductors in over-critical current conditions from ultra-fast V-I pulsed current measurements", Journal of Applied Physics, 126, (2019), 023902. https://doi.org/10.1063/1.5095637

[RD00]   D.Rodrigues Jr., J.P.Barros Machado, "Development of (Nb,Ta)3Sn Multifilamentary Superconductor Wire for High Current Applications", Materials Research, 3, (2000), 99-103. https://doi.org/10.1590/S1516-14392000000400002

[RS04]   L.Rossi, "Superconducting Cable and Magnets for the Large Hadron Collider", LHC-Project-Report-694, Accelerators and Storage Rings, CERN, (2004). https://cds.cern.ch/record/729430/files/lhc-project-report-694.pdf

[RX18]   C. Roux, P. A.Bartolome, A.Bleile, E.Fischer, G.Golluccio, F.Kaether, J.Ketter, J.P.Meier, A.Mierau, C.Omet, K.Sugita, P.Szwangruber, A.Warth, H.Weiss, and P.Spiller, "Superconducting Dipoles for SIS100", 9th International Particle Accelerator Conference, IPAC2018, Vancouver, BC, Canada, WEPML035, 2768-2771. JACoW Publishing. https://accelconf.web.cern.ch/ipac2018/papers/wepml035.pdf

[RZ13]   E.Rizzo, "Simulations for the optimization of High Temperature Superconductor current leads for nuclear fusion applications", Dissertation Thesis, KIT Karlsruhe Institute of Technology Scientific Publishing, Band 014, ISBN 978-3-7315-0132-9, Print on Demand, (2013), Digitized by Google, https://doi.org/10.5445/KSP/1000037132

[SC08]   J.Schwartz, T.Effio, X.Liu, Q.V.Le, A.L.Mbaruku, H.J.Schneider-Muntau, T.Shen, H.Song, U.P.Trociewitz, X.Wang, and H.W.Weijers, "High Field Superconducting Solenoids Via High Temperature Superconductors", IEEE Transaction on Applied Superconductivity, 18, (2008), 70-81. https://doi.org/10.1109/TASC.2008.921363

[SC14]   C.H.Schroeder, F.Walter, A.Breidert, B.Streicher, T.Eisel, W.Fisel, and H.Kollmus, Poster Presented at 25th International Cryogenic Engineering Conference and the International Cryogenic Materials Conference, 2014 July 7 – 11, University of Twente, Enschede, Netherlands. Session: Wed-Af-Posters Session 2.1.; identifier No. 51. https://indico.cern.ch/event/244641/contributions/1563448/

[SC19] C.Schroeder and H.Kollmus, "Cryogenic Supply for the Series Test Facility (STF) for SIS100 Magnet Testing", Indico Talk, Lund, 07-08/10/2019. https://indico.esss.lu.se/event/1176/contributions/9681/attachments/9513/15054/2019_Cryogenic_Supply_for_the_Series_Test_Facility_Lund_HKneu.pdf

[SC99] J.R.Schrieffer, "Theory of Superconductivity", Advanced Book Classic, Westview press, Perseus Book Group, 1999. ISBN 0-7382-0120-0 https://www.abebooks.it/servlet/BookDetailsPL?bi=30315273994

[SD10] S.V.Sudyev, A.K.shikov, V.I.Pantsyrny, A.E.Vorobieva, N.A.Beliakov, V.V.Sergreev, I.A.Golovchanskly, S.M.Zzernov, and K.M.Abramushin, "Recent progress in development of Nb_3Sn internal tin strand for fusion application", 9th European Conference on Applied Superconductivity (EUCAS 09), Journal of Phys. Conf. Series 234, (2010), p.022037. https://doi.org/10.1088/1742-6596/234/2/022037

[SG15] A.Saggese, G.Iannone, U.Gambardella, N.Califano, and A.Ferrentino, "20 kA HTS Current Leads for the INFN Magnet Test Facility", IEEE Transaction on Applied Superconductivity, 25, (2015), 4801304. https://doi.org/10.1109/TASC.2014.2368052

[SH17] N.W.Ashcroft and N.D.Mermin, "Solid State Physics", Harcourt College Publishers, (1976). ISBN 0-03-083993-9 (College Edition), 5th edition, ISBN 8-13-150052-7. https://www.abebooks.it/products/isbn/9788131500521

[SL11] E.Sili, F.Koliatene, and J.P.Cambronne, "Pressure and temperature effects on the Paschen curve", Annual Report Conference on Electrical Insulation and Dielectric Phenomena, Cancun, (2011), 464-467. https://doi.org/10.1109/CEIDP.2011.6232695

[SM63] P.F.Smith, "Protection of Superconducting Coils", The Review of Scientific Instruments, 34, (1963), 368-373. https://doi.org/10.1063/1.1718368

[SN00] SuNAM, "Inspection Report", Product Type SuNAM 2G HTS Wire (to EPL), Lot No. SCN12500-1405 15-01. Private Communication.

[SN14] C.Senatore, M.Alessandrini, A.Lucarelli, R.tediosi, D.Uglietti, and Y.Iwasa, "Progresses and challenges in the development of high-field solenoidal magnets based on RE123 coated conductors", Superconductor Science and Technology, 27, (2014), 103001. https://doi.org/10.1088/0953-2048/27/10/103001

[SN16] C.Senatore, C.Barth, M.Bonura, M.Kulich, and G.Mondonico, "Field and temperature scaling of the critical current density in commercial REBCO coated conductors", Superconductor Science and Technology, 29 (2016) 014002. http://doi.org/10.1088/0953-2048/29/1/014002

[SN17]   J.B.Song, Y.H.Choi, D.G.Yang, Y.G.Kim, K.L.Kim, and H.G.Lee, "Review of core technologies for development of 2G HTS NMR/MRI magnet: A status report of progress in Korea University", Results in Physics, 7, (2017), 3264-3276. https://doi.org/10.1016/j.rinp.2017.08.046

[SR19]   F.Sirois, F.Grilli, and A.Morandi, "Comparison of Constitutive Laws for Modeling High-Temperature Superconductors", IEEE Transaction on Applied Superconductivity, 29, (2019), 8000110. https://doi.org/10.1109/TASC.2018.2848219

[SS03]   M.Sjostrom, B.Dutoit, and J.Dutoit, "Equivalent Circuit Model for Superconductors", IEEE Transaction on Applied Superconductivity, 13, (2003), 1890-1893. https://doi.org/10.1109/TASC.2003.812941

[SS06]   P.Sessa, "Misure di Correnti e stabilità in nastri superconduttori", Graduation thesis in Electronic Engineering, University of Salerno, Italy, 2006. (Unpublished)

[ST06]   A.Stenvall, A.Korpela, R.Mikkonen, and G.Grasso, "Stability considerations of multifilamentary MgB2 tape", Superconductor Science and Technology, 19, (2006), 184–189. http://doi.org/10.1088/0953-2048/19/2/006

[ST77]   H.0.Stevens, M.J.Superczynsk, T.J.Doyle, J.H.Harrison, and H.Messinger, "Superconducting Machinery for Naval Ship Propulsion", IEEE Transaction on Magnetics, MAG-13, (1977), 269-274. https://doi.org/10.1109/TMAG.1977.1059460

[SZ19]   P.Szwangruber, V.Raginel, W.Freisleben, and C.Roux, "Electro-thermal 1D model of the SIS100 superconducting dipole magnet", CHATS-AS 2019 Workshop, CHATS on Applied Superconductivity, Faculty of Mechanical Engineering and Mechatronics of the West Pomeranian University of Technology, Szczecin 2019, 9 – 12 July 2019. https://indico.cern.ch/event/776034/book-of-abstracts.pdf

[TC00]   EutecRod© 157, "Tin-Silver Brazing Rod for Stainless Steels, Brass, Bronze and Nickel Alloys", Technical Data Document, Product of Castolin, Eutectic Corporation. https://www.castolin.com/sites/default/files/EutecRod-157.pdf

[TC08]   Eutec Rod 157 DataSheet, Castolin Eutectic, Eutectic Corporation, TM 07-15 © 2008, Eutectic Corporation, ® Reg. T.M., Printed in the U.S.A.

[TK17]   T.Takagi, T.Ariyama, T.Takao, and O.Tsukamoto, "Sensitive Quench Detection of the HTS Coil with the Co-winding Coil", Teion Kogaku, 52,(2017), 44-51. ISSN 0389-2441 https://doi.org/10.2221/jcsj.52.44

[TL90]   D.R.Tilley and J.Tilley, "Superfluidity and Suerconductivity", Graduate Student Series in Physics Series, General Editors D.F.Brewer, 3rd edition, IOP Publishing Ltd., (1990). ISBN 0-75030-033-7 (pbk) https://www.abebooks.it/servlet/BookDetailsPL?bi=30452496047

[TN96]   M.Tinkham, "Introduction to Superconductivity", 2nd edition, McGraw-Hill inc., (1996). ISBN 0-07-064878-6
https://www.abebooks.it/servlet/BookDetailsPL?bi=30593831915

[TR03]   F.Trillaud, H.Palanki, U.P.Trociewitz, S.H.Thompson, H.W.Weijers, and J.Schwartz, "Normal zone propagation experiments on HTS composite conductors", Cryogenics 43, (2003), 271–279. https://doi.org/10.1016/S0011-2275(03)00044-4

[TR05]   F.Trillaud, F.Ayela, A.Devred, M.Fratini, D.Leboeuf, and P.Tixador, "Quench Propagation Ignition Using Single-mode Diode Laser", IEEE Transaction on Applied Superconductivity, 15, (2005), 3648-3651.
https://doi.org/10.1109/TASC.2005.849381

[VN07]   K.Vinod, R.G.Abhilash Kumar, and U.Syamaprasad, "Prospects for MgB2 superconductors for magnet application", Superconductor Science and Technology, 20, (2007), R1–R13. http://doi.org/10.1088/0953-2048/20/1/R01

[WH65] C.N.Whetstone and C.E.Roos, "Thermal Phase Transitions in Superconducting Nb-Zr Alloys", Journal of Applied Physics, 36, (1965), 783-791.
https://doi.org/10.1063/1.1714218

[WK00] Wikipedia contributors, "Paschen's law", Wikipedia, The Free Encyclopedia, Revision 5 May 2020 13:38. https://en.wikipedia.org/w/index.php?title=Paschen%27s_law
see also the page https://it.wikipedia.org/w/index.php?title=Curve_di_Paschen

[WL02] N.M.Wilson, "Superconducting Magnets", Oxford Clarendon Press, 2002. ISBN 0-19-854810-9 https://www.abebooks.it/servlet/BookDetailsPL?bi=30553723499

[WL08] M.N.Wilson, "NbTi superconductors with low ac loss: A review", Cryogenics 48 (2008) 381–395. https://doi.org/10.1016/j.cryogenics.2008.04.008

[WS99] Y.Iwasa, "Case study in superconducting Magnets: design and operational", 2nd Ed., Springer, 2009. ISBN 978-0-387-09799-2. https://doi.org/10.1007/b112047
https://www.abebooks.it/servlet/BookDetailsPL?bi=22818063476

[WE00] GSI Web pages, https://www.gsi.de/en/about_us/history.htm , Visited on July 2020.

[XU20] Y.Xu, T.Feng, G.Chen, X.Li, Z.Chen, Y.Yue, L.Ren, J.Shi, J.Li, W.Wang, Z.Hu, B. Zhang, Y.Tang, C.Xu, and L.Chen, "Critical Current Degradation of YBCO Tape With Different Stabilizing Layers Under Cyclic Mechanical Strains", IEEE Transactions on Applied Superconductivity, 30, (2020), 8400607. https://doi.org/10.1109/TASC.2020.2970386

[YM88] S.Yamamoto, T.Yamada, and M.Iwamoto, "Quench protection of persistent current switches using diodes in cryogenic temperature", PESC '88 Record., 19th Annual IEEE Power Electronics Specialists Conference, Kyoto, Japan, (1988), 321-325. https://doi.org/10.1109/PESC.1988.18150

[ZH06] B.Zhi-Ming, W.Xia, W.Chun-li, and W.Jin-xing, "Quench Propagation Properties Analysis of High-Temperature Superconductors Using Finite Element methods", Physica C: Superconductivity and its applications, 436 (2006), 99-102. https://doi.org/10.1016/j.physc.2006.02.004

[ZH10] G.M.Zhang, L.Z.Lin, L.Y.Xiao, Y.J.Yu, S.V.Pamidi, and J.Schwartz, "Quench Behavior of $Bi_2Sr_2Ca_2Cu_3O_xAg$ Tape With AC and DC Transport Currents and a Comparison With $YBa_2Cu_3O_x$ Conductors", IEEE Transaction on Applied Superconductivity, 20, (2010), 2146-2149. https://doi.org/10.1109/TASC.2010.2040376

[ZH16] T.Zhou, K.Ding, C.Liu, K.Lu, Q.Ran, Y.Song, E.Niu, P.Bauer, A.Devred, S.Lee, T.Taylor, and Y.Yang, "Manufacture and Test of ITER 10-kA HTSCL Prototypes", IEEE Transaction on Applied Superconductivity, 26, (2016), 4802505. https://10.1109/TASC.2016.2519421

[ZH19] D.Zhang, M.D.Sumption, M.Majoros, C.Kovacs, E.W.Collings, D.Panik, M.Rindfleisch, D.Doll, M.Tomsic, C.Poole, and M.Martens, "Quench, normal zone propagation velocity, and the development of an active protection scheme for a conduction cooled, react-and-wind, MgB_2 MRI coil segment", Superconductor Science and Technology, 32, (2019), 125003. https://doi.org/10.1088/1361-6668/ab48cd

[ZH91] Z.P.Zhao and Y.Iwasa, "Normal Zone propagation in Adiabatic Superconducting Magnets Part 1: Normal Zone Propagation velocity in Superconductive Composites", Cryogenics, 31, (1991), 817-825. https://doi.org/10.1016/0011-2275(91)90141-I

[ZL02] A.V.Zlobin, E.Barzi, D.Chichili, Yu.Huang, V.V.Kashikhin, M.Lamm, P.J.Limon, N.Mokhov, I.Novitski, T.Peterson, J.B.Strait, and S.Yadav, "Large-Aperture Nb3Sn Quadrupoles for 2 generation LHC IRs", Proceedings of EPAC 2002 Conference Paris France, C02-06-03.1, (2002), 2451-2453, FERMILAB-CONF-02-437-TD. http://inspirehep.net/record/610057/

[ZN06] R. Zanino and L. Savoldi Richard, "A review of thermal-hydraulic issues in ITER cable-in-conduit conductors", Cryogenics, 46, (2006), 541-555. https://doi.org/10.1016/j.cryogenics.2006.01.007